Dissertation zur Erlangung des Doktorgrades PhD
an der Medizinischen Fakultät der Universität Hamburg

New ways of controlling neurons with light:

optogenetic tools designed for multimodal neuronal manipulations

vorgelegt von:

Silvia Rodriguez-Rozada
aus Gijón, Spanien

Hamburg 2021

UNIVERSITÄTSKLINIKUM HAMBURG-EPPENDORF

Zentrum für Molekulare Neurobiologie Hamburg

Prof. Dr. rer. nat. J. Simon Wiegert

New ways of controlling neurons with light: optogenetic tools designed for multimodal neuronal manipulations

Dissertation

zur Erlangung des Doktorgrades Dr. rer. biol. hum. / PhD
an der Medizinischen Fakultät der Universität Hamburg

vorgelegt von:

Silvia Rodriguez-Rozada
aus Gijón, Spanien

Hamburg 2021

(wird von der Medizinischen Fakultät ausgefüllt)

Angenommen von der
Medizinischen Fakultät der Universität Hamburg am: 12.10.2021

Veröffentlicht mit Genehmigung der Medizinischen Fakultät der Universität Hamburg.

Prüfungsausschuss, der/die Vorsitzende: Prof. Dr. Simon Wiegert

Prüfungsausschuss, zweite/r Gutachter/in: Prof. Dr. Alexander Gottschalk

Prüfungsausschuss, dritte/r Gutachter/in: Prof. Dr. Stefan Herlitze

Above all, don't fear difficult moments. The best comes from them.

Rita Levi-Montalcini

Table of Contents

List of Figures

Discussion

Appendix

Research Summary

This dissertation describes the development and characterization of new optogenetic tools for the interrogation of neuronal circuits and is structured in three main parts.

Optogenetics, i.e. the use of light-sensitive proteins to manipulate cellular activities, provides a spatiotemporally precise method to reversibly turn on or off the activity of genetically defined neuronal types in intact tissue (Deisseroth et al., 2006). The versatility, minimal invasiveness, and high temporal and spatial precision of optogenetic tools, grant them several advantages over conventional methods for probing neuronal function. Thus, optogenetics is considered one of the most groundbreaking innovations in the field of neuroscience in recent years (Baker, 2011; Deisseroth, 2011) and has facilitated circuit analysis in the brain and other systems across a broad range of model organisms and behaviors (Fenno et al., 2011; Yizhar, et al., 2011).

Part I. Since its discovery, the light-gated cation channel channelrhodopsin-2 (ChR2) (Nagel et al., 2003) and several variants have been widely used for optical activation of neurons. Yet, to probe neuronal circuit function, it is often more informative to inactivate specific neurons at will. In contrast to neuronal activation, optogenetic silencing has proven to be technically more challenging. The development of anion (i.e. chloride) conducting channelrhodopsins (ACRs) by targeted mutagenesis of cation conducting channelrhodopsins (CCRs) (Berndt et al. 2014; Wietek et al. 2014) and the discovery of natural ACRs (Govorunova et al. 2015) introduced a new class of inhibitory optogenetic tools that overcome some of the limitations of the commonly used ion pumps Halorhodopsin (Han & Boyden, 2007; Zhang et al., 2007) and Archaeorhodopsin (Chow et al., 2010). In this part of my dissertation I aimed at developing novel ACRs with altered kinetics and spectrally shifted activation spectra to expand the possibilities for optical silencing of neurons.

Part II. A second, long-standing challenge is the independent optogenetic activation of two defined neuronal populations. All rhodopsins are activated to a certain extent by blue light, which hinders the combination of a blue- and a red-light sensitive opsin without cross-activation. During the course of my PhD project I characterized ChrimsonSA, a red-shifted ChR mutant with reduced blue-light sensitivity. I assessed its efficacy for neuronal spiking with far-red light and its potential use for dual-color optogenetic experiments.

Part III. Lastly, to prove necessity and sufficiency of a particular neuronal population for a specific function, it is desirable to both faithfully inhibit and activate this exact same population of neurons. Balanced co-expression of an excitatory and an inhibitory opsin in a region of interest is not trivial, especially when viral transduction of the optogenetic actuators is required *in vivo*. To overcome this challenge, I worked on the development and characterization of BiPOLES, a tool combining in a single tandem construct a cation-conducting and an anion-conducting channelrhodopsin with distinct action spectra, allowing bidirectional control of the same set of neurons using light of different wavelengths.

Results

Part I: Anion-conducting channelrhodopsins with color-shifted action spectra and altered kinetics

To extend the spectral and temporal range for ACR-mediated inhibition, our lab transferred the set of mutations used to create the first generations of ACRs to other well-characterized CCRs with a broader scope of biophysical properties. Two new ACRs with spectrally shifted activation spectra, namely Phobos (peak activation wavelength: 460 nm) and Aurora (peak activation wavelength: 520 nm), were obtained. Furthermore, introduction of a step-function point mutation (C128A) (Berndt et al., 2009) slowed-down the photocycle of the ACRs and enabled reversible switching between open and closed states using two different

wavelengths (Fig. I A). I functionally characterized these new ACR variants in hippocampal slice cultures and showed that they exhibit blue- and red-shifted action spectra and step-function properties, efficiently inhibiting neuronal activity for many seconds following a brief light flash. In addition, I performed behavioral assays on *Drosophila* larvae to evaluate the performance of the novel ACRs *in vivo*. This work is published in the journal *Scientific Reports* (Wietek et al. 2017).

Despite the vast progress in the development and identification of new ACRs, neuronal silencing for extended periods of time at the scale of several minutes to hours remains a challenge. Using our engineered blue-shifted, step-function ACR Phobos^{CA} as a basis, we further developed Aion, an ACR with an even longer-lasting conducting state that permits faithful silencing of neurons over many hours with short light pulses spaced 5 minutes apart (Fig. I B). Similar to its parental construct Phobos^{CA}, Aion can be brought back to its closed state with light of a longer wavelength, granting precisely timed termination of silencing. Since efficient Aion-mediated neuronal silencing can be sustained over time with minutes-long dark interstimulus intervals, it is an ideal tool for behavioral paradigms requiring prolonged periods of inhibition.

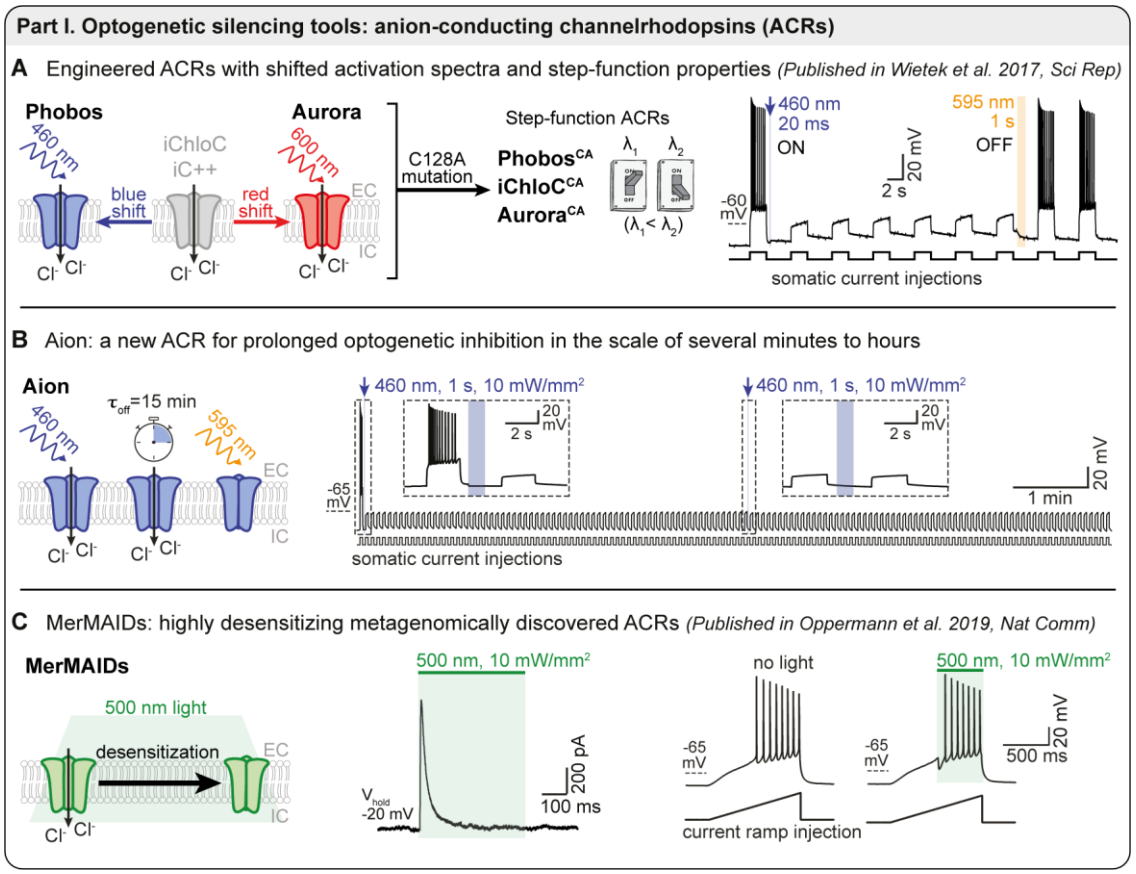

Figure I. Anion-conducting channelrhodopsins with color-shifted activation spectra and altered kinetics. (A) Left: schematic drawing showing the second generation of engineered ACRs (iChloC and iC++) and the development of the blue- and red-shifted ACRs Phobos and Aurora, respectively. Introduction of the point-mutation C128A yielded the step-function variants Phobos^{CA}, iChloC^{CA} and Aurora^{CA}, which can be toggled between ON and OFF states using light of two different wavelengths (λ_1 and λ_2). Right: membrane voltage trace showing reversible suppression of depolarization-induced spiking by photoswitching Phobos^{CA} with blue and orange light. **(B)** Left: schematic drawing of the ACR Aion highlighting its main features: reversibility and long-lasting conducting state. Right: 10-minute current-clamp recording in an Aion-expressing CA1 neuron showing efficient block of action potentials (APs) by stimulating with 1 s light pulses spaced 5 minutes apart. **(C)** Left: schematic drawing of a MerMAID channel showing its rapid desensitization during continuous illumination. Middle: MerMAID6-mediated chloride current evoked by illumination with 500 nm-light. Right: green-light illumination for 500 ms blocks single current ramp-evoked APs without affecting subsequent spiking in MerMAID6-expressing CA1 neurons.

During the course of my PhD project I also contributed to the evaluation of MerMAIDs, a new family of natural ACRs, as optogenetic tools for inhibiting neuronal activity. MerMAIDs are metagenomically identified ACRs that exhibit almost complete photocurrent desensitization with exposure to continuous bright light. When expressed in neurons, I showed that MerMAIDs can be used to block single

action potentials with high temporal precision and without affecting subsequent firing events (Fig. I C). This work is published in the journal *Nature Communications* (Oppermann et al. 2019).

Part II: ChrimsonSA, a red-shifted cation-conducting ChR with reduced sensitivity to blue light

In 2014, Chrimson was identified as the CCR variant with the most red-shifted absorption peak at 590 nm (Klapoetke et al. 2014). However, Chrimson has a broad spectral sensitivity and can also be activated by blue light. This limits the combination of Chrimson with blue-light-activated tools for dual-color optogenetics, especially when high light intensities are used. For this reason, I characterized the functionality of a new Chrimson mutant, ChrimsonSA, in hippocampal slices and showed that it shows an even further red-shifted action spectrum, less sensitivity to blue light and accelerated closing kinetics (Fig. II). These features make ChrimsonSA more suitable for dual-color applications than wild-type (WT) Chrimson is. This work is published in the journal *Nature Communications* (Oda et al. 2018).

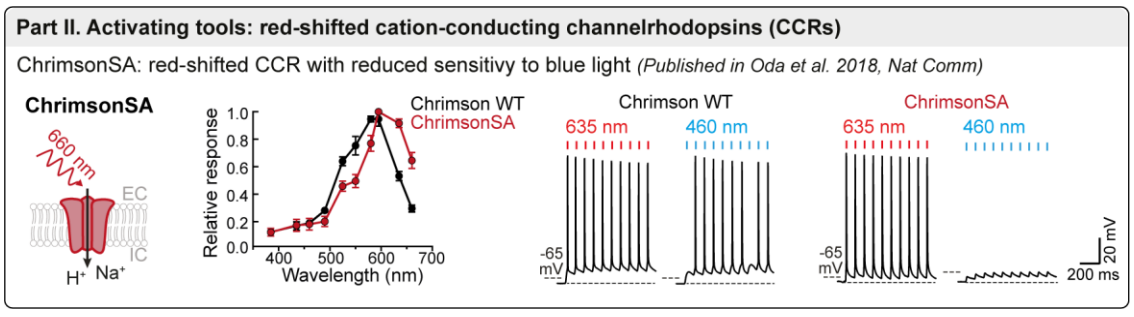

Figure II. ChrimsonSA: a red-shifted CCR with reduced sensitivity to blue light. Left: schematic drawing of ChrimsonSA (S169A, Super red-shifted and Accelerated Chrimson mutant). Middle: ChrimsonSA shows a more red-shifted activation spectrum compared to WT Chrimson. Right: action potentials can be evoked by short blue light pulses in CA1 pyramidal cells expressing WT Chrimson, but not in those expressing ChrimsonSA, at the minimum irradiance that triggers action potentials with red light.

Part III: BiPOLES, a tool for bidirectional dual-color optogenetic control of neurons

The implementation of a dual-color system for bidirectional control of neuronal activity has been a long-sought goal in optogenetics. Using the tandem gene-fusion strategy (Kleinlogel et al. 2011) as a basis, our lab developed BiPOLES in collaboration with the group of Peter Hegemann. BiPOLES is a single fusion protein combining the blue-light-sensitive ACR *Gt*ACR2 and the red-light-sensitive CCR Chrimson, enabling both inhibition and excitation of the same neurons in a single experiment with light of two different wavelengths. Unlike strategies based on an internal ribosomal entry site or self-cleaving viral 2A peptide bridges, BiPOLES displays a fixed 1:1 stoichiometry and colocalization of excitatory and inhibitory currents, so that each transduced cell exhibits the same excitation-inhibition ratio. I validated the bidirectional action and the applicability of BiPOLES and somBiPOLES (a soma-targeted and trafficking-optimized version of BiPOLES) as optogenetic tools in rat hippocampal slice cultures. BiPOLES enables potent and reliable blue-light-mediated silencing and red-light-mediated spiking of pyramidal neurons (Fig. III). Furthermore, since *Gt*ACR2 shunts any residual Chrimson-mediated excitatory photocurrents in the blue part of the spectrum, I combined BiPOLES with a second, blue-light sensitive CCR for independent excitation of two distinct neuronal populations using red and blue light, respectively. Lastly, I showed that BiPOLES allows wavelength-dependent optical tuning of the membrane voltage.

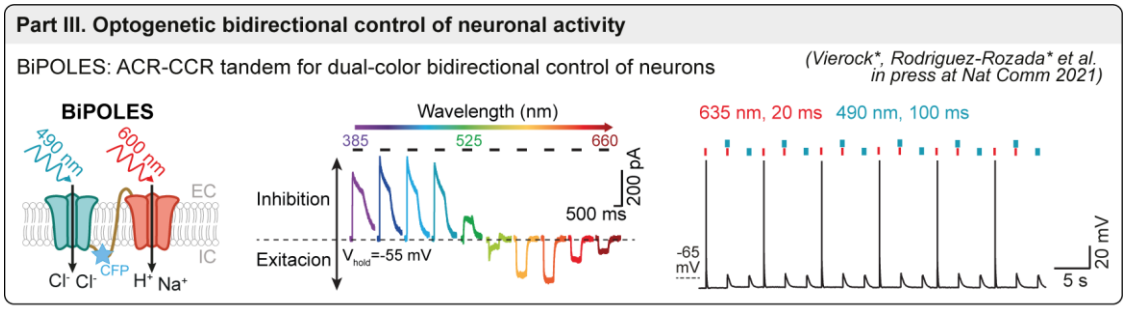

Figure III. BiPOLES: a tool for bidirectional dual-color optogenetic control of neurons. Left: schematic drawing of BiPOLES depicting the fusion of the blue-light-sensitive *Gt*ACR2 with the red-light-sensitive Chrimson via a transmembrane linker containing a cyan fluorescent protein. Middle:

Photocurrents of a BiPOLES-expressing CA1 neuron showing anion- and cation-conductances in a wavelength-dependent manner. Right: bidirectional optical spiking-control with somBiPOLES. Action potentials are elicited with red light and can be blocked by a concomitant blue light pulse.

Conclusions

Optogenetics has revolutionized the field of neuroscience by facilitating specific manipulation of neuronal populations. The new optogenetic tools presented in this study expand the possibilities for optical control of neuronal networks. While Phobos and Aurora expand the available toolkit of optogenetic silencers in the spectral range, Aion broadens it in the temporal domain, allowing inhibition of neurons at the scale of several minutes to hours. ChrimsonSA is suitable for neuronal spiking with far-red light beyond 600 nm. Finally, BiPOLES allows multiple new applications including reliable bidirectional control of neuronal activity dual-color spiking of two distinct populations when used together with a second, blue-light sensitive CCR, and optical tuning of the neuronal membrane voltage.

1. Introduction

One of the fundamental quests in neuroscience research is to unravel the neural substrates underlying specific brain functions and behaviors. Understanding how different kinds of neurons interact with each other to implement a specific computation requires tools to precisely control neuronal activity, as well as compatible readout methods. Classical neuronal manipulation techniques such as electrical stimulation cannot readily distinguish different neuronal types and affect all cells within a given volume. In contrast, pharmacological and genetic manipulations can be specific to cells with certain expression profiles, but lack temporal and spatial precision, often displaying slow kinetics and poor reversibility.

In 1979, Nobel laureate Francis Crick indicated that one major prerequisite for understanding neuronal circuits was to develop "*a method by which all neurons of just one type could be inactivated, leaving the other more or less unaltered* " (Crick, 1979). Crick later speculated that light would be an ideal signal to control neurons in a rapid manner (Crick, 1999). Despite setting a conceptual inspiration for optogenetics, a technology to engineer a particular cell type to be sensitive to light seemed, at the time, far-fetched.

Rhodopsins of vertebrate and invertebrate eyes are naturally occurring light-sensitive proteins, mainly responsible for animal vision, but also play roles in circadian rhythm and pigment regulation (Shichida & Yamashita, 2003). These type II opsins, consist of a G-protein-coupled receptor (GPCR) bound to the chromophore retinal (Palczewski et al., 2000), and were one of the first experimental strategies used to render neurons light sensitive. More specifically, light stimulation of hippocampal neurons expressing chARGe, a combination of three *Drosophila* proteins, namely an Arrestin-2, a blue-light sensitive Rhodopsin, an α G_q-protein subunit, resulted in selective neuronal firing (Zemelman et al., 2002). However, while chARGe represents the first light-driven tool to optically evoke action potentials

(APs) in mammalian cells, it exhibited slow kinetics and high cell-to-cell variability, mainly due to its multicomponent nature.

The emergence of a single-component, rapid system was key for the broader adoption of optogenetics, and channelrhodopsins (ChRs), directly light-gated cation-conducting channels, held the answer (Nagel et al., 2002, 2003; Zhang et al., 2011). The microbial type I opsins ChR1 and ChR2 were identified in a DNA data bank from the green algae *Chlamydomonas reinhardtii* and further cloned and expressed in *Xenopus* oocytes and human kidney embryonic (HEK) cells, where large light-induced membrane depolarizations were successfully recorded (Nagel et al., 2002, 2003). In 2005, ChR2 was used to optically evoke APs with millisecond-precision in cultured hippocampal neurons (Boyden et al., 2005). Furthermore, in that same year, the lab of Stefan Herlitze applied ChR2 to drive neuronal activity in intact embryos *in ovo*. In addition, they used the vertebrate rhodopsin RO4 to inhibit AP firing via hyperpolarization of the somato-dendritic membrane as well as presynaptically via reduction of neurotransmitter release (Li et al., 2005). At that time, the term “optogenetics” emerged to refer to the combination of optics and genetics to control well-defined events within specified cells of living tissue (Deisseroth et al., 2006). The high spatial and temporal precision of optogenetic tools overcame the main limitations of previous methods and revolutionized the field of neuroscience by facilitating specific manipulation of neuronal populations to address questions ranging from the synaptic to the behavioral level.

1.1. Optogenetic silencers

Loss-of-function experiments test necessity of a neuronal population for a specific circuit function. To achieve effective and robust neuronal silencing, inhibition strategies must suppress action potential (AP) initiation or propagation and/or block synaptic neurotransmitter release for the entire duration of the experiment. In contrast to optogenetic excitation, which typically entails depolarization by an

increased cation conductance, optogenetic inhibition employs a wide range of cellular mechanisms (Fig. 1.1), each having their inherent biological, physical and electrochemical constraints (for a review see Wiegert et al., 2017).

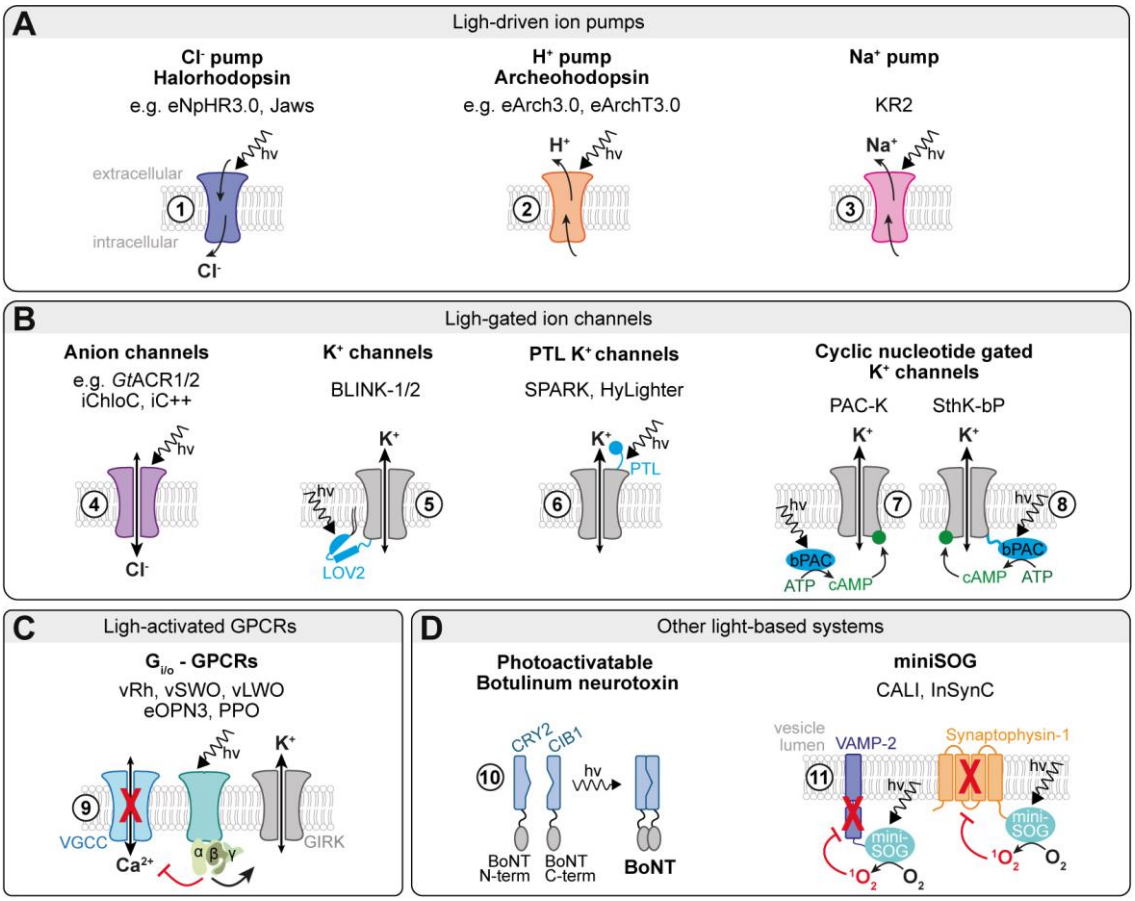

Figure 1.1. Optogenetic tools for neuronal silencing. Overview of optogenetic silencers applied in neurons, grouped according to their mechanism of action. See main text for tool-specific references. Inspired by Wiegert *et al.* (Wiegert et al., 2017). **(A)** The group of light-driven microbial rhodopsin pumps comprises chloride pumps (1), proton pumps (2) and sodium pumps (3). **(B)** The group of light-gated ion channels can be subdivided in two main classes: anion-conducting channelrhopsins (4) and potassium (K^+) channels (5-8). The latter includes LOV-domain-activated K^+channels (5), K^+ channels coupled to photoswitched tethered ligands (PTL) (6), and cyclic nucleotide-gated K^+ channels coupled to the photoactivated adenylyl cyclase bPAC (with bPAC free in the cytosol or fused to the channel, 7 and 8, respectively). **(C)** Light-activated G-protein-coupled receptors (GPCRs). Depending on the cell compartment GPCRs can act through G-protein-coupled inward-rectifying K^+ (GIRK) channels (somatodendritic inhibition), or by blocking voltage-gated calcium channels (VGCC) (synaptic inhibition, mainly eOPN3 and PPO). **(D)** Other light-based systems include the photoactivatable botulinum neurotoxin B (BoNT) (10), which can be reconstituted upon illumination by interaction of the CRY2 and CIB1 photodimerizers, and miniSOG-based tools (11) that damage the vesicle release machinery by light-driven oxidation of the synaptic vesicle proteins VAMP-2 or synaptophysin-1.

1.1.1. Light-driven ion pumps

One direct approach to prevent a neuron from firing is to hyperpolarize it, hence increasing the voltage difference between the membrane potential and the AP threshold. This mechanism was utilized by light-driven ion pumps originating form archaea, fungi or bacteria (Fig. 1.1 A). Neural hyperpolarization can be achieved either by transporting anions inside the cell, or by moving cations or protons from the intracellular to the extracellular space. In 2007, two years after ChR2 allowed light-evoked neuronal spiking (Boyden et al., 2005; Li et al., 2005), the light-driven inward directed chloride (Cl^-) pump halorhodopsin from *Natronomonas pharaonis* (*Np*HR) was applied to block AP firing in neurons (Han & Boyden, 2007; Zhang et al., 2007). In the following years, the light-driven outward directed proton pump archaerhodopsin (Arch) (Chow et al., 2010) and the sodium pump KR2 (Inoue et al., 2013) entered the pool of inhibitory tools.

Ion pumps transport only one ion per absorbed photon, thus requiring high expression levels at the plasma membrane and high light irradiances for efficient neuronal silencing. Vast optimization efforts led to the enhanced versions of Arch (eArch3.0 and eArchT3.0) (Mattis et al., 2011) and *Np*HR (eNpHR3.0) (Gradinaru et al., 2010) that are most commonly used today, along with the engineered red-shifted Cl^- pump Jaws (Chuong et al., 2014a). Nevertheless, ion pumps still present several limitations, such as inactivation when illuminated for prolonged periods of time (Mattis et al., 2011) and alterations of cellular ion homeostasis. Sustained activation of the H^+ pump Arch results in an increase in intracellular pH (Mahn et al., 2016), while the Cl^- pump *Np*HR temporarily shifts the Cl^- reversal potential, eventually leading to *gamma*-aminobutyric acid (GABA)-mediated excitation (Raimondo et al., 2012).

1.1.2. Light-activated ion channels

A second class of inhibitory optogenetic tools that overcome some of the limitations of the ion pumps are light-gated ion channels selective for Cl^- or

potassium (K^+) (Fig. 1.1 B), which ideally conduct many ions per absorbed photon. In contrast to ion-pumping rhodopsins that actively translocate ions across the plasma membrane in a given direction independent of electrochemical gradients, ion flux through light-gated channels depends on the driving force for the conducted ion. Since in most mature neurons, both the Cl^- and K^+ reversal potentials are close to or more negative than the resting membrane potential (typically between -65 mV and -75 mV), opening of light-gated Cl^- or K^+ channels efficiently ''shunts'' membrane depolarization, preventing the generation of new APs.

Light-activated anion channels

In 2012 the crystal structure of the ChR chimera C1C2 was resolved (Kato et al., 2012), opening new possibilities for researchers to engineer ChRs in order to convert the channel's ion selectivity from cations to anions. Two different strategies led to ChR variants with increased anion selectivity. While this marked a milestone in the field of optogenetic tool development, the first engineered ACRs (eACR), namely ChloC (Wietek et al., 2014) and iC1C2 (Berndt et al., 2014), still showed residual proton conductance, limiting their use as silencing tools. Further improvements yielded the highly anion-selective eACRs iChloC (Wietek et al., 2015a) and iC++ (Berndt et al., 2016).

One benefit of engineering ACRs from existing CCRs, is the large array of well-described CCR variants and mutants with diverse biophysical properties. Of particular interest are CCR variants with slow off-kinetics that allow sustained modulation of neuronal activity without continuous light delivery (Yizhar et al., 2011). These so-called step-function ChRs were generated by mutating the residues cysteine-128 (C128) and aspartic acid-156 (D156), which are referred to as the DC-gate (Kato et al., 2012; Volkov et al., 2017) (Fig. 1.2 A). Mutations in this pair decelerate the photocycle of ChR2 by modulating the interaction with the retinal, stabilizing and extending the lifetime of the conducting state (Bamann et al., 2010;

Berndt et al., 2009) (Fig. 1.2 B, C). Notably, the accumulation of channels in the conducting state after photoactivation yields orders-of-magnitude greater operational light sensitivity and therefore, step-function ChR variants require lower photon flux to stay open over time. Furthermore, closing can be accelerated using light of a longer wavelength (Fig. 1.2 B, green arrow) (Berndt et al., 2009). Based on these CCR variants with slow off-kinetics, step-function eACRs had been developed by targeted introduction of point mutations in the DC-gate residues . Step-function eACRs do not only show enhanced operational light sensitivity but also allow sustained neuronal inhibition for several seconds with a single light flash (Berndt et al., 2014, 2016; Wietek et al., 2014). In particular, the D156N ChloC mutant (slowChloC) showed a mean open state lifetime of ~10 s (Wietek et al., 2014), and for the C128A iC++ mutant (SWiChR++) a closing time constant of 115.5 ± 9.0 s was reported (Berndt et al., 2016). Moreover, photoswitching the bi-stable eACR SWiChR++ between open and closed states using light of different wavelengths enabled precise termination of silencing (Berndt et al., 2016).

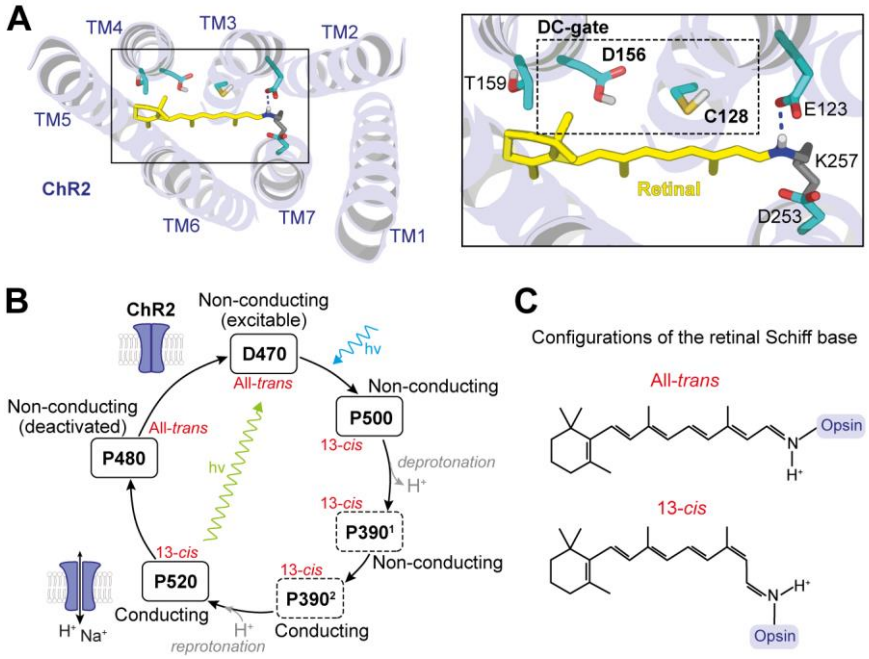

Figure 1.2. Structural model and photocycle of ChR2. (A) ChR2 model structure as seen from the extracellular side of the plasma membrane (modified from Supplemental Fig. 1 in (Wietek et al., 2014)). The retinal chromophore is shown in yellow. Inset shows a magnified view of the retinal

binding pocket, highlighting the residues D156 and C128 that form the DC-gate. **(B)** Model for the photocycle of ChR2 (based on (Ritter et al., 2008)). The configuration of the retinal Schiff base in each photocycle step is shown in red. The closed dark state D470 is converted by a light-induced (blue arrow) isomerization of retinal into the intermediate P500, which via transient Schiff base deprotonation leads to the early intermediate $P390^1$. $P390^1$ converts into the late $P390^2$, and after reprotonation of the Schiff base and subsequent structural alterations the fully open state P520 is reached. Translocation of cations across the membrane occurs during the late $P390^2 \leftrightarrow$P520 equilibrium. The recovery of the D470 dark state proceeds thermally via the P480 intermediate. Alternatively, the closed D470 state can be recovered directly by green light absorption of P520 (green arrow). In ChR step-function variants (C128/D156 mutants), the lifetime of the conducting state P520 is extended, and green-yellow light can be used to accelerate the closing kinetics of the channel (Berndt et al., 2009). **(C)** Distinct configurations of the retinal Schiff base. Top: retinal in the all-*trans* state, as found in the dark state of ChR2. Bottom: retinal in 13-*cis* configuration.

In parallel to the development of eACRs from CCRs, natural light-gated anion-conducting ChRs (nACRs) were identified by genomic screening from the cryptophyte alga *Guillardia theta* (Govorunova et al. 2015). The green and blue-light sensitive *Gt*ACR1 and *Gt*ACR2, respectively, exhibit several-fold larger photocurrents than the engineered ACRs, and have been extensively used over the past years in numerous model organisms such as mice, *D. melanogaster*, *C. elegans* and zebrafish (Li et al., 2019; Mahn et al., 2018; Mohamed et al., 2017; Mohammad et al., 2017; Yamanashi et al., 2019). Since the discovery of the first nACRs, extensive screening efforts have led to the identification of new families of nACRs with a wide variety of biophysical properties (see *Box 1* for a more detailed overview of the timeline of ACR development and discovery).

Upon illumination, ACRs function in a similar way to endogenous ionotropic $GABA_A$ receptors, and therefore, the ability of ACRs to inhibit neuronal activity depends on the intrinsic ability of Cl^- to shunt membrane depolarization in a given system or experimental condition. For this reason, in cases where the Cl^- reversal potential is depolarizing, such as early stages during development, or in specific cellular compartments (i.e. axon terminals) (Kaila et al., 2014; Wright et al., 2011), alternative silencing methods should be considered.

Light-activated potassium channels

Light-activated K^+ channels have the potential to overcome the limitations posed by ACRs in cases where the Cl^- reversal potential is depolarizing. Since K^+ conductance underlies the resting state of neurons, activation of K^+ channels leads to inhibition via hyperpolarization without major changes in transmembrane ion gradients, mimicking nature's own repolarization mechanism (Simpson et al., 1988). However, no naturally occurring light-gated K^+ channel has been reported to date, and engineering of a purely selective K^+ channel from a general CCR has not yet been successful. An alternative strategy consisted of covalently attaching synthetic photoswitched tethered ligands (PTLs) to either a natural or a chimeric K^+ channel, which yielded the tools SPARK (Banghart et al., 2004) and HyLighter (Janovjak et al., 2010), respectively (Fig. 1.1, 6). While PTL-gated K^+ channels allow reversible activation and inactivation of a K^+ current upon illumination, the requirement to deliver an additional cofactor (i.e. the PTL) has hampered their widespread application. A different approach was followed to develop the blue-light-induced K^+ channel BLINK1 (Cosentino et al., 2015), consisting of the photosensory domain LOV2 fused to the small viral K^+ channel Kcv (Fig. 1.1, 5). The initial BLINK1 was further improved to BLINK2 (Alberio et al., 2018), however none of the variants have been extensively used by the neuroscience community, mainly due to poor expression in mammalian cells.

***Box 1**. Emergence of anion-conducting channelrhodopsins*

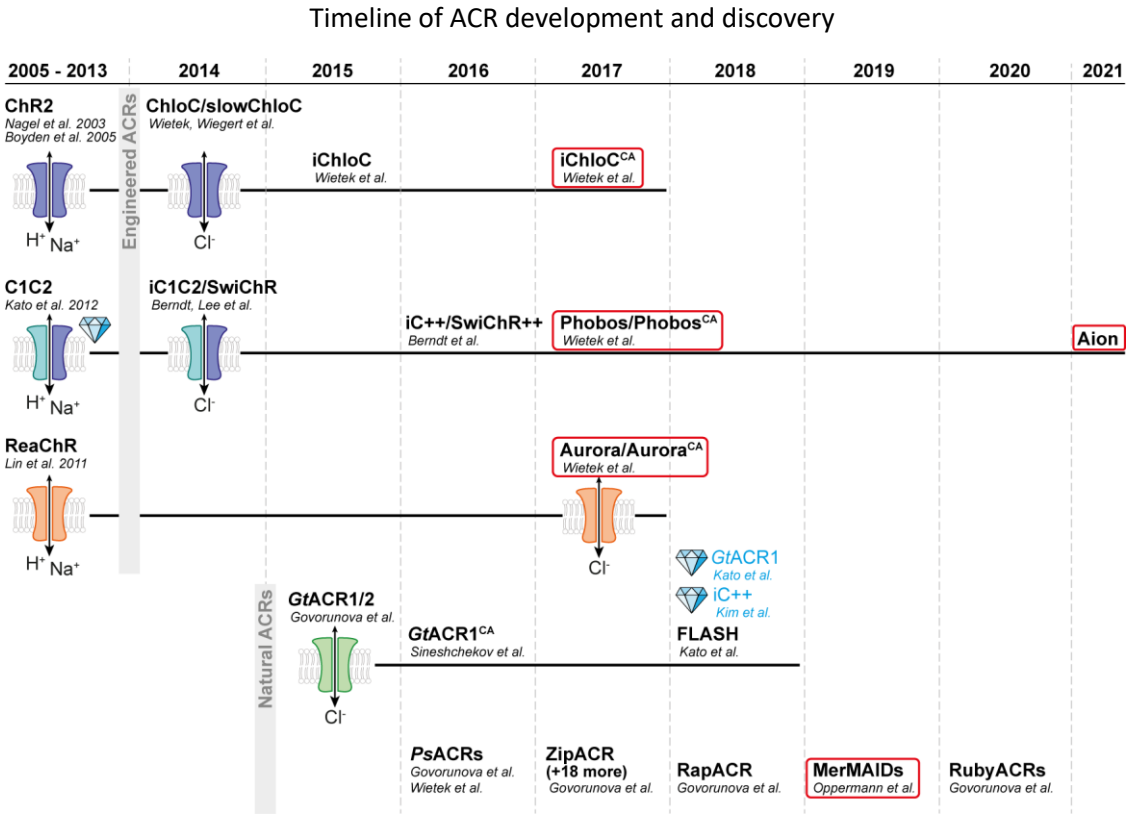

The first **engineered ACRs** (eACRs) were developed in 2014 using two different site-directed mutagenesis strategies. This was possible because the crystal structure of the ChR chimera C1C2 was resolved in 2012 (indicated by the crystal symbol). One engineering approach used ChR2 as a template and exchanged a single acidic amino acid for a basic one (E90R) in the central gate of the channel, which yielded the eACRs ChloC and slowChloC (Wietek et al., 2014). The second strategy was based on replacing negative amino acids in the extracellular outer pore of C1C2 for positive or neutral ones, leading to the eACR iC1C2. In addition, adding a step-function mutation (C128A) yielded SwiChR, the first bistable ACR (Berndt et al., 2014). In 2015 and 2016, improved versions of the initial eACRs were developed that showed no residual proton conductance and high-anion selectivity. iChloC was derived from ChloC (Wietek et al., 2015a), and iC++ and SwiChR++ from iC1C2 and SwiChR, respectively (Berndt et al., 2016). In 2017, iChloC^{CA}, a step-function version of iChloC was generated by adding the point mutation C128A (Wietek et al., 2017). In the same study, blue- and red-shifted eACRs variants were developed. The blue-light activated Phobos, and its step-function version Phobos^{CA}, were derived from iC++; while the red-shifted variants Aurora and Aurora^{CA} were based on the red-light sensitive CCR ReaChR. During the course of my PhD project our lab developed Aion, a new eACR based on Phobos^{CA} that shows the longest known conducting state.

The **natural ACRs** (nACRs) *Gt*ACR1 and *Gt*ACR2 were identified in the genome of the cryptophyte alga *Guillardia theta* and first described in 2015 (Govorunova et al., 2015). A

year later, a step-function mutation was introduced in the nACR *Gt*ACR1, yielding *Gt*ACR1^{CA} (Sineshchekov et al., 2016). Also in 2016, new green-light absorbing nACRs were discovered from *Proteomonas sulcata* (Govorunova, et al., 2016; Wietek et al., 2016). Throughout 2017 and 2018, the Spudich lab identified several nACR homologs in the transcriptomes of diverse cryptophyte species. In particular, ZipACR and RapACR were interesting tools for precise photoinhibition of individual APs even at high frequencies, due to their fast kinetics. Moreover, in 2018 the crystal structures of the nACR *Gt*ACR1 (Kato et al., 2018) and the eACR iC++ (Kim et al., 2018) were resolved, providing new mechanistic insights that led to the generation of FLASH, a mutated fast variant of *Gt*ACR1 (Kato et al., 2018). In 2019, MerMAIDs, a new family of metagenomically discovered marine anion-conducting and intensely desensitizing ChRs were described (Oppermann et al., 2019). In 2020, Govorunova and colleagues reported a previously unknown family of nACRs, which they named RubyACRs as they exhibit the most red-shifted absorption spectra up to date (Govorunova et al., 2020).

The ACRs that I have functionally characterized in neurons and constitute one of the main topics described in this dissertation are highlighted by a red frame. For further details see the Results section 3.1.

More recently, two similar strategies were used to design a K^+-based hyperpolarizing tool, based on the combination of a *Beggiatoa* photoactivated adenylyl cyclase (bPAC) with a cyclic nucleotide-gated (CNG) K^+ channel (Beck et al., 2018; Bernal Sierra et al., 2018) (Fig. 1.1, 6-7). Blue light activates either a soluble (Bernal Sierra et al., 2018) or a channel-linked (Beck et al., 2018) variant of bPAC, which in turn catalyzes the conversion of adenosine triphosphate (ATP) to cyclic adenosine monophosphate (cAMP). cAMP then binds to the small cAMP-gated K^+ channel SthK, resulting in robust K^+ efflux and subsequent hyperpolarization. The silencing efficacy of both tools, PAC-K (Bernal Sierra et al., 2018) and SthK-bP (Beck et al., 2018), has been shown in invertebrate *in vivo* models. Additionally, PAC-K was used to suppress hippocampal CA1 unit activity in anesthetized mice (Bernal Sierra et al., 2018). While these new cAMP/K^+-based tools could be of particular interest for situations in which ACRs cannot be applied due to a depolarizing Cl^- reversal potential, cAMP-mediated side effects, such as induction of intracellular signaling cascades or changes in cellular metabolism and

gene expression, cannot be excluded and should be taken under consideration for each experimental setting.

1.1.3. Light-activated G-protein-coupled receptors

GPCRs are seven-transmembrane proteins that couple to heterotrimeric G proteins or to ß-arrestin, triggering canonical signaling pathways that control a wide range of cellular processes and physiological functions (Premont & Gainetdinov, 2007). In the context of neuronal silencing, GPCRs coupled to the $G_{i/o}$ protein class are of particular interest, as they reduce adenylyl cyclase activity, inactivate voltage gated calcium channels (VGCCs) and activate G-protein coupled inwardly rectifying K^+ (GIRK) channels (Wettschureck & Offermanns, 2005), all processes then can mediate hyperpolarization or inhibition of neurotransmitter release (Fig. 1.1 C). In animals, visual perception is mediated by type-II rhodopsins, which are light-activated GPCRs. When heterologously expressed in neurons, vertebrate rhodopsins (vRh) from rod cells can couple to $G_{i/o}$ proteins, and on that account, vRh-4 (RO4) was the first light-sensitive protein used to reduce neuronal excitability in mammalian neurons *in vivo* (Li et al., 2005). A potential limitation of vRh is that upon light absorption, the retinal undergoes an isomerization form 11-*cis* to all-*trans*, which then dissociates from the opsin – an effect known as bleaching – and must then be replaced by a fresh 11-*cis* retinal molecule for another round of signaling (Hofmann et al., 2009). Hence, vRh photocycle and continued action depend on the availability of 11-*cis* retinal. However, this seems not to be an issue in the mammalian brain, where sufficient amounts of *cis*-retinal are present. Indeed, rhodopsins from murine visual cones were shown to enable repetitive photoactivation of $G_{i/o}$ signalling (Masseck et al., 2014).

In contrast to vRh, invertebrate rhodopsins and other bi-stable opsin-based pigments do not release the retinal after light absorption, thus showing reduced photobleaching. The resulting stable photoproducts revert to their original dark state

upon subsequent light absorption, which allows wavelength-dependent regulation of signal transduction (Koyanagi & Terakita, 2014). (Masseck et al., 2014). Recently, two novel photoswitchable GPCR-based opsins for rapid and reversible optical control of the inhibitory $G_{i/o}$ protein signaling pathway were reported. One of them, termed eOPN3, is a mosquito-derived homolog of the mammalian encephalopsin/panopsin (Mahn et al., 2021); while the other is a lamprey parapinopsin (PPO) (Copits et al., 2021). Both eOPN3 and PPO inhibit neurotransmitter release in a similar manner to native presynaptic metabotropic $GABA_B$ receptors. Upon illumination, $G_{i/o}$ signaling in presynaptic terminals reduces the probability of neurotransmitter vesicle release through various mechanisms: (1) inhibition of voltage-gated Ca^{2+} channels; (2) interference with the SNARE complex, i.e. the protein machinery that facilitates the fusion of synaptic vesicles; and (3) reduction in cAMP production by inhibiting adenylyl cyclase (Copits et al., 2021; Mahn et al., 2021). These light-activated GPCR-based tools open new possibilities for silencing axonal projections and synaptic transmission with precise spatiotemporal resolution, which was not easily achievable with previous methods.

However, eOPN3 and PPO are less potent for somatic inhibition, as compared to other K^+-channel-based hyperpolarizing tools (Beck et al., 2018; Bernal Sierra et al., 2018) or soma-targeted ACRs (Mahn et al., 2018). Notably, the use of $G_{i/o}$-mediated inhibition for the manipulation of neuronal activity depends on the intracellular G-protein content and the presence of other effector proteins, which might differ among cell types and subcellular compartments.

1.1.4. Other light-based systems

An alternative approach to decrease synaptic transmission is the use of a photoactivatable botulinum neurotoxin B (BoNT) (Liu et al., 2019) (Fig. 1.1, 10). Blue-light-induced reconstitution of BoNT results in robust proteolysis of the synaptic vesicle protein VAMP-2, a SNARE protein required for neurotransmitter release.

Synaptic inhibition using this tool has been demonstrated in brain slices and *C.elegans* (Liu et al., 2019).

Another strategy for optogenetic inhibition by disruption of presynaptic vesicular release is based on miniSOG (mini Singlet Oxygen Generator) (Fig. 1.1, 11). miniSOG is a genetically encoded tool for reactive oxygen species generation in response to blue light (Shu et al., 2011). Fusion of miniSOG to the synaptic vesicle proteins VAMP-2 or synaptophysin-1 inactivates the release machinery via light-mediated protein oxidation (InSynC; Lin et al., 2013).

However, both the photoactivatable BoNT and the miniSOG-based system are not as temporally precise as direct optogenetic manipulations, and are therefore more suitable for chronic experiments that require synaptic inhibition in the range of many minutes to hours.

1.2. Red-shifted optogenetic activators

Low transmission of visible light in organic tissue is one of the major drawbacks in optogenetics, making it especially challenging to target deep brain regions in *in vivo* experiments. In this context, red-light-activated ChR variants (Fig. 1.3) are particularly interesting, as longer wavelength light allows deeper tissue penetration (Johansson, 2010; Yaroslavsky et al., 2002), enhancing the usefulness of the tools both in basic scientific research and in translational or clinical applications (Chen et al., 2021; Sengupta et al., 2016). Moreover, red-light-activated ChRs enable dual-color experiments in combination with blue-light-activated optogenetic tools (Klapoetke et al., 2014).

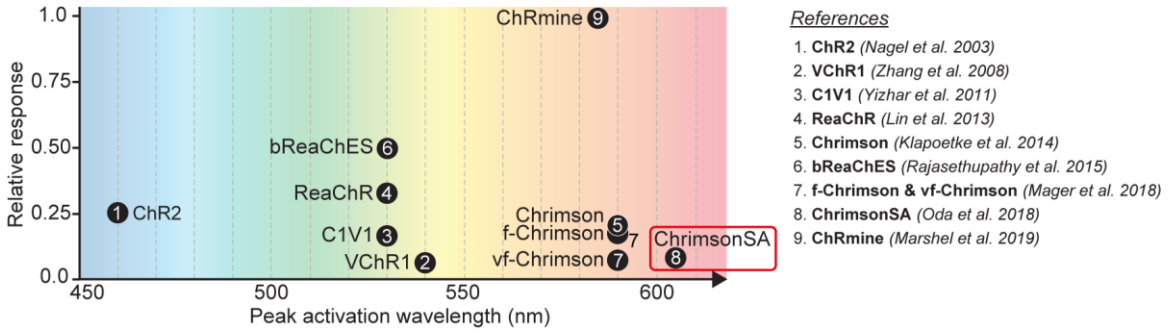

Figure 1.3. Overview of red-shifted cation-conducting channelrhodopsins (CCRs). Schematic diagram showing the currently available red-shifted CCRs sorted according to their reported peak activation wavelength (x axis) and approximate photocurrent amplitude (y axis) relative to the most potent red-CCR ChRmine. The blue-light-activated ChR2 is shown for comparison. Grey dashed lines indicate increments in wavelength of 10 nm. CCRs are numbered according to their year of publication (corresponding references are listed on the right). The red frame highlights ChrimsonSA, a Chrimson mutant with the most red-shifted activation spectrum, which I have functionally characterized in hippocampal organotypic slices. For further details see the Results section 3.2.

The first CCR activated by red-shifted light was identified from the alga *Volvox carteri* (Zhang et al., 2008). *Volvox carteri* ChR1 (VChR1) shows maximum excitation at 540 nm, which is ~80 nm red-shifted compared with the original ChR2 from *Chlamydomonas reinhardtii* (Nagel et al., 2003) (Fig. 1.3). However, VChR1 exhibited poor expression in mammalian neurons, yielding only small photocurrents and limiting its application (Zhang et al., 2008). To overcome this issue, in the following years several engineered VChR1 constructs, such as C1V1 (Yizhar et al., 2011) and ReaChR (Lin et al., 2013) were developed, which maintained the red-shifted activation spectrum of VChR1 while yielding enhanced photocurrents. Notably, the large current of ReaChR allowed to use light at off-peak wavelengths above 600 nm to achieve efficient activation of neurons through intact bone in adult mice (Lin et al., 2013). In a later study, ReaChR was further modified to generate a red-shifted opsin termed bReaChES with higher light-induced spiking fidelity and robust trafficking in long-range projections (Rajasethupathy et al., 2015).

In 2014, Chrimson, a ChR from *Chlamydomonas noctigama*, was identified as the most red-shifted CCR variant to date with an absorption peak at 590 nm (Klapoetke et al., 2014) (Fig. 1.3). In the same study, Klapoetke and colleagues

discovered Chronos, a blue/green light-drivable ChR with high light sensitivity, and successfully combined it with Chrimson for two color activation of independent neuronal populations in mouse brain slices using blue (470 nm) and red (625 nm) light, respectively. In recent years, several Chrimson mutants with accelerated closing kinetics have been engineered (Mager et al., 2018; Oda et al., 2018). Of special interest for optogenetic applications is f-Chrimson, a mutant which shows 4-fold faster kinetics without a compromised photocurrent amplitude, enabling high frequency spiking up to 100 Hz with short 595 nm-light pulses in mouse auditory cortex neurons *in vivo* (Mager et al., 2018).

In addition to combinatorial experiments with blue-light-activated tools, opsins with red-shifted activation wavelengths are better suited for simultaneous two-photon calcium (Ca^{2+}) imaging, since they allow experimental integration of commonly used green fluorescent reporter tools with minimal optical cross-talk. Several studies have successfully used C1V1 in combination with GCaMP Ca^{2+} sensors (Chen et al., 2013; Nakai et al., 2001) for all-optical manipulation and imaging of neural circuit activity with cellular resolution *in vivo* (Packer et al., 2015; Rickgauer et al., 2014; Yang et al., 2018). However, due to the slow kinetics and low conductivity of the opsin C1V1, light-evoked spikes show significant jitter (5.6 ± 0.8 ms; Packer et al., 2015) and the number of neurons that can be photostimulated simultaneously is limited (for a review see Emiliani et al., 2015). Recently, a new naturally-occurring red-shifted CCR has been identified through structure-guided genome mining. This newly discovered opsin termed ChRmine (Marshel et al., 2019) is two orders of magnitude more light-sensitive than ReaChR and Chrimson. The extremely large photocurrents of ChRmine (Fig. 1.3) and its efficient two-photon excitation enable two-photon optogenetics with millisecond spike-timing fidelity (Marshel et al., 2019). Furthermore, a new study has successfully stimulated ChRmine-expressing neurons in deep brain regions such as the ventral tegmental area (VTA) and the dorsal raphe nucleus using a transcranial light source, thus

controlling neural circuits without the need for intracranial surgery (Chen et al., 2021).

Although red-shifted ChRs overcame to some extent the obstacle of light scattering in brain tissue, they only allow for combination with blue light-sensitive ChRs under limited and carefully controlled illumination conditions, due to a still considerable activation of the red-shifted CCRs in the blue part of the spectrum (Lin et al., 2013; Yizhar et al., 2011). More specifically, Yizhar et al. combined the C1V1 mutant E122T/E162T (C1V1-ET/ET), which shows stronger photocurrents and faster off-kinetics than the parental CCR, with the blue-light-activated enhanced ChR2 mutant ChR2(H134R) (Nagel et al., 2005), to achieve specific activation of cortical pyramidal neurons or parvalbumin interneurons in mice with 560-nm and 405-nm light, respectively (Yizhar et al., 2011). An additional study concerning independent two-color activation of distinct neuronal types in *C. elegans* reported activation of C1V1-ET/ET even at 400 nm (3–3.5 % activation at 0.5 mW/mm^2; no notable responses at 0.01 mW/mm^2). Therefore, implementation of a dual-color excitation paradigm required the generation of a highly efficient blue ChR2, the H134R/T159C double mutant (ChR2-HR/TC) to achieve blue-light activation with low light intensities that would not co-activate C1V1-ET/ET (Erbguth et al., 2012).

Due to its red-shifted activation spectrum Chrimson represents one of the most promising ChRs for many applications, however, it is important to notice that, as previously shown for C1V1-ET/ET, the remaining blue-light sensitivity of Chrimson demands careful adjustment of irradiance to avoid cross-talk when used in combination with blue-light-activated tools. In this regard, Chrimson-expressing cells were shown to start spiking when stimulated with blue light at irradiances above 0.5 mW/mm^2 (Klapoetke et al., 2014), leaving only a narrow energetic window to exclusively activate the blue-light driven ChR. Therefore, in order to achieve truly independent two-color excitation of distinct neuronal populations a more red-shifted

CCR with less blue-light sensitivity is required. Alternatively, a system that counteracts the activation of the red-light sensitive CCR in the blue part of the spectrum could also circumvent the cross-activation issue.

1.3. Optogenetic bidirectional control of neurons

To prove necessity and sufficiency of a particular neuronal population for a specific function, it is desirable to both faithfully inhibit and activate this exact same population of neurons. While optogenetic interventions in principle allow such experiments, excitation and inhibition of the neuronal population of interest is commonly done in separate experiments, where either an excitatory or an inhibitory opsin is expressed. Alternatively, if both opsins are co-expressed in the same cells it is essential to achieve a defined ratio between excitatory and inhibitory action at the respective wavelengths (Fig. 1.4), so that neuronal activation and silencing can be precisely controlled in all transduced cells. Furthermore, precise co-localization of the two opsins is especially important when local, subcellular stimulation is required, or when control of individual neurons is intended, for example with 2-photon holographic illumination (Shemesh et al., 2017). Meeting these criteria is particularly challenging *in vivo*, where the optogenetic actuators are either expressed in transgenic lines or from separate viral vectors that are exogenously transduced (Fig. 1.4 B). Ideally, both opsins are expressed from the same gene locus or delivered to the target neurons by a single viral vector. Moreover, for expression with fixed stoichiometry, the opsins should be encoded in a single open reading frame (ORF).

Two strategies for stoichiometric expression of an inhibitory and an excitatory opsin from a single ORF have been reported using either a 2A ribosomal skip sequence (Gradinaru et al., 2010; Tang et al., 2009) (Fig. 1.4 C) or a gene fusion

approach (Kleinlogel et al., 2011) (Fig. 1.4 D). In both cases, a blue-light sensitive CCR for excitation was combined with a red-shifted rhodopsin Cl^- pump for inhibition.

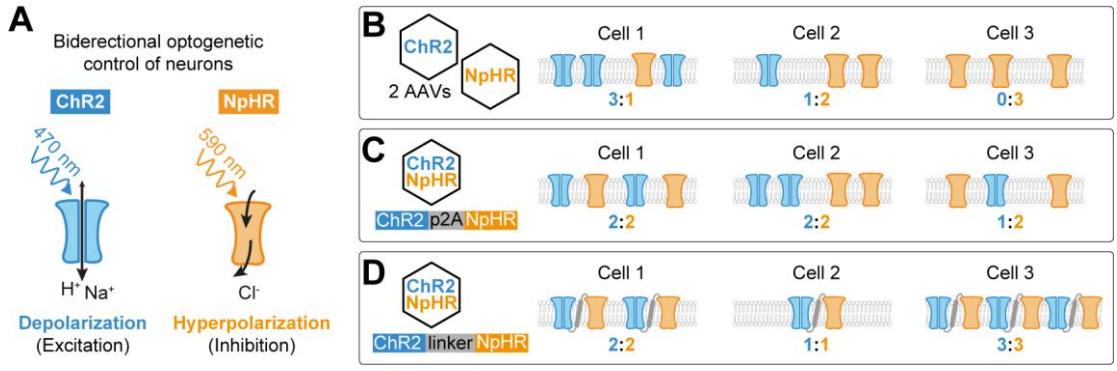

Figure 1.4. Strategies for co-expression of two optogenetic actuators for bidirectional control of neurons. (A) Schematic drawing showing the blue-light-activated CCR ChR2 and the orange-light-activated pump NpHR that have been previously used to achieve dual-color bidirectional control of neurons. **(B)** Delivery of ChR2 and NpHR via separate adeno-associated viral vectors (AAVs) may result in highly variable expression ratios between the CCR and the pump in each transduced cell. In extreme cases, some cells may get transduced only by one of the two AAVs (Cell 3). **(C,D)** Co-expression from ChR2 and NpHR from a single AAV and a single open reading frame. **(C)** Using a 2A ribosomal skip sequence does not ensure co-localized expression of the two rhodopsins since they may get differentially distributed in the plasma membrane (Cell 1 vs Cell 2) and can have different degradation rates leading to variable stoichiometries of expression (Cell 3). **(D)** The gene fusion strategy allows fixed 1:1 stoichiometric and co-localized expression of ChR2 and NpHR in a single fusion protein. Cells might exhibit differences in the number of tandem construct copies (Cell 1 vs Cell 2 vs Cell 3), but the overall ratio between the excitatory and inhibitory tool remains constant.

1.3.1. Bicistronic tools for bidirectional control of neurons

One of the first approaches allowing co-expression of multiple heterologous proteins in neurons was based on the use of internal ribosomal entry sites (IRES) (Douin et al., 2004). However, it has been reported that, in the resulting bicistronic mRNAs, the upstream ORF is more strongly translated than the ORF downstream of the IRES (Hennecke et al., 2001).

A second approach employed self-processing viral peptide bridges, namely 2A ribosomal skip sequences, for simultaneous expression of up to three proteins under the control of a single promoter (Tang et al., 2009). Using this strategy, a triple

construct co-expressing ChR2-HR (Gradinaru et al., 2007), eNpHR (Gradinaru et al., 2008), and the yellow fluorescent protein (YFP) Venus (Nagai et al., 2002) was generated using two 2A elements. The functionality of both rhodopsins could be confirmed by electrophysiological recordings in organotypic hippocampal slices. However, in this configuration, the Venus fluorophore was freely diffusible after translation of the 2A sequence, and thus did not serve as a localization marker for the rhodopsins (Tang et al., 2009).

A year later, eNPAC, a bicistronic construct combining ChR2-HR and a targeting-enhanced version of eNpHR (eNpHR3.0) via a P2A linker was described and validated *in vitro* (Gradinaru et al., 2010). Since NpHR-YFP expression has been reported to generate intracellular opsin accumulations (Gradinaru et al., 2008, 2010), in a second version of eNPAC, namely eNPAC2.0, the YFP reporter was fused to ChR2-HR instead of eNpHR3.0, resulting in an improved expression of eNpHR3.0 (Carus-Cadavieco et al., 2017). eNPAC2.0 was successfully used *in vivo* to control either excitation or inhibition of neuronal activity using blue and orange light, respectively (Carus-Cadavieco et al., 2017; Heikenfeld et al., 2020). Recently, eNPAC2.0 was used for optogenetic induction of local oscillations in mouse retrosplenial cortex by delivering blue and orange light in a specific rhythmic pattern (Vesuna et al., 2020).

Nevertheless, these bicistronic expression strategies do not ensure co-localization of the two rhodopsins since after translation they may get differentially distributed in the plasma membrane. Since they also can have different degradation rates, their stoichiometry of expression might vary from cell to cell (Fig. 1.4 C).

1.3.2. Gene-fusion strategy

To overcome the main limitations of the bicistronic strategies, Kleinlogel at al. developed a genetic tandem cassette that yields a covalently linked fusion protein of two rhodopsins (Kleinlogel et al., 2011). Therefore, membrane trafficking or

degradation of both opsins occur at identical rates, and excitatory and inhibitory currents remain at a fixed 1:1 ratio despite variations in expression levels between cells (Fig. 1.4. D). This gene-fusion approach was used to systematically combine the inhibitory ion pumps bacteriorhodopsin, NpHR, or Arch with a number of ChR2 mutants, which were fused via a transmembrane linker consisting of a fluorophore and the ß-helix of the rat gastric H^+/K^+ ATPase (ßHK) to maintain correct membrane topology of both rhodopsins (Kleinlogel et al., 2011). In cultured neurons, the fusion protein consisting of ChR2 and NpHR induced action potential firing upon blue-light illumination, and hyperpolarization during illumination with orange light, thus enabling bidirectional control of the same neurons (Kleinlogel et al., 2011).

While this was the first strategy ensuring co-localized expression of an inhibitory and an excitatory opsin at a 1:1 stoichiometric ratio and provided important mechanistic insights in their relative ion-transport rates, membrane trafficking was not as efficient as with individually expressed opsins, thus limiting the potency of these fusion constructs for reliable control of neuronal activity.

1.3.3. Restricting the action spectrum of red-shifted ChRs

So far, all strategies to achieve dual-color bidirectional control of neurons have been based on the combination of a blue-light sensitive CCR for excitation with a red-shifted rhodopsin for inhibition. Inversion of the excitatory and inhibitory action spectra, that is pairing a red-light-activated CCR with a blue-light-activated ACR, would restrict depolarization to a narrow, orange-red spectral window, since the inhibitory opsin compensates the residual blue-light-activated currents of the excitatory red-shifted CCR (Fig. 1.5 A, B). Therefore, this red-CCR/blue-ACR tandem configuration would enable mutually exclusive dual-color excitation of two neuronal populations when combined with a second blue-light-sensitive CCR, at light irradiances spanning multiple orders of magnitude (Fig. 1.5 C, right). As discussed above (see section 1.2), this was not possible before, since spiking two

distinct sets of neurons with individually expressed red- and blue-light-activated opsins , requires careful calibration and dosing of blue light to avoid activation of the red-shifted opsin (Erbguth et al., 2012; Klapoetke et al., 2014; Yizhar et al., 2011) (Fig. 1.5 C, left).

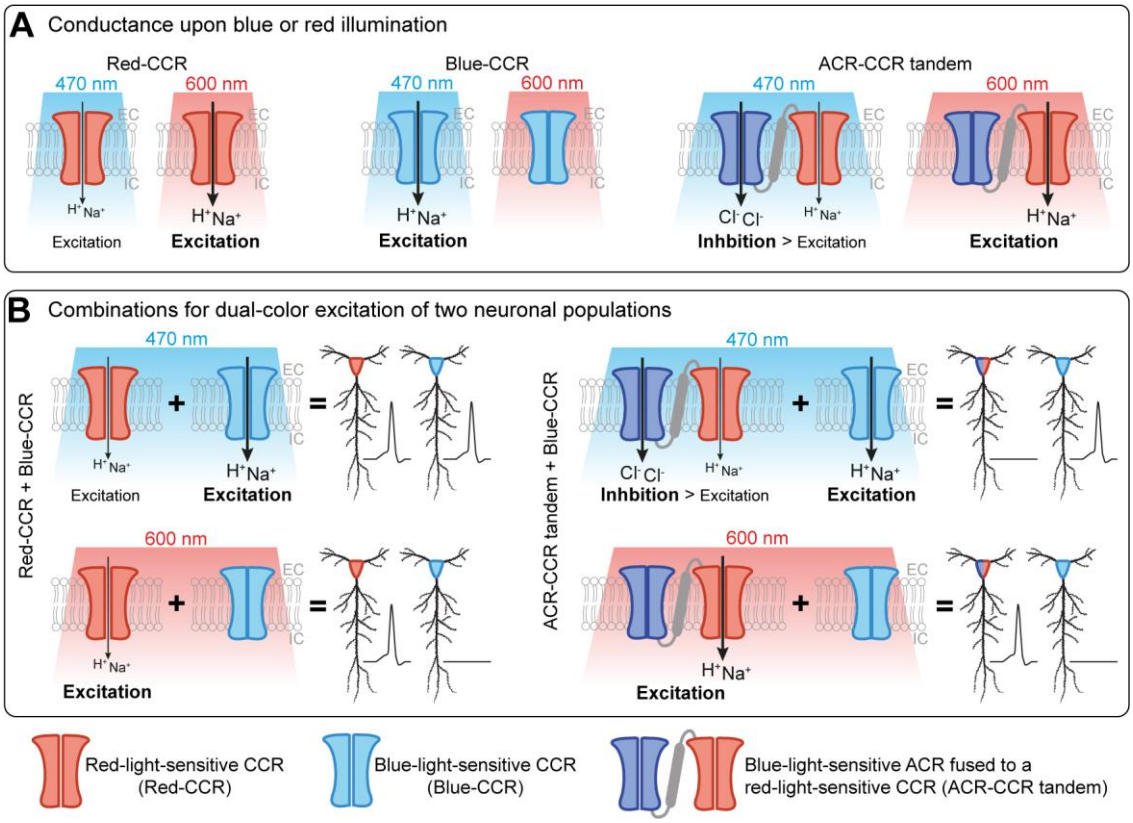

Figure 1.5. Pairing a red-light-sensitive CCR with a blue-light-sensitive ACR restricts excitation to the red spectrum, allowing mutual exclusive two-color excitation of two neuronal populations when combined with a second blue-light-sensitive CCR. (A) Wavelength-dependent conductances for a red-CCR (left), a blue-CCR (middle) and the ACR-CCR tandem (right). While the red-CCR is maximally activated by red light (600 nm) it still shows partial activation by blue light (470 nm, left). Note that in the ACR-CCR tandem, illumination with blue light elicits strong inhibitory currents that compensate the residual excitatory currents of the red-CCR (right). **(B)** Combination of a single red-CCR (left) or the ACR-CCR tandem (right) with a second blue-CCR for dual-color independent excitation of two distinct neuronal populations. Only the latter combination allows for exclusive spiking with either blue (top right) or red light (bottom right).

1.4. Research purpose

In the past 20 years there have been numerous studies that successfully employed optogenetic tools to tackle a wide range of scientific questions (for a review see: Adamantidis et al., 2015; Lee et al., 2020). However, there are still some remaining challenges in the field of optogenetics that demand refinement and further development of optogenetic tools with new biophysical properties.

Inhibition of specific neurons by optogenetic means is a powerful approach to probe neuronal circuit function. While there is a vast range of light-activated silencers, an optogenetic tool that allows precise, reversible and long-term silencing of neurons is still missing. Therefore, one part of my PhD project focused on the development and characterization of novel ACRs with spectrally shifted action spectra and step-function properties that expand the available toolkit of optogenetic silencers in the spectral and temporal domains (Part I, Results section 3.1). I focused my work on the newly developed eACR Aion, which exhibits the longest-known conducting state upon photoactivation, permitting faithful and reversible silencing of neurons in the range of several minutes to hours without the need for continuous illumination (Fig. 1.6 A).

A second challenge when manipulating neuronal circuits using optogenetic tools is the independent activation of two defined neuronal populations (Fig. 1.6 B). All rhodopsins, even the red-shifted ones such as Chrimson, are activated to a certain extent by blue light, especially when illuminated at high light irradiances. In dual-color experiments, this leaves only a narrow spectral and energetic window to activate the blue- but not the red-light sensitive ChR. To address this issue, I explored ChrimsonSA, an engineered variant of Chrimson with a more red-shifted activation spectrum and reduced blue-light sensitivity, and its applicability as a tool for red-light mediated neuronal spiking (Part II, Results section 3.2).

An alternative way to overcome the spectral cross-activation problem is by pairing a red-light-sensitive CCR with a blue-light-sensitive ACR. In this

configuration, upon illumination with blue light the strong inhibitory photocurrents from the ACR would shunt any residual excitatory photocurrents from the CCR, thereby restricting optical excitation to the orange-red spectrum. To explore this concept, in the last part of this dissertation I characterized BiPOLES, a new optogenetic tool combining in a single fusion protein the blue-light-sensitive ACR *Gt*ACR2 and the red-light-sensitive CCR Chrimson (Part III, Results section 3.3). Furthermore, the 1:1 stoichiometric expression of *Gt*ACR2 and Chrimson in BiPOLES enables potent spiking and silencing of the same neurons using red and blue light, respectively, which overcomes the long-sought challenge of all-optical dual-color bidirectional modulation of neuronal activity (Fig. 1.6 C).

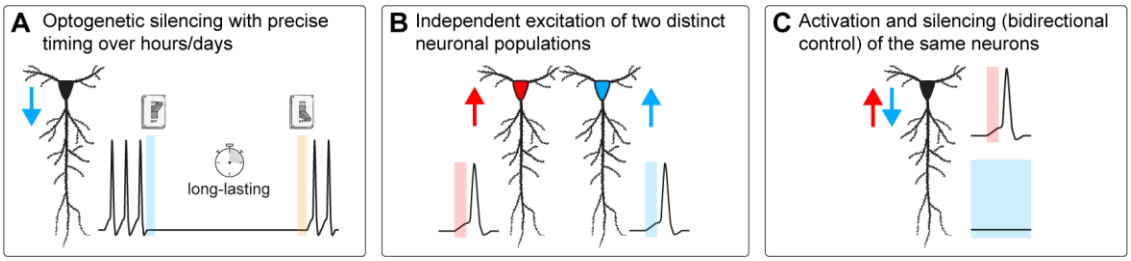

Figure 1.6. Some remaining challenges in the field of optogenetics which are addressed in this dissertation (A) Optogenetic silencing with precise timing for extended periods of time at the scale of several minutes to hours or even days remains a challenge, with inhibition time being dictated by the activation and inactivation kinetics of the silencing tool. **(B)** Independent excitation of two distinct neuronal populations is challenging due to the fact that all rhodopsins, regardless of their excitation spectra, can be activated to some extent by blue light. **(C)** Dual-color bidirectional control of neurons has been hindered by the spectral cross-over between tools as well as by the challenge of achieving 1:1 stoichiometric expression of the excitatory and the inhibitory optogenetic actuators.

2. Materials and Methods

2.1. Characterization of optogenetic tools in hippocampal organotypic slice cultures

2.1.1. Hippocampal organotypic slice culture preparation

Organotypic hippocampal slices were prepared from Wistar rats at post-natal day 5-7 as previously described (Gee et al., 2017). Briefly, rat pups were decapitated at the level of the cervical medulla using large scissors. Brains were removed and kept in ice cold bubbled dissection medium (see Table 1). Under a stereomicroscope both hippocampi were dissected along with part of the entorhinal cortex. Subsequently, hippocampi were transferred to a teflon specimen dish on the stage of a tissue chopper (McIlwain type 10180, Ted Pella). and arranged perpendicular to the blade before cutting into 350 µm slices. Chopped hippocampi were placed in a prechilled 60-mm petri dish containing cold dissection medium and slices were carefully separated from one another by sliding a fine forceps between them. Slices were placed on a porous membrane (Millicell CM, Millipore) using a spatula and maintained at 37°C, in a 95 % O_2/5 % CO_2 atmosphere in slice culture medium (see Table 1). Slice cultures were allowed to mature for at least 2 weeks in the incubator before experimental assessment. No antibiotics were added to the culture medium. Pre-warmed medium was replaced twice per week.

Table 1 – Cell culture solutions

SOLUTION	COMPOSITION
Dissection medium	1 mM $CaCl_2$, 5 mM $MgCl_2$, 10 D-Glucose, 4 mM KCl, 26 mM $NaHCO_3$, 0.001 % Phenol red, 2 mM kynurenic acid, oxygenated with carbogen (5 % CO_2/95 % O_2) to set pH at 7.2
Slice culture medium	80% MEM, 20% heat-inactivated horse serum, 1 mM L-glutamine, 0.00125% ascorbic acid, 0.01 mg/ml insulin, 1.44 mM $CaCl_2$, 2 mM $MgSO_4$, 13 mM D-glucose

2.1.2. Transgene delivery in organotypic slices

Single-cell electroporation

For neuronal expression the coding sequence of the different optogenetic tools was cloned into pAAV DNA-backbones encoding the human synapsin (hSyn) promoter (see Table 2 for a list of the optogenetic tools used in this study).

Table 2 – List of optogenetic tools used in this work

INSERT	SHORT DESCRIPTION
iChloC^{CA}-citrine	Step-function eACR (C128A mutant)
Phobos^{CA}-citrine	Blue-shifted step-function eACR (C128A)
Aurora^{CA}-citrine	Red-shifted step-function eACR (C128A)
Phobos^{CADN}-citrine	Blue-shifted step-function eACR with long conducting state (C128A; D156N)
Aion-citrine	Blue-shifted step-function eACR with long conducting state (C128A; D156C)
Aion-citrine-Kv2.1 (somAion)	Soma-targeted version of Aion-citrine
Aion-citrine-5HT$_{1A}$	Soma-targeted version of Aion-citrine
Aion-ts-citrine-ER	Trafficking enhanced version of Aion-citrine
*Gt*ACR1^{CA}-citrine	Slow-cycling variant of the nACR *Gt*ACR1 (C102A)
MerMAID1-citrine	Fast desensitizing nACR
MerMAID6-citrine	Fast desensitizing nACR
Chrimson-mCerulean	Red-shifted natural CCR from *Chlamydomonas noctigama*
ChrimsonSA-mCerulean	Chrimson mutant (S169A) with red-shifted peak activation wavelength and accelerated closing kinetics
ChrimsonSA2.0-mCerulean	Trafficking enhanced version of ChrimsonSA
ChrimsonSA2.0-Kv2.1-mCerulean	Soma-targeted and trafficking enhanced version of ChrimsonSA
*Gt*ACR2-ts-mCerulean-bHK-Chrimson (BiPOLES)	Tandem construct combining a blue-ACR and a red-CCR for dual-color bidirectional control of neurons

*Gt*ACR2-ts-mCerulean-bhK-Chrimson-Kv2.1 (somBiPOLES)	Soma-targeted version of BiPOLES
*Gt*ACR2-ts-mCerulean-bhK-vf-Chrimson-Kv2.1 (vf-somBiPOLES)	Fast kinetics version of somBiPOLES with vf-Chrimson
*Gt*ACR2-ts-mCerulean-bhK-f-Chrimson-Kv2.1 (vf-somBiPOLES)	Fast kinetics version of somBiPOLES with f-Chrimson
*Gt*ACR2-ts-mCerulean-Kv2.1	Soma-targeted version of the blue-light sensitive nACR *Gt*ACR2
eNpHR3.0-ts-p2A-ChR2(HR)-eYFP (eNPAC2.0)	Bicistronic construct encodin an orange-activated Cl^- pump and a blue-CCR for dual-color bidirectional control of neurons

Individual CA1 pyramidal cells were transfected by single-cell electroporation between DIV 14-16 as previously described (Wiegert et al., 2017a). Usually, a plasmid encoding a fluorescent protein was co-electroporated with the opsin-encoding plasmid and served as a morphology marker. pCI-hSyn-mCerulean was used together with opsins coupled to the yellow fluorescent protein citrine; pAAV-hSyn-mKate2 was used with opsins coupled to mCerulean. Plasmids were diluted to the desired working concentration (between 5 and 20 ng/µl for opsins; between 25 and 50 ng/µl for fluorescent proteins) in K-gluconate-based solution (see Table 3). Once the pipette containing the plasmid mix was touching the membrane of the target cell, an Axoporator 800A (Molecular Devices) was used to deliver a train of 50 hyperpolarizing pulses (-12 V, 0.5 ms) at 50 Hz. During electroporation slices were maintained in pre-warmed (37°C) HEPES-buffered solution (see Table 3).

Table 3 – **Solutions for transgene delivery**

SOLUTION	COMPOSITION (mM)
HEPES-buffered solution	145 NaCl, 10 HEPES, 25 D-glucose, 2.5 KCl, 1 $MgCl_2$ and 2 $CaCl_2$ (pH 7.4, sterile filtered)
K-gluconate-based solution	135 K-gluconate, 4 $MgCl_2$, 4 Na_2-ATP, 0.4 Na-GTP, 10 Na_2-phosphocreatine, 3 ascorbate, 0.2 EGTA, and 10 HEPES (pH 7.2, sterile filtered)

Transduction with recombinant adeno-associated viral (rAAV) vectors

To target specific neuronal populations in a promoter-dependent manner and to achieve opsin expression in a larger number of neurons, targeted viral vector-based transduction of organotypic slice cultures was used (Wiegert et al., 2017b) (see Table 4 for a list of used rAAV vectors). Briefly, rAAV particles of the mosaic serotype 2/9 were pressure injected (2-2.5 bar, 100 ms duration) using a Picospritzer (Parker, Hannafin) under visual control into the CA3 or CA1 regions between DIV 2-5. During rAAV transduction, membranes carrying the slices were kept on pre-warmed HEPES-buffered solution (see Table 3). Slice cultures were maintained in the incubator for 12-15 days allowing for virus expression.

Table 4 – **List of rAAVs used for experiments in organotypic slice cultures**

rAAV2/9	Short Description
mDlx-BiPOLES-mCerulean *titer 2.8 x 10^{13} vg/ml*	Allows expression of BiPOLES in GABAergic neurons
hSyn-DIO-BiPOLES-mCerulean *titer 7.0 x 10^{13} vg/ml*	Allows conditional Cre-dependent expression (Cre-On) of BiPOLES (DIO: Double-floxed Inverse Orientation)
hSyn-DIO-somBiPOLES-mCerulean *titer 3.4 x 10^{13} vg/ml*	Allows conditional Cre-dependent expression (Cre-On) of somBiPOLES
CaMKIIa(0.4)-somBiPOLES-mCerulean *titer 2.5 x 10^{13} vg/ml*	Allows expression of somBiPOLES in excitatory and projection neurons
CaMKIIa(0.4)-DO-CheRiff-ts-mScarlet-ER *titer 8.15 x 10^{11} vg/ml*	Allows expression of the blue-light-sensitive CCR CheRiff in non-Cre-expressing cells (Cre-Off; DO: Double-floxed Orientation)
mDlx-H2B-EGFP *titer 2.8 x 10^{10} vg/ml*	Allows nuclear expression of the enhanced green fluorescent protein (EGFP) in GABAergic neurons. EGFP is fused to the human histone H2B gene.
CaMKIIa-Cre *titer 3.0 x 10^{12} vg/ml*	Allows expression of Cre recombinase in excitatory and projection neurons

2.1.3. Patch-clamp electrophysiology

Hippocampal slice cultures between DIV 19-23 were placed in the recording chamber of the patch-clamp setup and submerged in artificial cerebrospinal fluid (ACSF) (see Table 3). Experiments were done at room temperature (21-23°C). Whole-cell recordings of wild-type or transfected neurons were performed under visual guidance using a BX 51WI microscope (Olympus) equipped with Dodt-gradient contrast and a Double IPA integrated patch amplifier controlled with SutterPatch software (Sutter Instrument). Patch pipettes were made using a vertical micropipette puller (PC-100, Narishige) to pull borosilicate glass capillaries (1.5/0.84 mm OD/ID, World Precision Instruments) to a resistance tip of 3-4 MΩ when filled with intracellular solution (see Table 5). In experiments where synaptic transmission was blocked, 10 µM CPPene, 10 µM NBQX, and 100 µM picrotoxin (Tocris) were added to the extracellular solution. In experiments analyzing synaptic inputs onto postsynaptic cells, ACSF 4/4 was used to reduce the overall excitability. Measurements were corrected for a liquid junction potential of -14,5 mV, which was empirically determined for the solutions used in this work. Access resistance of the recorded neurons was continuously monitored and recordings above 30 MΩ were discarded.

Passive and active membrane parameters were measured in opsin-expressing and non-transduced, wild-type CA1 pyramidal cells. Resting membrane potential, membrane resistance and membrane capacitance were recorded and automatically calculated by the Sutterpatch software in voltage-clamp mode (V_{hold} = -75 mV) in response to a -5 mV test pulse of 100 ms . The number of elicited APs was counted in response to a 500 ms current step of 300 or 500 pA in current-clamp mode (0 pA holding current). For the 1st elicited AP, the voltage threshold, peak voltage and amplitude were measured.

Table 5 – **Solutions for patch-clamp recordings**

SOLUTION	COMPOSITION (mM)
ACSF 1/2 (extracellular solution)	135 NaCl, 2.5 KCl, 2 $CaCl_2$, 1 $MgCl_2$, 10 Na-HEPES, 12.5 D-glucose, 1.25 NaH_2PO_4 (pH 7.4)
ACSF 4/4 (extracellular solution)	135 NaCl, 2.5 KCl, 4 $CaCl_2$, 4 $MgCl_2$, 10 Na-HEPES, 12.5 D-glucose, 1.25 NaH_2PO_4 (pH 7.4)
Intracellular solution	135 K-gluconate, 4 MgCl2, 4 Na2-ATP, 0.4 Na-GTP, 10 Na2-phosphocreatine, 3 ascorbate, 0.2 EGTA, and 10 HEPES (pH 7.2, sterile filtered)

***Box 2**. Calculation of the chloride reversal potential*

Based on the ionic composition of the intracellular and extracellular (ACSF 1/2) solutions given in Table 5, the E_{Cl^-} was calculated using the Nernst equation as follows:

$$\text{Nernst equation: } E_X = \frac{RT}{zF} \ln\left(\frac{[X]_{out}}{[X]_{in}}\right)$$

E_X is the reversal or Nernst potential for a given ion *X*.
R is the universal gas constant and is equal to 8,314 J K^{-1} mol^{-1}.
T is the temperature in Kelvin (K = °C + 273,15).
z is the valence of the ionic species *X*.
F is the Faraday's constant and is equal to 96485 C mol^{-1}.
$[X]_{out}$ is the concentration of the ionic species *X* in the extracellular fluid.
$[X]_{in}$ is the concentration of the ionic species X in the intracellular fluid.

$$E_{Cl^-} = \frac{8{,}314 \text{ J K}^{-1} \text{ mol}^{-1} \text{ x } 295{,}15 \text{ K}}{-1 \text{ x } 96485 \text{ C mol}^{-1}} \ln\left(\frac{143{,}5 \text{ mM}}{8{,}0 \text{ mM}}\right) = -73{,}42 \text{ mV}$$

Light application for optogenetic stimulation of neurons

The epifluorescence pathway of the microscope (BX 51WI, Olympus) was used to optically stimulate neurons within the field of view during patch-clamp recordings. A 16 channel LED light engine (CoolLED pE-4000) coupled to the microscope through a liquid light guide, was used to deliver light pulses at the

desired irradiance and wavelength (ranging from 385 to 635 nm) under TTL control. Irradiance was measured in the object plane with a 1918 R power meter equipped with a calibrated 818 ST2 UV/D detector (Newport) and divided by the illuminated field of the Olympus LUMPLFLN 60XW objective (0.134 mm^2).

In experiments where stimulation of neurons outside the field of view was required (for example, to stimulate CA3 presynaptic neurons while the objective is being used to visualize and stimulate CA1 postsynaptic neurons), a blunt light fiber (400 µm diameter, 0.39 NA, Thorlabs) coupled to an LED was positioned above the area to be stimulated using a micromanipulator.

Characterization of ACRs

Photocurrent recordings: for photocurrent measurements in voltage-clamp mode, ACR-expressing CA1 cells were held above the chloride Nernst potential at membrane voltages of -35, -40 or -50 mV to detect outward anionic currents elicited by ACR photoactivation (see corresponding figure legends and main text for further details). To calculate photocurrent densities, the peak and stationary photocurrent amplitudes (in pA) were divided by the cell membrane capacitance (in pF) which was automatically recorded by the Sutterpatch software in voltage-clamp mode (V_{hold} = -75 mV). Furthermore, to characterize the light-induced closing of step-function eACRs, photocurrents were terminated by red-shifted light. For the MerMAIDs, the recovery kinetics of the peak photocurrent after light-mediated desensitization was further assessed by delivering two light pulses and varying the dark interval between them.

Inhibition of current-evoked action potentials: in current-clamp experiments holding current was injected to maintain CA1 cells near their resting membrane potential (-75 to -80 mV). To assess the capability of the step-function eACRs to block AP firing, a light pulse at their respective peak activation wavelength was

delivered after 5 s during a train of somatic current step injections (300 pA, 2 s, 2.5 s ISI, for 1 min). To assess effective termination of silencing for each eACR, a light pulse at their respective peak inactivation wavelength was delivered after 35 s (for iChloC^{CA}, Phobos^{CA} and Aurora^{CA}; Fig. 3.1.2) or 45 s (for Phobos^{CADN}, Aion and *Gt*ACR1^{CA}; Fig. 3.1.6). Spiking rate was calculated for the periods before opening (0-5 s), after opening (5-35 s or 5-45 s) and after closing (35-55 s or 45-55 s) of the respective ACR by dividing the number of current-evoked APs by the respective time interval.

In addition, the ability to block AP firing was quantified over a period of 5 minutes for Aion and *Gt*ACR1^{CA}. For this, the change in membrane depolarization (after median filtering of the raw voltage traces) during somatic current step injections was measured before and after a brief light stimulus (1 s, 10 mW/mm^2, Aion: 460 nm, *Gt*ACR1^{CA}: 525 nm; Fig. 3.1.8). Moreover, Aion-mediated inhibition of depolarization-induced APs was evaluated after overnight (12 h) blue-light stimulation of Aion-expressing cells in a custom-made LED chamber inside the incubator (3 s 460-nm light pulses every 5 min, 0.3 mW/mm^2).

In the case of MerMAID1 and 6, the capacity to block a single AP was evaluated by illumination with a short (10 ms) or a longer (500 ms) green light pulse during injection of a depolarizing current ramp. The onset of the light stimulation was synchronized with the first AP that occurred during darkness.

Rheobase shift measurements over 1 minute: to measure the ability of Phobos^{CADN}, Aion, Aion-ts-citrine-ER and somAion to shift the rheobase upon light-activation, 13 depolarizing current ramps (2 s, from 0-600 pA up to 0-1000 pA) were injected into CA1 neurons over 1 minute 2.5 s ISI) in dark and light conditions (1 s light pulse of 460 nm between 1st and 2nd current ramp injections) at irradiance values ranging from 0.001 to 10 mW/mm^2. For each ramp, the injected current at the time of the first AP was defined as the rheobase. The rheobase shift over time

was calculated by subtracting the rheobase of each ramp after light stimulation from the rheobase value before light stimulation (1st ramp). The relative change in the number of ramp-evoked APs was calculated counting the total number of APs elicited during each current ramp injection after light stimulation and normalized to the number of APs elicited at the same time point in the absence of light. The same experiment was conducted for *Gt*ACR1^{CA}, but using 525 nm light.

Characterization of ChrimsonSA

Photocurrent recordings: for photocurrent measurements in voltage-clamp mode CA1 cells expressing WT Chrimson, ChrimsonSA, ChrimsonSA2.0 or ChrimsonSA2.0-Kv2.1 were held at -75 mV to measure currents elicited by a 10 ms light pulse (1 mw/mm^2) of different wavelengths ranging from 385 to 660 nm. To compare activation by blue and red light, the photocurrent amplitude measured upon illumination with 460 nm was normalized to the one obtained with 635 nm.

Irradiance threshold for light-induced spiking: in current-clamp experiments holding current was injected to maintain CA1 cells near their resting membrane potential (-75 to -80 mV). To determine the irradiance threshold for AP firing with WT Chrimson and ChrimsonSA under illumination with blue (460 nm) or red (635 nm) light, a train of 10 light pulses (10 ms pulse duration) was delivered at 10 Hz. For each wavelength, an initial irradiance of 0.1 mW/mm^2 was used and subsequently increased until at least one AP was elicited. To determine the irradiance threshold needed to spike CA1 cells with ChrimsonSA2.0 and ChrimsonSA2.0-Kv2.1, 460 and 635 nm light ramps going from 0 to 10 mW/mm^2 over 1 s were delivered in current-clamp mode. The irradiance value at the time of the first spike was defined as the irradiance threshold (in mW/mm^2) needed to evoke AP firing.

Characterization of tools for bidirectional control of neurons

Photocurrent recordings: for photocurrent density measurements in voltage-clamp mode CA1 cells expressing BiPOLES, somBiPOLES, vf-somBiPOLES, f-somBiPOLES, Chrimson or som*Gt*ACR2 were held at -75 or -55 mV to detect inward (cationic) or outward (anionic) currents elicited by red (635 nm, 20 ms, 1 and 10 mW/mm^2) and blue light (490 nm, 100 ms, 10 mW/mm^2), respectively. For each cell, the peak photocurrent amplitude (in pA) was divided by the cell membrane capacitance (in pF) which was automatically recorded by the Sutterpatch software in voltage-clamp mode (V_{hold} = -75 mV). To determine the reversal potential under blue- and red-light illumination, photocurrents were measured while holding the neurons at different membrane potentials (from -95 to 6 mV; Fig. 3.3.1). Additionally, for BiPOLES and eNPAC2.0, light-evoked photocurrents were recorded across the visible spectrum (385 – 660 nm) at a holding voltage of -55 mV.

Restriction of somBiPOLES to the somatodendritic compartment: to functionally assess the putative expression of somBiPOLES in the axon terminals of CA3 pyramidal cells, slice cultures were transduced with a rAAV2/9 encoding for CaMKIIa-somBiPOLES-mCerulean (see Table 4 for details). Red-light evoked EPSCs were recorded in postsynaptic CA1 cells during local illumination either in CA3 at the somata (two light pulses of 5 ms delivered 40 ms apart using a fiber-coupled LED (400 µm fiber, 0.39 NA, 625 nm, Thorlabs) controlled by a Mightex Universal 4-Channel LED Driver (1.6 mW at fiber tip), or in CA1 at axon terminals of somBiPOLES-expressing CA3 cells (two light pulses of 5 ms delivered 40 ms apart through the 60x microscope objective, 635 nm, 50 mW/mm^2). Axonal light stimulation was done in the presence of tetrodotoxin (TTX, 1 µM) and 4-aminopyridine (4-AP, 100 µM) to avoid antidromic spiking of CA3 cells and rather elicit direct, opsin-mediated depolarization in the terminals to trigger Neurotransmitter release.

Spiking probability: in current-clamp experiments holding current was injected to maintain CA1 cells near their resting membrane potential (-75 to -80 mV). To determine the spiking probability of vf- somBiPOLES, f- somBiPOLES, somBiPOLES and Chrimson under illumination with light of different wavelengths (470, 595 and 635 nm), a train of 20 light pulses (5 ms pulse duration) was delivered at 5 Hz. For each wavelength, irradiance values from 0.1 to 100 mW/mm^2 were used. For comparisons with eNPAC2.0, only light of 470 nm was used, which is the peak activation wavelength of ChR2(HR). AP probability was calculated by dividing the number of light-triggered APs by the total number of light pulses. In addition, the high-frequency spiking limit with somBiPOLES and f-somBiPOLES was evaluated by triggering APs at frequencies ranging from 10 to 100 Hz using 40 light pulses (595 nm, pulse width 3 ms, 10 mW/mm^2).

To compare the irradiance threshold needed to spike CA1 cells with somBiPOLES, eNPAC2.0 and Chrimson, 470 and 595 nm light ramps going from 0 to 10 mW/mm^2 over 1 s were delivered in current-clamp mode. In the case of somBiPOLES the blue light ramp went up to 100 mW/mm^2 to rule out that high blue-light irradiance might still spike neurons. The irradiance value at the time of the first spike was defined as the irradiance threshold (in mW/mm^2) needed to evoke AP firing.

Rheobase shift measurements: to measure the ability of BiPOLES, somBiPOLES, and som*Gt*ACR2 to shift the rheobase upon blue-light illumination, depolarizing current ramps (from 0–100 to 0–900 pA) were injected into CA1 neurons in the dark and during illumination with 490 nm light at irradiance values ranging from 0.001 to 100 mW/mm^2. The injected current at the time of the first AP was defined as the rheobase. The relative change in the number of ramp-evoked APs was calculated counting the total number of APs elicited during the 9 current ramp injections (from 0–100 to 0–900 pA) for each irradiance and normalized to the

number of APs elicited in the absence of light. The same experiment was conducted for eNPAC2.0, but using 580 nm light ranging from 0.01 to 100 mW/mm^2.

Bidirectional optical spiking-control: to assess the suitability of BiPOLES, somBiPOLES, vf-somBiPOLES and f-somBiPOLES as dual-color neuronal excitation and silencing tools, alternating pulses of red (635 nm, 20 ms, 10 mW/mm^2), blue (490 nm, 100 ms, 10 mW/mm^2) and a combination of these two (onset of blue light 40 ms before red light) were delivered to elicit and block APs. For eNPAC2.0 alternating pulses of blue (470 nm, 20 ms, 10 mW/mm^2), yellow (580 nm, 100 ms, 10 mW/mm^2) and a combination of these two (onset of yellow light 40 ms before blue light) were used.

Optical tuning of the membrane potential: to optically clamp the neuronal membrane potential using somBiPOLES, simultaneous illumination with blue and orange light at varying ratios was used. In current-clamp experiments, 470 and 595 nm light ramps (5 s) of opposite gradient (1 to 0 mW/mm^2 and 0 to 1 mW/mm^2, respectively) were applied. In a second set of experiments, a protocol consisting of five blocks of 10 s illumination at the following 470/595 nm light ratios (in 1 mW/mm^2) was used: 1.0/0.0, 0.5/0.5, 0.8/0.2, 0.2/0.8, and 0.4/0.6. Alternatively, optical clamping of the membrane potential was achieved by tuning a single wavelength between 385 and 660 nm (2 s light pulses, 0.1 mW/mm^2). Voltage traces were median-filtered to remove orange/red-light-mediated spikes and reveal the slow change in membrane voltage during illumination.

Two-color excitation of two distinct neuronal populations with somBiPOLES and CheRiff: for mutually exclusive optogenetic activation of two distinct populations of neurons, organotypic slice cultures from VIP-*Cre* mice were transduced with two different rAAV2/9 vectors (see Table 4 for details): first, a double-floxed inverted

open reading frame (DIO) construct encoding somBiPOLES (hSyn-DIO-somBiPOLES-mCerulean) to target VIP-positive interneurons, and second, a double-floxed open reading frame (DO) construct encoding CheRiff (hSyn-DO-CheRiff-ts-mScarlet-ER) to target CA1 pyramidal neurons and exclude expression in VIP-positive cells. Synaptic input from these two populations was recorded in VIP-negative *stratum oriens* GABAergic neurons (putative *oriens-lacunosum molecualare* [O-LM] interneurons). In CA1, O-LM neurons receive innervation both from local CA1 pyramidal cells and VIP-positive GABAergic neurons (Booker & Vida). To facilitate identification of putative GABAergic postsynaptic neurons in *stratum oriens*, slices were transduced with an additional rAAV2/9 encoding mDlx-H2B-EGFP (see Table 4 for details). In the absence of synaptic blockers light-evoked excitatory and inhibitory postsynaptic currents (EPSCs and IPSCs, respectively) were recorded while holding the postsynaptic cell at different membrane potentials (-80, -65, -55, -45 and 6 mV) in whole-cell voltage clamp mode. A blue (460 nm, 0.03 - 84.0 mW/mm^2) and a red (635 nm, 6.0 – 97.0 mW/mm^2) light pulse were delivered 500 ms apart from each other through a Leica HC FLUOTAR L 25x/0.95 W VISIR objective.

2.1.4. Two-photon microscopy

Neurons in organotypic slice cultures were imaged with two-photon microscopy to check for the live expression and subcellular localization of the different optogenetic tools. The custom-built two-photon imaging setup was based on an Olympus BX-51WI upright microscope upgraded with a multiphoton imaging package (DF-Scope, Sutter Instrument), and controlled by ScanImage 2017b software (Vidrio Technologies). Fluorescence was detected through the objectives (Leica HC FLUOTAR L 25x/0.95 W VISIR or LUMPLFLN 60XW, Olympus) and the oil immersion condenser (NA 1.4) by two pairs of GaAsP photomultiplier tubes (Hamamatsu, H11706-40). Dichroic mirrors (560 DXCR, Chroma Technology) and

emission filters (ET525/70m-2P, ET605/70m-2P, Chroma Technology) were used to separate green and red fluorescence. Excitation light was blocked by short-pass filters (ET700SP-2P, Chroma Technology). A tunable Ti:Sapphire laser (Chameleon Vision-S, Coherent) was set to 810, 930 or 980 nm to excite mCerulean, EGFP or citrine, respectively. An Ytterbium-doped 1070-nm pulsed fiber laser (Fidelity-2, Coherent) was used to excite the red fluorophores mKate2 and mScarlet. In some experiments, the 1070-nm laser was also used to excite citrine, which was detected in the green channel. The open-source software Fiji (Schindelin et al., 2012) was used for visualization and processing of images.

2.1.5. Immunohistochemistry and confocal imaging

The subcellular localization of BiPOLES and somBiPOLES in hippocampal neurons was assessed by immunohistochemistry and subsequent confocal imaging 20 days after virus transduction. Hippocampal organotypic slice cultures were fixed in a solution of 4% (w/v) paraformaldehyde (PFA) in PBS for 30 min at room temperature (RT). Next, slices were washed in PBS (3 x 10 min), blocked for 2 h at RT (10% [v/v] normal goat serum [NGS] in 0.3% [v/v] Triton X-100 containing PBS) and subsequently incubated for 48 h at 4°C with a primary antibody against GFP to amplify the mCerulean signal (chicken, anti-GFP, Invitrogen, A10262, Lot 1972783) at 1:1000 in carrier solution (2% [v/v] NGS, in 0.3% [v/v] Triton X-100 containing PBS). Following 3 rinses of 10 min with PBS, slices were incubated for 3 h at RT in carrier solution (same as above) with an Alexa Fluor® dye-conjugated secondary antibody (1:1000, Alexa Fluor 488 goat anti-chicken Alexa-488, Invitrogen; A11039). Slices were washed again, transferred onto glass slides and mounted for visualization with Shandon Immu-Mount (Thermo Scientific; 9990402).

Confocal images were acquired using a laser-scanning microscope (Zeiss, LSM 900) equipped with a 40x oil-immersion objective lens (Zeiss EC Plan-Neofluar 40x/1,3 oil). Excitation/emission filters were appropriately selected for Alexa 488

using the dye selection function of the ZEN software. The image acquisition settings were optimized once and kept constant for all images within an experimental data set. Z-stack images were obtained using a 1 µm z-step at a 1024×1024-pixel resolution scanning at 8 µs per pixel. Fiji (Schindelin et al., 2012) was used to quantify fluorescence intensity values along a line perpendicular to the cell equator and spanning the cell diameter. For each cell, grey values above 80% of the maximum intensity were distributed in 10 bins according to their location along the line.

2.1.6. Statistics

All statistical analyses were performed using GraphPad Prism 6.0-9.0. Normally distributed data were tested for significant differences (*$p<0.05$, **$p<0.01$, ***$p<0.001$) with one-way repeated-measures analysis of variance (ANOVA) followed by Tukey's multiple comparisons test. Not normally distributed data were tested with either the nonparametric Kruskal-Wallis test or the Friedmann test, followed by Dunn's multiple comparisons test. In all graphs individual data points are presented together with mean ± standard error of the mean (SEM) or with median values. No statistical measures were used to estimate sample size since effect size was unknown. N values represent biological replicates (i.e. neurons).

2.2. Characterization of Phobos^{CA} in *Drosophila melanogaster* larvae

2.2.1. Generation of *Drosophila melanogaster* transgenic lines

Drosophila melanogaster transgenic lines were generated using the binary expression systems Gal4-UAS (Brand & Perrimon, 1993) (Fig. 2.1 A) and LexA-lexAop (Lai & Lee, 2006). cDNA encoding Phobos^{CA} was codon-optimized for

Drosophila and cloned into a 20xUAS vector. For locomotion experiments, a Gal4 line expressing in glutamatergic neurons including motor neurons (*OK371-Gal4*) was used (Mahr & Aberle, 2006). For nociception experiments, the lines *27H06-LexA* and *82E12-Gal4* (Vogelstein et al., 2014) were used for expression of *Cs*Chrimson in C4da sensory neurons and Phobos^{CA} in A08n neurons, respectively.

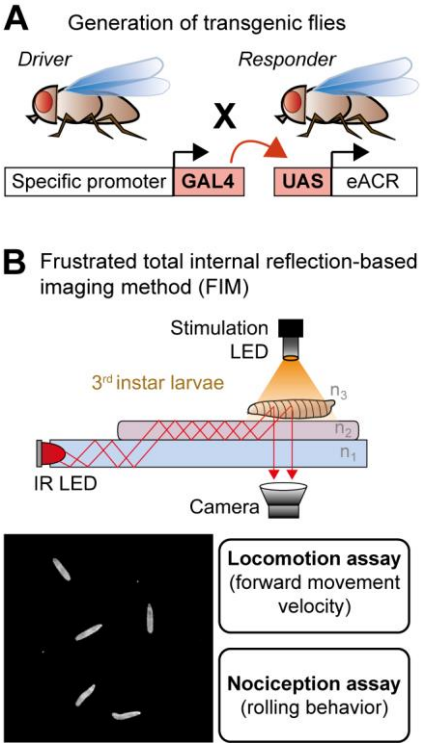

Figure 2.1. Functional characterization of eACRs in *D. melanogaster* larvae. (A) Generation of transgenic flies. The transcriptional activator Gal4 is under the control of a cell type-specific promoter and drives the expression of a target gene (in this case the eACR Phobos^{CA}) upon binding the Gal4 upstream activating sequence (UAS). **(B)** Top: schematic drawing of the FIM setup and the principle of frustrated internal reflection (inspired by Risse et al. 2013). An acrylic glass plate (blue) is flooded with infrared (IR) light (indicated by red lines). Due to the differences in the refractive indices of acrylic glass (n_1) and air, IR light is completely reflected at the glass/air boundary. Since the agar plate (lilac) has a higher refractive index (n_2) than the acrylic glass, reflection is frustrated at the glass/agar interface and the IR light enters the agar. *Drosophila* larvae have an even higher refractive index (n_3), and thus, when it reaches the animal, IR light enters the larval body, where is then reflected and, because the reflection angle is smaller than the critical angle, the light passes through the different layers and can finally be detected with a camera equipped with an IR filter and mounted below the tracking table. For optogenetic stimulation a light guide with custom collimator lenses was used to illuminate the entire surface of the agar plate. Bottom: example image of 5 larvae acquired with the FIM system (left). Using this strategy, larvae were tracked during two behavioral tests, namely a locomotion and a nociception assay (right).

2.2.2. Locomotion and nociception assays in *D. melanogaster* larvae

D. melanogaster larvae were staged in darkness on grape agar plates and fed with yeast paste containing 5 mM all-*trans*-retinal. Third instar larvae (96 h ± 3 h after egg laying) were used for all experiments. Animals were carefully collected under low red light illumination (>700 nm) and transferred to a 2 % agar plate on a frustrated total internal reflection (FTIR) based tracking system (FIM) (Risse et al., 2013) (Fig. 2.1 B). Five freely moving larvae per trial were video-captured with a

CMOS camera (ac2040-25gm, Basler) and tracked at a frequency of 10 frames/s for up to 90 s. For optogenetic stimulation, larvae were illuminated from a pE-4000 (CoolLED) coupled to a light guide with custom collimator lenses. The FIMtracking software (Risse et al., 2013) was used for analysis, and only animals displaying continuous locomotion before the first light stimulus were kept. Each genotype was tested multiple times on different days and data from all trials were combined.

For activation of Phobos^{CA} during the locomotion assay, larvae were illuminated for 5 s with 460 nm (80 µW/mm^2). After 40 s, an orange light pulse (595 nm, 5 s, 6.9 µW/mm^2) was directly applied on top of individual larvae to terminate Phobos^{CA}-mediated inhibition. Locomotion velocity was analyzed over time. For comparison, velocities were averaged over a 5 s interval, each before, during and after light-mediated inhibition with Phobos^{CA}.

For the nociceptive assay, larvae were illuminated with either 460 nm (5 s, 80 µW/mm^2) or 635 nm light (5 s, 55 µW/mm^2) for Phobos^{CA} or *Cs*Chrimson activation, respectively. The behavioral response was visually scored *post-hoc* as non-nociceptive (no response, stop, stop and turn) or nociceptive (bending, rolling). For analysis, only nocifensive rolling behavior (full 360° turn along the body axis) was compared between groups. Statistical significance was calculated using a chi^2 test.

2.3. Evaluation of Aion expression in mice

2.3.1. Mice

Adult (3-9 months of age) C57BL/6J mice of either sex were used in this study. They were housed and bred in pathogen-free conditions at the University Medical Center Hamburg-Eppendorf. The light/dark cycle was 12/12 h and the humidity and temperature were kept constant (40% relative humidity; 22°C). Food

and water were available ad libitum. All procedures were in agreement with the German national animal care guidelines and approved by the Hamburg state authority for animal welfare (BGV; license 32/17) and the animal welfare officer of the University Medical Center Hamburg-Eppendorf.

2.3.2. Virus injection

Mice were anesthetized via intraperitoneal injection of midazolam/medetomidine/fentanyl (5.0/0.5/0.05 mg/kg, diluted in NaCl) and placed on a heating blanket to maintain the body temperature. The fur of the head was removed with a fine trimmer. Prior to surgery, the depth of anesthesia and analgesia was evaluated with a toe-pinch to test the paw-withdrawal reflex. Subsequently, mice were fixed in a stereotactic frame, and eyes were covered with eye ointment (Vidisic, Bausch + Lomb) to prevent drying. The scalp was disinfected with Iodide solution (Betaisodona; Mundipharma) and an incision was made along the midline (1-2 cm). The skull was cleaned using a bone scraper (Fine Science Tools) and a small craniotomy was drilled with a dental drill (Foredom) above the injection site (dorsal CA1 area of the right hippocampus: -2.0 mm AP, +1.3 mm ML, -1.5 mm DV, relative to Bregma). 0.4 µl of virus suspension (AAV9-hSyn-Aion-citrine, titer = 4,08 x 10^{13} vg/ml) was injected at a speed of 0.1 µl/min using a custom-made air pressure system connected to a glass micropipette. After the injection, the micropipette was left in place for at least of 5 minutes before it was withdrawn and the scalp was closed with sutures. For complete reversal of anesthesia, mice received an intraperitoneal injection of flumazenil/atipamezole/buprenorphine (0.5/2.5/0.1 mg/kg, diluted in NaCl). Carprofen was given subcutaneously for additional analgesia and to avoid inflammation. During the three days following surgery animals were provided with Meloxicam mixed into soft food.

2.3.3. *Ex vivo* brain processing and imaging

Mice were sacrificed 27-29 days after virus injection via intraperitoneal injection of ketamine/xylazine (100/10 mg/kg) followed by intracardial perfusion with 4% PFA (Roth). Brains were extracted and stored in 4% PFA for at least 24 h at 4°C. Before sectioning, brains were washed with 1xPBS for 20 min at RT. Subsequently, brains were sliced in 60 µm coronal sections using a vibratome (Leica VT100S) and collected in PBS. To evaluate expression of Aion-citrine in the dorsal CA1 region, six brain sections were selected from -1.7 to -2.3 mm posterior from Bregma. Sections were washed in PBS (3 x 5 min, RT) and mounted onto glass slides using Shandon Immu-Mount (Thermo Scientific; 9990402).

Images were acquired with a custom-built two-photon imaging setup (see section 2.1.5) using 10x (Olympus UMPLFLN 10x/0.30 W) and 25x (Leica HC FLUOTAR L 25x/0.95 W VISIR) objective lenses. An Ytterbium-doped 1070-nm pulsed fiber laser (Fidelity-2, Coherent) was used to excite the fluorophore citrine. The open-source software Fiji (Schindelin et al., 2012) was used for visualization and processing of images.

3. Results

3.1. Part I: Anion-conducting channelrhodopsins with color-shifted activation spectra and altered kinetics

3.1.1. Blue- and red-shifted ACRs with step-function properties

The first generation of eACRs (Berndt et al., 2014, 2016; Wietek et al., 2014, 2015b) was developed by targeted mutagenesis of the CCRs C1C2 (Kato et al., 2012) and ChR2 (Boyden et al., 2005; Nagel et al., 2003), and thus displayed similar kinetics and spectral properties, limiting their application range. In particular, eACRs with red-shifted activation spectra are highly interesting, since they allow silencing of larger volumes at reduced light energies due to the deeper tissue penetration of light of longer wavelength (Johansson, 2010; Yaroslavsky et al., 2002). In addition, many animals are blind to light beyond ~600 nm (Peirson et al., 2018; Ward et al., 2008; Xiang et al., 2010), and thus, red light activation reduces direct effects of the light pulse on behavior during *in vivo* experiments. Furthermore, having blue- and red-shifted eACRs enables combinatorial experiments with other spectrally separated tools or sensors.

To extend the temporal and spectral range for inhibition, the set of mutations used to create the first eACRs were transferred to other well-characterized CCRs with a broader scope of biophysical properties (Wietek et al., 2017) (Appendix Fig. A.1 A, B). Two functional eACRs were obtained, namely Phobos and Aurora, with blue- and red-shifted activation spectra, respectively (Fig. 3.1.1 A; Appendix Fig. A.1 C). Furthermore, the introduction of a step-function point mutation (C128A) decelerated channel closing kinetics and enabled reversible switching between open and closed states. Notably, due to their slowed-down photocycle, the step-function eACRs display increased operational light sensitivity, as shown in HEK cells by Dr. Jonas Wietek (Wietek et al., 2017) (Appendix Fig. A.1 D, E).

Functional characterization of iChloC^{CA}, Phobos^{CA} and Aurora^{CA} in neurons

I characterized the newly developed step-function variants iChloC^{CA}, Phobos^{CA} and Aurora^{CA} in CA1 pyramidal neurons in organotypic slices of rat hippocampus using whole-cell patch-clamp electrophysiology.

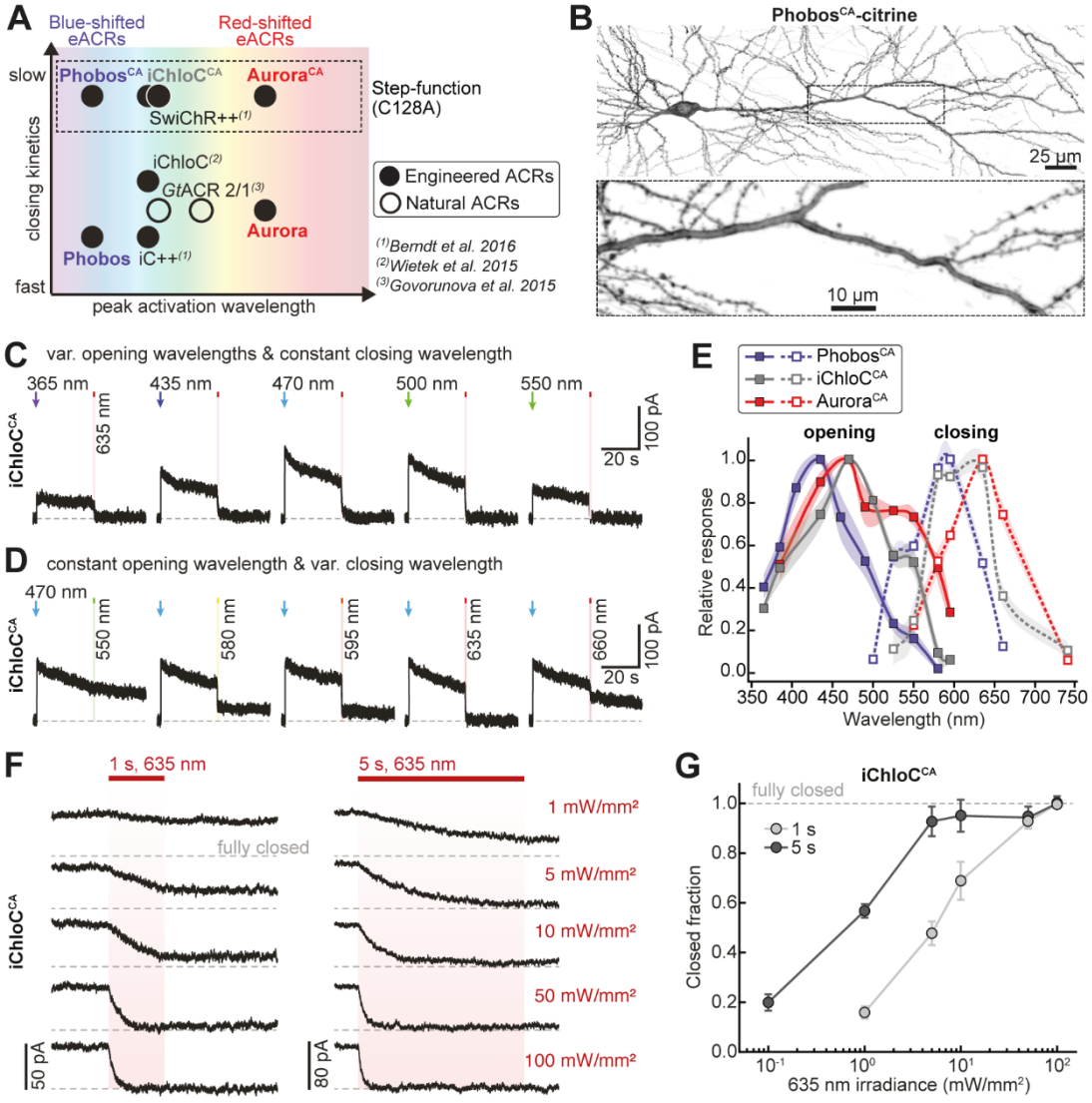

Figure 3.1.1. Photocurrent characterization of step-function eACRs with color-shifted activation spectra in CA1 pyramidal cells in organotypic hippocampal slice cultures. (A) Schematic diagram showing the available ACRs up to 2017, the year in which we developed the blue-shifted ACR Phobos and the red-shifted ACR Aurora, as well as their respective step-function variants Phobos^{CA} and Aurora^{CA}, in addition to iChloC^{CA}. The ACRs are sorted according to their approximate peak activation wavelength (x axis) and closing kinetics (y axis). Engineered and natural ACRs are depicted as filled and empty circles, respectively. The newly developed eACRs expanded the toolkit in the spectral and temporal range. **(B)** CA1 pyramidal neuron expressing Phobos^{CA}-citrine (stitched maximum intensity projections of two-photon Z-stack images, fluorescence intensity shown as inverted gray values). Inset shows magnified view of the apical dendrite. Citrine fluorescence was

mainly localized to the plasma membrane. **(C)** Representative recordings of photocurrents in an iChloC^{CA}-expressing CA1 cell. Neurons were held above the chloride Nernst potential at a membrane voltage of -50 mV. Photocurrents were evoked by opening the channel with a 20 ms light pulse of different activation wavelengths and closing with 1 s 635-nm light (10 mW/mm^2). **(D)** Photocurrent traces in the same cell evoked with 470 nm light and channel closing at indicated wavelengths. **(E)** Activation (solid lines) and inactivation spectra (dashed lines) of Phobos^{CA}, iChloC^{CA} and Aurora^{CA} leading to opening and closing of the channel. Lines are interpolations of data points and shaded areas represent SEM. **(F)** Example recordings showing light-accelerated channel closing of iChloC^{CA} by illumination with 635 nm light at indicated powers for 1 s (left) or 5 s (right). **(G)** Quantification of channel closure for the experiments shown in (F). Averages are shown as circles ± SEM (n=5).

Four to six days after transfection via single-cell electroporation CA1 neurons showed bright, membrane-localized expression of the citrine-labeled eACRs, indicating their proper membrane insertion (Fig. 3.1.1 B shows expression for Phobos^{CA}). CA1 cells were clamped at a membrane voltage of -50 mV, which is above the Nernst potential for chloride (E_{Cl^-} = -73.4 mV, see section 2.3), thus resulting in entry of Cl^- ions and outward-directed photocurrents upon opening of a Cl^- conducting channel. Various stimulation wavelengths (at the same irradiance) were used to determine the activation (channel opening) and inactivation (channel closing) spectra of each eACR (Fig. 3.1.1 C-E). iChloC^{CA} was maximally activated at 470 nm and inactivated at 635 nm light. Phobos^{CA} showed a blue-shifted action spectrum with maximal activation at 435 nm and inactivation at 595 nm, whereas Aurora^{CA} was more red-shifted, displaying a broader spectral activation shoulder around 520 nm, while inactivation was maximal at 635 nm (Fig. 3.1.1 E). Since light-accelerated closing of bi-stable ChRs is a function of light energy (Hososhima et al., 2015), the off-kinetics of eACR C128A variants might be further accelerated with red light at high irradiances. To investigate this in more detail, light-induced closing of iChloC^{CA} was evoked by illumination with 635 nm light at various irradiances (ranging from 0.1 to 100 mW/mm^2) for either 1 s or 5 s (Fig. 3.1.1 F). Full channel closing could be achieved with 5 mW/mm^2 over 5 s or 50 mW/mm^2 over 1 s (Fig. 3.1.1 G).

As brief photoactivation of iChloC^{CA}, Phobos^{CA} and Aurora^{CA} results in sustained Cl^- influx for several seconds (t_{off} = 128 ± 9 s, 249 ± 10 s, and 424 ± 15 s, respectively) (Appendix Fig. A.1 D, E), I next asked whether these new step-function eACRs are suitable to block action potentials (APs) for an extended time period after a brief light pulse and whether this block could be reverted with red-shifted illumination. Indeed, all three eACRs suppressed current-evoked APs in CA1 neurons in the 55 s following channel opening (20 ms light pulse, 10 mW/mm^2, Phobos^{CA}: 460 nm, iChloC^{CA}: 470 nm, Aurora^{CA}: 525 nm) (Fig. 3.1.2 A).

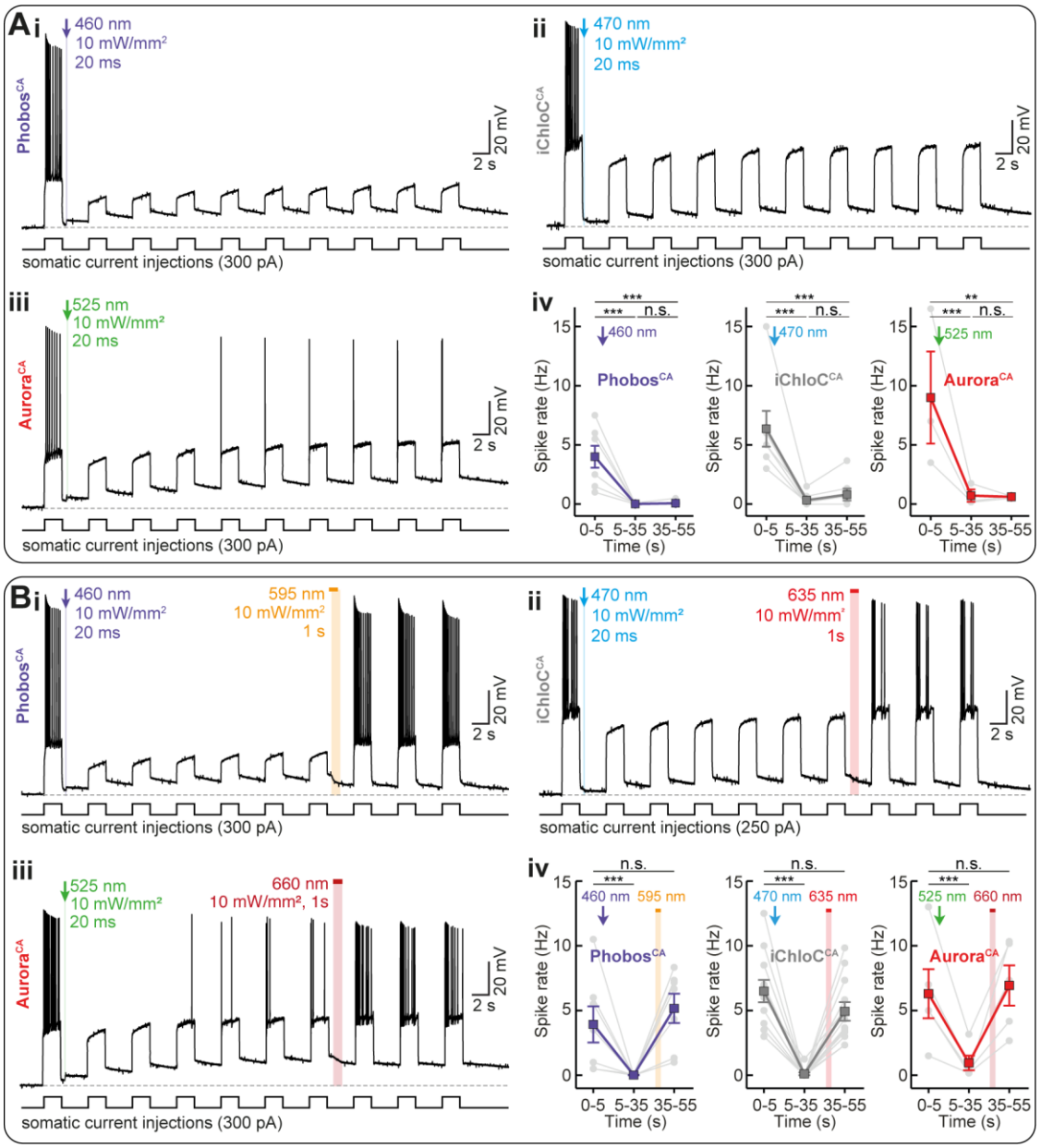

Figure 3.1.2. Action potential inhibition in CA1 pyramidal cells with Phobos^{CA}, iChloC^{CA} and Aurora^{CA}. (A, i-iii) Representative membrane voltage traces showing suppression of depolarization-induced action potentials (APs) for 55 s after activation of Phobos^{CA} (i), iChloC^{CA} (ii) or Aurora^{CA} (iii) with a short light pulse at indicated wavelengths (20 ms, 10 mW/mm^2). Dashed grey lines indicate resting membrane potential. **(A, iv)** Quantification of spike rate before (0-5 s) and after channel opening (5-35 and 35-55 s) for all three eACRs (left to right: Phobos^{CA}, iChloC^{CA} and Aurora^{CA}, n= 7, 7 and 3, respectively). **(B, i-iii)** Same as (A, i-iii) but current-evoked APs were recovered 30 s after channel opening by photoswitching the respective eACR back to its closed state using light of a longer wavelength (1 s, 10 mW/mm^2, Phobos^{CA}: 595 nm (i), iChloC^{CA}: 635 nm (ii), Aurora^{CA}: 660 nm (iii)). Note that activation of AuroraCA caused a slight depolarization of the resting membrane potential (A,B, iii). **(B, iv)** Quantification of spike rate during current injection at indicated time intervals: before channel opening (0-5 s), after channel opening (5-35 s), and after channel closing (35-55 s) in CA1 neurons expressing Phobos^{CA} (n=7), iChloC^{CA} (n=12) or Aurora^{CA} (n=5). In all plots grey circles indicate measurements in individual cells. Mean values ± SEM are shown as rectangular colored symbols. Repeated measures one-way ANOVA followed by Tukey's multiple comparisons test, *p < 0.05, **p < 0.01, ***p < 0.001, n.s.= not significant.

Furthermore, baseline AP firing could be recovered with high temporal precision by accelerating channel closure with a light pulse at the peak inactivation wavelength for each eACR (1 s light pulse, 10 mW/mm^2, Phobos^{CA}: 595 nm, iChloC^{CA}: 635 nm, Aurora^{CA}: 660 nm) (Fig. 3.1.2 B). It should be noted that a slight depolarization of the resting membrane potential in Aurora^{CA}-expressing cells was observed during current injection in the dark, suggesting the presence of a depolarizing leak conductance. This membrane depolarization became more apparent after light activation of Aurora^{CA}, which prevented complete spike block (Fig. 3.1.2 A-B, panel iii). These limitations, which were not observed for iChloC^{CA} or Phobos^{CA}, should be taken into account when considering Aurora^{CA} as a silencing tool in neurons.

Modulation of behavioral responses in *Drosophila*

The most promising eACR variants were further tested in the invertebrate model organism *Drosophila melanogaster*. The fast generation of transgenic flies and simple, yet meaningful behavioral assays based on various standardized tests, make *Drosophila* larvae an ideal model to assess the neuronal silencing potential of ACRs *in vivo*. I characterized the performance of the blue-shifted step-function

eACR Phobos^{CA} in *Drosophila* larvae using two established behavioral assays (Fig. 3.1.3).

First, Phobos^{CA} was expressed in larval glutamatergic motor neurons to optically inhibit forward locomotion. Brief activation of Phobos^{CA} (5 s, 460 nm, 80 µW/mm^2) was sufficient to inhibit larval locomotion for up to 210 s after light stimulation (Fig. 3.1.2 B), indicating a long-lasting silencing effect of Phobos^{CA} on the motor system of *Drosophila* larvae. Reverting the open-state of Phobos^{CA} with 595-nm illumination efficiently recovered locomotion within 20 s (Fig. 3.1.3 C, D). As expected, wild-type (*wt*) control animals only slowed down during application of the blue light pulse due to photoavoidance (Xiang et al., 2010) and regained full locomotion speed after light shutoff (Appendix Fig. A.2).

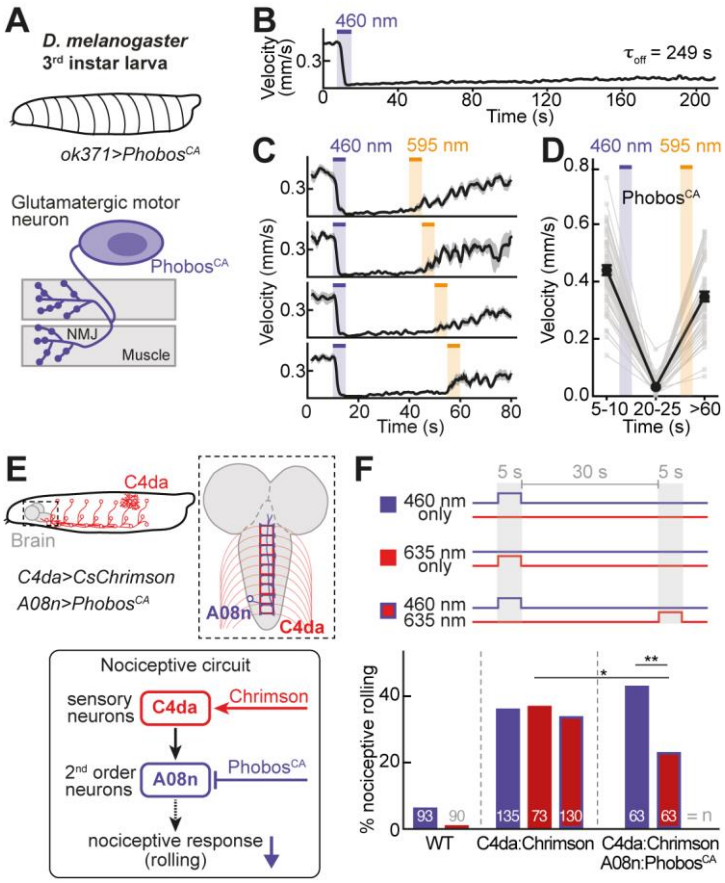

Figure 3.1.3. Phobos^{CA} in *Drosophila* larval locomotion and nociception. (A) Phobos^{CA} expressed in motor neurons of *D. melanogaster* larvae (*ok371-Gal4*) enables inhibition of forward locomotion by body relaxation. Scheme of a Phobos^{CA}-expressing glutamatergic motor neuron innervating muscle fibers. **(B)** Average larval velocity over time showing inhibition of locomotion after light-induced activation of Phobos^{CA} (5 s, 460 nm, 80 µW/mm^2). **(C)** Average larval velocity upon activation and inactivation (5 s, 595 nm, 6.9 mW/mm^2) of Phobos^{CA} at indicated time points (40–60 s). **(D)** Average velocities before animals, black symbols: mean ± SEM). **(E)** Top: Scheme of a *Drosophila* larva expressing *Cs*Chrimson in sensory C4da neurons (*27H06-LexA*), and Phobos^{CA} in A08n neurons (*82E12-Gal4*). Bottom: simplified diagram of the mechano-nociceptive circuit in *Drosophila* larvae. Red-light-activation of *Cs*Chrimson-expressing C4da neurons triggers nociceptive responses (rolling). Prior

blue-light activation of Phobos^{CA} in A08n neurons downstream of C4da neurons is expected to reduce *Cs*Chrimson-evoked nociceptive rolling. **(F)** Top: experimental paradigm showing the 3 different light stimulation protocols (460 nm, 80 µW/mm^2; 635 nm, 55 µW/mm^2) Bottom: light-induced nociceptive rolling of WT larvae, and larvae expressing *Cs*Chrimson in C4da neurons alone or together with Phobos^{CA} in A08n neurons. Bar color corresponds to the light stimulus conditions as indicated above. *p < 0.05, **p < 0.01, chi^2 test.

In a second set of experiments, I performed all-optical interrogation of the larval mechano-nociceptive circuit by combining Phobos^{CA} with the red-shifted CCR *Cs*Chrimson (Fig. 3.1.3 E). In *Drosophila* larvae, Class IV dendritic arborization (C4da) neurons are the primary nociceptors, responding to a wide variety of harmful stimuli such as harsh mechanical touch (Zhong et al., 2010), noxious temperatures (Tracey et al., 2003) and strong UV and blue light (Xiang et al., 2010). The subsequent C4da-mediated nocifensive response, characterized by a stereotyped rolling behavior, has been previously reproduced by optogenetic activation of C4da neurons (Hwang et al., 2007). Recently, A08n neurons have been identified as downstream targets of C4da neurons (C. Hu et al., 2017). To confirm this hierarchical network organization, transgenic larvae expressing *Cs*Chrimson in C4da neurons and Phobos^{CA} in A08n were generated (Fig. 3.1.3 E). As expected, nociceptive rolling, evoked by *Cs*Chrimson-mediated activation of sensory C4da neurons, was reduced by Phobos^{CA}-mediated silencing of downstream A08n neurons (Fig. 3.1.3 F), thus providing proof of concept that Phobos^{CA} can be combined with other, spectrally distinct optogenetic tools to efficiently modulate neuronal activity.

The work described in section 3.1.1. is published in the journal *Scientific Reports* (Wietek et al., 2017).

3.1.2. Aion: an eACR for extended long-term silencing of neurons

Despite the significant progress in the development and identification of new ACRs, optogenetic silencing for extended periods of time at the scale of tens of minutes to hours with precise timing while avoiding continuous illumination remains a challenge (Wiegert et al., 2017). The duration of inhibition mediated by step-function ACRs is dictated by their activation and inactivation kinetics (Andre Berndt et al., 2016; Sineshchekov et al., 2016; Wietek et al., 2017). Using the blue-shifted, step-function eACR Phobos^{CA} as a basis, we sought to develop new variants with an even longer-lasting conducting state. As shown above (section 3.1.1), the point-mutation C128A extends the lifetime of the conducting state of Phobos^{CA}, conferring step-function properties to the ACR. To further decelerate the closing kinetics of Phobos^{CA} we systematically mutated the residue D156 (Fig. 3.1.4 A), which together with C128 forms the DC gate, a structural component important for channel gating kinetics (Kato et al., 2012) (see section 1.1.2, Fig. 1.2). We hypothesized that disrupting the hydrogen bond between the oxygen of the D156 carboxyl group and the hydrogen of the water molecule w5, which is required for a functional DC gate, would slow down the photocycle (Volkov et al., 2017; Watanabe et al., 2013). Therefore, we exchanged D156 for either C, asparagine (N), serine (S), or histidine (H), all amino acids that are not likely to form a hydrogen bond with w5, while maintaining a similar spatial conformation of the DC gate due to a comparable size and carbon backbone as aspartic acid. From all tested mutants, only the D156N (Phobos^{CADN}) and D156C (Phobos^{CADC}) showed functional neuronal expression and were further investigated for their potential use as optogenetic tools for long-term silencing. In particular, Phobos^{CADC}, from here on termed Aion after the Greek God of unbounded time (Levi, 1944), is the ACR with the longest known conducting state (Fig. 3.1.4 B).

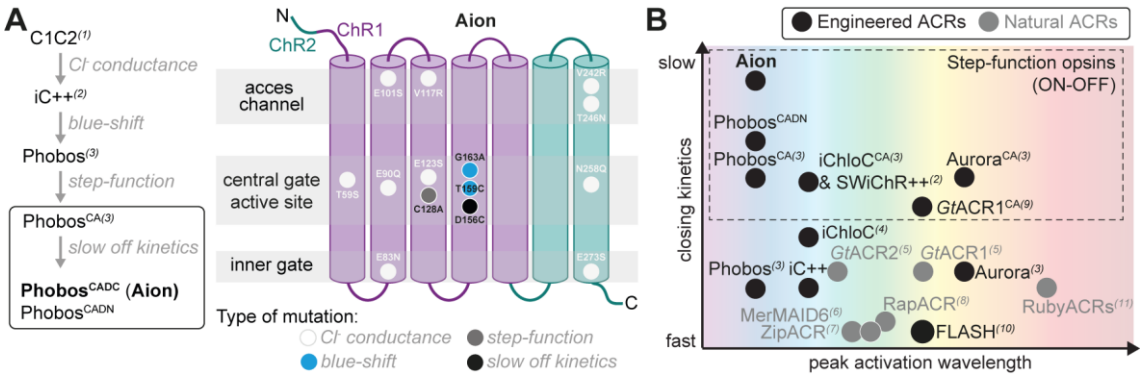

Figure 3.1.4. Development of Aion and Phobos^{CADN} and comparison to other available anion-conducting channelrhodopsins. (A) Left: Engineering strategy yielding Aion and Phobos^{CADN}, two new blue-shifted, step-function ACRs with extra-long-conducting state. Mutation of the D156 residue either to C or N (yielding Aion and Phobos^{CADN}, respectively) greatly slows down the closing kinetics of the ACRs compared to its closest predecessor Phobos^{CA}. This mutagenesis step is highlighted by a black frame. Right: Molecular scheme of Aion displaying the point mutations as circles at the relative position within the respective transmembrane helix. **(B)** Schematic diagram showing some of the available anion-conducting channelrhodopsins (ACRs) used as optogenetic silencers in neurons (except for RubyACRs which, so far, have only been tested in HEK293 cells). The ACRs are sorted according to their approximate peak activation wavelength (x axis) and closing kinetics (y axis). Engineered and natural ACRs are depicted as black and grey circles, respectively. For simplicity, in the figure references are indicated by numerical superindexes: 1 (Kato et al., 2012), 2 (Berndt et al., 2016), 3 (Wietek et al., 2017), 4 (Wietek et al., 2015a), 5 (Govorunova et al., 2015), 6 (Oppermann et al., 2019), 7 (Govorunova et al., 2017), 8 (Govorunova et al., 2018), 9 (Govorunova et al., 2018; Sineshchekov et al., 2016), 10 (Kato et al., 2018), 11 (Govorunova et al., 2020).

Functional characterization of Phobos^{CADN}, Aion and *Gt*ACR1^{CA}

I characterized the functional properties of Phobos^{CADN} and Aion and tested their silencing ability in CA1 neurons in organotypic hippocampal slice cultures (Fig. 3.1.5 – 3.1.9). I further compared their performance to *Gt*ACR1-C102A (*Gt*ACR1^{CA}) (Govorunova et al., 2018; Sineshchekov et al., 2016), an engineered step-function variant of the potent, natural *Gt*ACR1. *Gt*ACR1^{CA} has been shown to inhibit neuronal spiking in mammalian neurons for at least 10 s after a brief light stimulus (Govorunova et al., 2018). Additionally, *Gt*ACR1^{CA} enabled light-induced body wall muscle relaxation when expressed in motor neurons of *C. elegans* (Bergs et al., 2018). I first evaluated the expression of citrine-labelled Phobos^{CADN}, Aion and *Gt*ACR1^{CA} in CA1 pyramidal neurons. All three ACRs were readily detected 4–5 days after single-cell electroporation and showed membrane-localized distribution (Fig.

3.1.5 A). However, *Gt*ACR1^{CA} did not traffic evenly throughout the cell and displayed some accumulations (Fig 3.1.5 A, right panel).

Using whole-cell patch-clamp recordings I next measured light-induced Cl^- currents. Opsin-expressing neurons were held above the E_{Cl-} at a membrane voltage of −35 mV, conditions under which entry of Cl^- ions resulted in outward-directed photocurrents. A short light pulse at the peak activation wavelength (460 nm for Phobos^{CADN} and Aion; 525 nm for *Gt*ACR1^{CA}) elicited Cl^- photocurrents that were maintained for several seconds to minutes after light offset (Fig. 3.1.5 B). While all ACRs showed similar peak currents (Fig. 3.1.5 C), Phobos^{CADN}- and *Gt*ACR1^{CA}-mediated Cl^- photocurrents decayed faster after channel opening, showing peak-normalized mean photocurrent amplitudes of 25.6 ± 1.2 % and 14.6 ± 1.1 % (Phobos^{CADN}), and 20.2 ± 1.1 % and 6.1 ± 1.8 % (*Gt*ACR1^{CA}), at 30 s and 120 s after light stimulation, respectively (Fig. 3.1.5 D, E). In contrast, Aion-mediated stationary Cl^- currents were relatively stable over the whole 3-minutes recording (Fig. 3.1.5 B, middle right trace), with peak-normalized mean photocurrent amplitudes of 22.1 ± 1.2 % and 17.7 ± 1.1, at 30 s and 120 s after channel opening, respectively (Fig. 3.1.5 D, E). This is in accordance with photocurrent kinetics measured in HEK cells by Dr. Jonas Wietek, where Aion showed a several-fold larger channel closing time constant compared to Phobos^{CADN} and *Gt*ACR1^{CA} (Appendix Fig. A.3).

Similar to their parental construct Phobos^{CA}, the closing of both Phobos^{CADN} and Aion could be accelerated at any time point by 1 s illumination with orange light (595 nm), bringing the photocurrents back to baseline (Fig. 3.1.5 B top and middle traces, F, G). On the contrary, accelerated closing of *Gt*ACR1^{CA} with red-shifted light (660 nm) was not efficient. 1 s-illumination 35 s after opening reduced the I current only by 21% (Fig. 3.1.5 B bottom left trace, F). Moreover, red light stimulation 198 s after channel opening, a time by which *Gt*ACR1^{CA} was mostly closed via thermal relaxation of the open state, elicited a Cl^- current with an amplitude of 20.5 % compared to the green-light induced peak current (Fig. 3.1.5 B bottom right trace,

G). This indicates that red light likely brings *Gt*ACR1^{CA} to an intermediate conducting state in the photocycle, rather than to the dark ground state.

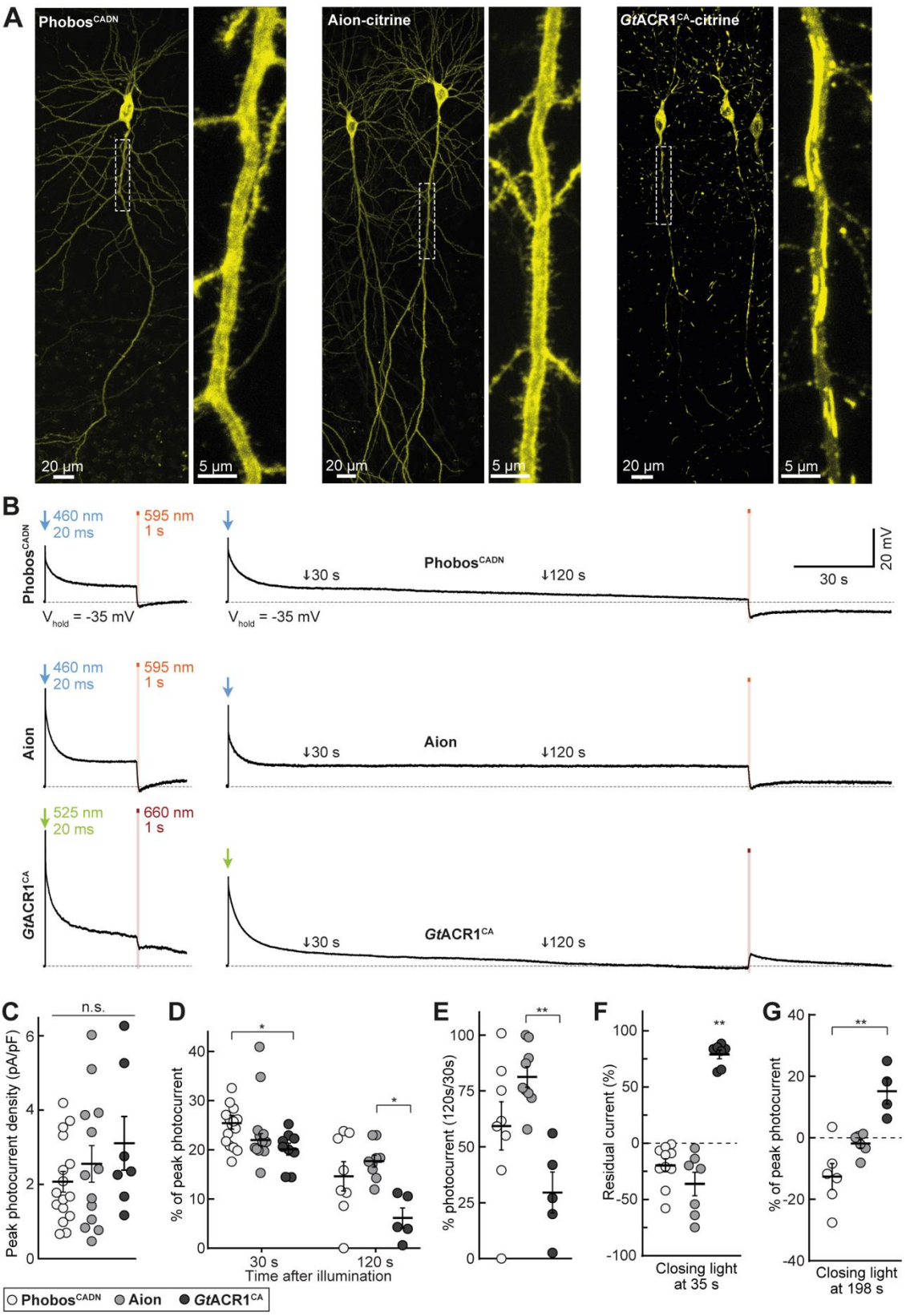

Figure 3.1.5. Expression and photocurrent characterization of Phobos^{CADN}, Aion and *Gt*ACR1^{CA} in CA1 pyramidal neurons (A) Maximum-intensity projection images of two-photon stacks showing expression of Phobos^{CADN} (left), Aion (middle) and GtACR1^{CA} (right) in CA1 pyramidal neurons after single-cell electroporation in organotypic hippocampal slice cultures. Insets show magnified view of the main apical dendrite. **(B)** Representative photocurrent traces of Phobos^{CADN} (top) and Aion (middle) compared to the established step-function ACR *Gt*ACR1^{CA} (bottom), evoked by a 20 ms light pulse at the respective peak activation wavelength (460 nm for Phobos^{CADN} and Aion, 525 nm for *Gt*ACR1^{CA}) and equal irradiance of 10 mW/mm^2. CA1 neurons were held above the chloride Nernst potential at a membrane voltage of -35 mV. Channel closing was facilitated with red-shifted light (1 s, 10 mW/mm^2, 595 nm for Phobos^{CADN} and Aion, 660 nm for *Gt*ACR1^{CA}) at 34 (left) or 197 s (right) after channel opening. Note that red light at 197 s elicited partial opening of *Gt*ACR1^{CA} instead of closing, indicated by an outward current after light stimulation. The arrows at 30 and 120 s after channel opening indicate the time points at which stationary photocurrent amplitude was quantified in D-E. **(C)** Quantification of peak photocurrent density for Phobos^{CADN}, Aion and *Gt*ACR1^{CA}. **(D)** Quantification of photocurrent amplitude at 30 and 120 s after channel opening with respect to peak photocurrent. **(E)** Photocurrent ratio at 120 compared to 30 s. **(F)** Residual current upon channel closing 34 s after opening. Photocurrent amplitude was measured in the 5 s before and after the closing light pulse. **(G)** Quantification of photocurrent amplitude upon channel closing 197 s after opening with respect to the peak photocurrent. Mean values ± SEM are shown (black lines) together with single measurement data points (circles, n = 5-16). Kruskal-Wallis test with Dunn's multiple comparisons test, *$p < 0.05$, **$p < 0.01$.

Next I tested whether Phobos^{CADN}, Aion and *Gt*ACR1^{CA} were suitable to block action potentials (APs) for an extended time period after a brief light flash and whether this block could be reverted with red-shifted illumination. Both Phobos^{CADN} and Aion efficiently blocked depolarization-induced APs for 40 s following a 20 ms blue light pulse. Furthermore, AP firing could be recovered with high temporal precision after closing the respective channel with orange light (Fig. 3.1.6 A, B). Activation of *Gt*ACR1^{CA} (20 ms 525nm-light pulse) also resulted in sustained inhibition of current-evoked APs, however, AP firing could not be restored upon red light illumination (Fig. 3.1.6. C). This is consistent with the photocurrent recordings, in which only partial reduction of *Gt*ACR1^{CA} conductance was observed upon red illumination (Fig. 3.1.5 B bottom left trace, F), leaving a residual Cl^- conductance big enough to prevent AP recovery. Thus, unlike Phobos^{CADN} and Aion, *Gt*ACR1^{CA} does not allow precisely timed termination of the inhibition time period.

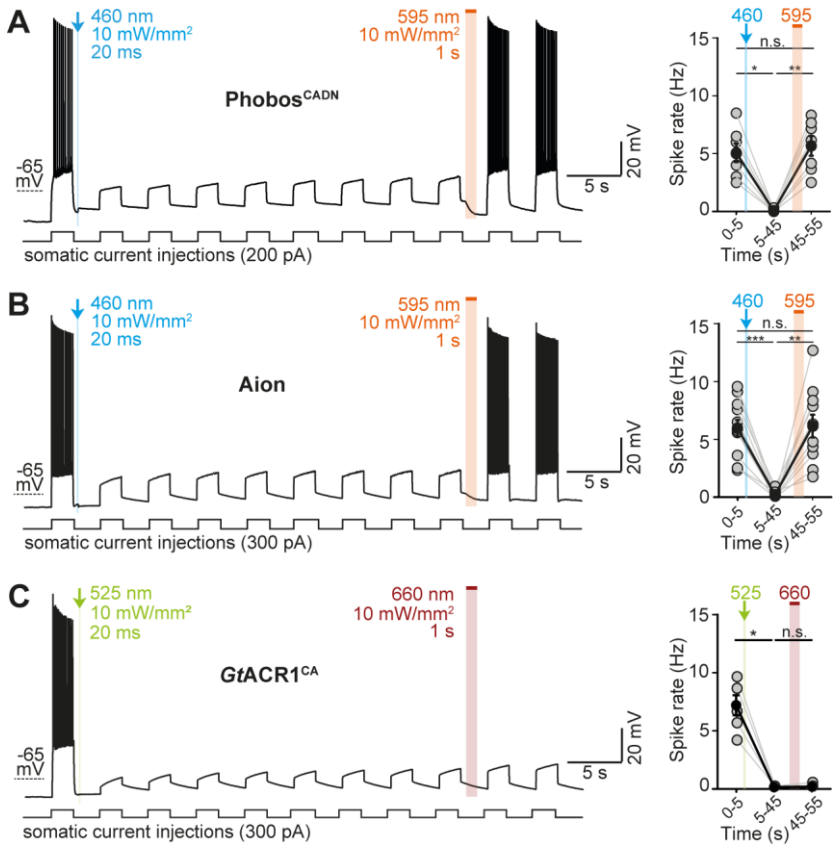

Figure 3.1.6. Reversible action potential inhibition with Phobos^{CADN} and Aion. (A) Left: Membrane voltage trace showing reversible suppression of depolarization-induced action potentials (APs) by photoswitching Phobos^{CADN} between open and closed state with a blue (460 nm, 20 ms, 10 mW/mm^2) and orange light pulse (595 nm, 1 s, 10 mW/mm^2), respectively. Right: Quantification of spike rate during current injection at indicated time intervals: before channel opening (0-5 s), after channel opening (5-45 s), and after channel closing (45-55 s) in Phobos^{CADN}-expressing CA1 neurons (n=7). **(B)** Same as (A) but for Aion-expressing cells (n=10). **(C)** Same as (A) but for neurons expressing *Gt*ACR1^{CA} (n=5). Channel was opened with a green (525 nm, 20 ms, 10 mW/mm^2) and closed with a red light pulse (660 nm,1 s, 10 mW/mm^2). Note that in *Gt*ACR1^{CA}-expressing cells AP firing cannot be recovered immediately after illumination with red light, probably due to only partial closing of the channel. In all plots grey circles represent single measurement data points and black circles correspond to mean values ± SEM, Friedman test, *p < 0.05, **p < 0.01, ***p < 0.001, n.s.= not significant.

To compare the silencing performance of the three step-function ACRs in a more quantitative manner, I measured their capacity to shift the rheobase (i.e. minimum current required to reach AP threshold) to higher values upon light activation. Depolarizing current ramps (2 s duration, up to 1000 pA) were repeatedly injected into ACR-expressing CA1 neurons at an interval of 0.2 Hz for one minute. For each ramp, the injected current at the time of the first spike was defined as the

rheobase. To open the respective ACR a 1 s light pulse was applied after the first current ramp (Phobos^{CADN} and Aion: 460 nm; *Gt*ACR1^{CA}: 525 nm; irradiances ranging from 0.001 to 10 mW/mm^2) (Fig. 3.1.7 A-C, panel i). Although all three ACRs shifted the rheobase towards larger currents for several seconds after light stimulation, differences in efficacy were observed.

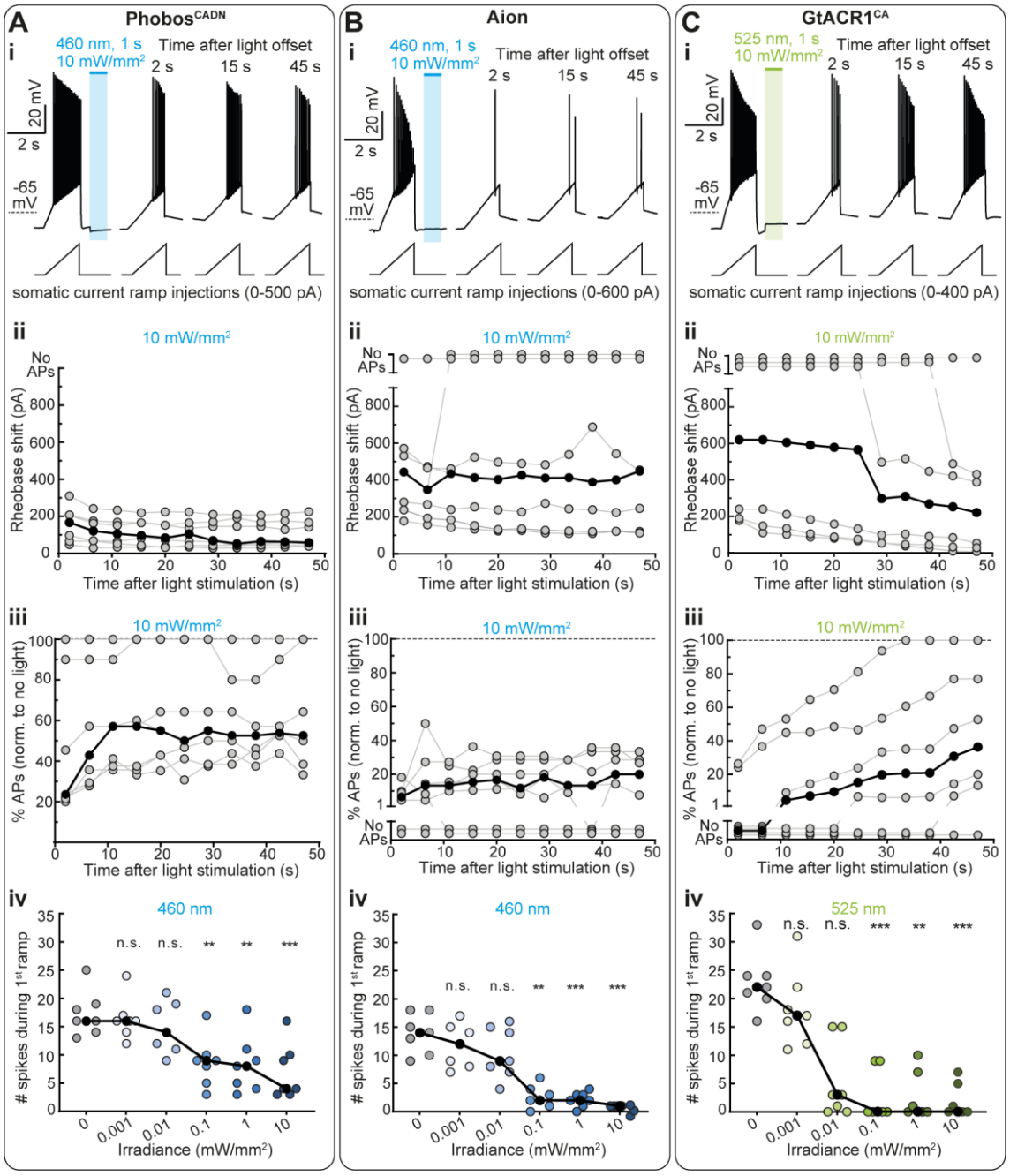

Figure 3.1.7. Silencing efficiency of Phobos^{CADN}, Aion and *Gt*ACR1^{CA} over 1 minute in CA1 pyramidal neurons. (A) Current ramps were injected into Phobos^{CADN}-expressing neurons to induce APs before and after illumination with a short blue light pulse (460 nm, 1 s, irradiances from

0.001 to 10 mW/mm^2). For each ramp, the injected current at the time of the first action potential was defined as the rheobase. **(i)** Example membrane voltage traces are shown for the trial in which a light intensity of 10 mW/mm^2 was used. **(ii)** Quantification of the rheobase shift and **(iii)** the relative change in the number of current ramp-evoked APs over 1 minute after light stimulation (460 nm, 1 s, 10 mW/mm^2) (n=7). **(iv)** Relative change in the number of APs evoked during the first current ramp after opening of Phobos^{CADN} with 1 s blue light at indicated irradiances. Significant AP block was achieved at 0.1 mW/mm^2 (n = 7). **(B, i-iv)** Same experiment as shown in (A, i-iv) but for Aion-expressing cells (n=7). Note that 1 s illumination with 460 nm light of 10 mW/mm^2 activated Aion-mediated Cl^- currents that reliably shifted the rheobase and shunted APs for an entire minute after light stimulation (B, ii-iii). **(C, i-iv)** Same experiment as shown in (A, i-iv) except that CA1 neurons express *Gt*ACR1^{CA} (n=6-7) and 525nm-light was used for channel opening. Note that *Gt*ACR1^{CA} silencing efficacy decays already within the 1st minute after light stimulation (C, ii-iii). In all plots grey circles represent single measurement data points and black circles correspond to medians, Friedman test, *p < 0.05, **p < 0.01, ***p < 0.001, n.s.= not significant.

Phobos^{CADN} showed the weakest silencing capacity, only shifting the rheobase by 157.5 ± 32.7 pA immediately after illumination, which was not sufficient to completely block APs (Fig 3.1.7 A, panels ii and iii). Aion-mediated inhibition was more potent, yielding a rheobase shift of 463.2 ± 98.0 pA which was maintained for at least 47 s after light stimulation (Fig 3.1.7 B, panel ii). As a result, the median number of current-evoked APs was suppressed by 85.3 % (range: 80.0 – 93.3 %), with complete AP block in 2 out of 7 cells (Fig 3.1.7 B, panel iii). *Gt*ACR1^{CA} also led to strong inhibition immediately after light stimulation, shifting the rheobase by 601.3 ± 162.9 pA and fully suppressing APs in 4 out of 6 cells. However, unlike Aion, *Gt*ACR1^{CA} silencing capacity was not sustained over time and after 47 s the shift in rheobase dropped to 318.2 ± 142.6 pA (a reduction of 52.9 %), yielding 56.2 % (range: 0.0 – 100 %) suppression of APs (Fig 3.1.7 C, panels ii and iii). All three ACRs significantly decreased AP firing starting at an irradiance of 0.1 mW/mm^2, while *Gt*ACR1^{CA} showed complete block of APs already at 0.01 mW/mm^2 in 2 out of 7 cells (Fig 3.1.7 A-C, panel iv).

Taking into account the weak performance of Phobos^{CADN}, only Aion and *Gt*ACR1^{CA} were further assessed for their applicability as long-term silencing tools. Aion reliably blocked depolarization-induced APs over a 10-minute period when

activated by 2 brief light pulses (1 s, 460 nm, 10 mW/mm²) delivered 5 minutes apart (Fig. 3.1.8 A). Accordingly, the Aion-mediated decrease in membrane depolarization of 54.5 % (range: 48.2 - 62.4 %) was stable for 300 s (i.e. 5 min) after light stimulation (Fig. 3.1.8 C). Conversely, in neurons expressing *Gt*ACR1^{CA} current-evoked AP firing was generally recovered within the first minute (46.0 ± 10.5 s in 3 cells, 201.6 s in 1 cell) after opening of the channel by a short light pulse (1 s, 525 nm, 10 mW/mm²), and the initial reduction of 59.3 % (range: 52.7 % - 66.9 %) in membrane depolarization went back to baseline values after 3.6 ± 0.3 min (Fig. 3.1.8 B, D).

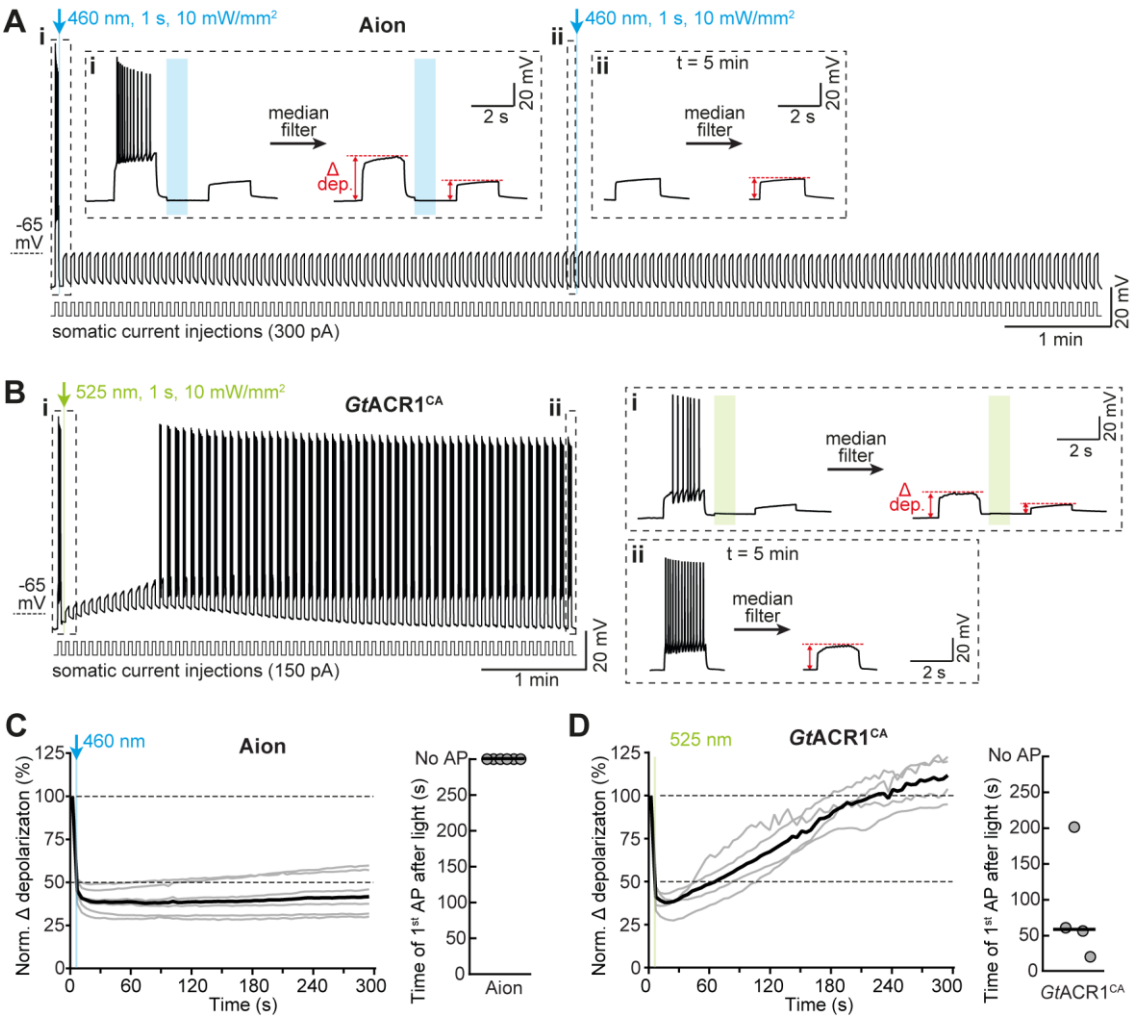

Figure 3.1.8. Silencing efficiency of Aion and *Gt*ACR1^{CA} over several minutes in CA1 pyramidal neurons. (A) Aion silencing capacity was evaluated over 10 minutes. Example membrane voltage trace of an Aion-expressing CA1 neuron showing reliable suppression of depolarization-induced APs (2 s current injections every 2.5 s) for 10 min by activating Aion with short

blue light pulses every 5 min (460 nm, 1 s, 10 mW/mm^2). **(i, ii)** Insets show magnified view of the membrane potential at the indicated time points. Voltage traces were median-filtered to calculate the change in membrane depolarization after light stimulation of Aion (as shown by the red arrows). **(B)** *Gt*ACR1^{CA} silencing capacity was evaluated over 5 minutes. Example membrane voltage trace of a *Gt*ACR1^{CA}-expressing CA1 neuron showing reliable suppression of depolarization-induced action potentials for 5 min by activating *Gt*ACR1^{CA} with a short green light pulse (525 nm, 1 s, 10 mW/mm^2). **(i, ii)** same as (A, i-ii) but for *Gt*ACR1^{CA}. **(C)** Left: Quantification of Aion-mediated change in membrane depolarization over a time period of 5 min after light stimulation (460 nm, 1 s, 10 mW/mm^2) as shown in (A). Right: Time at which the 1st current-evoked AP occurred after opening of Aion. Note that Aion reliably blocked all APs for 5 min after light stimulation (n = 6). Grey circles represent single measurement data points and black lines correspond to medians. **(D)** Same as (C) but for *Gt*ACR1^{CA} (n=4; 525 nm, 1 s, 10 mW/mm^2). Note that the change in membrane depolarization went back to baseline approx. 3.5 min after light stimulation (left) and neurons started firing within the first 200 s after light stimulation (right).

Finally, I sought to determine whether Aion is suitable for continuous neuronal silencing over several hours and whether such long-term Aion-mediated Cl^- conductance comprised cell health. Having shown that brief light stimulations every 5 minutes allow reliable suppression of AP firing in Aion-expressing CA1 neurons, a similar protocol was used to stimulate neurons overnight inside the incubator in a custom-made blue-LED chamber (Fig. 3.1.9 A). Whole-cell current-clamp recordings in Aion-expressing cells after 12 h of light-stimulation showed that current-evoked AP firing was still efficiently blocked for at least 5 min by a single blue light pulse with similar properties to the ones applied In the Incubator. Thus, Aion was still fully functional and silencing via a Cl^- channel was still efficient (Fig. 3.1.9 A, B).Passive and active membrane parameters of Aion-expressing neurons after 12 h of light stimulation were similar to those of non-transfected CA1 cells and neurons only expressing the fluorescent label citrine. Therefore, continuous activation of Aion for 12 h was well tolerated by CA1 pyramidal neurons and did not lead to obvious alterations of Cl^- homeostasis (Fig. 3.1.9 C).

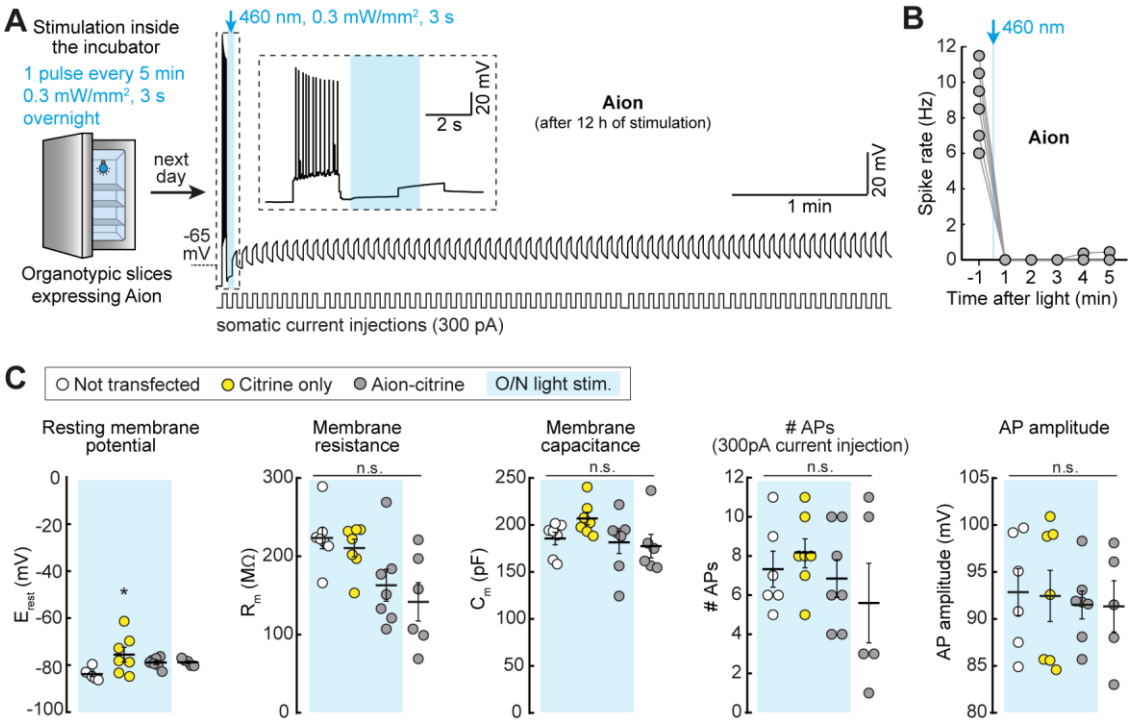

Figure 3.1.9. Long-term silencing of CA1 pyramidal cells with Aion. (A) Left: Organotypic slices with CA1 cells expressing Aion were stimulated overnight (O/N) in a custom-made LED chamber inside the incubator (3 s 460-nm light pulse every 5 min, 0.3 mW/mm^2). Right: example membrane voltage trace of an Aion-expressing CA1 neuron recorded after 12 h of light stimulation in the incubator. Depolarization-induced APs (2 s current injections every 2.5 s) were reliably blocked for 5 min by activating Aion with a 3 s blue light pulse (same conditions as O/N stimulation). Inset shows magnified view of the membrane potential during light stimulation. **(B)** Quantification of spike rate before and in the 5 minutes following light stimulation showing that after 12 h of stimulation, Aion is still functional and efficiently blocks AP firing. **(C)** Cell viability and tolerability of Aion (also after 12 h of light stimulation) was assessed by measuring the following basic neuronal parameters: resting membrane potential, membrane resistance, membrane capacitance, number of APs and amplitude (of the 1st AP) evoked by somatic current injection (300 pA, 500 ms). Neighbouring non-transfected CA1 pyramidal cells and cells expressing only the fluorescent protein citrine (which is coupled C-terminal to the opsin in the Aion-expressing cells) that were stimulated O/N under the same conditions as Aion-expressing cells served as controls. Black lines: mean values ± SEM, Non-transfected n=6, citrine-only n=7, Aion n=7, Aion with no light stimulation n=6, one-way ANOVA, *p < 0.05, n.s.= not significant.

In summary, Aion expands the available toolkit of optogenetic silencers in the temporal domain, allowing neuronal inhibition over many hours with short light pulses spaced several minutes apart.

Improved and soma-targeted expression of Aion

For the functional characterization of Aion, CA1 cells were electroporated with a plasmid concentration of 20 ng/µl, which was well tolerated by the cells and did not alter basic neuronal parameters (Fig. 3.1.9. C). Despite efficient membrane-localized expression (Fig. 3.1.5 A), in some cases, accumulations of Aion were detectable in the soma, basal dendrites and in the proximal region of the main apical dendrite (Fig. 3.1.10 A). Lowering the plasmid concentration to avoid Aion accumulations resulted in reduced silencing capacity (data not shown). Furthermore, such accumulations were also apparent when Aion was virally expressed in the hippocampus of mice *in vivo* (Fig. 3.1.10 B). I therefore aimed to optimize Aion trafficking.

To improve protein export and prevent accumulations, the membrane trafficking signal (ts: KSRITSEGEYIPLDQIDINV) from the mammalian inward rectifying K^+ channel Kir2.1 was added between the coding sequences for Aion and citrine and the Kir2.1 ER export signal (ER: FCYENEV) was introduced at the C-terminus of the construct. Both signals have been previously shown to reduce intracellular aggregation of the ACR *Gt*ACR2 (Mahn et al., 2018) and the Cl^- pump NpHR (Gradinaru et al., 2010). The resulting plasmid, termed Aion-ts-citrine-ER, displayed enhanced membrane trafficking with no detectable intracellular accumulations already when electroporated in CA1 neurons at a concentration of 5 ng/µl (Fig. 3.1.11 A). At this concentration, Aion-ts-citrine-ER showed similar silencing capacity as the non-trafficking-enhanced Aion used at 20 ng/µl, yielding a sustained rheobase shift of 404.5 ± 111.3 pA and efficient suppression of APs (82.6 % (range: 67.5 - 100 %) during the entire 50 s recording period after stimulation with a brief blue light pulse (Fig. 3.1.11 B-E).

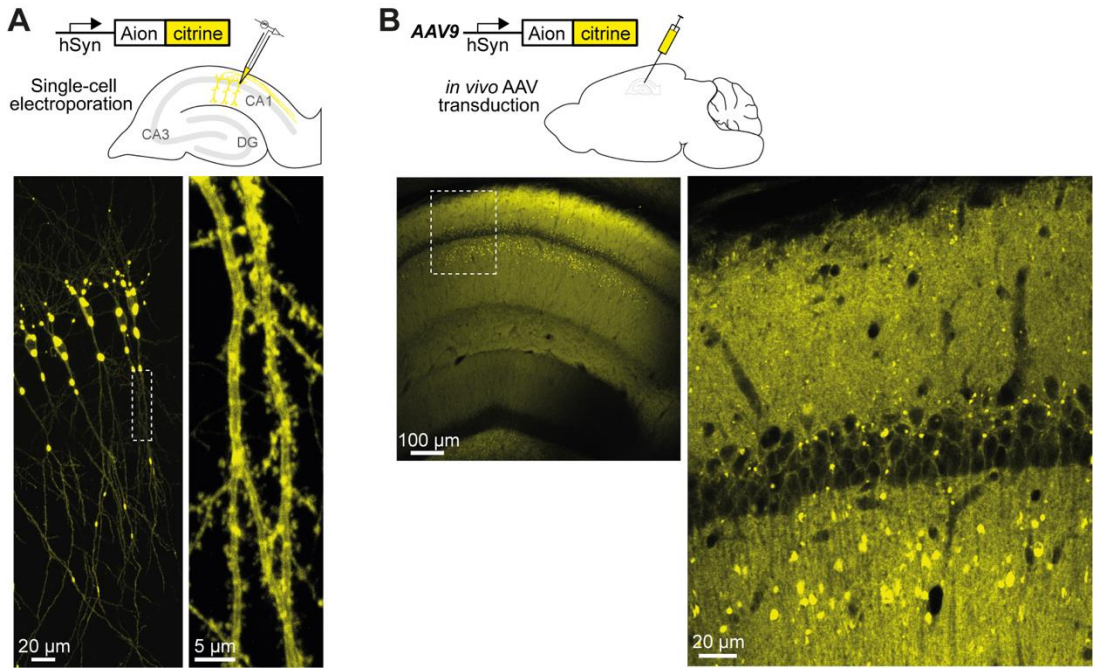

Figure 3.1.10. Overexpression of Aion and opsin accumulations. (A) Maximum-intensity projection image of two-photon stacks showing overexpression of Aion-citrine in CA1 pyramidal neurons after single-cell electroporation in organotypic hippocampal slice cultures. Opsin accumulations were very prominent in the soma, basal dendrites and in the proximal region of the main apical dendrite. Inset shows magnified view of a portion of the main apical dendrite with no accumulations and efficient membrane localization. **(B)** Two-photon image showing overexpression of Aion-citrine in the dendrites of CA1 pyramidal cells in hippocampal sections of perfused WT mice that were injected with an AAV9 vector encoding hSyn-Aion-citrine. Inset shows magnified view. At the soma Aion-expression was finely localized to the plasma membrane, but protein accumulations were abundant throughout the proximal apical dendrites.

An alternative approach to improve membrane trafficking, is to attach a C-terminal Kv2.1-trafficking sequence, which in addition, restricts expression to the somatodendritic compartment (Lim et al., 2000). Soma targeting has the benefit of avoiding expression of the construct in axon terminals, a cell compartment where functionality of Aion might be limited due to an excitatory Cl^- reversal potential (Mahn et al., 2018; Wright et al., 2011). The soma-targeted variant of Aion (somAion) showed improved membrane localization and was confined to the soma and main apical dendrite (Fig. 3.1.12 A). Citrine-fluorescence drastically decayed along the main dendrite, with only 17.9 ± 0.5 % of the maximum intensity observed 136 µm away from the soma, a distance at which the signal from the morphology marker

mCerulean was still 37.1 ± 1.9 % (Fig. 3.1.12 B). somAion blue-light mediated photocurrents were similar in magnitude (peak: 1.5 ± 0.3 pA/pF; stationary: 0.4 ± 0.1 pA/pF) to those in neurons expressing the non-soma targeted Aion (peak: 1.3 ± 0.3 pA/pF; stationary: 0.3 ± 0.1 pA/pF) (Fig. 3.1.12 C-D). Furthermore, compared to Aion, under the same stimulation conditions somAion rendered stronger inhibition, shifting the rheobase to higher values leading to a complete block of current-evoked APs in most cells (4 out of 6 cells) for 47 s after light stimulation (Fig. 3.1.12 E-G). Taken together, soma-targeting of Aion helped overcome the suboptimal trafficking, while avoiding expression in axon terminals, yielding a more effective tool for optogenetic inhibition at the cell soma.

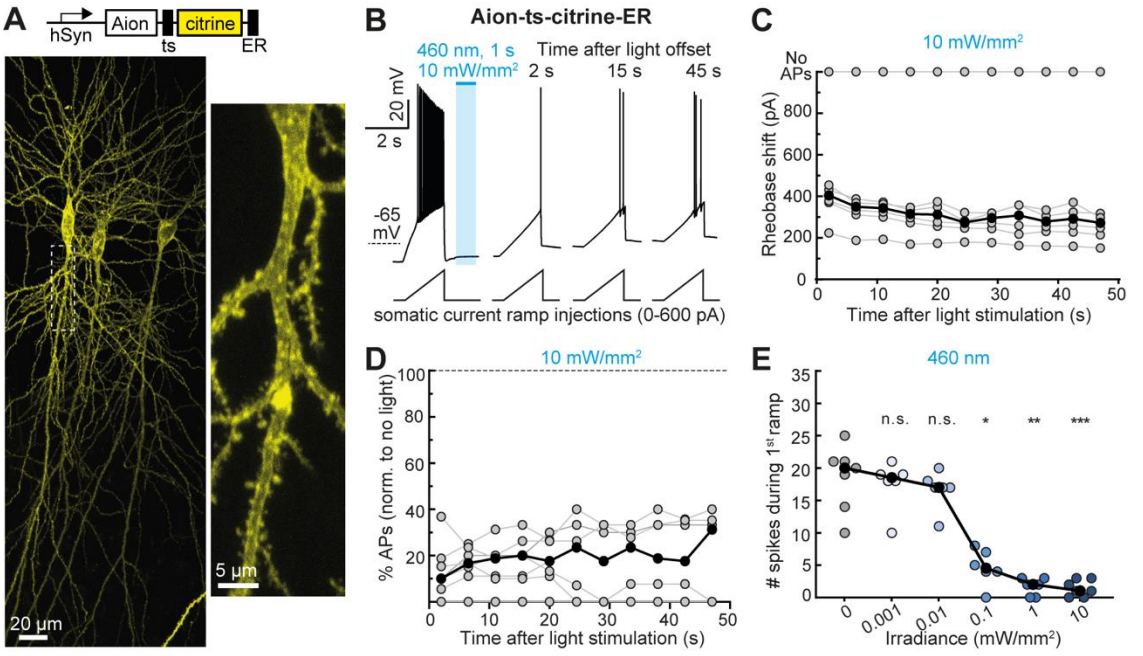

Figure 3.1.11. Aion-ts-citrine-ER: a variant of Aion with improved membrane trafficking. (A) Maximum-intensity projection image of two-photon stacks showing expression of Aion-ts-citrine-ER in CA1 pyramidal neurons after single-cell electroporation (5 ng/µl) in organotypic hippocampal slice cultures. Efficient membrane localization with no opsin accumulations was observed throughout the cell. Inset shows magnified view of the main apical dendrite. **(B)** Example membrane voltage traces in response to current ramps injected into Aion-ts-citrine-ER-expressing neurons before and after illumination with a 1 s blue light pulse. For each ramp, the injected current at the time of the first action potential was defined as the rheobase. **(C)** Quantification of the rheobase shift and **(D)** the relative change in the number of current ramp-evoked APs over 1 minute after light stimulation (460 nm, 1 s, 10 mW/mm^2) (n=6). **(E)** Relative change in the number of APs evoked during the first current ramp after opening of Aion-ts-citrine-ER with 1 s blue light at indicated irradiances. Significant AP

block was achieved at 0.1 mW/mm^2 (n = 7). In all plots grey circles (or blue in E) represent single measurement data points and black circles correspond to medians, Friedman test, *p < 0.05, **p < 0.01, ***p < 0.001, n.s.= not significant.

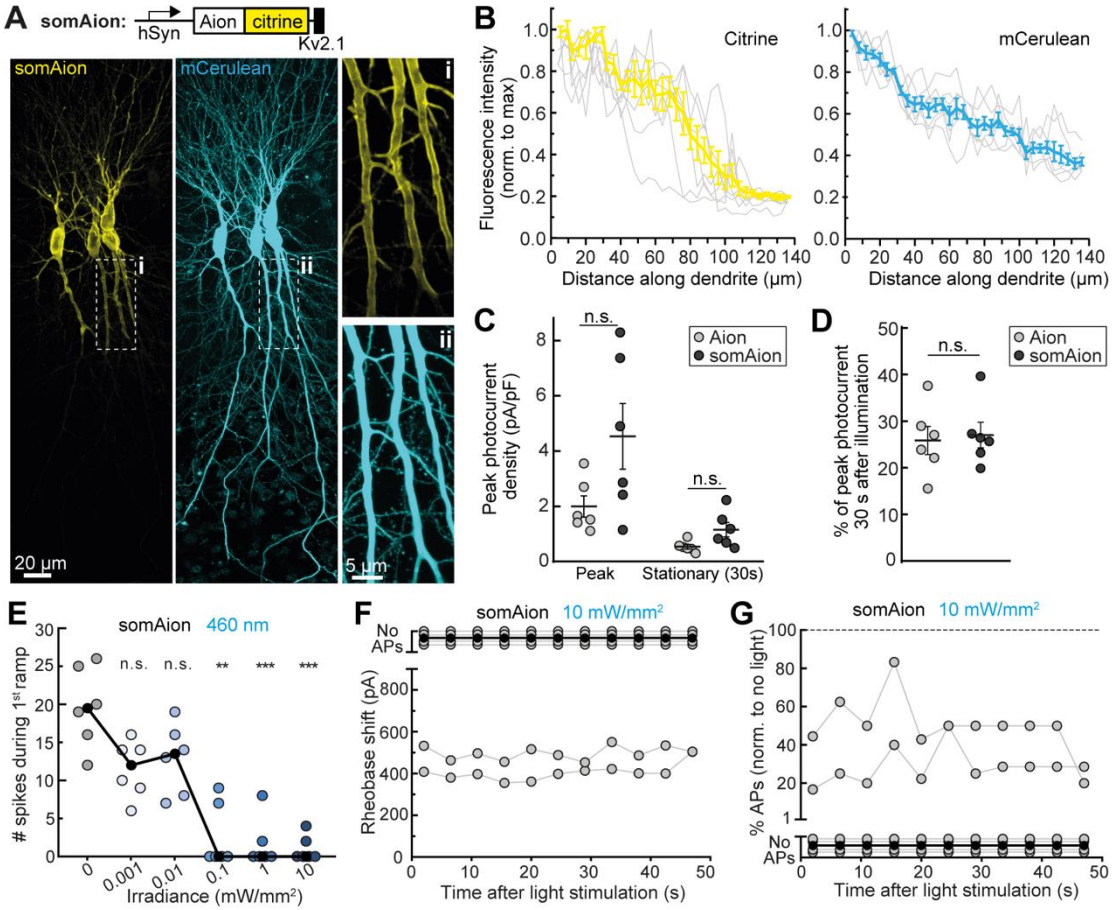

Figure 3.1.12. somAion: a soma-targeted and more potent variant of Aion. (A) Maximum-intensity projection images of two-photon stacks showing expression of a soma-targeted variant of Aion (somAion) in CA1 pyramidal neurons after single-cell electroporation in organotypic hippocampal slice cultures (left image, inset i). Citrine fluorescence was localized at the plasma membrane and restricted to the somato-dendritic compartment. mCerulean was co-electroporated together with somAion and served as a morphology marker (right image, inset ii).
(B) Quantification of citrine (left) and mCerulean (right) fluorescence along the main apical dendrite of somAion-expressing neurons (n=7). Yellow and blue lines indicate mean ± SEM and thin grey lines correspond to measurements in individual cells. **(C)** Comparison of Aion and somAion peak and stationary photocurrent density evoked by a short 460-nm light pulse (1 s, 10 mW/mm^2). Stationary photocurrent amplitude was measured 30 s after light stimulation. **(D)** Quantification of photocurrent amplitude at 30 s after channel opening with respect to peak photocurrent. Mean values ± SEM are shown (black lines) together with single measurement data points (circles, n =6). t-test, n.s.= not significant. **(E-G)** Current ramps were injected into somAion-expressing neurons before and after illumination with a 1 s blue light pulse. For each ramp, the injected current at the time of the first

action potential was defined as the rheobase. **(E)** Relative change in the number of APs evoked during the first current ramp after opening of somAion with blue light at indicated irradiances. Significant AP block was achieved at 0.1 mW/mm^2 (n = 6). **(F)** Quantification of the rheobase shift and **(G)** the relative change in the number of current ramp-evoked APs over 1 minute after light stimulation (460 nm, 1 s, 10 mW/mm^2) (n=6). In most cells activation of somAion led to complete AP block. Grey circles (or blue in E) represent single measurement data points and black circles correspond to medians, Friedman test, *p < 0.05, **p < 0.01, ***p < 0.001, n.s.= not significant.

3.1.3. MerMAIDs: highly desensitizing metagenomically discovered ACRs

Another approach to obtain ACRs with unique biophysical properties, such as fast kinetics or shifted absorption spectra, is to turn to nature and screen for microbial rhodopsins showing homology to chlorophyte CCRs. This strategy has led to the discovery of the potent green and blue-light sensitive *Gt*ACR1 and *Gt*ACR2 (Govorunova et al., 2015), the fast ZipACR (Govorunova et al., 2017) or the recently reported RubyACRs with the most red-shifted activation spectra up-to-date (Govorunova et al., 2020), amongst many others (see section 1.1.2, *Box 1*). Following this screening approach, the natural ACRs MerMAIDs, which represent a new phylogenetic branch in the ChR superfamily, were identified from the *Tara* Oceans metagenomic datasets of marine microorganisms (see Appendix, Fig. A.2) (Oppermann et al., 2019). In HEK cells, MerMAIDs selectively conduct anions but rapidly desensitize during exposure to continuous light due to rapid accumulation of a non-conducting photocycle intermediate (Oppermann et al., 2019).

Functional characterization of MerMAIDs in neurons

From the seven identified MerMAIDs, MerMAID1 and 6 displayed the highest photocurrents in HEK cells (Oppermann et al., 2019). Therefore, I characterized the functionality and biophysical properties of these 2 variants in neurons and evaluated their potential application as optogenetic silencers. Four to five days after transfection via single-cell electroporation CA1 neurons showed membrane-localized expression of the citrine-labeled MerMAIDs (Fig. 3.1.13 B shows

expression for MerMAID6). Although some fraction of the opsin displayed a speckled cellular distribution, MerMAID6-expressing CA1 cells exhibited large, transient Cl^- photocurrents upon light activation that decayed rapidly after light onset (Fig. 3.1.13 A, C). Both MerMAID6 and 1 were maximally activated by green light of 500 nm (Fig. 3.1.13 D), and the evoked photocurrents reverted at -78.3 ± 0.8 mV and -81.4 ± 1.9 mV, respectively (Fig. 3.1.13. E, F), which is near the E_{Cl-}, indicating that MerMAIDs are anion-selective channels.

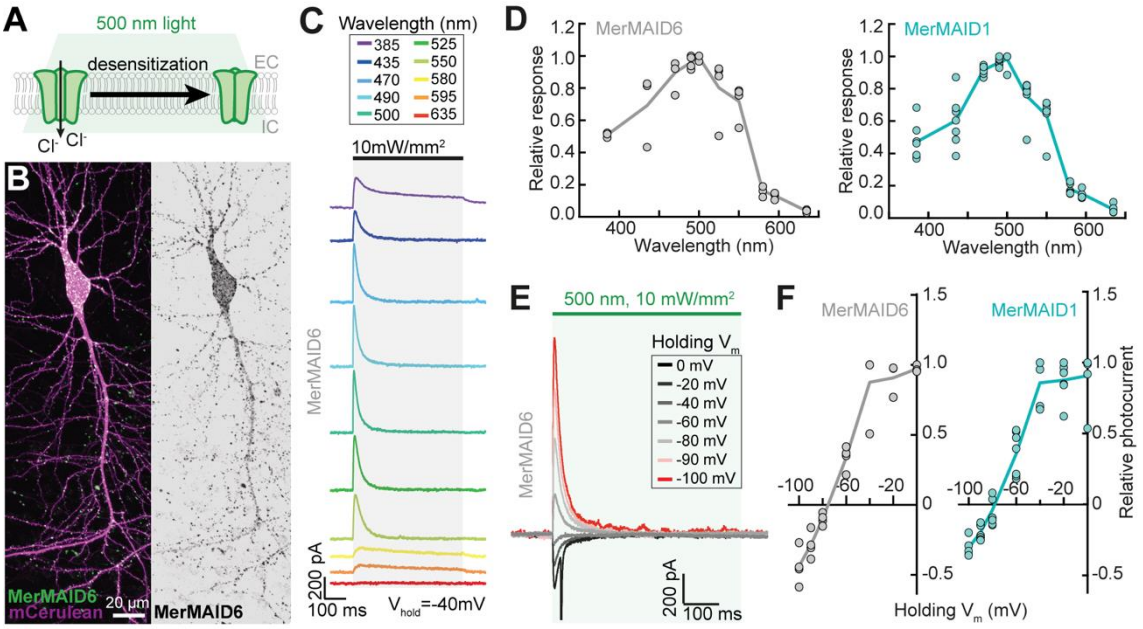

Figure 3.1.13. Characterization of spectral activation and ion selectivity of MerMAID6 and MerMAID1 in CA1 pyramidal cells. (A) Schematic drawing of a MerMAID channel highlighting its rapid desensitization during continuous illumination. **(B)** CA1 pyramidal neuron expressing MerMAID6-citrine (stitched maximum intensity projections of two-photon Z-stack images). Left: mCerulean (magenta) was co-electroporanted with MerMAID6-citrine (green) to visualize neuronal morphology. Right: MerMAID6-citrine fluorescence intensity shown as inverted gray values. **(C)** Representative photocurrent traces of MerMAID6 elicited with light of various wavelengths and equal photon flux (black bar, 500 ms, 10 mW/mm^2) at a holding potential (V_{hold}) of -40 mV. **(D)** Normalized activation spectrum of MerMAID6 (left, n=4 cells) and MerMAID1 (right, n=7 cells). **(E)** Example photocurrent traces of MerMAID6 elicited with 500 nm light (green bar, 500 ms, 10 mW/mm^2) light at membrane potentials (holding V_m) ranging from -100 to 0 mV. **(F)** Current-voltage relation of MerMAID6 (left, n=4 cells) and MerMAID1 (right, n=7 cells) peak photocurrents. Filled circles represent single measurements and solid lines connect mean values.

To determine the time required for peak photocurrent recovery after light-mediated desensitization of MerMAIDs, I performed double-pulse measurements varying the duration between the light pulses (dark interval) (Fig. 3.1.14 A). When activating MerMAID6 and 1 with 100 ms light pulses, a dark interval of 5 s was required to reach 81.4 ± 0.8 % and 97.3 ± 0.9 % of the peak photocurrent, respectively (Fig. 3.1.14 B, C, left panels). After stimulation of MerMAID6 and 1 with a longer light pulse of 500 ms, both ACRs fully recovered peak photocurrent following a dark period of at least 9 s (Fig. 3.1.14 B, C, right panels).

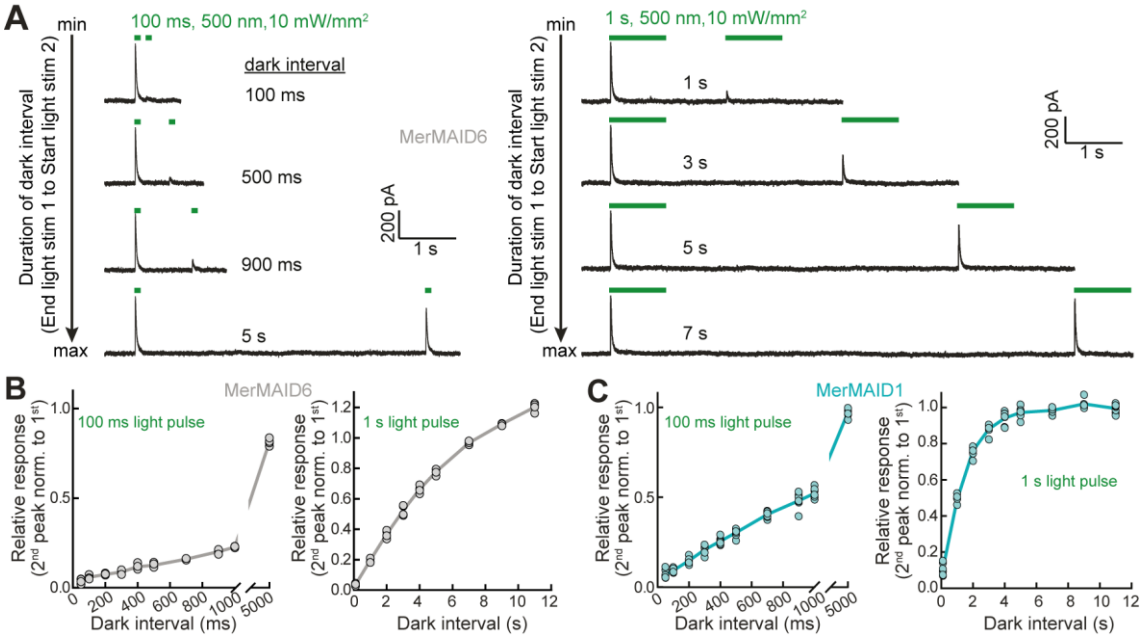

Figure 3.1.14. Recovery kinetics of MerMAID6/1 peak photocurrent. (A) Example photocurrent traces of MerMAID6 in a double-light pulse experiment at -40 mV to determine the time for peak current recovery. Left: the dark interval between two light pulses of 100 ms each (green bars, 500 nm, 10 mW/mm^2) ranged from 100 ms to 5 s. Right: same as left panel but using two light pulses of 1 s each and a dark interval up to 11 s. **(B)** Relative response of MerMAID6 to a second light stimulation after dark intervals of increasing duration. The duration of the two light stimuli was 100 ms (left) or 1 s (right), as shown in example traces in (A). **(C)** Same as (B) but for MerMAID1. Filled circles represent measurements in single cells (MerMAID6: n=4, MerMAID1: n=7) and solid lines connect mean values.

While the unique desensitization of the MerMAIDs prevents their applicability for constant silencing of neurons, it could offer an advantage to block single APs without affecting subsequent neuronal firing. To test this, I injected depolarizing

current ramps into the somata of MerMAID6- and MerMAID1-expressing cells to precisely determine the rheobase for AP firing in the dark. For both ACRs, a short 10 ms light pulse synchronized with the first AP that occurred during darkness suppressed the generation of this AP (Fig. 3.1.15 A, B, panel i). Furthermore, illumination with a longer light pulse of 500 ms, lasting throughout the complete duration of the current ramp, also resulted in precise suppression of only the first AP (Fig. 3.1.15 A, B, panel ii). Thus, MerMAID6 and MerMAID1 can be used to block single APs with high temporal precision without affecting subsequent APs even during extended illumination.

This work has been published in the journal *Nature Communications* (Oppermann et al., 2019).

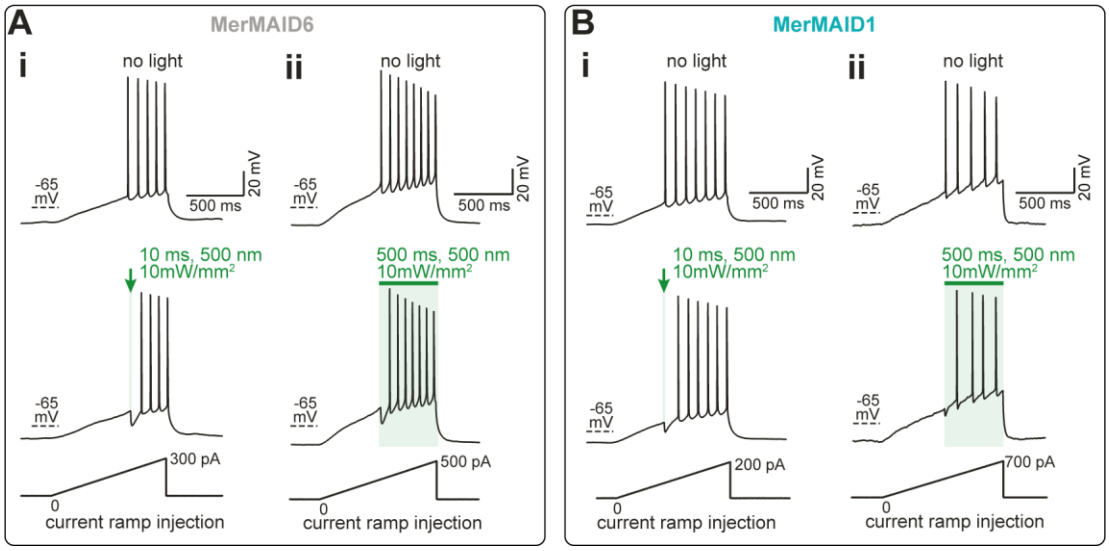

Figure 3.1.15. Neuronal application of MerMAID6/1 as optogenetic silencers. (A) Membrane voltage traces in response to depolarizing current ramps injected into the soma of MerMAID6-expressing cells. Illumination with green light (500 nm, 10 mW/mm^2) for a brief (10 ms, panel i, bottom) or a longer (500 ms, panel ii, bottom) time period blocked single APs without affecting subsequent spiking. **(B)** Same as (A) but for MerMAID1.

3.2. Part II: ChrimsonSA, a red-shifted cation-conducting ChR with accelerated kinetics and reduced sensitivity to blue light

Chrimson is the CCR with the most red-shifted absorption peak up-to-date. However, due to its broad spectral sensitivity, it and can also be activated by blue light at high intensities(Klapoetke et al., 2014). In 2018, Oda and colleagues resolved the crystal structure of Chrimson (Oda et al., 2018), providing new mechanistic insights into its photocycle and the structural features responsible for the red-shifted absorbtion spectrum. The point mutation S169A was hypothesized to shift the activation of Chrimson further to the red range of the spectrum and, additionally, accelerate the closing kinetics of the channel.

Functional characterization of ChrimsonSA in neurons

I characterized the functionality of the mutant ChrimsonSA (S169A, Super red-shifted and Accelerated) and compared it to WT Chrimson, in hippocampal slices. mCerulean-labeled ChrimsonSA was readily detectable in CA1 pyramidal cells 5 days after electroporation. It mainly displayed membrane-localized expression, however, additional bright puncta indicative of protein mislocalization and intracellular accumulation were also observed (Fig. 3.2.1 A). Using whole-cell recordings I showed that ChrimsonSA has a more red-shifted activation spectrum compared to WT Chrimson, with 635 nm-light (10 ms, 1 mW/mm^2) yielding 91.6 ± 2.9 % activation of the S169A mutant but only 53.2 ± 4.3 % activation of the WT variant (Fig. 3.2.1 B). Moreover, ChrimsonSA-expressing neurons showed a significantly smaller ratio of blue-light to red-light-evoked photocurrents (0.18 ± 0.02), as compared to neurons expressing WT Chrimson (0.36 ± 0.02) (Fig. 3.2.1 C). I next evaluated light-evoked spiking properties for each variant. Due to the accelerated channel closing kinetics of the S169A mutant, the recovery of the membrane potential after each spike was faster as compared to neurons expressing WT Chrimson, leading to a more natural waveform of light-evoked APs (Fig. 3.2.1 D,

E). The threshold for red-light irradiance to evoke APs at 10 Hz with WT Chrimson was 1.2 ± 0.5 mW/mm^2, which is similar to the light power needed to evoke APs with blue light (1.9 ± 0.7 mW/mm^2) (Fig. 3.2.1 F). In contrast, ChrimsonSA required 5.4 ± 1.3 mW/mm^2 red-light to evoke APs, an irradiance that was not sufficient to elicit spiking with blue light, which was only reached at 22.8 ± 7.1 mW/mm^2 (Fig. 3.2.1 G).

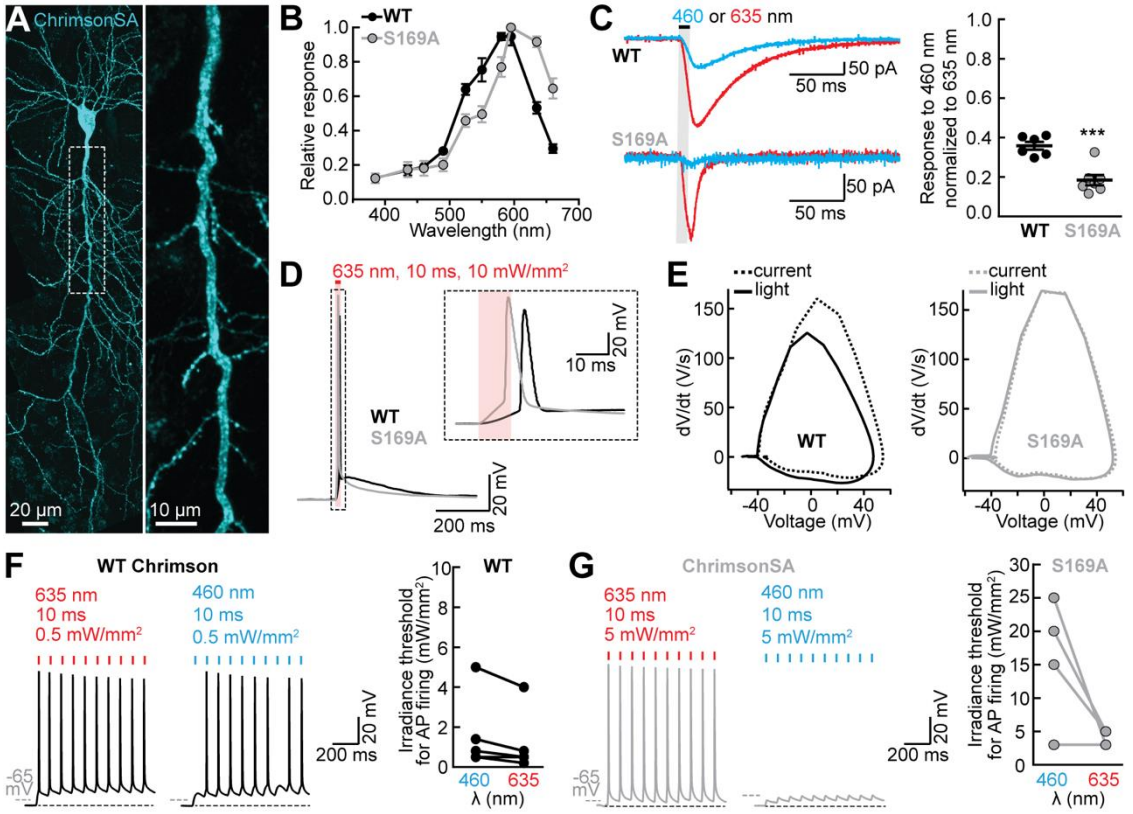

Figure 3.2.1. Characterization of ChrimsonSA in CA1 pyramidal neurons. (A) CA1 pyramidal neuron expressing ChrimsonSA-mCerulean, 5 days after electroporation (stitched maximum intensity projections of two-photon images). The inset shows a magnified view of the main apical dendrite. **(B)** Activation spectra of WT Chrimson (black) and ChrimsonSA (S169A, grey) in CA1 pyramidal neurons. Circles show mean ± SEM (n_{WT}=4; n_{S169A}=4). Lines are interpolations of data points. **(C)** Left: Representative photocurrent traces of WT Chrimson (top) and ChrimsonSA (bottom) evoked by a 10 ms light pulse (1 mw/mm^2) of either 460 nm (blue trace) or 635 nm (red trace). CA1 cells were held at -75 mV. For comparison of kinetics, ChrimsonSA traces were peak-scaled to WT Chrimson. Right: Quantification of relative response to blue light normalized to the response to red light. Lines show mean ± SEM, circles represent measurements in individual cells (n_{WT}= 6; n_{S169A}= 7), Mann-Whitney test, ***p < 0.001. **(D)** Left: Single action potential triggered in WT Chrimson- or ChrimsonSA-expressing neurons (black and grey trace, respectively) by a 10 ms red light pulse (10 mW/mm^2). Inset shows magnified view of AP peak for better comparison of kinetics. **(E)** Average phase plot of

10 APs evoked either by light stimulation (635 nm, 10 ms, at irradiance threshold to evoke APs) or by somatic current injection in a WT Chrimson- or a ChrimsonSA-expressing neuron. **(F)** Left: example traces of APs triggered by red or blue light pulses at a frequency of 10Hz in cells expressing WT Chrimson at (red) threshold light intensity of 0.5 mW/mm^2. Grey dashed lines represent the membrane resting potential. Right: quantification of the irradiance threshold required to evoke APs with 460 or 635 nm light. Circles represent individual cells (n=4). **(G)** Same as (F) but for neurons expressing ChrimsonSA (n=4). In this case, a light intensity of 5 mW/mm^2 was used to elicit APs with both red and blue light. Notably, APs were triggered by blue light with WT Chrimson, but not with ChrimsonSA.

In summary, due to its reduced blue-light sensitivity, ChrimsonSA expands the energetic window in which a red-shifted CCR can be combined with second blue-light sensitive CCR without cross-activation in the blue part of the spectrum, therefore facilitating the control of two neuronal populations.

This work has been published in the journal *Nature Communications* (Oda et al., 2018).

Improved and soma-targeted expression of ChrimsonSA

In principle, the low blue-light sensitivity of ChrimsonSA confers an advantage over WT Chrimson for combination with other blue-light activated optogenetic actuators. However, ChrimsonSA shows overall reduced photocurrents and often failed to reliably induce AP firing with red light at irradiance values below 10 mW/mm^2, especially when using short pulses of 2 to 5 ms, which are generally required to spike neurons at high frequencies. In an attempt to overcome this limitation and to enhance photocurrent amplitudes, a trafficking-optimized variant of ChrimsonSA was generated by adding an N-terminal ER-export sequence. This cleavable leucine-rich signal peptide, termed Lucy tag (Shepard et al., 2013), has been shown to improve *Gt*ACR1 expression and membrane trafficking in *Xenoupus* oocytes and tobacco plant, resulting in increased photoactivated anion currents (Zhou et al., 2021).

Using two-photon microscopy I assessed the expression of the new trafficking-optimized version of ChrimsonSA, namely ChrimsonSA2.0, and its soma-targeted form ChrimsonSA2.0-Kv2.1. While both variants showed improved membrane localization, ChrimsonSA2.0 still displayed some fraction of the protein accumulated inside the cell in the periphery of the cell nucleus (Fig. 3.2.2 A). As expected, ChrimsonSA2.0-Kv2.1-expression was restricted to the soma and the proximal region of the basal and main apical dendrites (Fig. 3.2.2 B). Voltage-clamp recordings from neurons expressing ChrimsonSA2.0 revealed red-light-induced photocurrents that were not significantly different in amplitude to those obtained with the non-trafficking-optimized ChrimsonSA (437.1 ± 108.8 pA and 119.7 ± 36.8 pA, respectively) (Fig. 3.2.2 C), indicating that introduction of the Lucy tag alone was not sufficient to significantly enhance opsin performance. In contrast, ChrimsonSA2.0-Kv2.1 showed increased photocurrents (Fig. 3.2.2 D), while maintaining a low blue/red light irradiance threshold ratio to evoke APs (median ratio 5.4, range: 4.2 – 10.5); compared to 4.4, range: 2.9 – 12.3, for ChrimsonSA) (Fig. 3.2.2 E-G). Furthermore, APs could be reliably driven up to 50 Hz with ChrimsonSA2.0-Kv2.1 using short 2-ms red-light pulses at an irradiance of 1 mW/mm^2 (Fig. 3.2.2 H). These results indicate that soma-targeting of ChrimsonSA2.0 did not only improve membrane trafficking, but it enhanced the overall potency of the tool.

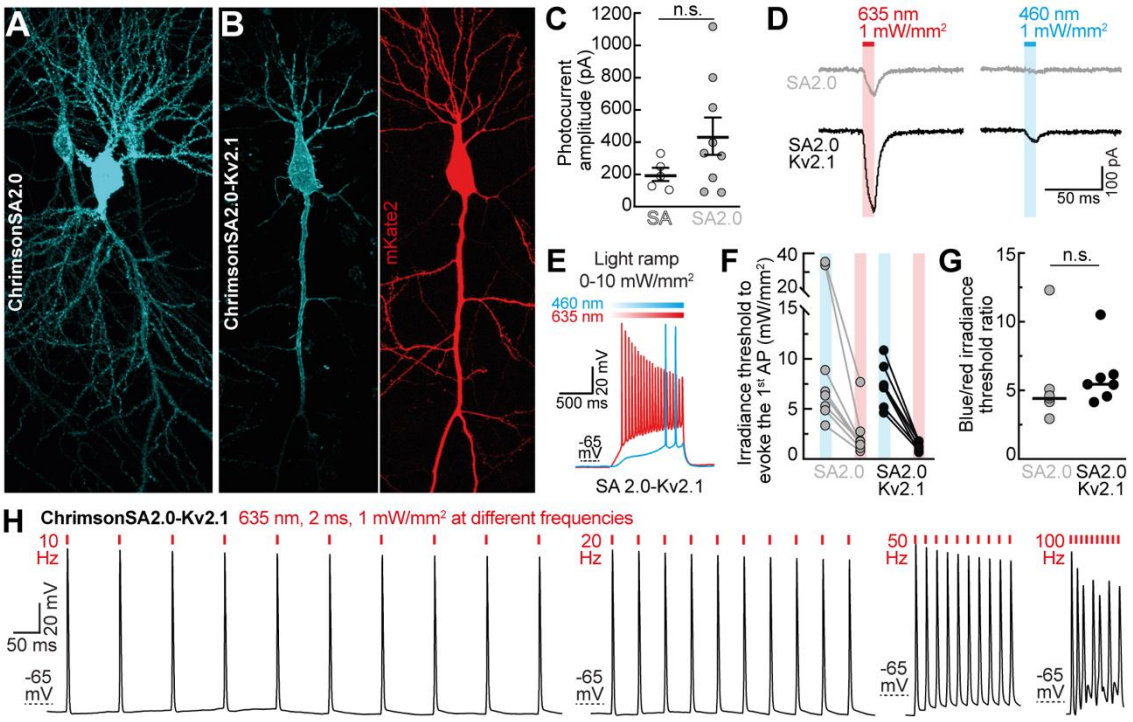

Figure 3.2.2. ChrimsonSA2.0 and its soma-targeted version ChrimsonSA2.0-Kv2.1 in CA1 pyramidal neurons. (A,B) CA1 pyramidal neurons expressing the trafficking-enhanced ChrimsonSA2.0 (A) and the soma-targeted variant ChrimsonSA2.0-Kv2.1 (B) 5 days after electroporation (stitched maximum intensity projections of two-photon stack images). In (B) mCerulean-labelled ChrimsonSA2.0-Kv2.1 is shown in cyan (left) and the red-fluorescent protein mKate2 served as morphology marker (right). Notably, expression of ChrimsonSA2.0-Kv2.1 was restricted to the soma and the proximal fraction of the basal and main apical dendrites. **(C)** Quantification of photocurrent amplitude elicited by a 10 ms red-light pulse (635 nm, 10 mW/mm^2) in ChrimsonSA- or ChrimsonSA2.0-expressing neurons. Lines show mean ± SEM, circles represent measurements in individual cells (ChrimsonSA: white, n=5; ChrimsonSA2.0: grey, n=9). Mann-Whitney test, n.s. = not significant. **(D)** Example photocurrent traces of ChrimsonSA2.0 (grey) and ChrimsonSA2.0-Kv2.1 (black) evoked by a 10 ms light pulse (1 mw/mm^2) of either 635 nm (left) or 460 nm (right). CA1 cells were held at -75 mV. **(E)** Light-ramp stimulation to determine the AP threshold irradiance for blue and red light. Representative membrane voltage traces measured in a ChrimsonSA2.0-Kv2.1 -expressing CA1 pyramidal cell. Light was ramped linearly from 0 to 10 mW/mm^2 over 1 s (460 nm: blue trace, 635 nm: red trace). For the blue-light ramp, when AP firing was not reached by an irradiance of 10 mW/mm2, light was ramped up to 50 mW/mm^2. **(F)** Quantification of the irradiance threshold at which the first AP was evoked during the light-ramp stimulation (as shown in E) for ChrimsonSA2.0 (grey) and ChrimsonSA2.0-Kv2.1 (black) when using 460 or 635-nm light (blue and red rectangles). **(G)** Blue/red irradiance threshold ratio to evoke the first AP. Grey circles represent measurements in individual cells and black lines correspond to medians (ChrimsonSA2.0: grey, n=8; ChrimsonSA2.0-Kv2.1: black, n=7). Mann-Whitney test, n.s. = not significant. **(H)** Membrane voltage traces at different light-pulse frequencies in CA1 cells expressing ChrimsonSA2.0-Kv2.1. APs were triggered by 10 pulses (635 nm, pulse width 2 ms, 1 mW/mm^2). Under this conditions, APs were elicited with high fidelity up to 50 Hz.

3.3. Part III: BiPOLES, a tool for bidirectional dual-color optogenetic control of neurons.

The implementation of a dual-color excitation/inhibition system to achieve independent up- and downregulation of neuronal activity has been a long-sought goal in optogenetics. The main challenge arises from the fact that all rhodopsins, regardless of their excitation spectra, can be activated to some extent by blue light. Even far-red-shifted tools with low blue-light sensitivity, such as the above described ChrimsonSA, can respond to blue light, especially at high irradiances. One way to overcome this cross-activation problem, is to pair a red-shifted CCR with a blue-shifted ACR so that the latter compensates residual excitation of the red CCR in the blue part of the spectrum (see section 1.3.3, Fig. 1.4). A second challenge is to achieve fixed stoichiometric expression of each optogenetic actuator for balanced excitation and inhibition in every cell. For this purpose, using the tandem gene-fusion strategy (Kleinlogel et al., 2011) as a basis, our lab, in collaboration with the group of Peter Hegemann, developed BiPOLES, a new optogenetic tool for dual-color bidirectional control of neurons. BiPOLES (for Bidirectional Pair of Opsins for Light-induced Excitation and Silencing) combines in a single fusion protein the blue-light-sensitive ACR *Gt*ACR2 (Govorunova et al., 2015) and the red-light-sensitive CCR Chrimson (Klapoetke et al., 2014) (Fig. 3.3.1 A).

Part of this work has been published in the open access preprint repository bioRXiv (Vierock, Rodriguez-Rozada et al., 2020), and is currently in press in the journal *Nature Communications*.

Functional evaluation of BiPOLES in CA1 pyramidal neurons

I first validated BiPOLES as an optogenetic tool for bidirectional control of neuronal activity in hippocampal slice cultures. mCerulean-labelled BiPOLES was readily detected in CA1 pyramidal cells four to six days after single-cell electroporation, with expression observed most strongly in the somatodendritic

compartment (Fig. 3.3.1 B). Illumination of BiPOLES-expressing CA1 neurons triggered photocurrents that reversed at -71.0 ± 0.8 mV, near the Cl^-reversal potential (E_{Cl^-} = -73.4 mV, see section 2.1.3, *Box 2*) when using blue light, and at -10.6 ± 2.9 mV when stimulating with red light, which is near the cation reversal potential ($E_{cations}$ = 0 mV), indicative of anion- and cation-conductance, respectively (Fig. 3.3.1 C, D). At a membrane potential between the E_{Cl^-} and $E_{cations}$, illumination with fixed irradiance over a wide spectral range induced outward anionic-currents in the blue part of the spectrum (385-525 nm) and inward cationic-currents beyond 550 nm (Fig. 3.3.1 E, F), with 540.8 ± 5.1 nm being the wavelength of photocurrent inversion (reversal wavelength) (Fig. 3.3.1 G). Notably, the inhibitory/excitatory photocurrent ratio showed little variability between cells (1.2 ± 0.2), indicating a reproducible stoichiometry of Chrimson and *Gt*ACR2 currents (Fig. 3.3.1 H).

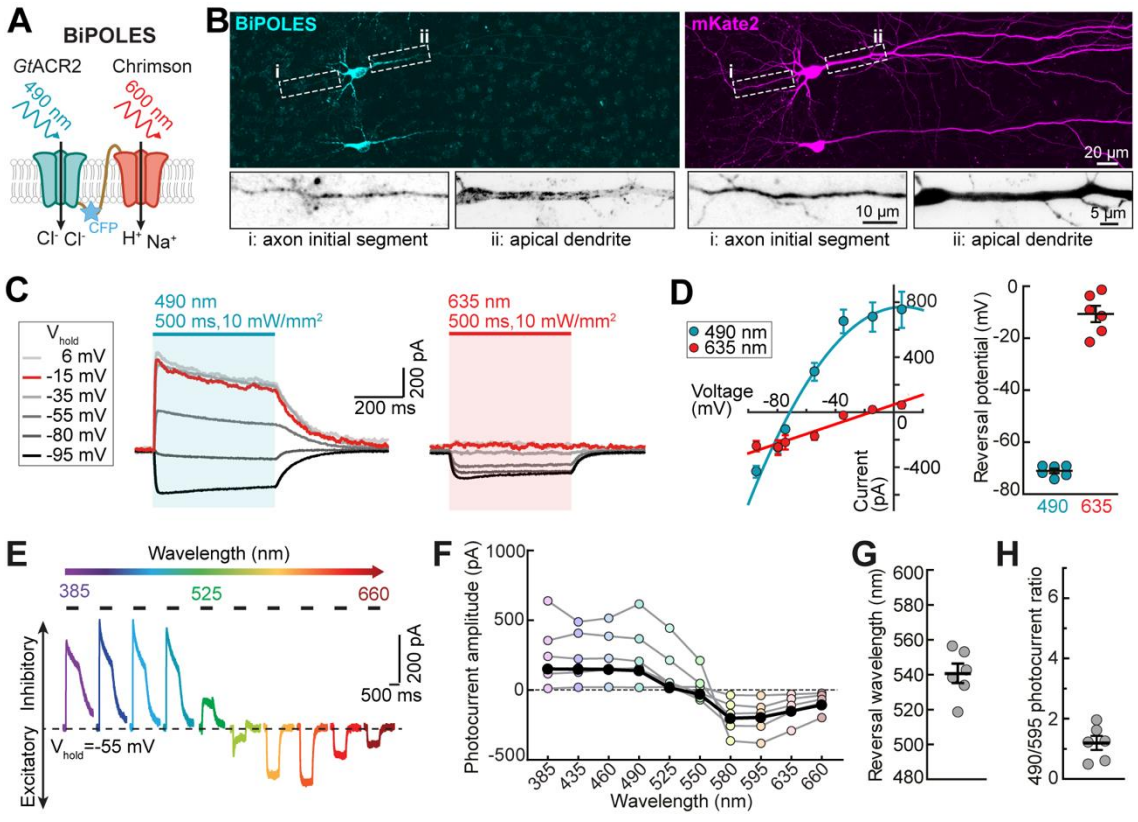

Figure 3.3.1. Characterization of BiPOLES-mediated excitatory and inhibitory currents in CA1 pyramidal cells. (A) Schematic drawing of BiPOLES. The blue-light-activated natural anion channel *Gt*ACR2 was fused to the red-light-activated cation channel Chrimson by a transmembrane linker region consisting of a trafficking signal, a cyan fluorescent protein (mCerulean3) and the

transmembrane ß helix of the rat gastric H^+/K^+ ATPase. **(B)** Maximum-intensity projection images of 2-photon stacks showing expression of mCerulean-labelled BiPOLES (left) or the morphology marker mKate2 (right) in CA1 pyramidal cells of organotypic hippocampal slices. Insets show magnified views of axonal (i) or dendritic (ii) compartments as inverted gray-scale images. **(C)** Representative photocurrent traces of a BiPOLES-expressing neuron at indicated membrane voltages (V_{hold}) upon illumination with 490 or 635 nm (500 ms, 10 mW/mm^2). **(D)** Quantification of photocurrent-voltage relationship (left) and reversal potential (right) under 490 or 635 nm illumination (mean ± SEM, n=6). **(E)** Representative photocurrents of BiPOLES showing inhibitory anion-conductances and excitatory cation-conductances in a wavelength-dependent manner (385-660 nm, 500 ms, 10 mW/mm^2). CA1 cells were held at a membrane voltage of -55 mV. **(F)** Quantification of photocurrent amplitudes at indicated wavelengths. Individual data points are shown for each wavelength, black circles: medians, n=6. **(G)** Quantification of photocurrent reversal wavelength at -55 mV (mean ± SEM, n=6). **(H)** Ratio of inhibitory (490 nm, peak activation wavelength of *Gt*ACR2) over excitatory (595 nm, peak activation wavelength of Chrimson) photocurrents (mean ± SEM, n=6). Note that the photocurrent ratio shows little variability between cells, indicating a reproducible stoichiometry of Chrimson and *Gt*ACR2 currents.

These results demonstrate that BiPOLES enables selective activation of anion and cation currents with spectrally well-separated wavelengths.

Next, I thoroughly assessed expression and subcellular localization of the tandem construct using hippocampal slices transduced with an AAV9 viral vector encoding mCerulean-labelled BiPOLES. Membrane-localized BiPOLES expression was observed most strongly in the somatodendritic compartment, with some fraction of the protein accumulating inside the cell in the periphery of the cell nucleus, indicating sub-optimal membrane trafficking of BiPOLES (Fig. 3.3.2 A). To enhance membrane trafficking, we generated a soma-targeted variant (somBiPOLES) by attaching the C-terminal Kv2.1-trafficking sequence (Lim et al., 2000). Soma targeting has the additional benefit of eviting expression of the construct in axon terminals, where functionality of BiPOLES might be limited due to an excitatory Cl^- reversal potential and subsequent depolarizing action of *Gt*ACR2 (Mahn et al., 2018). somBiPOLES showed greatly improved membrane localization at the cell soma and in proximal dendrites with no detectable intracellular accumulations (Fig. 3.3.2 A).

To verify the confinement of somBiPOLES to the somatodendritic compartment I transduced area CA3 in hippocampal slice cultures with somBiPOLES and recorded optically evoked EPSCs in postsynaptic WT CA1 cells (Fig. 3.3.2 B). Local illumination with red light in CA3 triggered large excitatory postsynaptic currents (EPSCs), while local red illumination of axon terminals in CA1 did not trigger synaptic release (Fig. 3.3.2 B, C), demonstrating efficient exclusion of somBiPOLES from the axon terminals, despite enhanced membrane trafficking in the somatodendritic compartment.

Furthermore, somBiPOLES did not only improve expression of the tandem construct compared to BiPOLES, but it strongly enhanced blue- and red-light mediated photocurrents (0.6-fold and 1.4-fold larger median photocurrent density for blue and red light at 10 mW/mm^2 and 1 mW/mm^2, respectively), rendering responses similar in magnitude to those recorded in neurons expressing either Chrimson (1.5 pA/pF, range: 0.6 – 2.7 pA/pF) or soma-targeted *Gt*ACR2 (som*Gt*ACR2) (4.1 pA/pF, range: 1.6 – 7.4 pA/pF), alone (Fig. 3.3.2 D, E).

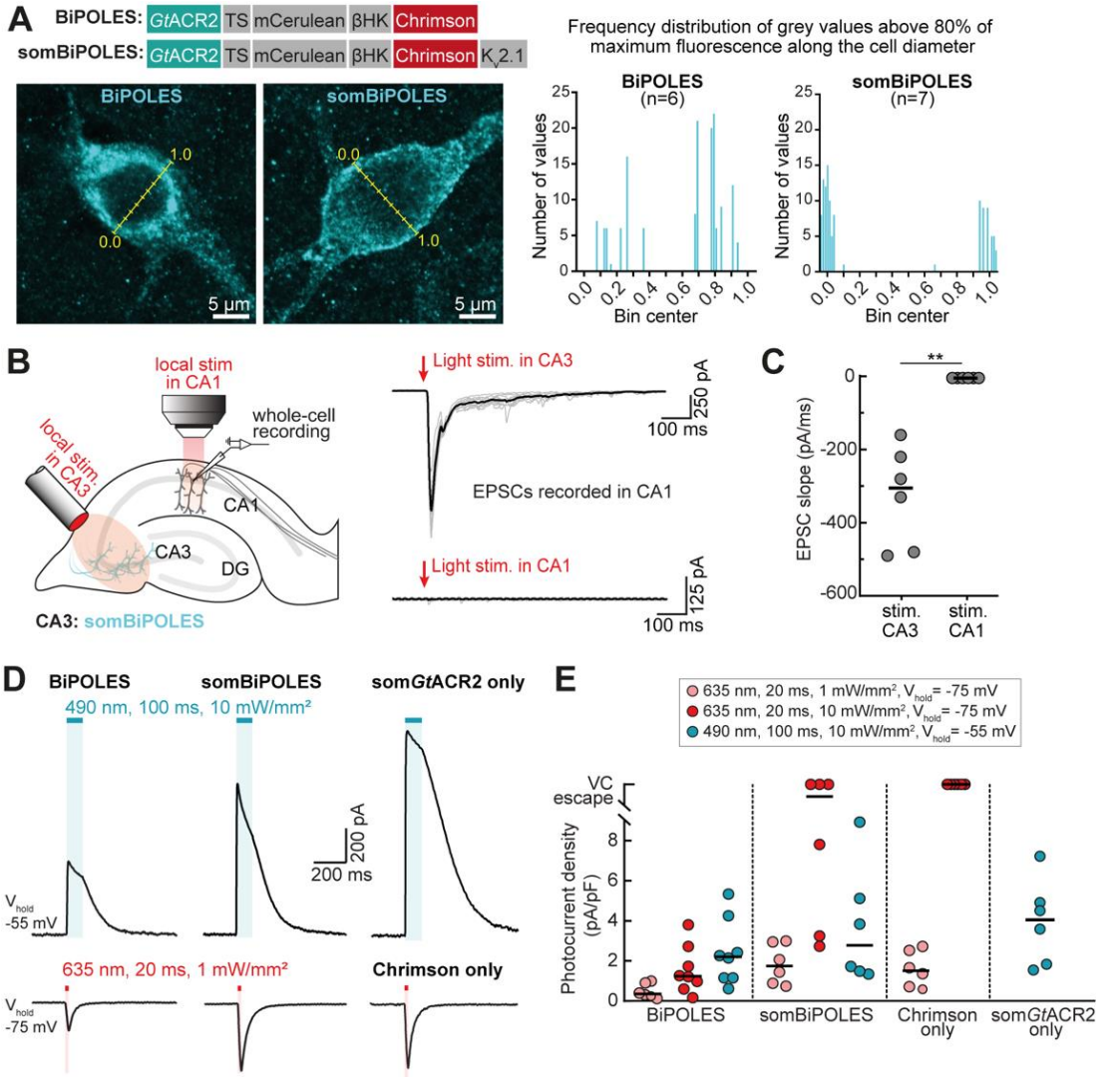

Figure 3.3.2. Expression and functional characterization of BiPOLES and somBiPOLES in hippocampal neurons. (A) Left: molecular scheme of BiPOLES and soma-targeted BiPOLES (somBiPOLES) as used in neurons. Representative maximum-intensity projection images of immunostainings showing expression of BiPOLES or somBiPOLES in CA3 pyramidal neurons of organotypic hippocampal slices. Yellow lines indicate the bins used to measure fluorescence intensity along the cell equator. Right: frequency distribution of grey values above 80% of the maximum fluorescence intensity measured along the cell diameter in BiPOLES- (n=6) and somBiPOLES-expressing CA3 cells (n=7). Note improved trafficking of somBiPOLES to the cell membrane, shown by the preferential distribution of brighter pixels around bins 0.0 and 1.0. **(B)** Left: schematic drawing depicting the experiment used to verify absence of somBiPOLES-expression in axon terminals of CA3 cells. Whole-cell voltage-clamp recordings were done in postsynaptic CA1 cells to determine red-light evoked EPSCs. Illumination was done locally either in CA3 at the somata or in CA1 at axon terminals of somBiPOLES-expressing CA3 cells. Axon stimulation was done in the presence of TTX to avoid antidromic spiking of CA3 cells and 4-AP to inhibit K^+-mediated fast repolarization. Right: example voltage-clamp recordings from CA1 cells upon red-light stimulation either in CA3 (top) or in axon terminals in CA1 (bottom). Black lines show average response of 10 repetitions (grey lines). **(C)** Quantification of experiment shown in (B). Grey circles represent single measurement data points and black lines correspond to medians. Mann-Whitney test, **p < 0.01. **(D)** Representative photocurrent traces measured in CA1

neurons expressing BiPOLES, somBiPOLES, Chrimson alone or soma-targeted *Gt*ACR2 (som*Gt*ACR2) alone. Outward anionic photocurrents evoked by a 490 nm light pulse (100 ms, 10 mW/mm^2) were recorded at a membrane voltage of -55 mV, and inward cationic photocurrents evoked by a 635 nm light pulse (20 ms, 1 mW/mm^2) were recorded at a membrane voltage of -75 mV. **(E)** Quantification of photocurrent densities for each opsin evoked under the indicated conditions. Circles show measurements in single cells and black lines correspond to medians (n=6-8).

To assess cell viability and tolerability of BiPOLES and somBiPOLES, I measured passive and active membrane parameters in opsin-expressing CA1 cells and compared to those of non-transduced, wild-type neurons (Fig. 3.3.3). There were no significant alterations in basic neuronal parameters, indicative of good tolerability in neurons.

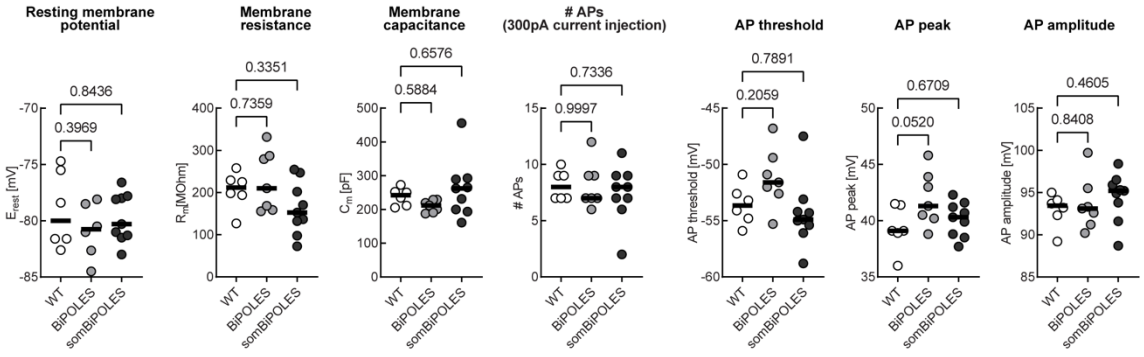

Figure 3.3.3. Basic neuronal parameters of WT, BiPOLES- and somBiPOLES-expressing CA1 pyramidal cells. The following parameters were measured to asses cell viability and tolerability of BiPOLES and somBiPOLES: resting membrane potential, membrane resistance, membrane capacitance, number of APs evoked by somatic current injection (300 pA, 500 ms), AP voltage threshold, peak voltage and AP amplitude of the 1st AP elicited by somatic current injection (black lines: medians, WT n = 6, BiPOLES n = 7, somBiPOLES n = 9, one-way ANOVA, exact P-values are shown).

Light-evoked spiking and inhibition parameters for somBiPOLES

Having shown that somBiPOLES is efficiently expressed in CA1 pyramidal cells, I next evaluated its capacity for neuronal activation and silencing. I characterized light-evoked spiking and inhibition parameters for somBiPOLES and systematically benchmarked it against the individually expressed excitatory or

inhibitory rhodopsin of the tandem construct (i.e. Chrimson and som*Gt*ACR2, respectively) (Fig. 3.3.4 A, F).

To compare spiking performance in somBiPOLES- or Chrimson-expressing CA1 pyramidal cells, trains of 5-ms blue (470 nm), orange (595 nm) or red (635 nm) light pulses were delivered at irradiances ranging from 0.1 to 100 mw/mm^2. AP probability in somBiPOLES neurons reached 100% at 0.5 mW/mm^2 with 595 nm and 10 mW/mm^2 with 635 nm light, similar to neurons expressing Chrimson alone (Fig. 3.3.4 B, C). In contrast to orange or red light, APs were not evoked at any blue light irradiance in somBiPOLES neurons due to the activity of the blue-light sensitive anion channel. On the contrary, neurons expressing Chrimson alone reached 100% AP firing probability at 10 mW/mm^2 with 470 nm (Fig. 3.3.4 B, C). To precisely determine the AP threshold with orange and blue light, I used light ramps with linearly increasing irradiance. The irradiance threshold for the first AP was similar for somBiPOLES and Chrimson at 595 nm (0.74 ± 0.06 mW/mm^2 for somBiPOLES and 0.68 ± 0.05 mW/mm^2 for Chrimson). In contrast, blue light triggered APs at 0.95 ± 0.09 mW/mm^2 in Chrimson expressing cells, but never in somBiPOLES neurons (Fig. 3.3.4 D, E). Thus, unlike Chrimson, somBiPOLES enables neuronal excitation exclusively within a narrow spectral window restricted to orange-red light, avoiding inadvertent blue-light mediated spiking.

Next, I quantified the silencing capacity of somBiPOLES and compared it to som*Gt*ACR2 alone by measuring the capacity to shift the rheobase to higher values upon illumination with blue light at increasing intensities (0.001 to 100 mW/mm^2). Both tools similarly shifted the rheobase towards larger currents starting at an irradiance of 0.1 mW/mm^2 with 490 nm light, leading to a complete block of APs in most cases (Fig. 3.3.4 G, H). Notably, neuronal silencing was efficient under 490 nm-illumination even at high irradiances (up to 100 mW/mm^2, Fig. 3.3.4 G), indicating that blue light cross-activation of Chrimson in somBiPOLES does not compromise neuronal shunting.

Taken together, these results show that somBiPOLES allows reliable neuronal activation exclusively with orange-red light and silencing with blue light. Moreover, somBiPOLES displays similar potency for neuronal excitation and inhibition as the individual tandem components Chrimson and som*Gt*ACR2 alone.

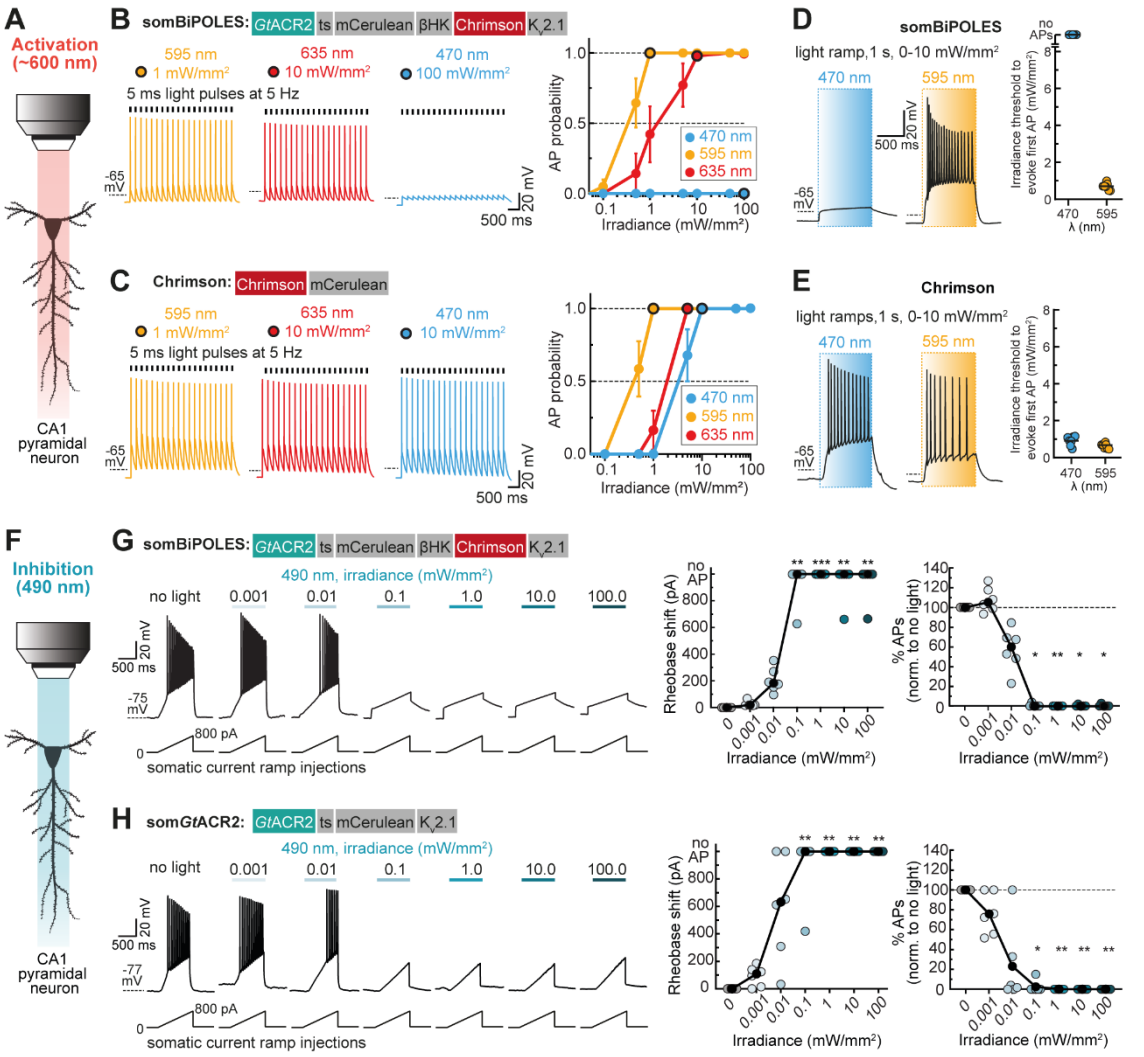

Figure 3.3.4. somBiPOLES-mediated spiking and silencing of the same neurons using red and blue light, respectively. (A) Quantification of neuronal excitation with somBiPOLES or Chrimson only**. (B)** Optical excitation is restricted exclusively to the orange/red spectrum in somBiPOLES-expressing neurons. Left: Example traces of current-clamp (IC) recordings in somBiPOLES-expressing CA1 pyramidal cells to determine light-evoked action potential (AP)-probability at different wavelengths. Right: quantification of light-mediated AP probability at indicated wavelengths and irradiances (mean ± SEM, n=8). Black outlined circles correspond to irradiance values shown in example traces on the left. **(C)** Same experiment as shown in (B), except that CA1 neurons express Chrimson only. Note blue-light excitation of Chrimson, but not somBiPOLES cells. **(D)** Light-ramp stimulation to determine the AP threshold irradiance. Left: Representative membrane voltage traces measured in somBiPOLES-expressing CA1 pyramidal neurons. Light was ramped

linearly from 0 to 10 mW/mm^2 over 1 s. Right: Quantification of the irradiance threshold at which the first AP was evoked. **(E)** Same experiment as shown in (D), except that CA1 neurons express Chrimson only. The threshold for action potential firing with 595 nm was similar between somBiPOLES- and Chrimson-expressing neurons, while somBiPOLES cells were not sensitive to blue light. Black horizontal lines: medians, n=7. **(F)** Quantification of neuronal silencing with somBiPOLES or som*Gt*ACR2 only. **(G)** somBiPOLES mediates neuronal silencing upon illumination with blue light. Left: Current ramps (from 0 - 100 to 0 - 900 pA) were injected into somBiPOLES-expressing CA1 pyramidal cells to induce APs during illumination with blue light at indicated intensities (from 0.001 to 100 mW/mm^2). The injected current at the time of the first action potential was defined as the rheobase. Right: Quantification of the rheobase shift and the relative change in the number of ramp-evoked action potentials. Illumination with 490 nm light of increasing intensities activated somBiPOLES-mediated Cl^- currents shifting the rheobase to higher values and shunting action potentials. **(H)** Same experiment as shown in (G), except that CA1 neurons express som*Gt*ACR2 only. Note similar silencing performance of somBiPOLES and *Gt*ACR2. Black circles: medians, n=6, Friedman test, *p < 0.05, **p < 0.01, ***p < 0.001.

Accelerating the kinetics of somBiPOLES excitatory component

Many types of neurons operate at high firing rates. For example, fast spiking cortical interneurons, (Hu et al., 2014), and spiral ganglion neurons in the auditory system (Liberman, 1978) fire APs at frequencies up to several hundred Hz.Therefore, for many optogenetic applications it is crucial to have fast actuators that can drive neuronal spiking with high fidelity even at high frequencies. Light-evoked spiking with Chrimson has been previously reported to be reliable (above 0.5 spiking probability) at frequencies up to 10-20 Hz (Klapoetke et al., 2014). In order to gain more precise temporal control of red-light excitation, I tested whether replacement of Chrimson with the very-fast (vf-Chrimson) and fast (f-Chrimson) mutants (Mager et al., 2018) in somBiPOLES (vf-somBiPOLES and f-somBiPOLES, respectively) could overcome the limitations for high-frequency spiking.

I first characterized light-evoked photocurrents and spiking parameters for vf-somBiPOLES and f-somBiPOLES, and compared it to the original somBiPOLES. Both vf- and f-somBiPOLES produced faster photocurrents upon stimulation with red light, but displayed strongly reduced response amplitudes (7.2 % and 12.9 % of the somBiPOLES response, respectively; Fig. 3.3.5 A). The reduced conductance of the vf-Chrimson mutant impeded reliable AP generation in CA1 cells expressing

vf-somBiPOLES upon stimulation with red or orange light at various pulse durations and irradiances (Fig. 3.3.5 B top, C left). In contrast, 20 ms red-light pulses (635 nm, 10 mW/mm^2) allowed AP firing with high fidelity in f-somBiPOLES neurons, which, in addition, could be blocked by a concomitant 100-ms blue-light pulse, indicating the suitability of f-somBiPOLES for bidirectional control of neurons (Fig. 3.3.5 B bottom). However, when using trains of shorter light pulses (5 ms, 595 and 635 nm), AP firing probability with f-somBiPOLES was not as efficient as with somBiPOLES, reaching only 100 % spiking with orange light at irradiances above 50 mW/mm^2 (Fig. 3.3.5 C, right).

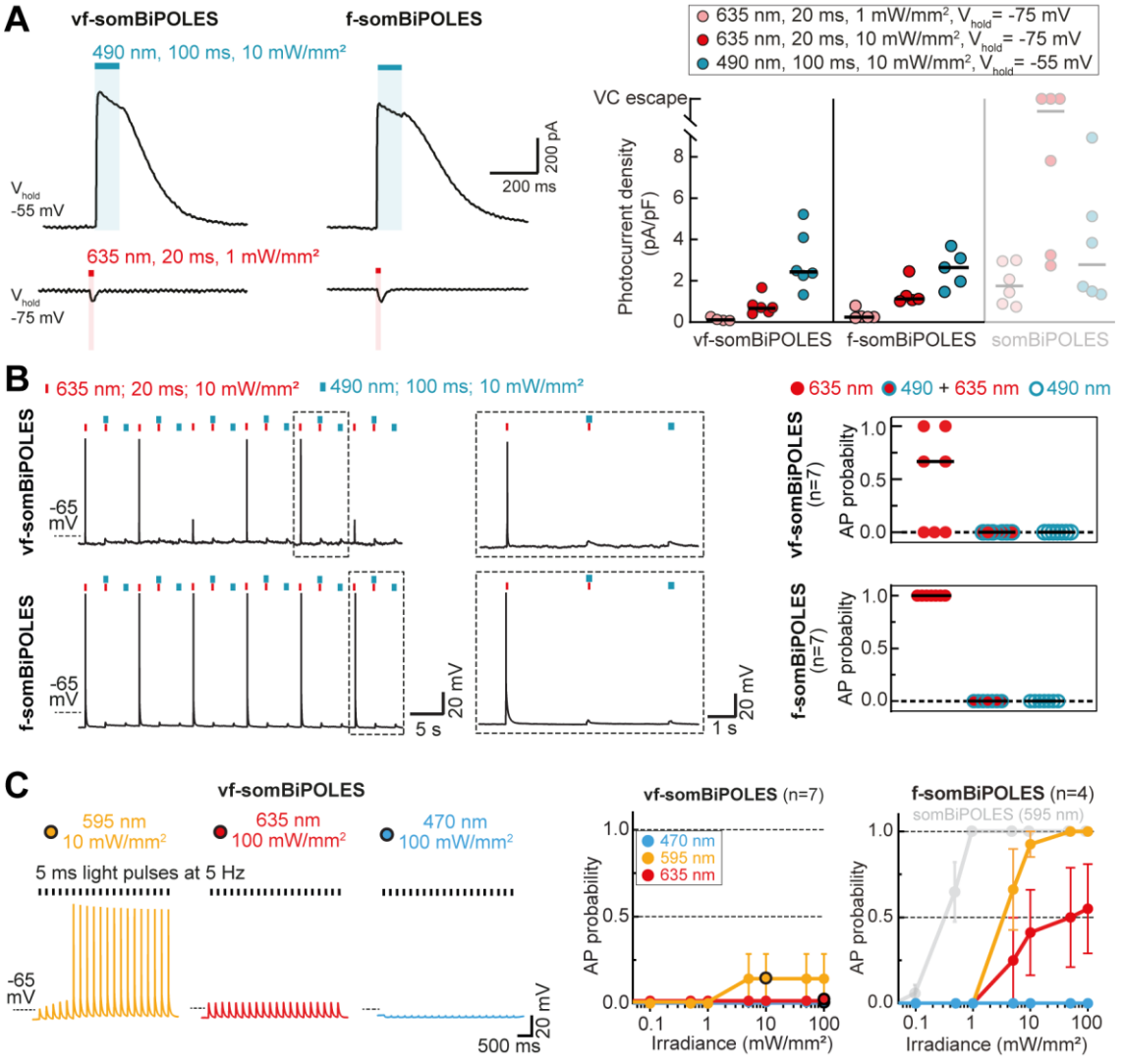

Figure 3.3.5. Characterization of light-evoked photocurrents and spiking parameters for vf-somBiPOLES and f-somBiPOLES. (A) Left: representative photocurrent traces measured in CA1 neurons expressing vf-somBiPOLES or f-somBiPOLES. Outward anionic photocurrents evoked by a

490 nm light pulse (100 ms, 10 mW/mm^2) were recorded at a membrane voltage of -55 mV, and inward cationic photocurrents evoked by a 635 nm light pulse (20 ms, 1 mW/mm^2) were recorded at a membrane voltage of -75 mV. Right: quantification of photocurrent densities for vf- and f-somBiPOLES evoked under the indicated conditions. Circles show measurements in single cells and black lines correspond to medians (n=5-6). Shaded symbols correspond to somBiPOLES values from Fig. 3.3.2 E and are plotted for direct comparison. Note that red-light-mediated photocurrent densities were strongly reduced with vf- and f-somBiPOLES compared to somBiPOLES, while *Gt*ACR2-mediated photocurrents remained unaltered. **(B)** Left: voltage traces of vf-somBiPOLES (top) and f-somBiPOLES (bottom) showing red-light-evoked APs (20 ms, 635 nm, 10 mW/mm^2), which were blocked by a concomitant blue-light pulse (100 ms, 490 nm, 10 mW/mm^2). Blue light alone did not trigger APs. Right: quantification of AP probability under indicated conditions (black horizontal lines: medians, n = 7 for both opsins). Note that some vf-somBiPOLES-expressing neurons (top) failed to trigger APs upon stimulation with red light. **(C)** Left: example traces of voltage recordings from a vf-somBiPOLES-expressing neuron to determine light-evoked AP probability at different wavelengths. Right: quantification of light-mediated AP probability at indicated wavelengths and irradiances for vf- an f-somBiPOLES (mean ± SEM, n = 7 and 4, respectively). Note that APs are not triggered by blue light at any irradiance up to 100 mW/mm^2, but in contrast to somBiPOLES (grey symbols), vf-somBiPOLES failed to reliably elicit APs with orange/red light (left) and f-somBiPOLES needed higher irradiances (right).

Next, I assessed orange light-evoked spiking at various stimulation frequencies using somBiPOLES and f-somBiPOLES. In CA1 pyramidal cells, APs could be reliably driven (above 0.5 AP probability) up to 10-20 Hz with somBiPOLES (Fig. 3.3.6 A), similar to what has been reported for Chrimson alone (Klapoetke et al., 2014). Due to its faster closing kinetics, f-somBiPOLES enabled faster recovery of the membrane potential after each spike as compared to somBiPOLES, resulting in lower plateau depolarization (see example voltage traces in Fig 3.3.6 A, B). Consequently, f-somBiPOLES allowed spiking at higher rates, showing an AP probability of 0.30 (range: 0.15 – 0.34) and 0.24 (range: 0.03 – 0.33) at 40 and 60 Hz, respectively (Fig. 3.3.6 B), frequencies that somBiPOLES cells could not follow (Fig. 3.3.6 A). However, while an irradiance of 10 mW/mm^2 was enough to evoke APs in all somBiPOLES-expressing neurons, for f-somBiPOLES 50 mW/mm^2 were required in some cases (Fig. 3.3.6 B, circles with red border).

Taken together, the reduced conductance of vf-Chrimson (Mager et al., 2018) yields a tandem construct (vf-somBiPOLES) with a weak excitatory

component. Although f-somBiPOLES enables spiking at frequencies above 40 Hz, which might be useful for some applications, it requires higher light powers. Thus, despite the slower kinetics of WT Chrimson, the potent conductance in somBiPOLES makes it a more suitable tool for reliable generation of APs at lower irradiances.

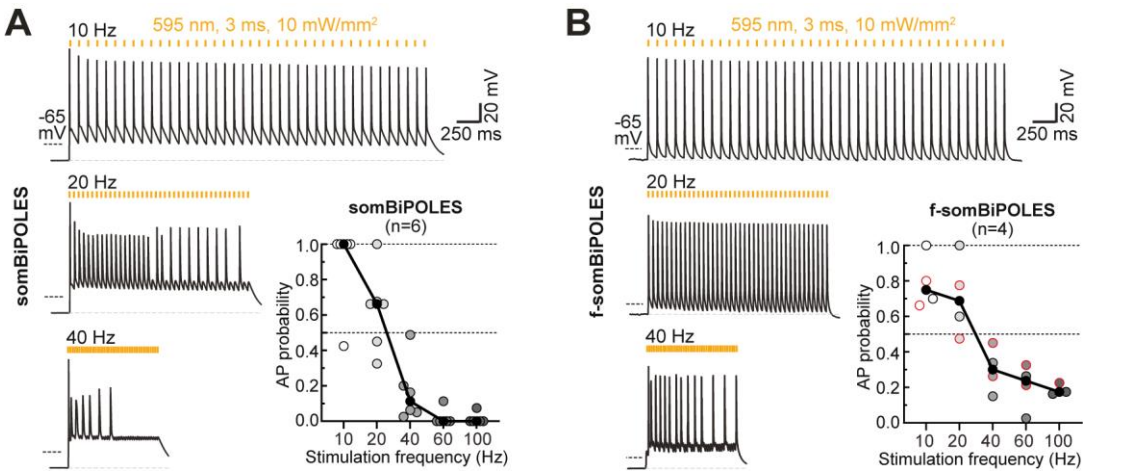

Figure 3.3.6. Characterization of somBiPOLES- and f-somBiPOLES-mediated spiking at different stimulation frequencies (A) Membrane voltage traces at different light-pulse frequencies in CA1 cells expressing somBiPOLES. APs were triggered by 40 pulses (595 nm, pulse width = 3 ms, saturating irradiance of 10 mW/mm^2). Bottom right: quantification of AP probability at increasing stimulation frequencies (from 10 to 100 Hz, black circles: medians, n = 6). To determine AP probability, the number of light-triggered APs was divided by the total number of light pulses. **(B)** Same as in (A) but for CA1 cells expressing f-somBiPOLES. Note that the recovery of the membrane potential after each spike was faster as compared to somBiPOLES. In 2 out of 4 cells (circles with red border), 595-nm light irradiance had to be increased to 50 mW/mm^2 to evoke spiking.

Comparison of somBiPOLES to eNPAC2.0

I compared somBiPOLES with eNPAC2.0, the most advanced optogenetic tool currently available for dual-color excitation and inhibition (Carus-Cadavieco et al., 2017) (Fig. 3.3.7). eNPAC2.0 is a bicistronic construct encoding for the blue-light-sensitive CCR ChR2(H134R) (Nagel et al., 2005), and the orange-light-driven Cl^- pump eNpHR3.0 (Gradinaru et al., 2010). In eNPAC2.0-expressing CA1 pyramidal neurons, depolarizing and hyperpolarizing photocurrents were present under blue and yellow/orange light, respectively (Fig. 3.3.7 A), consistent with its

inverted action spectrum compared to BiPOLES. Moreover, peak photocurrent ratios were more variable between cells (Fig. 3.3.7 A compared to Fig. 3.3.1 H), indicative of different stoichiometries between ChR2(H134R) and eNpHR3.0 in different neurons, probably because membrane trafficking and degradation of both opsins occur independently.

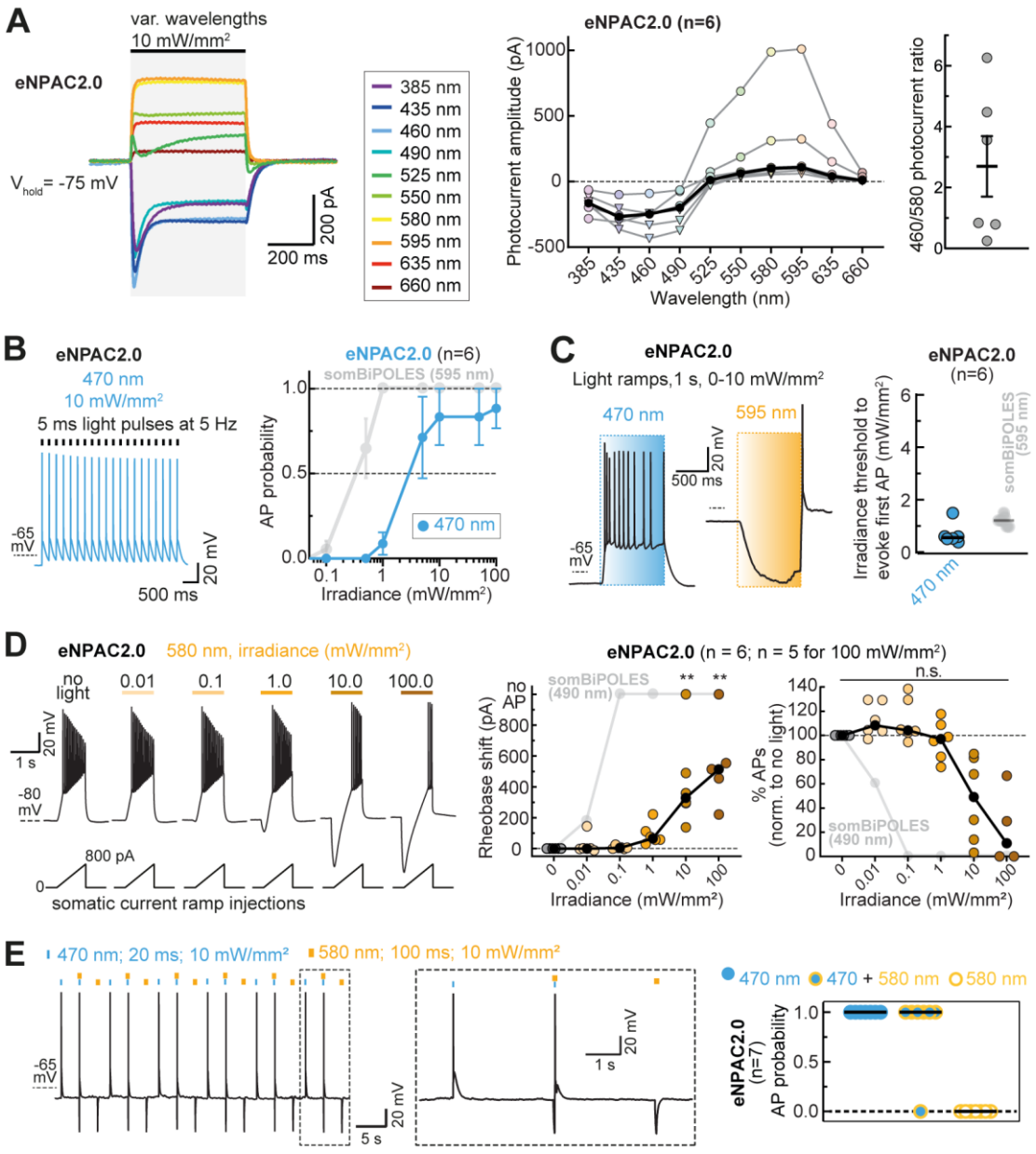

Figure 3.3.7. Characterization of bidirectional optogenetic manipulation of neuronal activity with eNPAC2.0. Grey symbols and lines in (B), (C) and (D) are somBiPOLES values from Fig. 3.3.4 plotted for direct comparison. **(A)** Left: representative eNPAC2.0 photocurrent traces in CA1 pyramidal neurons upon illumination with different wavelengths and equal photon flux at a membrane voltage of -75 mV. Middle: quantification of photocurrent amplitude along the spectrum

(black circles: medians, colored circles: photocurrents elicited by an irradiance of 10 mW/mm^2, colored triangles: photocurrents elicited by an irradiance of 1 mW/mm^2, n = 6). Right: quantification of the ratio of excitatory (460 nm) over inhibitory (580 nm) photocurrents (mean ± SEM, n = 6). **(B)** Left: example traces of voltage-clamp recordings of eNPAC2.0 to determine light-evoked AP probability with 460 nm. Right: quantification of light-mediated AP probability at indicated irradiances (mean ± SEM, n = 6). Note that even at an irradiance of 100 mW/mm^2 not all cells achieved 100% spiking probability. **(C)** Left: representative membrane voltage traces during light ramps at indicated wavelengths with irradiance increasing linearly from 0 to 10 mW/mm^2. A rebound spike was triggered after applying a 595-nm light ramp. Right: quantification of the irradiance threshold at which the first AP was evoked (black horizontal lines: medians, n = 6). **(D)** eNPAC2.0 mediates neuronal membrane voltage hyperpolarization upon illumination with yellow light. Left: current ramps (from 0–100 to 0–900 pA) were injected into eNPAC2.0-expressing CA1 pyramidal cells to induce APs during illumination with yellow light at indicated irradiances (from 0.01 to 100 mW/mm^2). Right: Quantification of the rheobase shift and the relative change in the number of ramp-evoked action potentials. Black circles: medians, n=6, Friedman test, *p < 0.05, **p < 0.01, ***p < 0.001. **(E)** Characterization of all-optical spiking and silencing with eNPAC2.0. Left: Voltage trace showing blue-light-evoked APs, which, under the indicated conditions, could not be blocked by stimulation of eNpHR3.0 with a concomitant yellow light pulse. Yellow light alone led to a hyperpolarization of membrane voltage, indicating chloride loading of the cell by eNpHR3.0. Right: quantification of AP probability under indicated conditions (black horizontal lines: medians, n=7).

Next, I measured spiking parameters of eNPAC2.0. When stimulating neurons with trains of 5-ms light pulses at 470 nm, the peak activation wavelength of ChR2(H134R), eNPAC2.0 required approx. 10-fold higher irradiance compared to somBiPOLES and did not reach 100% reliability (Fig. 3.3.7 B), which might be explained by cross-activation of eNpHR3.0 under high blue irradiance. However, eNPAC2.0 displayed a similar irradiance threshold to evoke the first AP when using 1 s light-ramp stimulation as compared to somBiPOLES (Fig. 3.3.7 C), probably due to a large steady-state photocurrent of ChR2(H134R) and overall slower closing kinetics (t_{off1} = 6.8 ± 1.9 ms, t_{off2} = 20.9 ± 2.2 ms) (Nagel et al., 2005) than Chrimson (t_{off} = 21.4 ± 1.1 ms) (Klapoetke et al., 2014).

Activation of eNPAC2.0 (i.e., eNpHR3.0) with yellow light (580 nm) caused strong membrane hyperpolarization followed by rebound spikes in some cases (Fig. 3.3.7 C). Furthermore, silencing of electrically evoked APs required in the range of 2 orders of magnitude higher irradiance with eNPAC2.0, compared to somBiPOLES, until a significant rheobase-shift was observed (Fig. 3.3.7 D). Finally, blue-light-

triggered APs could not be reliably blocked with concomitant yellow illumination at 10 mW/mm^2 (Fig. 3.3.7 E), suggesting that dual-color bidirectional control of the same neurons Is less straightforward than with somBiPOLES and might require precise calibration of light stimulation conditions.

somBiPOLES opens new possibilities for optical manipulation of neurons

Lastly, I evaluated somBiPOLES in the context of three distinct neuronal applications: (1) bidirectional control of neuronal activity, (2) optical tuning of membrane voltage, and (3) independent spiking of two distinct neuronal populations.

Bidirectional control of neuronal activity

Having shown that somBiPOLES allows reliable neuronal spiking exclusively with orange-red light (Fig. 3.3.4 A, B, D) and that it efficiently blocks current-evoked APs upon illumination with blue-light (Fig. 3.3.4 F, G), I next tested the suitability of somBiPOLES for dual-color all-optical excitation and inhibition of the same neurons (Fig. 3.3.8 A). As expected, red light pulses (635 nm, 20 ms, 10 mW/mm^2) reliably triggered APs in somBiPOLES-expressing neurons (Fig. 3.3.8 B, top). Concomitant blue illumination (490 nm, 10 mW/mm^2) for 100 ms supressed red-light evoked APs in all cases. In addition, blue light alone had only a minor impact on the resting membrane voltage, due to the anion channel-based shunting mechanism of *Gt*ACR2 in somBiPOLES and the close proximity of the Cl^- reversal potential to the resting potential of the cell (Fig. 3.3.8 B, top). While BiPOLES also showed reliable block of red-light-evoked APs during concomitant illumination with blue light, it failed to faithfully trigger APs under the same stimulation conditions as somBiPOLES, reaching only an AP probability of 0.58 (range: 0 – 1) (Fig. 3.3.8 B, middle). This is in accordance with the smaller red-light-mediated excitatory photocurrent amplitudes observed for BiPOLES in comparison to somBiPOLES (73.1 % smaller; Fig. 3.3.2 D, E).

Using the same experimental protocol, neurons expressing Chrimson alone showed APs under both red and blue illumination (Fig. 3.3.8 B, middle), which underlines the key role of the blue-light sensitive *Gt*ACR2 in (som)BiPOLES to avoid inadvertent blue light-mediated spiking with Chrimson.

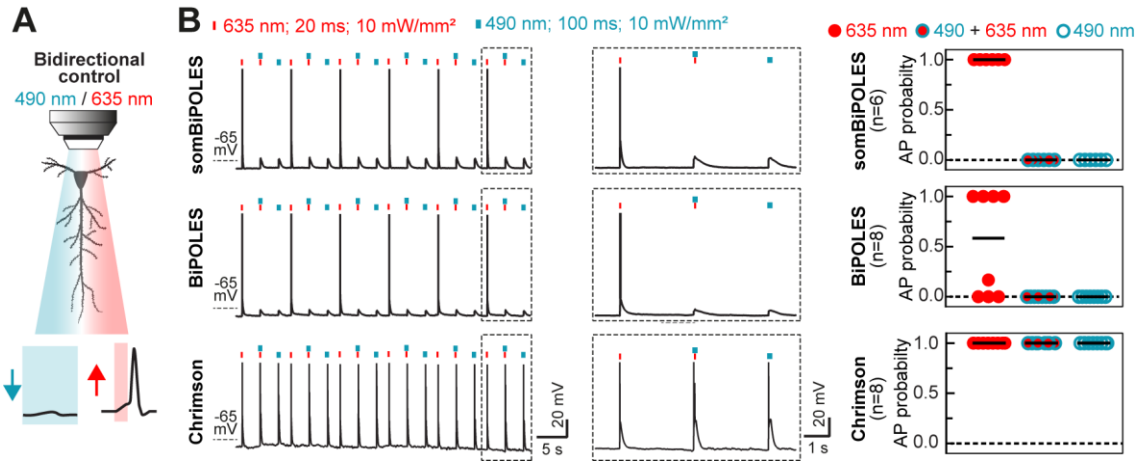

Figure 3.3.8. Bidirectional control of neuronal activity with (som)BiPOLES. (A) Schematic drawing illustrating bidirectional control of neurons with blue and red light (leading to shunting and action potential firing, respectively). **(B)** Current-clamp characterization of bidirectional optical spiking-control with somBiPOLES (top) and BiPOLES (middle) and comparison to optical spiking with Chrimson (bottom). Left: voltage traces showing red-light-evoked APs, which were blocked by a concomitant blue light pulse in (som)BiPOLES expressing cells due to *Gt*ACR2-mediated shunting. Note that in cells expressing Chrimson alone, both red and blue light elicited APs under the indicated conditions. Right: quantification of AP probability upon stimulation with red light (20 ms, 10 mW/mm^2), blue over red light (100 ms over 20 ms, both 10 mw/mm^2), or blue light alone (100 ms, 10 mW/mm^2), as shown in example traces (left). Black horizontal lines: medians, n=8, 6 and 8 for BiPOLES, somBiPOLES and Chrimson, respectively.

Optical tuning of membrane voltage

Aside from reliable dual-color spiking and inhibition, a major advantage of the fixed 1:1 stoichiometry between an ACR and a CCR with different activation spectra in somBiPOLES is the ability to precisely tune the ratio between anion- and cation-conductance with light. In neurons this allows to optically tune the membrane voltage between the Cl^- reversal potential and the action potential threshold (Fig. 3.3.9 A). Optical membrane voltage tuning was achieved either by a variable ratio of blue and orange light at the absorption peak wavelengths of *Gt*ACR2 and Chrimson (Fig.

3.3.9 B, C) or by using a single color with fixed irradiance over a wide spectral range (Fig. 3.3.9 D). Both approaches yielded reliable and reproducible membrane voltage shifts. By simultaneously illuminating somBiPOLES-expressing cells with two 5-s light ramps of 470 and 595 nm of opposite irradiance gradient (470: 1 – 0 mW/mm^2, 595: 0 – 1 mW/mm^2), the membrane voltage was effectively tuned to the E_{Cl^-} when only *Gt*ACR2 was activated with blue light, and the membrane gradually depolarized with an increasing 595/470 nm ratio, eventually passing the action potential threshold (Fig. 3.3.9 B). Moreover, the membrane voltage could be steadily tuned to a specific value for 10 s by choosing a particular 470/595 nm light ratio (Fig. 3.3.9 C). In the second approach, tuning a single wavelength between 385 nm and 490 nm clamped the cell near the E_{Cl^-}, while shifting the wavelength peak further towards red led to gradual depolarization, eventually triggering action potentials at 580 nm (Fig. 3.3.9 D). Depending on the available light source, both methods allow precise control of anion and cation fluxes at a fixed ratio and might be applied for locally defined subthreshold membrane depolarization in single neurons or to control excitability of networks of defined neuronal populations.

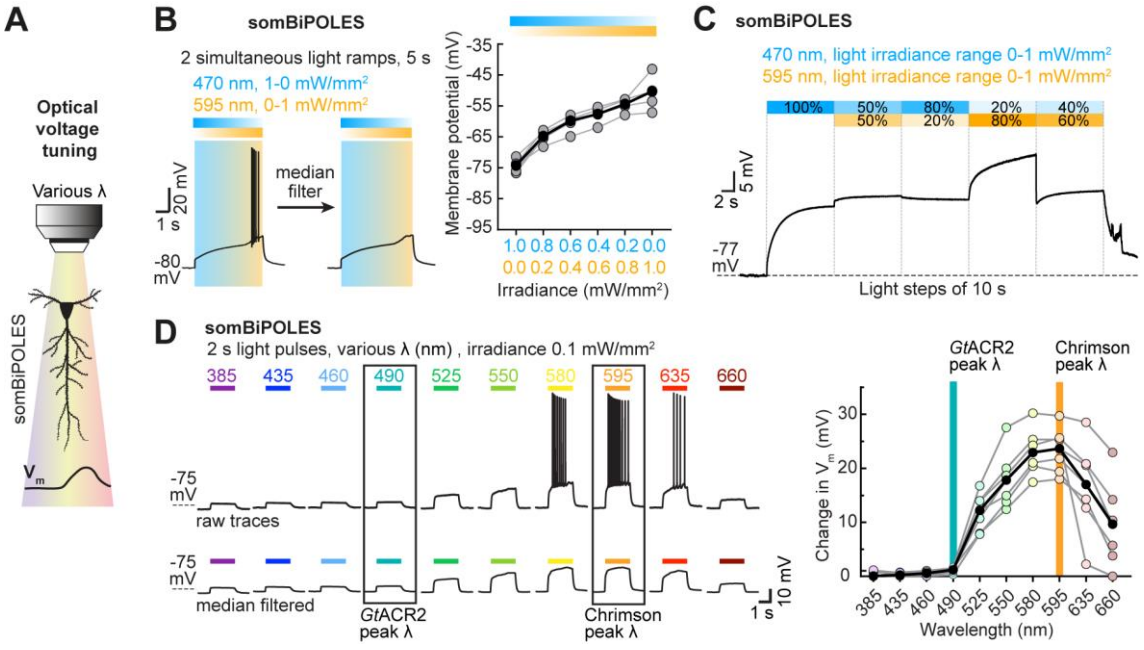

Figure 3.3.9. somBiPOLES allows optical tuning of the membrane potential. (A) Schematic drawing illustrating control of membrane voltage (V_m) with somBiPOLES. **(B)** Left: representative

membrane voltage traces from a somBiPOLES-expressing CA1 pyramidal cell during simultaneous illumination with 470- and 595-nm light ramps of opposite irradiance gradient. Voltage traces were median-filtered to reveal the slow change in V_m during the ramp protocol. Right: quantification of V_m at different 595/470 nm light ratios. Black circles: medians, n=5. **(C)** Example trace from a somBiPOLES-expressing neuron showing V_m tuning during a step protocol consisting of five blocks of 10 s illumination at different 595/470 nm light ratios. **(D)** Left: representative membrane voltage traces of somBiPOLES in CA1 pyramidal neurons upon illumination with different wavelengths at equal photon flux. As in (B) voltage traces were median-filtered to eliminate action potentials. Right: quantification of V_m along the spectrum showing optical voltage tuning at the indicated wavelengths. Peak wavelength for *Gt*ACR2 and Chrimson are indicated by an aquamarine and orange bar, respectively. Black circles: medians, an irradiance of 0.1 mW/mm^2 was kept constant for all wavelengths, n=6).

Independent spiking of two distinct neuronal populations

By pairing *Gt*ACR2 and Chrimson in a tandem construct, the blue-light-activated inhibitory photocurrents from *Gt*ACR2 shunt any residual Chrimson-mediated blue-light-activated excitatory photocurrents, thereby restricting optical excitation in somBiPOLES-expressing cells exclusively to the orange-red spectrum (Fig. 3.3.3 B, D; see also Fig. 1.4). This opens new possibilities for two-color excitation of genetically distinct but spatially intermingled neuronal populations using somBiPOLES together with a second, blue-light-activated ChR (Fig. 3.3.10 A). To demonstrate this, using a Cre-On/Cre-Off strategy, somBiPOLES was expressed in CA1 VIP interneurons and CheRiff, a blue-light-sensitive ChR (peak activation wavelength = 460 nm) (Hochbaum et al., 2014), was expressed in CA1 pyramidal neurons (Fig. 3.3.10 B). CheRiff-expressing pyramidal cells were readily spiking upon blue, but not red illumination up to 10 mW/mm^2 (Fig. 3.3.10 C, bottom). Conversely, red light evoked APs in somBiPOLES-expressing VIP neurons, while blue light up to 100 mW/mm^2 did not evoke APs (Fig. 3.3.10 C, top). Oriens-Lacunosum-Moleculare (OLM) interneurons are a common postsynaptic target of CA1 pyramidal cells (Blasco-Ibáñez & Freund, 1995; Sun et al., 2014) and VIP interneurons (Acsády et al., 1996; Turi et al., 2019) . Therefore, exclusive excitation of CA1 cells or VIP interneurons is expected to trigger excitatory and inhibitory (Tyan et al., 2014) postsynaptic currents (EPSCs and IPSCs), respectively. I recorded

synaptic inputs in VIP-negative, GABAergic neurons in stratum-oriens upon blue- or red-light stimulation (putative OLM-cells, Fig. 3.3.10 D). As expected, blue light triggered EPSCs (CheRiff) and red light triggered IPSCs (somBiPOLES), evident by their respective reversal potentials at 8.8 ± 10.4 mV and -71.4 ± 13.1 mV (Fig. 3.3.10 D, right). Thus, somBiPOLES, in combination with the blue-light sensitive CheRiff enabled independent activation of two distinct populations of neurons in the same field of view.

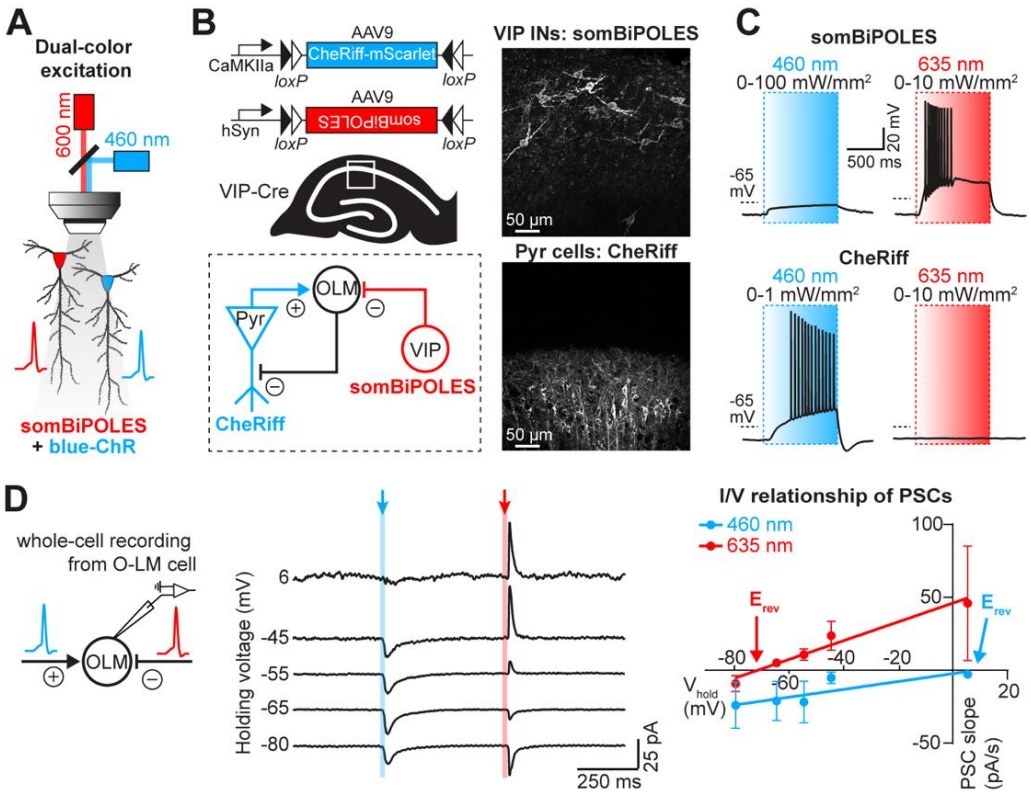

Figure 3.3.10. Independent two-color excitation of two distinct neuronal populations using somBiPOLES with a second blue-light-sensitive ChR. (A) Schematic drawing illustrating independent control of 2 neurons expressing either somBiPOLES (red) or a blue-light-sensitive ChR (blue). **(B)** Left: Cre-On/Cre-Off strategy to achieve mutually exclusive expression of CheRiff-mScarlet in CA1 pyramidal neurons and somBiPOLES in VIP-positive GABAergic neurons. Both cell types innervate OLM interneurons in CA1. Right: maximum-intensity projection images of 2-photon stacks showing expression of somBiPOLES in VIP-interneurons (top) and CheRiff-mScarlet in the pyramidal layer of CA1 (bottom). **(C)** Current-clamp recordings demonstrating mutually exclusive spiking of somBiPOLES- and CheRiff-expressing neurons under red or blue illumination. **(D)** Left: postsynaptic whole-cell voltage-clamp recordings from an OLM cell at indicated holding membrane voltages showing EPSCs and IPSCs upon blue- and red-light pulses, respectively. Right: quantification of blue- and red-light-evoked PSCs and their reversal potential (E_{rev}) (mean ± SEM, n =7).

In summary, somBiPOLES, expands the possibilities for optical manipulation of neuronal networks. It allows multiple new applications including (1) potent excitation and inhibition of the same neurons with red and blue light, (2) exclusive red-light activation of a neuronal subpopulation in multicolor experiments, thus enabling independent dual-color spiking of two distinct populations over light irradiances spanning multiple orders of magnitude, and (3) optical tuning of the membrane voltage between the E_{Cl^-} and the action potential threshold.

Finally, to further extend the applications of (som)BiPOLES to the mammalian brain, various conditional and non-conditional viral vectors were generated, in which the expression of the fusion construct is regulated by different promoters. Cre-dependent expression of somBiPOLES in specific mouse transgenic lines, allows targeting of defined neuronal populations, as described above for VIP interneurons (Fig. 3.3.10 B). Moreover, conditional expression of somBiPOLES in TH-Cre mice was employed by Dr. Alexander Dieter to target noradrenergic neurons in the Locus Coeruleus (see section 4.3.4, Fig. 4.2 G). In addition, I showed that expression of somBiPOLES under the CaMKIIa promoter and BiPOLES under the minimal *Dlx* promoter (mDlx) (Dimidschstein et al., 2016), enables bidirectional control of excitatory projection neurons (Fig. 3.3.11) and GABAergic neurons (Fig. 3.3.12) in hippocampal organotypic slices, respectively. Furthermore, viral expression of mDlx-BiPOLES in ferret secondary visual cortex permitted dual-color manipulation of the excitation/inhibtion ratio, as shown by the lab of Andreas Engel (see section 4.3.4, Fig. 4.2 H).

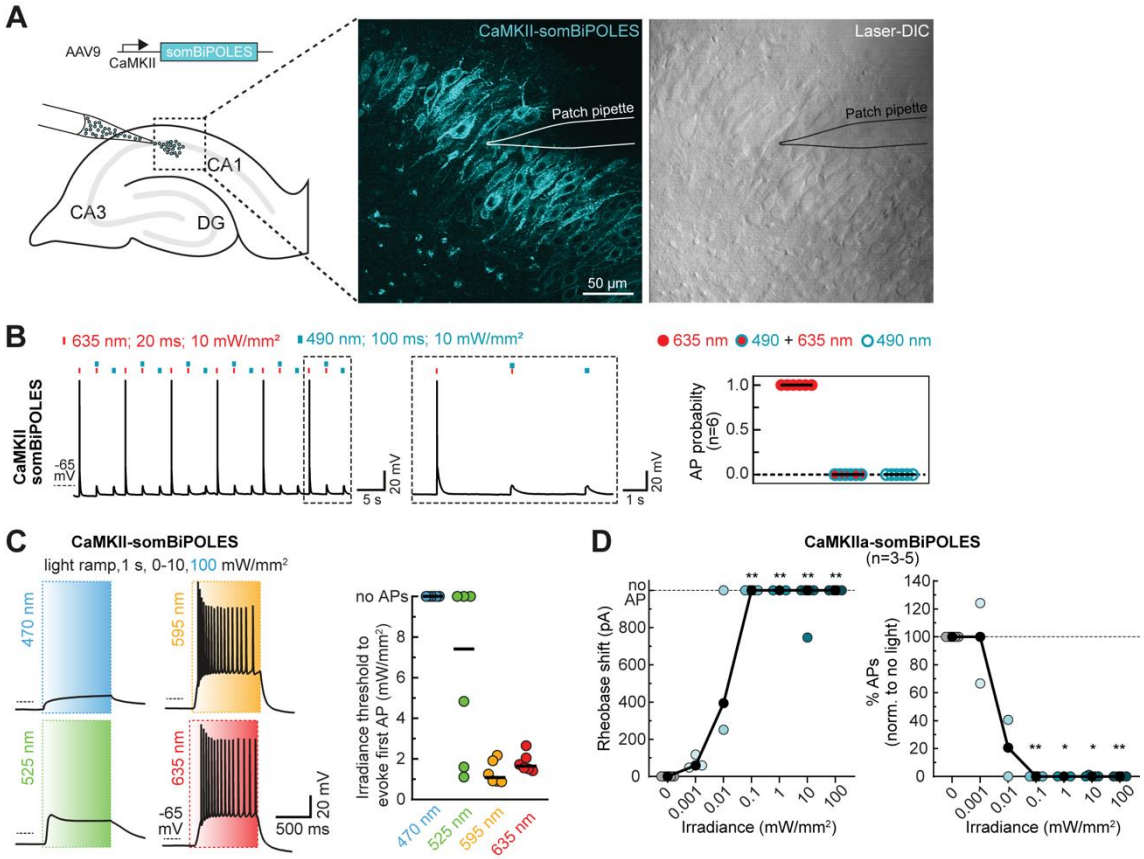

Figure 3.3.11. Virally expressed CaMKII-somBiPOLES enables bidirectional control of activity in excitatory neurons. (A) Viral transduction of CaMKII-somBiPOLES in hippocampal organotypic slice cultures. Right: Single-plane 2-photon fluorescence (cyan) and laser-DIC (gray) images showing expression of somBiPOLES in pyramidal cells of *stratum pyramidale* and cellular morphology, respectively. The position of the patch pipette is depicted by a drawing of its outline. **(B)** Bidirectional optical spiking-control with CaMKII-somBiPOLES. Left: Voltage traces showing red-light-evoked APs, which were blocked by a concomitant blue-light pulse. Blue light alone did not trigger APs. Right: quantification of AP probability under indicated conditions (black horizontal lines: medians, n = 6). **(C)** Left: representative membrane voltage traces during light ramps at indicated wavelengths with irradiance increasing linearly from 0 to 10 mW/mm^2 over 1 s, except for 470 nm ramps, which were ranging to 100 mW/mm^2 to rule out the possibility that high-irradiance blue light might still evoke APs. Right: Quantification of the irradiance threshold at which the first AP was evoked (black horizontal lines: medians, n = 6). **(D)** Quantification of CaMKII-somBiPOLES-mediated neuronal silencing. Current ramps (from 0–100 to 0–900 pA) were injected into cells to induce APs. The injected current at the time of the first AP was defined as the rheobase. Illumination with blue light of increasing irradiance (from 0.001 to 100 mW/mm^2) activated *Gt*ACR2-mediated Cl^- currents shifting the rheobase to higher values (black circles: medians, n = 6, Friedman test, **p < 0.01, ***p < 0.001).

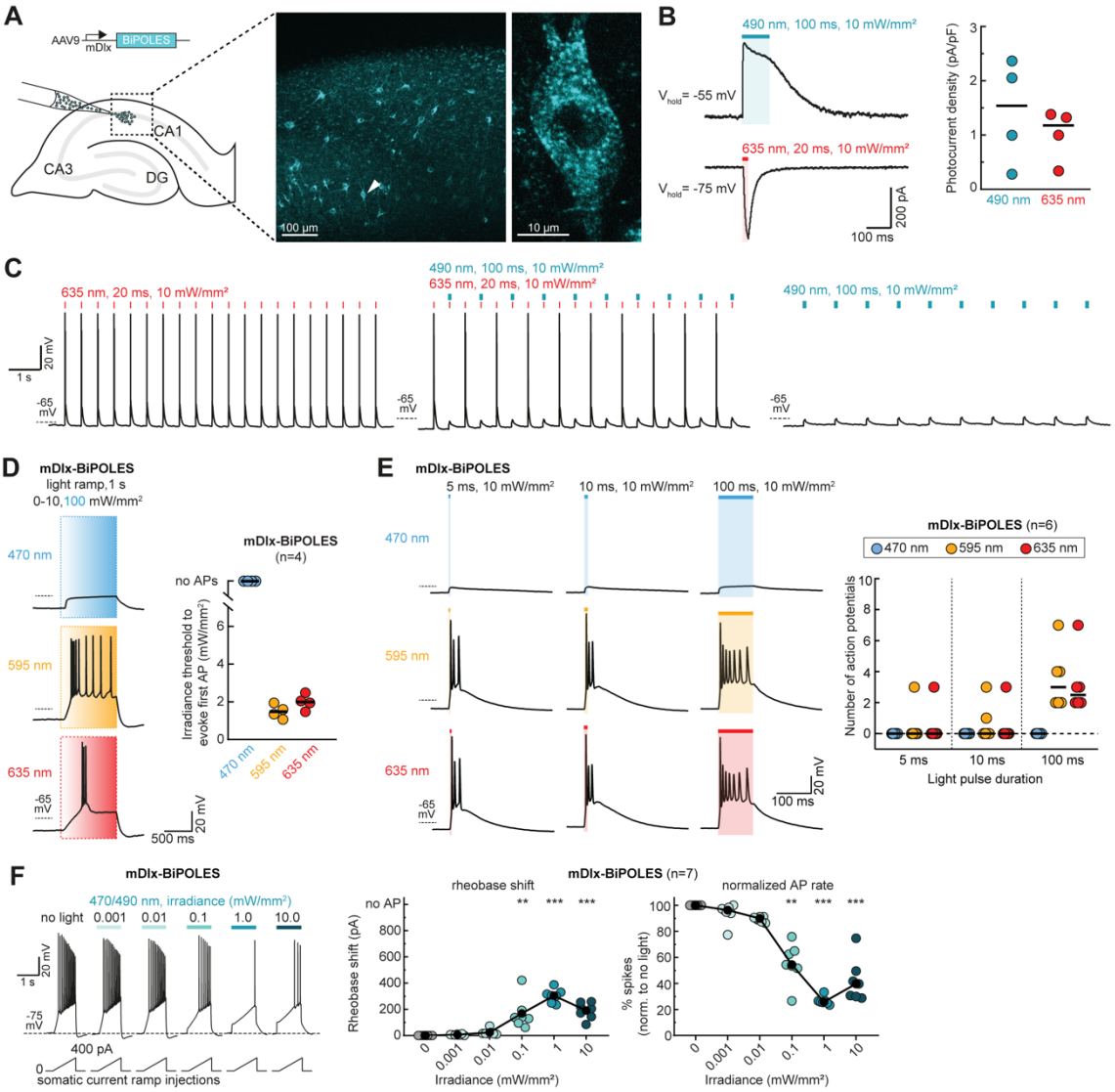

Figure 3.3.12. Virally expressed mDlx-BiPOLES enables bidirectional control of GABAergic neuronal activity. (A) Viral transduction of mDlx-BiPOLES in hippocampal organotypic slice cultures. Right: Maximum-intensity projection images of 2-photon stacks showing expression of BiPOLES in GABAergic neurons in CA1. Magnified view of a single neuron indicated by white arrowhead is shown on the right. **(B)** Left: Representative photocurrent traces measured in an mDlx-BiPOLES-expressing CA1 GABAergic neuron. Outward anionic photocurrents evoked by a 490 nm light pulse (100 ms, 10 mW/mm^2) were recorded at a membrane voltage of -55 mV, and inward cationic photocurrents evoked by a 635 nm light pulse (20 ms, 1 mW/mm^2) were recorded at a membrane voltage of -75 mV. Right: Quantification of photocurrent densities evoked under the indicated conditions (black horizontal lines: medians, n = 4). **(C)** Bidirectional optical spiking-control with mDlx-BiPOLES. Voltage traces showing red-light-evoked APs (left), which were blocked by a concomitant blue-light pulse (middle). Blue light alone did not trigger APs (right). **(D)** Left: representative membrane voltage traces during light ramps at indicated wavelengths with irradiance increasing linearly from 0 to 10 mW/mm^2 over 1 s, except for 470 nm ramps, which were ranging to 100 mW/mm^2 to rule out the possibility that high-irradiance blue light might still evoke APs. Right:

Quantification of the irradiance threshold at which the first AP was evoked. **(E)** Extended duration of illumination increased the probability and number of APs. Left: Representative membrane voltage traces measured in mDlx-BiPOLES-expressing neurons illuminated as indicated. Right: quantification of the number of APs evoked by the different illumination protocols (black horizontal lines: medians, n = 6). **(F)** Quantification of mDlx-BiPOLES-mediated neuronal silencing. Current ramps (from 0–100 to 0–900 pA) were injected into cells to induce APs. The injected current at the time of the first AP was defined as the rheobase. Illumination with blue light of increasing irradiance (from 0.001 to 10.0 mW/mm^2) activated *Gt*ACR2-mediated Cl^- currents shifting the rheobase to higher values. Middle: Quantification of the rheobase shift at different light intensities. Right: Relative change in the number of ramp-evoked APs upon illumination with blue light at indicated irradiance values (black circles: medians, n = 7, Friedman test, $^{**}p < 0.01$, $^{***}p < 0.001$).

4. Discussion

Since the discovery of ChR2 (Boyden et al., 2005; Nagel et al., 2003), optogenetic manipulations have become the method of choice to probe neuronal circuit function, thus shedding light on the mysteries of the brain. The versatility, relatively low invasiveness, and high temporal, spatial and genetic precision of optogenetic interventions, grant them several advantages over traditional pharmacological approaches or electrical stimulation techniques. However, the choice of an appropriate tool to achieve the desired effect on neuronal activity or function is often not easy. Even in the relative simple case where neuronal activation via direct membrane depolarization is required via CCRs there are a number of factors to consider. For example, key biophysical properties of the optogenetic tool, such as relative ion conductance, kinetics, desensitization, light sensitivity or activation spectra, should be taken into account (Lin, 2011) in addition to the specifics of the experimental setup and type of preparation. Thus, an appropriate choice from a wide range of CCR variants with unique features and limitations (Schneider et al., 2015) is essential for a successful experiment.

In the following paragraphs I present some considerations and general constraints that apply to the tools I characterized in this work.

4.1. Part I: Expanding the temporal and spectral range for neuronal inhibition

In part I (see section 3.1), I functionally characterized novel step-function eACRs, namely iChloC^{CA} and the spectrally-shifted Phobos^{CA} and Aurora^{CA}, which emerged from systematic conversion of a wide variety of CCRs followed by an exhaustive biophysical characterization. CCRs that were successfully converted to ACRs were further modified to slow-cycling variants by introduction of a point-

mutation to slow-down photocycle kinetics. I demonstrated their application in organotypic slices as well as in *Drosophila* larvae for *in vivo* all-optical interrogation of neuronal circuits (section 3.1.1). Furthermore, I developed Aion, a bi-stable eACR, engineered from Phobos^{CA}, that exhibits the longest-know conducting state for an ACR and permits faithful, continuous silencing of neurons for many hours with short light pulses applied several minutes apart (section 3.1.2). Lastly, I showed that MerMAID1 and 6, two nACR variants from a newly identified family of rapidly desensitizing ChRs, can be used to block single APs with high temporal precision and without affecting subsequent firing events (section 3.1.3).

In sum, the ACRs investigated in this study expand the available toolkit of optogenetic silencers in the spectral and temporal domains, thus broadening the possibilities for optical neuronal inhibition. However, a number of considerations should be taken into account to ensure their proper experimental implementation.

4.1.1. ACR function depends on the driving force for chloride ions

The silencing efficacy of ACRs in a given system or experimental condition is strongly dependent on the Cl^- driving force. Unlike Cl^- pumps, which upon illumination always lead to hyperpolarization by actively transporting Cl^- ions inside the cell (Han & Boyden, 2007b; Zhang et al., 2007), the flux of Cl^- upon opening of ACRs is tightly controlled by the electrochemical gradient across the cell membrane, similar to the mode of action of $GABA_A$ ionotropic receptors (Kaila, 1994). In most mature neurons, the E_{Cl-} is close to the resting membrane potential (typically between -65 mV and -75 mV) (Delpire & Staley, 2014). Therefore, in neurons at rest, light activation of ACRs barely affects the Cl^- gradient across the cell membrane or the membrane potential. By clamping the cell to the E_{Cl-}, ACRs efficiently shunt membrane depolarization, preventing the generation of new APs. Since it minimizes ionic flux in quiescent neurons, shunting represents an energetically efficient mode of inhibition. Moreover, it prevents non-physiological changes in intracellular Cl^-

concentration that can temporally shift the E_{Cl-} and eventually lead to GABA-mediated excitation (Raimondo et al., 2017), a side-effect that was reported to occur during prolonged activation of the Cl^- pump halorhodopsin (Raimondo et al., 2012).

However, the E_{Cl-} can vary under a number of circumstances: (1) during pathological conditions; (2) during development; (3) upon excessive activation of GABAergic inputs, which can alter Cl^- gradients across the plasma membrane ; (4) within distinct compartments of the same cell; or (5) among different neuronal cell types (for a review see Kaila et al., 2014; Wright et al., 2011). One of the most studied modulations of E_{Cl-}, leading to a shift in the ionic driving force for $GABA_A$ receptors from depolarizing to hyperpolarizing, occurs during development (Khazipov et al., 2004; Owens et al., 1996). In neurons, intracellular Cl^- concentration is mainly regulated by the Cl^- importer ($Na^+/K^+/2Cl^-$ cotransporter 1, NKCC1) and the chloride exporter (K^+/Cl^- cotransporter 2, KCC2) (Payne et al., 1996). Strong upregulation of KCC2 during early developmental stages (starting at postnatal day 5 in rat hippocampus, and 64 days post conception in human neocortex) yields a low intracellular Cl^- concentration that is maintained in adult central neurons and accounts for the hyperpolarizing action of $GABA_A$ receptors (Kaila et al., 2014; Rivera et al., 1999). Hence, the inhibitory action of ACRs would be compromised in immature neurons due to low expression levels of KCC2 and, thus, depolarizing Cl^- gradients.

A second condition in which activation of ACRs would lead to neuronal excitation rather than inhibition due to a positively shifted E_{Cl-}, is in presynaptic boutons. Intracellular Cl^- concentration is elevated in axon terminals, consistent with a reported lower expression of KCC2 (Szabadics et al., 2006), compared to the somatodendritic compartment. Indeed, Mahn and colleagues demonstrated that while local activation of *Gt*ACR1 at the soma efficiently suppresses AP generation, illumination of *Gt*ACR1-expressing axon terminals enhances neurotransmitter

release (Mahn et al., 2016). The same holds true for *Gt*ACR2, with axonal light stimulation causing antidromic spiking (Mahn et al., 2018; Malyshev et al., 2017).

Nevertheless, even in conditions with high intracellular Cl^- concentration the large conductance of *Gt*ACR1/2 might enable shunting (Govorunova et al., 2016). Notably, newborn hippocampal granule cells, which show a depolarized E_{Cl-}, can be activated or inhibited by GABAergic input, depending on its strength. More specifically, interneurons only support granule cell excitation in an intermediate synaptic conductance range (~ 1.5 nS), while shunting inhibition predominates at higher conductance values, with AP firing being effectively blocked by GABAergic inputs above 4 nS (Heigele et al., 2016). Thus, in the presence of depolarizing Cl^- gradients, large-conductance ACRs could, in principle, be applied for bidirectional control of neurons by using either brief/weak or long/strong activation protocols, resulting in excitation or shunting, respectively. However, this requires detailed knowledge of the ionic gradients and action of the ACRs in the neuronal compartment or cell type of interest. For example, in axon terminals of glutamatergic neurons, *Gt*ACR1 activation only results in phasic excitation, but fails to inhibit activity via shunting (Mahn et al., 2016)

Taken together, silencing efficiency of ACRs might be compromised in conditions where the E_{Cl-} is depolarizing, such as early stages during development, or in specific cellular types and subcellular compartments (i.e. axon terminals), for which alternative silencing approaches should be considered.

Soma-targeted ACRs and alternative approaches for synaptic silencing

One way to overcome inadvertent axonal excitation via ACRs, is to restrict their expression to the somatodendritic compartment. A soma-targeted version of *Gt*ACR2 (st*Gt*ACR2), generated by adding a C-terminal targeting motif from the soma-localized K^+ channel Kv2.1 (Lim et al., 2000), has been shown to display reduced axonal excitation in addition to increased membrane targeting and larger

anion photocurrents (Mahn et al., 2018). In accordance to these results, I demonstrated that a soma-targeted variant of the eACR Aion (somAion), generated by the same Kv2.1-based approach, showed enhanced membrane trafficking and stronger silencing efficiency compared to the non-soma-targeted variant (see Fig. 3.1.12). In addition to the C-terminus of the Kv2.1 channel, other targeting motifs have been fused to opsins to confine expression to the somatodendritic compartment. Adding a short amino-terminal segment of the kainate receptor KA2 subunit to the blue-light sensitive CCR CoChR yielded a soma-targeted variant (soCoChR) suitable for two-photon holographic stimulation (Shemesh et al., 2017b). However, soCoChR displays greatly reduced photocurrents compared to the original CoChR and to a recently reported soma-targeted variant generated using the Kv2.1 strategy (stCoChR; Forli et al., 2021). Another approach employed the C-terminus of the 5-HT_{1A} and 5-HT_{2A} receptors to target melanopsins to receptor-specific domains in neurons (Eickelbeck et al., 2019; Masseck et al., 2014). During the development of somAion I also tested the strategy based on the 5-HT_{1A} (Appendix Fig. A.5). While this approach restricted expression of Aion mainly to the soma of CA1 pyramidal cells, it displayed intracellular aggregates (Appendix Fig. A.5 B), which was also reported for the tool CaMello-5HT_{2A} where intracellular clusters colocalized with the endosome marker Rab7 (Eickelbeck et al., 2019). Thus, soma-targeting based on the addition of the Kv2.1 C-terminus sequence appears to be the most successful of all strategies employed so far.

Although soma-targeting of ACRs efficiently restricts expression to the somatodendritic compartment, thereby overcoming the issue of axonal excitation and antidromic spiking, it limits the application of ACRs to somatic inhibition. While in most cases this is sufficient to silence the main output of a particular neuron by preventing AP generation, inputs at distal dendrites cannot be suppressed. Notably, in some neuronal types, distal dendritic inputs convey unique information and are important for compartmentalized dendritic signaling (Magee, 2000). For example,

distal enthorino-cortical inputs to hippocampal CA1 pyramidal neurons have been shown to convey different information compared to proximal CA3 Schaffer collateral inputs (Gasparini & Magee, 2006; Lisman, 1999). Moreover, the timing between different dendritic inputs plays a key role in the induction of heterosynaptic plasticity, which occurs in the absence of somatic spiking but requires activation of both N-methyl-D-aspartate (NMDA) receptors and release of Ca^{2+} from internal stores (Dudman et al., 2007). Thus, depending on the experimental requirements, differently targeted ACRs might be preferable. If silencing of dendritic inputs is required, a non-soma targeted ACR is preferable. In contrast, if silencing AP initiation is the main goal, soma-targeted ACRs may be the tools of choice.

Notably, ACR-mediated somatic inhibition does not allow local silencing of presynaptic terminals, which is required to investigate the role of specific projections from one neuronal population to its target region. In this case, alternative silencing methods should be considered. A chemogenetic approach based on the designer receptor exclusively activated by designer drug (DREADD) hM4Di (Armbruster et al., 2007), has been shown to inhibit synaptic transmission by activating the $G_{i/o}$ pathway in synaptic terminals (Stachniak et al., 2014). However, the low temporal resolution of DREADDs compared to optogenetic methods does not allow for rapid manipulations of synaptic transmission, with silencing occurring at the minute-to-hour timescale (for a review see Wiegert et al., 2017). Recently, two optogenetic tools were developed that inhibit synaptic transmission in a similar way as hM4Di, but with the advantage of being controlled by light. Upon illumination, the $G_{i/o}$-coupled rhodopsins eOPN3 (Mahn et al., 2021b) and PPO (Copits et al., 2021) reduce the probability of neurotransmitter vesicle release by inhibiting voltage-dependent Ca^{2+} channels at presynaptic terminals, amongst other mechanisms (for more details see section 1.1.3, Fig. 1.1 C).

4.1.2. ACRs with slow off-kinetics: step-function variants

Step-function CCRs and ACRs are characterized by their slow off-kinetics and bi-stable or step-like behavior by which they can be switched between open and closed states with light of different wavelengths. This property enables sustained and precise temporal control of cations- and Cl^--conductivity with CCRs and ACRs, respectively (Berndt et al., 2009; Berndt et al., 2014; Yizhar et al., 2011). Moreover, due to their slow off kinetics, step-function ChRs exhibit increased operational light sensitivity, by integrating light over time and accumulation of more and more channels in the open state (Mattis et al., 2011). These features provide step-function ACRs with several advantages over ion pumps for neuronal inhibition.

First, since step-function eACRs yield effective inhibition with either short light pulses or with continuous light at low irradiance, their use reduces tissue heating in optogenetic silencing experiments (see Monte Carlo simulation of light-induced heat distribution in neuronal tissue in Fig. 3 of Wiegert et al. 2017). However, a putative caveat of the high operational light sensitivity of eACRs, is that they may get activated outside the target area under continuous illumination, even by low irradiances far away from the light source (Babl et al., 2019; Li et al., 2019). I showed that a single, 20-ms light pulse is sufficient to activate the step-function eACRs iChloC^{CA}, Phobos^{CA}, and Aurora^{CA}, which resulted in efficient suppression of AP firing for at least 55 s (Fig. 3.1.2). In contrast, ion pumps, where only a single ion is transported per absorbed photon, require continuous illumination at high irradiances for efficient neuronal silencing (Chow et al., 2010; Han & Boyden, 2007; Zhang et al., 2007). Light intensities in the order of 10 mW delivered through an optical fiber can cause significant heating of large volumes of brain tissue during continuous illumination, increasing local temperatures by several degrees Celsius (Stujenske et al., 2015) and leading to increased neuronal firing rates (Kim & Connors, 2012; Wang et al., 2011) and changes in blood flow (Rungta et al., 2017).

A second caveat of optogenetic silencers that require continuous illumination is the potential interference with behavior during *in vivo* experiments, which can ultimately lead to misinterpretations regarding the function of the neural circuit under scrutiny. Many animal species, including *Drosophila* larvae detect and avoid short-wavelength light in the UV-blue spectrum even at low-intensities (Keene & Sprecher, 2012; Xiang et al., 2010). This makes the implementation of optogenetic manipulations challenging in living animals, especially when illumination of the entire body is required. By expressing the step-function eACR Phobos^{CA} in motor neurons of *Drosophila* larvae, I showed that a single brief blue light pulse is sufficient to inhibit larval locomotion on the minute-time scale (at least 210 s), while WT larvae showed only a transient, innate response (Fig. 3.1.2 B, Appendix Fig. A.2). Therefore, Phobos^{CA} allows temporal dissociation of functional silencing and the physiological responses evoked by the light stimulus directly.

Further applications of Aion

Aion, by having the longest-known conducting state (i.e. the slowest closing kinetics, $t_{off} \approx 15$ min, Appendix Fig. A.3), takes the advantages of step-function ACRs to the extreme. I demonstrated that activation of Aion with a short blue light pulse every 5 min is sufficient to silence CA1 hippocampal neurons for long periods of time up to 12 h (Fig. 3.1.8 A, C; Fig. 3.1.9), which makes it is an ideal candidate tool for behavioral paradigms requiring periods of inhibition on the scale of several minutes to hours. Furthermore, the long interstimulus intervals during Aion-mediated inhibition can in principle facilitate monitoring of neuronal activity in the silenced neurons or in another neuronal population of interest in the same field of view. For such experiments, using one-photon imaging, Aion would require combination with a far red-shifted sensor, such as the near-infrared genetically encoded calcium indicator NIR-GECO with excitation and emission peaks at 670 nm and 700 nm, respectively (Qian et al., 2019, 2020) to not interfere with the peak inactivation

wavelength of Aion at 595 nm (see spectrum for Phobos^{CA}, the parental construct of Aion, in Fig. 3.1.1 E).

Recently, an extremely light-sensitive step-function variant of ChR2 was engineered (Gong et al., 2020) by combining point mutations in the DC-gate, namely C128S and D156A, which had been previously used to generate a slow-cycling step-function ChR2 (SSFO; Yizhar et al., 2011), with the T159C mutation that has been shown to increase photocurrents in ChR2 (Berndt et al., 2011). The resulting CCR, termed SOUL for Step-function Opsin with Ultra-high Light sensitivity, allows activation of neurons located in deep mouse brain regions via transcranial optical stimulation, as well as induction of oscillatory activity in macaque cortex via optical stimulation from outside the dura, which could be reverted by orange light-mediated accelerated closing of the channel (Gong et al., 2020). The long-lasting conducting state of Aion is granted by the mutations C128A and D156C. It would be interesting to test whether adding the T159C mutation in Aion can further enhance photocurrent amplitude and allow photoactivation under conditions of significantly attenuated light power, similar to what was reported for SOUL (Gong et al., 2020).

Noninvasive optogenetic inhibition was first achieved using the red-light-activated Cl^- pump Jaws, which successfully inhibited neurons in the mouse cortex over a range of 1–3 mm below the brain's surface upon stimulation with red light transcranially through the intact skull (Chuong et al., 2014b). However, as previously discussed (see section 1.1.1), ion pumps present some limitations, especially when prolonged inhibition periods are required (Wiegert et al., 2017). In this context, minimally invasive optogenetic inhibition with Aion could open new possibilities for clinical applications. Of particular interest are, for example, several mental and mood disorders, such as depression and anxiety, which have been related to impaired GABAergic function (Luscher et al., 2011; Nuss, 2015), and are often treated with benzodiazepines ($GABA_A$ receptor agonists) (Balon & Starcevic, 2020; Benasi et al., 2018; Petty et al., 1995). Ultimately, if cellular expression profiles can be achieved

with Aion or other ACRs that are similar to those of natural GABARs they might be used to mimic enhanced GABAR-mediated transmission with light. Thus, slow-cycling ACRs could be used to explore adverse effects associated with long-term use of benzodiazepines (Barker et al., 2004; Ford et al., 2014) and the repercussion of prolonged increases in GABAergic transmission.

Comparison of slow-cycling ACRs derived from engineered and natural ACRs

In section 3.1.2 (Fig. 3.1.5 to 3.1.8) I systematically compared the performance of Aion to *Gt*ACR1^{CA}, a slow-cycling variant engineered from the naturally-occurring *Gt*ACR1 by introduction of the point mutation C102A (Govorunova et al., 2018; Sineshchekov et al., 2015), which is homologous to the mutation C128A in Aion. However, in contrast to Aion, where the C128A mutation not only slows down channel closing kinetics, but also enables accelerated channel closure upon illumination with red-shifted light, light-induced channel closure was not possible with *Gt*ACR1^{CA}. In fact, when 660-nm light was delivered at a time point when *Gt*ACR1^{CA}-mediated photocurrents had almost decayed back to baseline (198 s after initial opening), an increase in Cl^- conductance was observed (Fig. 3.1.5 B, G), suggesting that red light brings *Gt*ACR1^{CA} to an intermediate conducting state in the photocycle rather than to the ground state. Hence, *Gt*ACR1^{CA} exhibits slow-cycling but not truly step-function properties, hindering its applicability for neuronal inhibition with precisely timed on and offset.

The second point mutation that confers Aion its characteristic long-lasting open state is on the second residue of the DC pair, namely D156. However, this residue is not conserved in nACRs, and most frequently replaced by a serine (S130) (Kim et al., 2018; Sineshchekov et al., 2015). Moreover, mutation of the corresponding S130 to alanine in *Gt*ACR1 did not show a strong effect on the off-kinetics (Sineshchekov et al., 2015). The different role of key residues in nACRs compared to CCR-derived eACRs emphasizes the differences in photocycle and

gating mechanisms. Certainly, structure-function insights derived from crystallography studies, such as the work by H. Kato, Y. Kim and colleagues who resolved the crystal structures of iC++ and *Gt*ACR1, are key to determine which properties and mutations are transferable between eACRs and nACRs (Kato et al., 2018; Kim et al., 2018).

4.1.3. Spectral multiplexing: blue- and red-shifted ACRs

One benefit of engineering ACRs from existing CCRs, is the large array of well-described CCR variants with diverse biophysical properties. Of particular interest is the generation of blue- and red- shifted eACRs that can facilitate dual-color experiments upon combination with spectrally different optogenetic actuators. The eACRs Phobos and Aurora allow for efficient neuronal inhibition under continuous blue and green/orange light, respectively, as shown in HEK cells, hippocampal neurons and *Drosophila* larvae (Wietek et al., 2017). In this work, I characterized the step-function variants (C128A mutants) of Phobos and Aurora and although both eACRs were able to inhibit AP generation, neurons expressing Aurora^{CA} displayed altered membrane parameters, probably resulting from a not fully closed channel configuration in the dark (see depolarized membrane resting potential in Aurora^{CA}-expressing neurons in Fig. 3.1.2 A-B, panel iii). Moreover, generation of transgenic flies expressing Aurora^{CA} in motor neurons was not possible due to negative effects on embryonal developmental . Hence, only the blue-light activated Phobos^{CA} represents a promising optogenetic silencer. Due to its blue-shifted spectrum, Phobos^{CA} can be combined with red-light-sensitive CCRs for all-optical circuit analysis. Indeed, I showed that in transgenic *Drosophila* larvae expressing the red-light-activated *Cs*Chrimson in C4da sensory neurons and Phobos^{CA} in downstream A08n neurons, activation of Phobos^{CA} with blue light could inhibit sensory input evoked by red-light induced activation of *Cs*Chrimson (Fig. 3.1.3 E, F). Under these experimental conditions, there is no risk that the red light

used to activate *Cs*Chrimson could also reduce Phobos^{CA} silencing capacity by inducing channel closure, since Phobos^{CA} requires orders of magnitude higher red-shifted light irradiance for effective accelerated closing (6.9 mW/mm^2 compared to 55 µW/mm^2 for *Cs*Chrimson activation). However, as described before (see section 1.3.3, Fig. 1.4), red-light-sensitive ChRs are also partially activated by blue light at high irradiances, and therefore, upon blue-light illumination, not only Phobos^{CA} but also *Cs*Chrimson was activated (Fig. 3.1.3. F, purple bars). In this case, the use of the step-function Phobos^{CA}, which has several-fold slower closing kinetics compared to *Cs*Chrimson, allowed to dissociate optogenetic inhibition from *Cs*Chrimson-mediated excitation a few milliseconds after the light offset. An alternative way to circumvent blue-light residual excitation of CsChrimson in this context, would be to distribute the radiant flux required to activate Phobos^{CA} over a longer period of time, exploiting its light-integrating properties. In this case, irradiance can be strongly reduced, so that it stays below the activation threshold for *Cs*Chrimson.

4.1.4. A new family of rapidly desensitizing ACRs: MerMAIDs

MerMAIDs are a distinct family of ACRs identified from DNA samples of various marine microorganisms collected by the *Tara* Oceans project (Oppermann et al., 2019). This finding raised the possibility that ChR-like genes were not limited to algae, such as chlorophytes and cryptophytes from which the natural CCRs and ACRs had been identified, but instead, could be found among other protists. Indeed, Govorunova and colleagues have recently reported two new distinct ACR families from labyrinthulea, a class of aquatic heterotrophic microbes, and haptophytes, flagellate algae distantly related to cryptophytes (Govorunova et al., 2020) (Fig. 4.1).

By the time of their discovery, MerMAIDs were distinct from all other ChRs due to their unique near-complete desensitization during exposure to continuous bright light. This form of desensitization results from the accumulation of a non-conducting photocycle intermediate during constant photoactivation (Oppermann

et al., 2019). I demonstrated that, because of this distinct feature, MerMAID1 and 6 can serve as transient optogenetic silencers to inhibit a single AP at the onset of illumination without affecting subsequent APs despite continuous illumination (see section 3.1.3, Fig. 3.1.15).

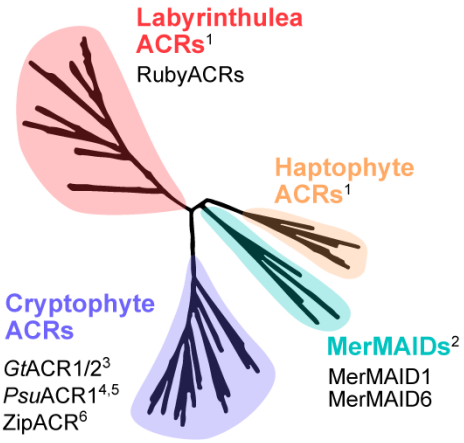

Figure 4.1. Families of natural ACRs. Schematic diagram of a phylogenetic tree encompassing the 4 different families of natural ACRs and selected members for their application in neurons (modified from (Govorunova et al., 2020)). Natural ACRs have been identified in labyrinthulea (red), haptophytes (orange), cryptophytes (purple) and various marine microorganisms (MerMAIDs, green). References: [1](Govorunova et al., 2020), [2](Oppermann et al., 2019), [3](Govorunova et al., 2015), [4](Govorunova et al., 2016), [5](Wietek et al., 2016), [6](Govorunova et al., 2017).

In principle, the ability to block a single AP does not confer a clear advantage for optogenetic manipulations compared to the more sustained inhibition achieved with other non-inactivating ACRs like *Gt*ACR1/2 (Govorunova et al., 2015) . However, combining MerMAIDs with spectrally overlapping calcium or voltage indicators could facilitate continuous monitoring of neuronal activity during short-duration inhibition at the same wavelength.

Interestingly, a recent study has identified the cation conducting "counterpart" of MerMAIDs, that is, two cryptophyte CCRs that also rapidly desensitize under continuous illumination due to accumulation of a long-lived non-conducting photocycle intermediate (Sineshchekov et al., 2020). Yet, the evolutionary advantage that strongly desensitizing ChRs confer to the host organism remains unknown. These rapidly desensitizing CCRs could be perhaps applied in neurons, together with MerMAIDs, for temporally precise spike generation and spike block in experiments investigating integration of accurately timed excitatory and inhibitory inputs or spike-timing-dependent plasticity.

4.2. Part II: ChrimsonSA

In part II (see section 3.2), I characterized ChrimsonSA as a red-shifted optogenetic tool for activation of neurons. Based on the crystal structure of Chrimson and an extensive mutational analysis, Oda and colleagues engineered ChrimsonSA by introducing the point mutation S169A, which decreased the polarity near the Schiff base, resulting in a CCR with a peak activation wavelength beyond 600 nm and 10-fold accelerated closing kinetics (Oda et al., 2018). ChrimsonSA represents the most red-shifted microbial rhodopsin known to date (see Fig. 1.3 for an overview of all available red-light activated CCRs), a feature that makes it attractive for optogenetic applications due to the deeper tissue penetration of light of longer wavelengths (Johansson, 2010; Yaroslavsky et al., 2002). In addition, the fast closing kinetics of ChrimsonSA are comparable to other recently engineered Chrimson variants with accelerated closing kinetics (f-Chrimson and vf-Chrimson) (Mager et al., 2018), which allow high-frequency spiking up to several hundred Hz, as naturally observed in some neuronal types such as parvalbumin cortical interneurons (Hu et al., 2014). The third factor that is relevant with respect to optogenetic applications, is the low sensitivity of ChrimsonSA to blue light compared to WT Chrimson, which could in principle facilitate combination with a second blue-light sensitive CCR for dual-color independent excitation of two distinct neuronal populations. However, I showed that ChrimsonSA displayed overall reduced photocurrents, requiring 4.5-fold higher red-light irradiance to evoke AP firing compared to WT Chrimson (Fig. 3.2.1), ultimately hindering its application for reliable neuronal firing at light irradiances below 10 mW/mm^2. Reduced photocurrents have also been reported for vf-Chrimson (Mager et al., 2018), rendering these 2 fast variants among the weakest red-shifted CCRs, especially when compared to bReaChES (Rajasethupathy et al., 2015) or ChRmine (Marshel et al., 2019) (Fig. 1.3).

Enhancing the performance of ChrimsonSA

Improving the trafficking of ChrimsonSA by adding an N-terminal, Leucine-rich ER-export sequence (Lucy tag) did not have a great impact on photocurrent amplitude (Fig. 3.2.2 A, B). While the Lucy tag has been shown to enhance the surface expression of olfactory receptors (Shepard et al., 2013), as well as the expression of *Gt*ACR1 in plants (Zhou et al., 2021), it had a neutral effect on membrane trafficking of the genetically encoded voltage sensor QuasAr3 (Adam et al., 2019), questioning the general applicability of this approach to improve membrane targeting.

In contrast, adding a C-terminal Kv2.1 soma-targeting sequence (Lim et al., 2000) did not only improve membrane trafficking, but it enhanced the overall potency of the ChrimsonSA (Fig. 3.2.2 B, D-H). A similar effect was observed for somAion (Fig. 3.1.12) and somBiPOLES (Fig. 3.3.2), and is in accordance with other studies that reported soma-targeted *Gt*ACR2 and CoChR (Forli et al., 2021; Mahn et al., 2018). However, unlike ACRs, in which soma-targeting has the additional benefit of avoiding inadvertent axonal excitation (see section 4.1.1 for a detailed discussion), there is no general functional advantage of restricting CCR expression to the somatodendritic compartment, since it limits optical excitation to the soma, thereby impeding local stimulation of synaptic terminals in a specific target region. Nevertheless, this might be desired in some experimental conditions in which imaging or optogenetic manipulations of cell bodies in the target area is wanted without affecting the axons of the projecting neurons. In addition, soma-targeting of CCRs has proven to be beneficial for holographic 2-photon excitation of opsins aiming at optogenetic stimulation with temporally precise single-cell resolution (Forli et al., 2021; Shemesh et al., 2017a).

4.3. Part III: Modulating excitation/inhibition ratio with light

In part III (see section 3.3) I characterized BiPOLES, a new optogenetic tool combining the blue-light-sensitive ACR *Gt*ACR2 and the red-light-sensitive CCR Chrimson in a single fusion protein, thereby allowing dual-color bidirectional control of neuronal activity.

4.3.1. Matching the inhibitory and excitatory components

Effective combination of anion- and cation-conducting channels for light-induced manipulation of neurons requires careful consideration of several biophysical properties for each opsin, namely single-channel conductance, spectral sensitivity and kinetics. Furthermore, the electrochemical conditions of the neuronal membrane should also be considered to achieve balanced excitation and inhibition. Since the resting membrane potential is close to the Nernst potential of Cl^-, ACRs displaying a large unitary conductance are needed to efficiently shunt depolarizing currents.

In BiPOLES a blue-light sensitive ACR was combined with a red-shifted CCR, which, as all red-light sensitive rhodopsins, can also be activated by blue light, especially at high irradiances (the choice of this color scheme is further discussed in section 4.3.2). If the red-shifted excitatory opsin shows too large, blue-light sensitive photocurrents, it may compromise the silencing capacity of the ACR. Conversely, if the action spectrum of the blue-light sensitive ACR extends too far towards longer wavelengths, efficient red-light evoked spiking may get impaired. Minimizing the optical cross-talk of both channels favors inhibitory conductance under blue light illumination and increases both the light intensity range and the spectral range that allows exclusive activation of the red-shifted CCR.

It is important to note that when using a blue-ACR together with a red-CCR in experimental paradigms involving periods of inhibition in the scale of several seconds, potential Cl^- loading of the cells and subsequent inversion of the Cl^-

gradient might occur. The reason behind this is that prolonged illumination with blue light even at moderate light irradiances activates the CCR in addition to the ACR (Appendix Fig. A.6 A), and the resulting cationic influx increases the driving force for chloride. Indeed, coincident glutamatergic depolarizations have been shown to enhance $GABA_A$ receptor-dependent Cl^- influx in mature neurons (Lombardi et al., 2021), which, in turn, affects the strength of GABAergic inhibition and can ultimately lead to a shift in the GABA reversal potential (Raimondo et al., 2012). In somBiPOLES-expressing neurons the amplitude of electrically evoked IPSCs was reduced after 1 s of blue light illumination (Appendix Fig. A.6 B), likely due to an increased intracellular concentration of Cl^- and a shift in the GABA reversal potential, a putative caveat that requires further investigation. A solution to overcome this problem, though not tested so far, could be to use a train of short blue light pulses instead of continuous illumination when longer inhibition periods are required. Since Chrimson has faster closing kinetics (t_{off} = 21.4 ± 1.1) (Klapoetke et al., 2014) compared to *Gt*ACR2 (t_{off} = 75.7 ± 8.1 ms) (Govorunova et al., 2015), Chrimson would be closed between the light pulses, thereby preventing strong changes in the driving force for Cl^-, while the *Gt*ACR2-mediated Cl^- conductance would be sustained, resulting in efficient shunting.

4.3.2. Comparison of BiPOLES to other available tools for bidirectional control of neurons

BiPOLES is not the first optogenetic tool allowing bidirectional control of neuronal activity. Various combinations of the blue-light-sensitive ChR2 and orange-light-sensitive inhibitory ion pumps such as NpHR, bR, or Arch3.0 were generated previously (Carus-Cadavieco et al., 2017; Gradinaru et al., 2010; Kleinlogel et al., 2011). However, among all these variants, only the combination of ChR2-HR and eNpHR3.0 (i.e. eNPAC2.0) was successfully used *in vivo* to address neuroscientific questions in mice (Carus-Cadavieco et al., 2017; Heikenfeld et al., 2020; Vesuna et

al., 2020). BiPOLES expands the possibilities of bidirectional neuronal manipulations, since, aside from efficiently expressing in a wider array of different model systems, it also features a number of additional advantages that are discussed below. However, there are also a number of caveats associated with the strategy employed to generate BiPOLES, which will be discussed as well.

Combination of an ACR and a CCR

Ion pumps only transport one charge per absorbed photon, thus requiring high irradiance and expression levels for efficient neuronal silencing. Therefore, combining two channels, such as *Gt*ACR2 and Chrimson, rather than a pump and a channel, provides a more balanced ionic flux per absorbed photon for the inhibitory and excitatory rhodopsin. This results in a high operational light sensitivity for both inhibition and excitation by blue and red light, respectively, which is especially important for *in vivo* applications in the mammalian brain, where light scattering and absorption lead to an exponential fall-off of the irradiance over distance (Yizhar et al., 2011).

In addition, the low quantum efficiency of ion pumps limits their use with 2-photon excitation. Thus, a tool for 2-photon bidirectional optogenetic control in the same cells was lacking. In BiPOLES, the large conductance of the two channels improves the efficacy with respect to the number of conducted ions per absorbed photon, which in addition to 1:1 ACR:CCR stoichiometry anywhere on the membrane ensures reliable and reproducible anion- and/or cation conductance under locally confined 2-photon excitation (experiments done in Valentina Emiliani's lab, see section 4.3.4 and Fig. 4.3.2 for an overview of the novel applications of BiPOLES).

Since BiPOLES is composed of two channels, photocurrents do not actively move ions against their gradients, which can cause adverse side-effects (Mahn et al., 2016; Raimondo et al., 2012), but, depending on the activation ratio of the two

channels, clamps the neuronal membrane voltage anywhere between the reversal potential of *Gt*ACR2 (i.e. E_{Cl-}) and Chrimson (i.e. $E_{cations}$). Thus, the membrane voltage can be tuned depending on the ratio of blue/red light or a by a single light source tuned to wavelengths between the absorption peaks of *Gt*ACR2 and Chrimson (see Fig. 3.3.9). However, as discussed before (section 4.1.1), the silencing ability of anion channels relies on the extra- and intracellular Cl^- concentration. In the case of a depolarized Cl^- Nernst potential, opening of the anion channel may produce depolarizing currents (Raimondo et al., 2017), which can trigger action potentials or neurotransmitter release (Mahn et al., 2016, 2018). Consequently, BiPOLES may not be suitable for bidirectional control of neurons or cellular compartments with a depolarized E_{Cl-}, such as immature neurons or axon terminals. In this case, eNPAC2.0 may be more efficient, despite the own limitations of rhodopsin pumps (Mahn et al., 2016; Wiegert et al., 2017). To avoid the risk of inadvertent blue-light mediated depolarization of axons while improving bidirectional optogenetic manipulation of the somatodendritic compartment, a soma-targeted variant of BiPOLES (somBiPOLES) was generated by adding the Kv2.1 C-terminal targeting motif (Lim et al., 2000) (Fig. 3.3.2).

Inversion of the color scheme

Inverting the color of the excitatory and inhibitory opsin, compared to previous tools, restricts optical excitation in BiPOLES-expressing cells exclusively to the orange/red spectrum (Fig. 3.3.4 B, D), as the blue-light-activated, inhibitory channel *Gt*ACR2 potently shunts Chrimson-mediated, blue-light-activated excitatory photocurrents (for an illustrated explanation see Fig. 1.4). This enables scale-free and mutually exclusive spiking of two neuronal populations in combination with a second, blue-light-sensitive ChR, expressed in the second population of neurons (Fig. 3.3.10). Other applications could employ multiplexing with genetically encoded activity-indicators that require blue light for photoconversion (Moeyaert et al., 2018; Perez-Alvarez et al., 2020) or with blue-light activated enzymes (Leopold

et al., 2018; Rost et al., 2017). For example, a recent study used the blue-light-activated adenylyl cyclase bPAC (Stierl et al., 2011) to increase cAMP levels in dentate gyrus (DG) granule cells during electrical tetanic stimulation of medial perforant path to granule cell (MPP-DG) synapses, and showed that transiently enhanced cAMP signaling during MPP activity strengthens synaptic transmission and facilitates long-term potentiation (Luyben et al., 2020). Mossy cells are glutamatergic neurons in the hilus of the DG that are considered to play a major role in controlling the activity of granule cells either by providing direct excitatory input or by driving local interneurons (Scharfman, 1995; Wenzel et al., 1997). In this context, it would be interesting to investigate the contribution of mossy cell activity to cAMP-dependent synaptic plasticity in granule cells. By expressing BiPOLES in mossy cells, activity could be independently driven in this neuronal population using red light, while blue-light activation of bPAC in granule cells would not excite BiPOLES-expressing mossy cells, thereby allowing specific circuit probing.

Trafficking optimized single fusion protein

In principle, multicistronic vectors encoding two opsins under a single promoter using either an IRES (Douin et al., 2004) or a 2A ribosomal skip sequence allow expression of both optogenetic actuators from a single AAV vector (Gradinaru et al., 2010; Tang et al., 2009). Although these strategies might allow more efficient trafficking of the individual opsins to distal compartments such as axon terminals compared to tandem proteins, they do not guarantee co-localized nor stoichiometric membrane expression of both opsins, since the two proteins might get differentially targeted and distributed in the plasma membrane (see Fig. 1.3). In experiments that require bidirectional control of large numbers of cells, this may not pose a strong limitation, since precise control of single-cell activity or sub-cellular ion gradients is not so crucial.

On the contrary, a fixed stoichiometry anywhere in the cell membrane is important if local, subcellular activation of the opsins is required, such as during 2-photon excitation or when a fixed ratio of cation and anion conductance is desired between different neurons or in particular neuronal compartments, such single dendrites. This is achieved with BiPOLES, where the 2 opsins are covalently linked in a single fusion protein, thus displaying a fixed 1:1 stoichiometry and co-localization of excitatory and inhibitory conductance anywhere in the membrane, with each transduced cell exhibiting the same ACR:CCR ratio.

Compared to the first generation of tandem constructs that employed the gene-fusion strategy, which showed weak expression in mammalian neurons (Kleinlogel et al., 2011), BiPOLES was optimized by adding a membrane trafficking signal (TS) (Gradinaru et al., 2010) in the transmembrane linker. Especially the soma-targeted variant, i.e. somBiPOLES, shows strongly improved membrane expression in mammalian neurons, enabling reliable and potent optogenetic spiking and inhibition even in deep brain regions *in vivo* (see section 4.3.4 and Fig. 4.2).

4.3.3. Alternative tandem partners with different kinetics and spectral properties

A seemingly trivial but valuable advantage of the tandem strategy, is its modular architecture, allowing easy tailoring of fusion constructs fulfilling specific experimental requirements. For the engineering of BiPOLES the focus was to achieve large spectral separation of the anion and the cation conductance, which among other features, enables control with two simple light sources, such as LEDs, without the requirement of sophisticated spectral control, making its use straightforward. Aside from *Gt*ACR2 and Chrimson, the following combinations of tandem partners might be useful for particular applications.

ZipACR and f-/vf-Chrimson: *Gt*ACR2 and Chrimson are relatively slow opsins (t_{off} = 75.7 ± 8.1 ms and 21.4 ± 1.1 ms, respectively) (Govorunova et al., 2015; Klapoetke et al., 2014), limiting the spiking frequency with somBiPOLES to 20 Hz. A tandem construct with a faster CCR could in principle allow light-mediated neuronal spiking with high fidelity even at high frequencies, therefore enabling optical control of naturally fast spiking neurons such as parvalbumin cortical interneurons (H. Hu et al., 2014), or spiral ganglion neurons in the auditory system (Liberman, 1978). I demonstrated that the combination of *Gt*ACR2 and f-Chrimson (f-somBiPOLES), results in a functional tandem construct with a faster excitatory component that enables spiking at 40-60 Hz (Fig. 3.3.6). In theory, employing vf-Chrimson should allow spiking at even faster frequencies (Mager et al., 2018). However, the tandem *Gt*ACR2-vf-Chrimson (vf-somBiPOLES) failed to reliably induce AP firing due to the strongly reduced conductance of vf-Chrimson, making this combination not suitable for faithful bidirectional control of neurons.

A potential solution to achieve more reliable high frequency spiking with red light would be to engineer a fast version of a more potent red-light-activated CCR. ChRmine is the most potent red-shifted CCR to date (Marshel et al., 2019b), showing two orders of magnitude higher light sensitivity than Chrimson (see section 1.2, Fig. 1.3). Similar to the development of fast Chrimson variants ChrimsonR, f-Chrimson, vf-Chrimson and ChrimsonSA, by site-directed mutagenesis (Mager et al., 2018; Oda et al., 2018), mutations in specific residues of ChRmine could yield variants with faster closing kinetics. However, being phylogenetically closer to proton-pumping proteorhodopsin genes (Marshel et al., 2019), ChRmine exhibits little sequence similarity to other CCRs. For this reason, the mutations used to create fast ChR variants might not be easily transferable to ChRmine, thus requiring further engineering efforts. Another important consideration when using ChRmine as a tandem partner of *Gt*ACR2 is that ChRmine shows a more blue-shifted action spectrum compared to Chrimson (see paragraph below: *GtACR2 and ChRmine*).

The exchange of *Gt*ACR2 for an ACR with faster kinetics would result in more precise temporal control of inhibition, which might be useful to induce fast neural oscillations with light. A recent study reported the combination of ZipACR, a fast blue-light-sensitive ACR (Govorunova et al., 2017), with a trafficking-optimized variant of vf-Chrimson (Mager et al., 2018) via a 2A sequence (Mermet-Joret et al., 2021). The new system, Zip-IvfChr, was shown to drive neuronal firing up to 20 Hz in response to red light pulses, which is considerably slower than the spiking frequency in the range of hundreds of Hz that can be achieved with vf-Chrimson alone (Mager et al., 2018). Regarding inhibition, Zip-IvfChr suppressed individual APs within trains of high-frequency firing with short blue light pulses (Mermet-Joret et al., 2021). However, in some cases ZipACR was activated with red light at irradiance values used to stimulate vf-Chrimson, due to a red-shifted action spectrum. Together with the previously reported depolarized reversal potential, indicative of a residual cationic conductance, and occasional light-induced spikes (Kato et al., 2018), ZipACR might be limited for a bidirectional tandem opsin approach. One way to overcome this would be to develop a variant of *Gt*ACR2 with faster closing kinetics. In 2018, Kim, Kato and colleagues resolved the crystal structure of the red-shifted nACR *Gt*ACR1 (Kim et al., 2018) and generated a fast variant termed FLASH (*Gt*ACR1(R83Q/N239Q)), via structure-guided engineering (Kato et al., 2018). The N239Q mutation yielded accelerated-decay kinetics, while R83Q increased photocurrents. In the same study, the N-to-Q mutation was also introduced in *Gt*ACR2, which resulted in accelerated closing kinetics (Kato et al., 2018). Yet, the functionality of the *Gt*ACR2(N235Q) mutant was only evaluated in HEK cells. Thus, it would be interesting to further explore its applicability in neurons. Combining a fast ACR with a fast CCR would enable temporally precise bidirectional modulation of neuronal membrane voltage at frequencies of naturally-occurring brain oscillations (Buzsáki & Draguhn, 2004).

Nevertheless, achieving fast inhibition is often not so crucial. Rather, to probe the function of specific neurons in a particular behavior or brain function, prolonged inhibition of AP generation is required. For this, precise silencing of each individual AP does not offer an advantage over opening an inhibitory conductance for the entire time period in which the neurons should be silenced. In this context, step-function ACRs, such as SwiChR++ (Berndt et al., 2016) or Aion would be ideal tools, since they allow prolonged periods of silencing at low light irradiances. A tandem construct combining a blue-light-sensitive step-function ACR with a fast red-shifted CCR could represent a valuable tool for optogenetic manipulations aiming at faithful neuronal silencing in the scale of minutes to hours and, while at the same time, permitting fast optical control of spiking.

GtACR2 and ChRmine: the red-light sensitive CCR ChRmine shows a more blue-shifted action spectrum compared to Chrimson and can be potently activated by green light around 530 nm (Marshel et al., 2019). Therefore, a *Gt*ACR2-ChRmine construct might be an interesting alternative if spectrally narrow light sources, such as lasers, are available, allowing bidirectional control of neurons in the blue-green range of the spectrum (Marshel et al., 2019)This would leave an additional spectral window in the red, that can be used for a third optogenetic actuator or sensor. For example, bidirectional control of neurons with *Gt*ACR2-ChRmine could be combined with monitoring of cellular activity using the near-infrared genetically encoded calcium indicator NIR-GECO (Qian et al., 2019, 2020), or the voltage sensors QuasAr2/3 with excitation and emission spectrum above 600 nm (Adam et al., 2019; Hochbaum et al., 2014).

Broad-band activatable opsins: a further application of the tandem strategy is the generation of synergistic combinations to extend the capabilities of single rhodopsins on their own. In this context, the combination of a blue-light-sensitive ACR (e.g. *Gt*ACR2 and Phobos) with a red-shifted ACR (e.g. *Gt*ACR1 and Aurora)

(Govorunova et al., 2015) (Wietek et al., 2017), would result in an inhibitory tandem construct with broad spectral sensitivity in the visible spectrum. The same could be achieved for excitatory ChRs by combining a blue-light-sensitive CCR with a red-shifted one. A broad-band activatable “white-opsin” has been previously generated by fusing the blue-light-sensitive ChR2 (Nagel et al., 2003a) with the red-shifted CCRs C1V1 (Yizhar et al., 2011) and ReaChR (Lin et al., 2013) using site-specific re-combinational cloning (Batabyal et al., 2015) The resulting white-opsin showed increased photosensitivity to white light, which could facilitate clinical translation of optogenetic activation for vision restoration by making white-opsin-expressing neurons in a degenerated retina more sensitive to ambient light (Batabyal et al., 2015).

GtACR1/Aurora and Chrimson: combination of the red-light-activated CCR Chrimson with red-shifted ACRs, such as *Gt*ACR1 (Govorunova et al., 2015)and Aurora (Wietek et al., 2017), which have activation peaks in the range of 500-550 nm, could potentially restrict the activation spectrum of Chrimson to wavelengths above 600 nm. Moreover, this combination leaves an additional spectral window in the UV/blue part of the spectrum that, though energetically narrow, could be employed for combination with a blue-emitting Ca^{2+} sensor (XCaMP-B; Inoue et al., 2019).

4.3.4. BiPOLES and somBiPOLES enable novel kinds of neuronal manipulations

For all its aforementioned features, (som)BiPOLES expands the possibilities for optical manipulation of neuronal circuits and might become the tool of choice to address a number of yet inaccessible questions in neuroscience. In addition to the work described in this dissertation, the functionality and applicability of

(som)BiPOLES has been demonstrated in various model systems including worms, flies, mice and ferrets (Fig. 4.2) (Vierock et al., 2020).

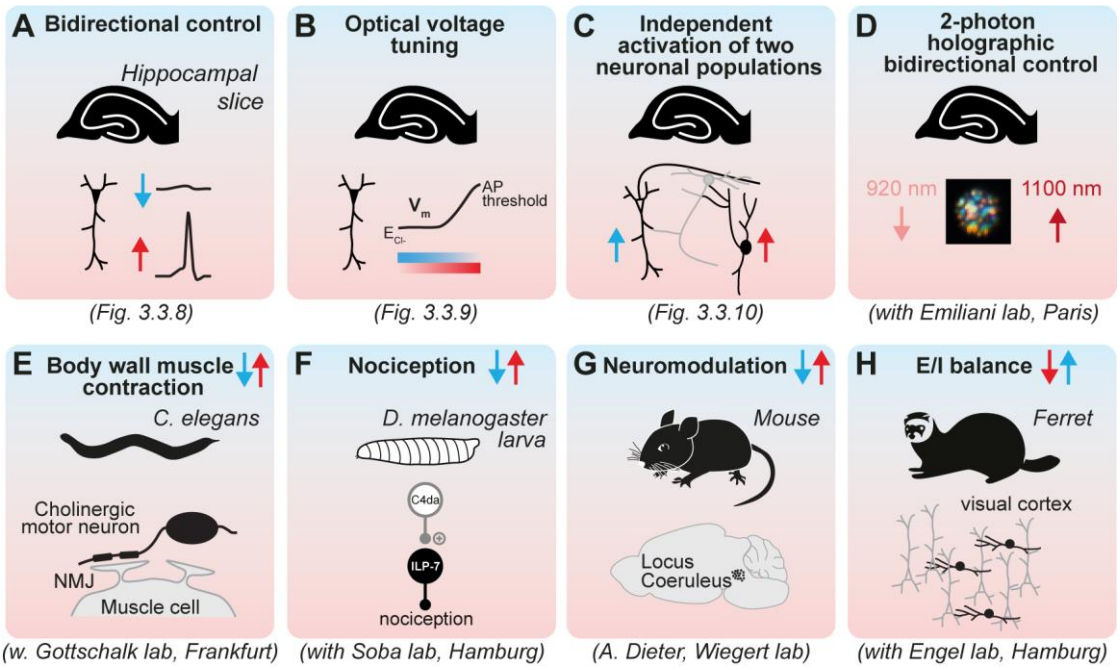

Figure 4.2 Applications of (som)BiPOLES. Schematic drawings illustrating the different manipulations of neuronal activity enabled by (som)BiPOLES with 1- or 2-photon excitation in hippocampal slices **(A-D)**, as well as its application in a wide range of invertebrate and vertebrate model organisms including worms **(E)**, fruit flies **(F)**, mice **(G)** and ferrets **(H)**. In each panel, the neurons in which (som)BiPOLES was expressed are shown in black.

In hippocampal neurons of organotypic slices I showed that (som)BiPOLES enables (1) dual-color spiking and silencing of the same neurons using red and blue light, respectively; (2) optical tuning of the membrane voltage between the Nernst potential for chloride and the action potential threshold; and (3) independent optogenetic control of two distinct neuronal populations when combined with a second, blue-light sensitive CCR (Fig. 4.2 A-C).

Moreover, somBiPOLES enables temporally precise bidirectional control of neuronal activity at single-cell resolution using holographic 2-photon excitation, as shown in hippocampal slices by the lab of Valentina Emiliani (Fig. 4.2 D). In invertebrate models, BiPOLES showed bidirectional modulation in the *C. elegans* motor system (experiments done in the lab of Alexander Gottschalk, Fig. 4.2 E), and

the *D. melanogaster* motor and nociceptive systems (experiments done in the lab of Peter Soba, Fig. 4.2 F). Regarding mammalian organisms, somBiPOLES allowed all-optical excitation and inhibition of noradrenergic neurons in the locus coeruleus in mice (experiments done in the lab of Simon Wiegert, Fig. 4.2 G); and in ferrets, BiPOLES was expressed in interneurons of the visual cortex, allowing dual-color optogenetic control of the excitation/inhibition ratio (experiments done in the lab of Andreas Engel, Fig. 4.2 H).

Further applications

Since somBiPOLES can be used to spike or inhibit the same population of mature neurons *in vivo*, a number of previously inaccessible questions can be addressed. During extracellular recordings, somBiPOLES may be useful for optogenetic silencing with blue light and concomitant optogenetic identification (optotagging) of the same neurons with red light (Lima et al., 2009). This will permit verification of the identity of silenced neurons by their spiking profiles. Moreover, in combination with a second, blue-light sensitive ChR, somBiPOLES can be used to map local networks of spatially intermingled neurons. For example, expressed in distinct types of molecularly defined GABAergic neurons, such as parvalbumin-, somatostatin- (etc…) positive cells, connectivity of these neurons to a postsynaptic target cell can be evaluated. Additional applications for somBiPOLES may encompass bidirectional control of engram neurons (Ramirez et al., 2013) to test both necessity and sufficiency of a particular set of neurons for memory retrieval, or switching the valence of a particular experience by inhibiting or activating the same or even two distinct populations of neuromodulatory neurons.

4.4. Conclusions

Perturbation of neural activity by optogenetic means is a powerful approach to assess the function of defined neuronal populations from the physiological to the behavioral level. In my thesis work, I have developed and characterized the functionality of various novel optogenetic tools that expand the possibilities for multimodal optical control of neuronal activity. In particular, three optogenetic manipulations that remained challenging with the existing toolkit, are now more easily achievable (Fig. 4.3):

1. Optogenetic silencing with precise timing for extended periods of time

2. Independent all-optical excitation of two distinct neuronal populations

3. Dual-color bidirectional control of the same neurons

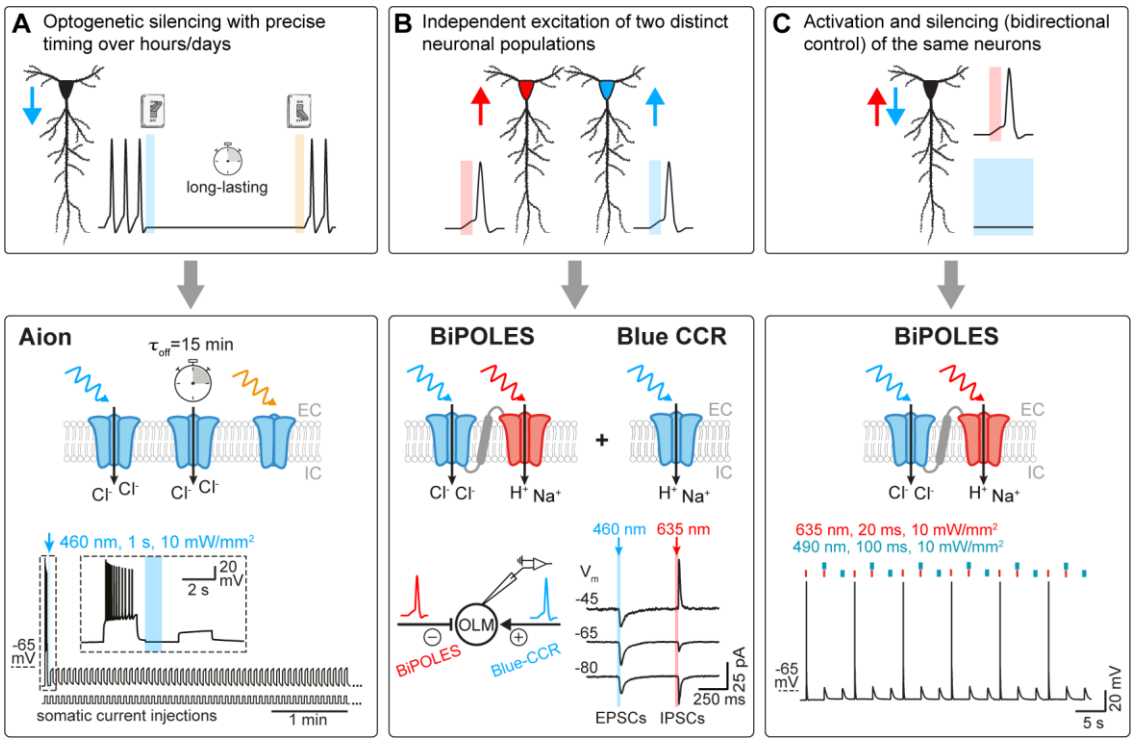

Figure 4.3. Aion and BiPOLES overcome some long-standing challenges in optogenetics. **(A)** Aion expands the available toolkit of optogenetic silencers in the temporal domain, allowing neuronal inhibition with precise timing for extended periods of time. **(B)** Optical excitation in BiPOLES-expressing cells is exclusively restricted to the orange-red spectrum, which opens new possibilities for two-color excitation of genetically distinct but spatially intermingled neuronal populations using

BiPOLES together with a second, blue-light-activated CCR. **(C)** By pairing a blue-light-sensitive ACR with a red-shifted CCR, BiPOLES allows dual-color bidirectional control of the same neurons.

In this study, I characterized a number of novel optogenetic tools with unique biophysical properties. Of those, the step-function eACR Aion and BiPOLES, a tandem construct combining *Gt*ACR2 and Chrimson, are of particular interest for the neuroscience community. Aion broadens the available toolkit of optogenetic silencers in the temporal domain, allowing precisely timed and reversible inhibition of neurons for several hours with short light pulses spaced 5 minutes apart. In addition, BiPOLES enables multiple new applications including reliable bidirectional control of neuronal activity with red and blue light, and dual-color spiking of two distinct neuronal populations when used together with a second, blue-light sensitive ChR. Altogether, the new tools will help to address a wide range of neuroscientific questions, thus shining light on the mysteries of the brain.

5. Abstract

Perturbation of neural activity by optogenetic means is a powerful approach to probe the function of defined neuronal populations from the synaptic to the behavioral level. Despite the numerous studies that in recent years have successfully employed optogenetic actuators to tackle a wide range of neuroscientific questions, there are still some remaining challenges in the field of optogenetics that demand refinement and further development of optogenetic tools with new biophysical properties.

In contrast to neuronal activation, optogenetic silencing has proven to be technically more challenging. Therefore, part of my thesis work aimed at developing and characterizing novel engineered anion-conducting channelrhodopsins (eACRs) with altered kinetics and spectrally shifted activation spectra. While the eACRs Phobos^{CA} and Aurora^{CA} expand the available toolkit of optogenetic silencers in the spectral range, Aion broadens it in the temporal domain, permitting faithful silencing of neurons over many hours with short light pulses spaced five minutes apart.

To prove necessity and sufficiency of a particular neuronal population for a specific function, it is desirable to both faithfully inhibit and activate this exact same population of neurons. In order to achieve equal subcellular distribution and a 1:1 ratio between excitatory and inhibitory action, I functionally characterized BiPOLES, a new optogenetic tool combining in a single fusion protein the blue-light-sensitive ACR *Gt*ACR2 and the red-light-sensitive cation-conducting channelrhodopsin (CCR) Chrimson. In addition to dual-color bidirectional control of neurons, BiPOLES enables multiple new applications including optical tuning of the neuronal membrane voltage, and mutual exclusive two-color excitation of two distinct neuronal populations when used together with a second, blue-light sensitive CCR.

In summary, in this work I present various novel optogenetic tools that expand the possibilities for multimodal optical control of neuronal activity, allowing manipulations that remained challenging with the existing toolkit.

Zusammenfassung

Die Manipulation neuronaler Aktivität durch optogenetische Methoden ist eine effiziente Strategie, um die Funktion definierter neuronaler Populationen von der synaptischen bis zur Verhaltensebene zu untersuchen. Trotz der zahlreichen Studien, in denen optogenetische Werkzeuge erfolgreich zur Klärung eines breiten Spektrums neurowissenschaftlicher Fragestellungen eingesetzt wurden, gibt es noch eine Vielzahl an Herausforderungen für diese Technik. Daher ist sowohl eine Optimierung und Weiterentwicklung existierender optogenetischer Werkzeuge als auch eine Entwicklung neuer Werkzeuge mit neuen biophysikalischen Eigenschaften nötig.

Im Vergleich zur Aktivierung hat sich die optogenetische Inhibition neuronaler Aktivität als technisch anspruchsvoller erwiesen. Daher zielte ein Teil meiner Dissertation auf die Entwicklung und Charakterisierung neuartiger Anionen-leitender Kanalrhodopsine (engl. ACRs) mit veränderter Kinetik und spektral verschobenen Aktivierungsspektren. Während die ACRs Phobos^{CA} und Aurora^{CA} den verfügbaren Satz optogenetischer Inhibitoren im Spektralbereich erweitern, ist Aion eine zeitlich optimierte Variante, die eine zuverlässige Inhibition von Neuronen über viele Stunden hinweg mit kurzen Lichtpulsen im Abstand von fünf Minuten erlaubt.

Um die Notwendigkeit und Hinlänglichkeit einer bestimmten neuronalen Population für eine spezifische Funktion nachzuweisen, ist es wünschenswert, genau diese Population von Neuronen sowohl zuverlässig zu inhibieren als auch zu aktivieren. BiPOLES ist ein neues optogenetisches Werkzeug, das in einem einzigen

Fusionsprotein das blaulichtempfindliche ACR *Gt*ACR2 und das rotlichtempfindliche kationenleitender Kanalrhodopsine (engl. CCR) Chrimson kombiniert. Ich habe gezeigt, dass BiPOLES eine gleichmäßige subzelluläre Verteilung und ein 1:1-Verhältnis zwischen stimulierender und inhibitorischer Wirkung zeigt. Neben der bidirektionalen Kontrolle von Neuronen mit zwei verschiedenen Wellenlängen, ermöglicht BiPOLES mehrere neue Anwendungen, darunter die präzise optische Kontrolle des neuronalen Membranpotentials und die exklusive zweifarbige Aktivierung zweier unterschiedlicher neuronaler Populationen, in Kombination mit einem zweiten, blaulichtempfindlichen CCR.

Zusammenfassend stelle ich in dieser Arbeit verschiedene neuartige optogenetische Werkzeuge vor, die die Möglichkeiten der multimodalen optischen Kontrolle neuronaler Aktivität erweitern und Manipulationen erlauben, die mit den bisher existierenden Werkzeugen nicht erreichbar waren.

6. Abbreviations

ACR anion-conducting channelrhodopsin

ACSF artificial cerebrospinal fluid

AP action potential

ATP adenosine triphosphate

ATR all-*trans* retinal

CA1 cornu Ammonis area 1

Ca^{2+} calcium

CA3 cornu Ammonis area 1

cAMP cyclic adenosine monophosphate

CCR cation-conducting channelrhodopsin

ChR channelrhodopsin

Cl^- chloride

CNG cyclic nucleotide-gated

DG dentate gyrus

DIO double-floxed inverse orientation

DIV days *in vitro*

DO double-floxed orientation

DREADD designer receptor exclusively activated by designer drug

eACR engineered ACR

$E_{cations}$ cations reversal (or Nernst) potential

E_{Cl^-} chloride reveral (or Nernst) potential

EGFP enhanced green fluorescent protein

EPSC excitatory postsynaptic current

EPSP excitatory postsynaptic potential

ER endoplasmic reticulum

FIM FTIR-based imaging method

FTIR frustrated total internal reflection

GABA *gamma*-aminobutyric acid

GECO genetically encoded calcium indicator

GPCR G-protein-coupled receptor

H^+	proton
IPSP	inhibitory postsynaptic potential
IR	infrared
IRES	internal ribosomal entry site
ISI	interstimulus interval
K^+	potassium
KCC2	K^+/Cl^- cotransporter 2
LED	light-emitting diode
nACR	natural ACR
NIR	near infrared
NKCC1	$Na^+/K^+/2Cl^-$ cotransporter 1
OLM	*oriens-lacunosum* moleculare
ORF	open reading frame
PAC	photoactivated nucleotidyl cyclase
PBS	phosphate-buffered saline
PFA	paraformaldehyde
PTL	photoswitched tethered ligand
rAAV	recombinant adeno-associated viral vector
RT	room temperature
TS	trafficking signal
TTL	transistor-transistor logic
UV	ultraviolet
VIP	vasoactive intestinal peptide
V_m	membrane voltage/potential
vRh	vertebrate rhodopsin
VTA	ventral tegmental area
WT	wild type
YFP	yellow fluorescent protein

7. Bibliography

Acsády, L., Görcs, T. J., & Freund, T. F. (1996). Different populations of vasoactive intestinal polypeptide-immunoreactive interneurons are specialized to control pyramidal cells or interneurons in the hippocampus. Neuroscience, 73(2), 317–334.

Adam, Y., Kim, J. J., Lou, S., Zhao, Y., Xie, M. E., Brinks, D., Wu, H., Mostajo-Radji, M. A., Kheifets, S., Parot, V., Chettih, S., Williams, K. J., Gmeiner, B., Farhi, S. L., Madisen, L., Buchanan, E. K., Kinsella, I., Zhou, D., Paninski, L., … Cohen, A. E. (2019). Voltage imaging and optogenetics reveal behaviour-dependent changes in hippocampal dynamics. Nature, 569(7756), 413–417.

Adamantidis, A., Arber, S., Bains, J. S., Bamberg, E., Bonci, A., Buzsáki, G., Cardin, J. A., Costa, R. M., Dan, Y., Goda, Y., Graybiel, A. M., Häusser, M., Hegemann, P., Huguenard, J. R., Insel, T. R., Janak, P. H., Johnston, D., Josselyn, S. A., Koch, C., … Wilson, R. I. (2015). Optogenetics: 10 years after ChR2 in neurons—views from the community. Nature Neuroscience, 18(9), 1202–1212.

Alberio, L., Locarno, A., Saponaro, A., Romano, E., Bercier, V., Albadri, S., Simeoni, F., Moleri, S., Pelucchi, S., Porro, A., Marcello, E., Barsotti, N., Kukovetz, K., Boender, A. J., Contestabile, A., Luo, S., Moutal, A., Ji, Y., Romani, G., … Moroni, A. (2018). A light-gated potassium channel for sustained neuronal inhibition. Nature Methods, 15(11), 969–976.

Armbruster, B. N., Li, X., Pausch, M. H., Herlitze, S., & Roth, B. L. (2007). Evolving the lock to fit the key to create a family of G protein-coupled receptors potently activated by an inert ligand. Proceedings of the National Academy of Sciences of the United States of America, 104(12), 5163–5168.

Babl, S. S., Rummell, B. P., & Sigurdsson, T. (2019). The Spatial Extent of Optogenetic Silencing in Transgenic Mice Expressing Channelrhodopsin in Inhibitory Interneurons. Cell Reports, 29(5), 1381-1395.e4.

Baker, M. (2011). Light tools. Nature Methods, 8(1), 19–22.

Balon, R., & Starcevic, V. (2020). Role of Benzodiazepines in Anxiety Disorders. Advances in Experimental Medicine and Biology, 1191, 367–388.

Bamann, C., Gueta, R., Kleinlogel, S., Nagel, G., & Bamberg, E. (2010). Structural Guidance of the Photocycle of Channelrhodopsin-2 by an Interhelical Hydrogen Bond. Biochemistry, 49(2), 267–278.

Banghart, M., Borges, K., Isacoff, E., Trauner, D., & Kramer, R. H. (2004). Light-activated ion channels for remote control of neuronal firing. Nature Neuroscience, 7(12), 1381–1386.

Barker, M. J., Greenwood, K. M., Jackson, M., & Crowe, S. F. (2004). Cognitive effects of long-term benzodiazepine use: a meta-analysis. CNS Drugs, 18(1), 37–48.

Batabyal, S., Cervenka, G., Ha, J. H., Kim, Y., & Mohanty, S. (2015). Broad-Band Activatable White-Opsin. PLOS ONE, 10(9), e0136958.

Beck, S., Yu-Strzelczyk, J., Pauls, D., Constantin, O. M., Gee, C. E., Ehmann, N., Kittel, R. J., Nagel, G., & Gao, S. (2018). Synthetic Light-Activated Ion Channels for Optogenetic Activation and Inhibition. Frontiers in Neuroscience, 12, 643.

Benasi, G., Guidi, J., Offidani, E., Balon, R., Rickels, K., & Fava, G. A. (2018). Benzodiazepines as a Monotherapy in Depressive Disorders: A Systematic Review. Psychotherapy and Psychosomatics, 87(2), 65–74.

Bergs, A., Schultheis, C., Fischer, E., Tsunoda, S. P., Erbguth, K., Husson, S. J., Govorunova, E., Spudich, J. L., Nagel, G., Gottschalk, A., & Liewald, J. F. (2018). Rhodopsin optogenetic toolbox v2.0 for light-sensitive excitation and inhibition in Caenorhabditis elegans. PLOS ONE, 13(2), e0191802.

Bernal Sierra, Y. A., Rost, B. R., Pofahl, M., Fernandes, A. M., Kopton, R. A., Moser, S., Holtkamp, D., Masala, N., Beed, P., Tukker, J. J., Oldani, S., Bönigk, W., Kohl, P., Baier, H., Schneider-Warme, F., Hegemann, P., Beck, H., Seifert, R., & Schmitz, D. (2018). Potassium channel-based optogenetic silencing. Nature Communications, 9(1), 4611.

Berndt, A., Lee, S. Y., Ramakrishnan, C., & Deisseroth, K. (2014). Structure-guided transformation of channelrhodopsin into a light-activated chloride channel. Science, 344(6182), 420–424.

Berndt, A., Lee, S. Y., Wietek, J., Ramakrishnan, C., Steinberg, E. E., Rashid, A. J., Kim, H., Park, S., Santoro, A., Frankland, P. W., Iyer, S. M., Pak, S., Ährlund-Richter, S., Delp, S. L., Malenka, R. C., Josselyn, S. A., Carlén, M., Hegemann, P., & Deisseroth, K. (2016). Structural foundations of optogenetics: Determinants of channelrhodopsin ion selectivity. Proceedings of the National Academy of Sciences of the United States of America, 113(4), 822–829.

Berndt, A., Schoenenberger, P., Mattis, J., Tye, K. M., Deisseroth, K., Hegemann, P., & Oertner, T. G. (2011). High-efficiency channelrhodopsins for fast neuronal stimulation at low light levels. Proceedings of the National Academy of Sciences of the United States of America, 108(18), 7595–7600.

Berndt, A., Yizhar, O., Gunaydin, L. A., Hegemann, P., & Deisseroth, K. (2009). Bi-stable neural state switches. Nature Neuroscience, 12(2), 229–234.

Blasco-Ibáñez, J. M., & Freund, T. F. (1995). Synaptic Input of Horizontal Interneurons in Stratum Oriens of the Hippocampal CA1 Subfield: Structural Basis of Feed-back Activation. European Journal of Neuroscience, 7(10), 2170–2180.

Booker, S. A., & Vida, I. (2018). Morphological diversity and connectivity of hippocampal interneurons. Cell and tissue research, *373*(3), 619–641.

Boyden, E. S., Zhang, F., Bamberg, E., Nagel, G., & Deisseroth, K. (2005). Millisecond-timescale, genetically targeted optical control of neural activity. Nature Neuroscience, 8(9), 1263–1268.

Brand, A. H., & Perrimon, N. (1993). Targeted gene expression as a means of altering cell fates and generating dominant phenotypes. Development, 118(2), 401–415.

Buzsáki, G., & Draguhn, A. (2004). Neuronal oscillations in cortical networks. Science, 304(5679), 1926–1929.

Carus-Cadavieco, M., Gorbati, M., Ye, L., Bender, F., van der Veldt, S., Kosse, C., Börgers, C., Lee, S. Y., Ramakrishnan, C., Hu, Y., Denisova, N., Ramm, F., Volitaki, E., Burdakov, D., Deisseroth, K., Ponomarenko, A., & Korotkova, T. (2017). Gamma oscillations organize top-down signalling to hypothalamus and enable food seeking. Nature, 542(7640), 232–236.

Chen, R., Gore, F., Nguyen, Q.-A., Ramakrishnan, C., Patel, S., Kim, S. H., Raffiee, M., Kim, Y. S., Hsueh, B., Krook-Magnusson, E., Soltesz, I., & Deisseroth, K. (2021). Deep brain optogenetics without intracranial surgery. Nature Biotechnology, 39(2), 161–164.

Chen, T.-W., Wardill, T. J., Sun, Y., Pulver, S. R., Renninger, S. L., Baohan, A., Schreiter, E. R., Kerr, R. A., Orger, M. B., Jayaraman, V., Looger, L. L., Svoboda, K., & Kim, D. S. (2013). Ultrasensitive fluorescent proteins for imaging neuronal activity. Nature, 499(7458), 295–300.

Chow, B. Y., Han, X., Dobry, A. S., Qian, X., Chuong, A. S., Li, M., Henninger, M. A., Belfort, G. M., Lin, Y., Monahan, P. E., & Boyden, E. S. (2010). High-performance genetically targetable optical neural silencing by light-driven proton pumps. Nature, 463(7277), 98–102.

Chuong, A. S., Miri, M. L., Busskamp, V., Matthews, G. A. C., Acker, L. C., Sørensen, A. T., Young, A., Klapoetke, N. C., Henninger, M. A., Kodandaramaiah, S. B., Ogawa, M., Ramanlal, S. B., Bandler, R. C., Allen, B. D., Forest, C. R., Chow, B. Y., Han, X., Lin, Y., Tye, K. M., … Boyden, E. S. (2014a). Noninvasive optical inhibition with a red-shifted microbial rhodopsin. Nature Neuroscience, 17(8), 1123–1129.

Copits, B. A., Gowrishankar, R., O'Neill, P. R., Li, J.-N., Girven, K. S., Yoo, J. J., Meshik, X., Parker, K. E., Spangler, S. M., Elerding, A. J., Brown, B. J., Shirley, S. E., Ma, K. K. L., Vasquez, A. M., Stander, M. C., Kalyanaraman, V., Vogt, S. K., Samineni, V. K., Patriarchi, T., … Bruchas, M. R. (2021). A photoswitchable GPCR-based opsin for presynaptic inhibition. Neuron, 109(11), 1791-1809.

Cosentino, C., Alberio, L., Gazzarrini, S., Aquila, M., Romano, E., Cermenati, S., Zuccolini, P., Petersen, J., Beltrame, M., van Etten, J. L., Christie, J. M., Thiel, G., & Moroni, A. (2015). Optogenetics. Engineering of a light-gated potassium channel. Science (New York, N.Y.), 348(6235), 707–710.

Crick, F. (1999). The impact of molecular biology on neuroscience. Philosophical transactions of the Royal Society of London. Series B, Biological sciences, 354(1392), 2021–2025.

Crick, F. (1979). Thinking about the brain. Scientific American, 241(3), 219–232.

Deisseroth, K. (2011). Optogenetics. Nature Methods, 8(1), 26–29.

Deisseroth, K., Feng, G., Majewska, A. K., Miesenböck, G., Ting, A., & Schnitzer, M. J. (2006). Next-generation optical technologies for illuminating genetically targeted brain circuits. The Journal of Neuroscience, 26(41), 10380–10386.

Delpire, E., & Staley, K. J. (2014). Novel determinants of the neuronal Cl− concentration. The Journal of Physiology, 592(Pt 19), 4099.

Dimidschstein, J., Chen, Q., Tremblay, R., Rogers, S. L., Saldi, G.-A., Guo, L., Xu, Q., Liu, R., Lu, C., Chu, J., Grimley, J. S., Krostag, A.-R., Kaykas, A., Avery, M. C., Rashid, M. S., Baek, M.,

Jacob, A. L., Smith, G. B., Wilson, D. E., … Fishell, G. (2016). A viral strategy for targeting and manipulating interneurons across vertebrate species. Nature Neuroscience, 19(12), 1743–1749.

Douin, V., Bornes, S., Creancier, L., Rochaix, P., Favre, G., Prats, A. C., & Couderc, B. (2004). Use and comparison of different internal ribosomal entry sites (IRES) in tricistronic retroviral vectors. BMC Biotechnology, 4(1), 16.

Dudman, J. T., Tsay, D., & Siegelbaum, S. A. (2007). A Role for Synaptic Inputs at Distal Dendrites: Instructive Signals for Hippocampal Long-Term Plasticity. Neuron, 56(5), 866–879.

Eickelbeck, D., Karapinar, R., Jack, A., Suess, S. T., Barzan, R., Azimi, Z., Surdin, T., Grömmke, M., Mark, M. D., Gerwert, K., Jancke, D., Wahle, P., Spoida, K., & Herlitze, S. (2019). CaMello-XR enables visualization and optogenetic control of Gq/11 signals and receptor trafficking in GPCR-specific domains. Communications Biology, 2(1), 60.

Emiliani, V., Cohen, A. E., Deisseroth, K., & Häusser, M. (2015). All-Optical Interrogation of Neural Circuits. The Journal of Neuroscience, 35(41), 13917–13926.

Erbguth, K., Prigge, M., Schneider, F., Hegemann, P., & Gottschalk, A. (2012). Bimodal Activation of Different Neuron Classes with the Spectrally Red-Shifted Channelrhodopsin Chimera C1V1 in Caenorhabditis elegans. PLoS ONE, 7(10), e46827.

Fenno, L., Yizhar, O., & Deisseroth, K. (2011). The Development and Application of Optogenetics. Annual Review of Neuroscience, 34(1), 389–412.

Ford, C., Law, F., Barjolin, J., Betterton, J., & Carnwath, T. (2014). Guidance for the use and reduction of misuse of benzodiazepines and other hypnotics and anxiolytics in general practice. London: European Monitoring Centre for Drugs and Drug Addiction.

Forli, A., Pisoni, M., Printz, Y., Yizhar, O., & Fellin, T. (2021). Optogenetic strategies for high-efficiency all-optical interrogation using blue-light-sensitive opsins. ELife, 10.

Gasparini, S., & Magee, J. C. (2006). State-dependent dendritic computation in hippocampal CA1 pyramidal neurons. The Journal of Neuroscience : The Official Journal of the Society for Neuroscience, 26(7), 2088–2100.

Gee, C. E., Ohmert, I., Wiegert, J. S., & Oertner, T. G. (2017). Preparation of Slice Cultures from Rodent Hippocampus. Cold Spring Harbor Protocols, 2017(2), pdb.prot094888.

Gong, X., Mendoza-Halliday, D., Ting, J. T., Kaiser, T., Sun, X., Bastos, A. M., Wimmer, R. D., Guo, B., Chen, Q., Zhou, Y., Pruner, M., Wu, C. W.-H., Park, D., Deisseroth, K., Barak, B., Boyden, E. S., Miller, E. K., Halassa, M. M., Fu, Z., … Feng, G. (2020). An Ultra-Sensitive Step-Function Opsin for Minimally Invasive Optogenetic Stimulation in Mice and Macaques. Neuron, 107(1), 38-51.e8.

Govorunova, E. G., Cunha, S. R., Sineshchekov, O. A., & Spudich, J. L. (2016). Anion channelrhodopsins for inhibitory cardiac optogenetics. Scientific Reports, 6(1), 33530.

Govorunova, E. G., Sineshchekov, O. A., Hemmati, R., Janz, R., Morelle, O., Melkonian, M., Wong, G. K.-S., & Spudich, J. L. (2018). Extending the Time Domain of Neuronal Silencing with Cryptophyte Anion Channelrhodopsins. Eneuro, 5(3).

Govorunova, E. G., Sineshchekov, O. A., Janz, R., Liu, X., & Spudich, J. L. (2015). NEUROSCIENCE. Natural light-gated anion channels: A family of microbial rhodopsins for advanced optogenetics. Science, 349(6248), 647–650.

Govorunova, E. G., Sineshchekov, O. A., Li, H., Wang, Y., Brown, L. S., & Spudich, J. L. (2020). RubyACRs, nonalgal anion channelrhodopsins with highly red-shifted absorption. Proceedings of the National Academy of Sciences of the United States of America, 117(37), 22833–22840.

Govorunova, E. G., Sineshchekov, O. A., Rodarte, E. M., Janz, R., Morelle, O., Melkonian, M., Wong, G. K.-S., & Spudich, J. L. (2017). The Expanding Family of Natural Anion Channelrhodopsins Reveals Large Variations in Kinetics, Conductance, and Spectral Sensitivity. Scientific Reports, 7, 43358.

Govorunova, E. G., Sineshchekov, O. A., & Spudich, J. L. (2016). Proteomonas sulcata ACR1: A Fast Anion Channelrhodopsin. Photochemistry and Photobiology, 92(2), 257.

Gradinaru, V., Thompson, K. R., & Deisseroth, K. (2008). eNpHR: a Natronomonas halorhodopsin enhanced for optogenetic applications. Brain Cell Biology, 36(1–4), 129–139.

Gradinaru, V., Thompson, K. R., Zhang, F., Mogri, M., Kay, K., Schneider, M. B., & Deisseroth, K. (2007). Targeting and readout strategies for fast optical neural control in vitro and in vivo. The Journal of Neuroscience : The Official Journal of the Society for Neuroscience, 27(52), 14231–14238.

Gradinaru, V., Zhang, F., Ramakrishnan, C., Mattis, J., Prakash, R., Diester, I., Goshen, I., Thompson, K. R., & Deisseroth, K. (2010). Molecular and cellular approaches for diversifying and extending optogenetics. Cell, 141(1), 154–165.

Han, X., & Boyden, E. S. (2007). Multiple-Color Optical Activation, Silencing, and Desynchronization of Neural Activity, with Single-Spike Temporal Resolution. PLoS ONE, 2(3), e299.

Heigele, S., Sultan, S., Toni, N., & Bischofberger, J. (2016). Bidirectional GABAergic control of action potential firing in newborn hippocampal granule cells. Nature Neuroscience, 19(2), 263–270

Heikenfeld, C., Mederos, S., Chen, C., Korotkova, T., Schnitzler, A., & Ponomarenko, A. (2020). Prefrontal - subthalamic pathway supports action selection in a spatial working memory task. Scientific Reports, 10(1), 10497.

Hennecke, M., Kwissa, M., Metzger, K., Oumard, A., Kröger, A., Schirmbeck, R., Reimann, J., & Hauser, H. (2001). Composition and arrangement of genes define the strength of IRES-driven translation in bicistronic mRNAs. Nucleic Acids Research, 29(16), 3327–3334.

Hochbaum, D. R., Zhao, Y., Farhi, S. L., Klapoetke, N., Werley, C. A., Kapoor, V., Zou, P., Kralj, J. M., Maclaurin, D., Smedemark-Margulies, N., Saulnier, J. L., Boulting, G. L., Straub, C., Cho, Y. K., Melkonian, M., Wong, G. K.-S., Harrison, D. J., Murthy, V. N., Sabatini, B. L., … Cohen, A. E. (2014). All-optical electrophysiology in mammalian neurons using engineered microbial rhodopsins. Nature Methods, 11(8), 825–833.

Hofmann, K. P., Scheerer, P., Hildebrand, P. W., Choe, H.-W., Park, J. H., Heck, M., & Ernst, O. P. (2009). A G protein-coupled receptor at work: the rhodopsin model. Trends in Biochemical Sciences, 34(11), 540–552.

Hososhima, S., Sakai, S., Ishizuka, T., & Yawo, H. (2015). Kinetic Evaluation of Photosensitivity in Bi-Stable Variants of Chimeric Channelrhodopsins. PLOS ONE, 10(3), e0119558.

Hu, C., Petersen, M., Hoyer, N., Spitzweck, B., Tenedini, F., Wang, D., Gruschka, A., Burchardt, L. S., Szpotowicz, E., Schweizer, M., Guntur, A. R., Yang, C.-H., & Soba, P. (2017). Sensory integration and neuromodulatory feedback facilitate Drosophila mechanonociceptive behavior. Nature Neuroscience, 20(8), 1085–1095.

Hu, H., Gan, J., & Jonas, P. (2014). Interneurons. Fast-spiking, parvalbumin^{+} GABAergic interneurons: from cellular design to microcircuit function. Science, 345(6196), 1255263.

Hwang, R. Y., Zhong, L., Xu, Y., Johnson, T., Zhang, F., Deisseroth, K., & Tracey, W. D. (2007). Nociceptive neurons protect Drosophila larvae from parasitoid wasps. Current Biology, 17(24), 2105–2116.

Inoue, K., Ono, H., Abe-Yoshizumi, R., Yoshizawa, S., Ito, H., Kogure, K., & Kandori, H. (2013). A light-driven sodium ion pump in marine bacteria. Nature Communications, 4, 1678.

Inoue, M., Takeuchi, A., Deisseroth, K., Kitamura, K., & Correspondence, H. B. (2019). Rational Engineering of XCaMPs, a Multicolor GECI Suite for In Vivo Imaging of Complex Brain Circuit Dynamics In Brief Quadricolor suite of genetically encoded calcium indicators for multiplex recording in the brain. Cell, 177.

Janovjak, H., Szobota, S., Wyart, C., Trauner, D., & Isacoff, E. Y. (2010). A light-gated, potassium-selective glutamate receptor for the optical inhibition of neuronal firing. Nature Neuroscience, 13(8), 1027–1032.

Johansson, J. D. (2010). Spectroscopic method for determination of the absorption coefficient in brain tissue. Journal of Biomedical Optics, 15(5), 057005.

Kaila, K. (1994). Ionic basis of GABAA receptor channel function in the nervous system. Progress in Neurobiology, 42(4), 489–537.

Kaila, K., Price, T. J., Payne, J. A., Puskarjov, M., & Voipio, J. (2014). Cation-chloride cotransporters in neuronal development, plasticity and disease. Nature Reviews Neuroscience, 15(10), 637–654.

Kato, H. E., Kim, Y. S., Paggi, J. M., Evans, K. E., Allen, W. E., Richardson, C., Inoue, K., Ito, S., Ramakrishnan, C., Fenno, L. E., Yamashita, K., Hilger, D., Lee, S. Y., Berndt, A., Shen, K., Kandori, H., Dror, R. O., Kobilka, B. K., & Deisseroth, K. (2018). Structural mechanisms of selectivity and gating in anion channelrhodopsins. Nature, 1.

Kato, H. E., Zhang, F., Yizhar, O., Ramakrishnan, C., Nishizawa, T., Hirata, K., Ito, J., Aita, Y., Tsukazaki, T., Hayashi, S., Hegemann, P., Maturana, A. D., Ishitani, R., Deisseroth, K., & Nureki, O. (2012). Crystal structure of the channelrhodopsin light-gated cation channel. Nature, 482(7385), 369–374.

Keene, A. C., & Sprecher, S. G. (2012). Seeing the light: photobehavior in fruit fly larvae. Trends in Neurosciences, 35(2), 104–110.

Khazipov, R., Khalilov, I., Tyzio, R., Morozova, E., Ben-Ari, Y., & Holmes, G. L. (2004). Developmental changes in GABAergic actions and seizure susceptibility in the rat hippocampus. European Journal of Neuroscience, 19(3), 590–600.

Kim, J. A., & Connors, B. W. (2012). High temperatures alter physiological properties of pyramidal cells and inhibitory interneurons in hippocampus. Frontiers in Cellular Neuroscience, 6, 27.

Kim, Y. S., Kato, H. E., Yamashita, K., Ito, S., Inoue, K., Ramakrishnan, C., Fenno, L. E., Evans, K. E., Paggi, J. M., Dror, R. O., Kandori, H., Kobilka, B. K., & Deisseroth, K. (2018). Crystal structure of the natural anion-conducting channelrhodopsin GtACR1. Nature, 561(7723), 343–348.

Klapoetke, N. C., Murata, Y., Kim, S. S., Pulver, S. R., Birdsey-Benson, A., Cho, Y. K., Morimoto, T. K., Chuong, A. S., Carpenter, E. J., Tian, Z., Wang, J., Xie, Y., Yan, Z., Zhang, Y., Chow, B. Y., Surek, B., Melkonian, M., Jayaraman, V., Constantine-Paton, M., … Boyden, E. S. (2014). Independent optical excitation of distinct neural populations. Nature Methods, 11(3), 338–346.

Kleinlogel, S., Terpitz, U., Legrum, B., Gökbuget, D., Boyden, E. S., Bamann, C., Wood, P. G., & Bamberg, E. (2011). A gene-fusion strategy for stoichiometric and co-localized expression of light-gated membrane proteins. Nature Methods, 8(12), 1083–1091.

Koyanagi, M., & Terakita, A. (2014). Diversity of animal opsin-based pigments and their optogenetic potential. Biochimica et Biophysica Acta (BBA) - Bioenergetics, 1837(5), 710–716.

Lai, S.-L., & Lee, T. (2006). Genetic mosaic with dual binary transcriptional systems in Drosophila. Nature Neuroscience, 9(5), 703–709.

Lee, C., Lavoie, A., Liu, J., Chen, S. X., & Liu, B. (2020). Light Up the Brain: The Application of Optogenetics in Cell-Type Specific Dissection of Mouse Brain Circuits. Frontiers in Neural Circuits, 14, 18.

Leopold, A. v, Chernov, K. G., & Verkhusha, V. v. (2018). Optogenetically controlled protein kinases for regulation of cellular signaling. Chemical Society Reviews, 47(7), 2454–2484.

Levi, D. (1944). Aion. Hesperia, 13(4), 269.

Li, N., Chen, S., Guo, Z. v, Chen, H., Huo, Y., Inagaki, H. K., Chen, G., Davis, C., Hansel, D., Guo, C., & Svoboda, K. (2019). Spatiotemporal constraints on optogenetic inactivation in cortical circuits. ELife, 8.

Li, X., Gutierrez, D. v, Hanson, M. G., Han, J., Mark, M. D., Chiel, H., Hegemann, P., Landmesser, L. T., & Herlitze, S. (2005). Fast noninvasive activation and inhibition of neural and network activity by vertebrate rhodopsin and green algae channelrhodopsin. Proceedings of the National Academy of Sciences of the United States of America, 102(49), 17816–17821.

Liberman, M. C. (1978). Auditory-nerve response from cats raised in a low-noise chamber. The Journal of the Acoustical Society of America, 63(2), 442–455.

Lim, S. T., Antonucci, D. E., Scannevin, R. H., & Trimmer, J. S. (2000). A novel targeting signal for proximal clustering of the Kv2.1 K+ channel in hippocampal neurons. Neuron, 25(2), 385–397.

Lima, S. Q., Hromádka, T., Znamenskiy, P., & Zador, A. M. (2009). PINP: a new method of tagging neuronal populations for identification during in vivo electrophysiological recording. PloS One, 4(7).

Lin, J. Y. (2011). A user's guide to channelrhodopsin variants: features, limitations and future developments. Experimental Physiology, 96(1), 19–25.

Lin, J. Y., Knutsen, P. M., Muller, A., Kleinfeld, D., & Tsien, R. Y. (2013). ReaChR: a red-shifted variant of channelrhodopsin enables deep transcranial optogenetic excitation. Nature Neuroscience, 16(10), 1499–1508.

Lin, J. Y., Sann, S. B., Zhou, K., Nabavi, S., Proulx, C. D., Malinow, R., Jin, Y., & Tsien, R. Y. (2013). Optogenetic inhibition of synaptic release with chromophore-assisted light inactivation (CALI). Neuron, 79(2), 241–253.

Lisman, J. E. (1999). Relating Hippocampal Circuitry to Function: Recall of Memory Sequences by Reciprocal Dentate–CA3 Interactions. Neuron, 22(2), 233–242.

Liu, Q., Sinnen, B. L., Boxer, E. E., Schneider, M. W., Grybko, M. J., Buchta, W. C., Gibson, E. S., Wysoczynski, C. L., Ford, C. P., Gottschalk, A., Aoto, J., Tucker, C. L., & Kennedy, M. J. (2019). A Photoactivatable Botulinum Neurotoxin for Inducible Control of Neurotransmission. Neuron, 0(0).

Lombardi, A., Jedlicka, P., Luhmann, H. J., & Kilb, W. (2021). Coincident glutamatergic depolarizations enhance GABAA receptor-dependent Cl- influx in mature and suppress Cl- efflux in immature neurons. PLOS Computational Biology, 17(1), e1008573.

Luscher, B., Shen, Q., & Sahir, N. (2011). The GABAergic deficit hypothesis of major depressive disorder. Molecular Psychiatry, 16(4), 383–406.

Luyben, T. T., Rai, J., Li, H., Georgiou, J., Avila, A., Zhen, M., Collingridge, G. L., Tominaga, T., & Okamoto, K. (2020). Optogenetic Manipulation of Postsynaptic cAMP Using a Novel Transgenic Mouse Line Enables Synaptic Plasticity and Enhances Depolarization Following Tetanic Stimulation in the Hippocampal Dentate Gyrus. Frontiers in Neural Circuits, 14, 24.

Magee, J. C. (2000). Dendritic integration of excitatory synaptic input. Nature Reviews Neuroscience, 1(3), 181–190.

Mager, T., Lopez de la Morena, D., Senn, V., Schlotte, J., D´Errico, A., Feldbauer, K., Wrobel, C., Jung, S., Bodensiek, K., Rankovic, V., Browne, L., Huet, A., Jüttner, J., Wood, P. G., Letzkus, J. J., Moser, T., & Bamberg, E. (2018). High frequency neural spiking and auditory signaling by ultrafast red-shifted optogenetics. Nature Communications, 9(1), 1750.

Mahn, M., Gibor, L., Patil, P., Cohen-Kashi Malina, K., Oring, S., Printz, Y., Levy, R., Lampl, I., & Yizhar, O. (2018). High-efficiency optogenetic silencing with soma-targeted anion-conducting channelrhodopsins. Nature Communications, 9(1), 4125.

Mahn, M., Prigge, M., Ron, S., Levy, R., & Yizhar, O. (2016). Biophysical constraints of optogenetic inhibition at presynaptic terminals. Nature Neuroscience, 19(4), 554–556.

Mahn, M., Saraf-Sinik, I., Patil, P., Pulin, M., Bitton, E., Karalis, N., Bruentgens, F., Palgi, S., Gat, A., Dine, J., Wietek, J., Davidi, I., Levy, R., Litvin, A., Zhou, F., Sauter, K., Soba, P., Schmitz, D., Lüthi, A., … Yizhar, O. (2021b). Efficient optogenetic silencing of neurotransmitter release with a mosquito rhodopsin. Neuron, 109(10), 1621-1635.e8.

Mahr, A., & Aberle, H. (2006). The expression pattern of the Drosophila vesicular glutamate transporter: a marker protein for motoneurons and glutamatergic centers in the brain. Gene Expression Patterns : GEP, 6(3), 299–309.

Malyshev, A. Y., Roshchin, M. v, Smirnova, G. R., Dolgikh, D. A., Balaban, P. M., & Ostrovsky, M. A. (2017). Chloride conducting light activated channel GtACR2 can produce both cessation of firing and generation of action potentials in cortical neurons in response to light. Neuroscience Letters, 640, 76–80.

Marshel, J. H., Kim, Y. S., Machado, T. A., Quirin, S., Benson, B., Kadmon, J., Raja, C., Chibukhchyan, A., Ramakrishnan, C., Inoue, M., Shane, J. C., McKnight, D. J., Yoshizawa, S., Kato, H. E., Ganguli, S., & Deisseroth, K. (2019b). Cortical layer-specific critical dynamics triggering perception. Science, 365(6453).

Masseck, O. A., Spoida, K., Dalkara, D., Maejima, T., Rubelowski, J. M., Wallhorn, L., Deneris, E. S., & Herlitze, S. (2014). Vertebrate Cone Opsins Enable Sustained and Highly Sensitive Rapid Control of Gi/o Signaling in Anxiety Circuitry. Neuron, 81(6), 1263–1273.

Mattis, J., Tye, K. M., Ferenczi, E. A., Ramakrishnan, C., O'Shea, D. J., Prakash, R., Gunaydin, L. A., Hyun, M., Fenno, L. E., Gradinaru, V., Yizhar, O., & Deisseroth, K. (2011). Principles for applying optogenetic tools derived from direct comparative analysis of microbial opsins. Nature Methods, 9(2), 159–172.

Mermet-Joret, N., Moreno, A., Zbela, A., Ellendersen, B. E., Krauth, N., Philipsborn, A. von, Piriz, J., Lin, J. Y., & Nabavi, S. (2021). Dual-color optical activation and suppression of neurons with high temporal precision. BioRxiv, 2021.05.05.442824.

Moeyaert, B., Holt, G., Madangopal, R., Perez-Alvarez, A., Fearey, B. C., Trojanowski, N. F., Ledderose, J., Zolnik, T. A., Das, A., Patel, D., Brown, T. A., Sachdev, R. N. S., Eickholt, B. J., Larkum, M. E., Turrigiano, G. G., Dana, H., Gee, C. E., Oertner, T. G., Hope, B. T., & Schreiter, E. R. (2018). Improved methods for marking active neuron populations. Nature Communications, 9(1), 4440.

Mohamed, G. A., Cheng, R.-K., Ho, J., Krishnan, S., Mohammad, F., Claridge-Chang, A., & Jesuthasan, S. (2017). Optical inhibition of larval zebrafish behaviour with anion channelrhodopsins. BMC Biology, 15(1), 103.

Mohammad, F., Stewart, J. C., Ott, S., Chlebikova, K., Chua, J. Y., Koh, T.-W., Ho, J., & Claridge-Chang, A. (2017). Optogenetic inhibition of behavior with anion channelrhodopsins. Nature Methods, 14(3), 271–274.

Nagai, T., Ibata, K., Park, E. S., Kubota, M., Mikoshiba, K., & Miyawaki, A. (2002). A variant of yellow fluorescent protein with fast and efficient maturation for cell-biological applications. Nature Biotechnology, 20(1), 87–90.

Nagel, G., Brauner, M., Liewald, J. F., Adeishvili, N., Bamberg, E., & Gottschalk, A. (2005). Light activation of channelrhodopsin-2 in excitable cells of Caenorhabditis elegans triggers rapid behavioral responses. Current Biology, 15(24), 2279–2284.

Nagel, G., Ollig, D., Fuhrmann, M., Kateriya, S., Musti, A. M., Bamberg, E., & Hegemann, P. (2002). Channelrhodopsin-1: a light-gated proton channel in green algae. Science (New York, N.Y.), 296(5577), 2395–2398.

Nagel, G., Szellas, T., Huhn, W., Kateriya, S., Adeishvili, N., Berthold, P., Ollig, D., Hegemann, P., & Bamberg, E. (2003). Channelrhodopsin-2, a directly light-gated cation-selective membrane channel. Proceedings of the National Academy of Sciences of the United States of America, 100(24), 13940–13945.

Nakai, J., Ohkura, M., & Imoto, K. (2001). A high signal-to-noise Ca(2+) probe composed of a single green fluorescent protein. Nature Biotechnology, 19(2), 137–141.

Nuss, P. (2015). Anxiety disorders and GABA neurotransmission: a disturbance of modulation. Neuropsychiatric Disease and Treatment, 11, 165–175.

Oda, K., Vierock, J., Oishi, S., Rodriguez-Rozada, S., Taniguchi, R., Yamashita, K., Wiegert, J. S., Nishizawa, T., Hegemann, P., & Nureki, O. (2018). Crystal structure of the red light-activated channelrhodopsin Chrimson. Nature Communications, 9(1), 3949.

Oppermann, J., Fischer, P., Silapetere, A., Liepe, B., Rodriguez-Rozada, S., Flores-Uribe, J., Peter, E., Keidel, A., Vierock, J., Kaufmann, J., Broser, M., Luck, M., Bartl, F., Hildebrandt, P., Wiegert, J. S., Béjà, O., Hegemann, P., & Wietek, J. (2019). MerMAIDs: a family of metagenomically discovered marine anion-conducting and intensely desensitizing channelrhodopsins. Nature Communications, 10(1), 3315.

Owens, D. F., Boyce, L. H., Davis, M. B., & Kriegstein, A. R. (1996). Excitatory GABA responses in embryonic and neonatal cortical slices demonstrated by gramicidin perforated-patch recordings and calcium imaging. The Journal of Neuroscience, 16(20), 6414–6423.

Packer, A. M., Russell, L. E., Dalgleish, H. W. P., & Häusser, M. (2015). Simultaneous all-optical manipulation and recording of neural circuit activity with cellular resolution in vivo. Nature Methods, 12(2), 140–146.

Palczewski, K., Kumasaka, T., Hori, T., Behnke, C. A., Motoshima, H., Fox, B. A., le Trong, I., Teller, D. C., Okada, T., Stenkamp, R. E., Yamamoto, M., & Miyano, M. (2000). Crystal structure of rhodopsin: A G protein-coupled receptor. Science (New York, N.Y.), 289(5480), 739–745.

Payne, J. A., Stevenson, T. J., & Donaldson, L. F. (1996). Molecular characterization of a putative K-Cl cotransporter in rat brain. A neuronal-specific isoform. The Journal of Biological Chemistry, 271(27), 16245–16252.

Peirson, S. N., Brown, L. A., Pothecary, C. A., Benson, L. A., & Fisk, A. S. (2018). Light and the laboratory mouse. Journal of Neuroscience Methods, 300, 26–36.

Perez-Alvarez, A., Fearey, B. C., O'Toole, R. J., Yang, W., Arganda-Carreras, I., Lamothe-Molina, P. J., Moeyaert, B., Mohr, M. A., Panzera, L. C., Schulze, C., Schreiter, E. R., Wiegert, J.

S., Gee, C. E., Hoppa, M. B., & Oertner, T. G. (2020). Freeze-frame imaging of synaptic activity using SynTagMA. Nature Communications, 11(1), 2464.

Petty, F., Trivedi, M. H., Fulton, M., & Rush, A. J. (1995). Benzodiazepines as antidepressants: does GABA play a role in depression? Biological Psychiatry, 38(9), 578–591.

Premont, R. T., & Gainetdinov, R. R. (2007). Physiological Roles of G Protein–Coupled Receptor Kinases and Arrestins. Annual Review of Physiology, 69(1), 511–534.

Qian, Y., Cosio, D. M. O., Piatkevich, K. D., Aufmkolk, S., Su, W.-C., Celiker, O. T., Schohl, A., Murdock, M. H., Aggarwal, A., Chang, Y.-F., Wiseman, P. W., Ruthazer, E. S., Boyden, E. S., & Campbell, R. E. (2020). Improved genetically encoded near-infrared fluorescent calcium ion indicators for in vivo imaging. PLOS Biology, 18(11), e3000965.

Qian, Y., Piatkevich, K. D., Mc Larney, B., Abdelfattah, A. S., Mehta, S., Murdock, M. H., Gottschalk, S., Molina, R. S., Zhang, W., Chen, Y., Wu, J., Drobizhev, M., Hughes, T. E., Zhang, J., Schreiter, E. R., Shoham, S., Razansky, D., Boyden, E. S., & Campbell, R. E. (2019). A genetically encoded near-infrared fluorescent calcium ion indicator. Nature Methods, 16(2), 171–174.

Raimondo, J. v, Kay, L., Ellender, T. J., & Akerman, C. J. (2012). Optogenetic silencing strategies differ in their effects on inhibitory synaptic transmission. Nature Neuroscience, 15(8), 1102–1104.

Raimondo, J. v., Markram, H., & Akerman, C. J. (2012). Short-term ionic plasticity at GABAergic synapses. Frontiers in Synaptic Neuroscience, 4, 5.

Raimondo, J. v, Richards, B. A., & Woodin, M. A. (2017). Neuronal chloride and excitability - the big impact of small changes. Current Opinion in Neurobiology, 43, 35–42.

Rajasethupathy, P., Sankaran, S., Marshel, J. H., Kim, C. K., Ferenczi, E., Lee, S. Y., Berndt, A., Ramakrishnan, C., Jaffe, A., Lo, M., Liston, C., & Deisseroth, K. (2015). Projections from neocortex mediate top-down control of memory retrieval. Nature, 526(7575), 653–659.

Ramirez, S., Liu, X., Lin, P.-A., Suh, J., Pignatelli, M., Redondo, R. L., Ryan, T. J., & Tonegawa, S. (2013). Creating a false memory in the hippocampus. Science (New York, N.Y.), 341(6144), 387–391.

Rickgauer, J. P., Deisseroth, K., & Tank, D. W. (2014). Simultaneous cellular-resolution optical perturbation and imaging of place cell firing fields. Nature Neuroscience, 17(12), 1816–1824.

Risse, B., Thomas, S., Otto, N., Löpmeier, T., Valkov, D., Jiang, X., & Klämbt, C. (2013). FIM, a Novel FTIR-Based Imaging Method for High Throughput Locomotion Analysis. PLoS ONE, 8(1), e53963.

Ritter, E., Stehfest, K., Berndt, A., Hegemann, P., & Bartl, F. J. (2008). Monitoring light-induced structural changes of Channelrhodopsin-2 by UV-visible and Fourier transform infrared spectroscopy. The Journal of Biological Chemistry, 283(50), 35033–35041.

Rivera, C., Voipio, J., Payne, J. A., Ruusuvuori, E., Lahtinen, H., Lamsa, K., Pirvola, U., Saarma, M., & Kaila, K. (1999). The K+/Cl− co-transporter KCC2 renders GABA hyperpolarizing during neuronal maturation. Nature, 397(6716), 251–255.

Rost, B. R., Schneider-Warme, F., Schmitz, D., & Hegemann, P. (2017). Optogenetic Tools for Subcellular Applications in Neuroscience. Neuron, 96(3), 572–603.

Rungta, R. L., Osmanski, B.-F., Boido, D., Tanter, M., & Charpak, S. (2017). Light controls cerebral blood flow in naive animals. Nature Communications, 8(1), 14191.

Scharfman, H. E. (1995). Electrophysiological evidence that dentate hilar mossy cells are excitatory and innervate both granule cells and interneurons. Journal of Neurophysiology, 74(1), 179–194.

Schindelin, J., Arganda-Carreras, I., Frise, E., Kaynig, V., Longair, M., Pietzsch, T., Preibisch, S., Rueden, C., Saalfeld, S., Schmid, B., Tinevez, J.-Y., White, D. J., Hartenstein, V., Eliceiri, K., Tomancak, P., & Cardona, A. (2012). Fiji: an open-source platform for biological-image analysis. Nature Methods, 9(7), 676–682.

Schneider, F., Grimm, C., & Hegemann, P. (2015). Biophysics of Channelrhodopsin. Annual Review of Biophysics, 44, 167–186.

Sengupta, A., Chaffiol, A., Macé, E., Caplette, R., Desrosiers, M., Lampič, M., Forster, V., Marre, O., Lin, J. Y., Sahel, J., Picaud, S., Dalkara, D., & Duebel, J. (2016). Red-shifted channelrhodopsin stimulation restores light responses in blind mice, macaque retina, and human retina. EMBO Molecular Medicine, 8(11), 1248–1264.

Shemesh, O. A., Tanese, D., Zampini, V., Linghu, C., Piatkevich, K., Ronzitti, E., Papagiakoumou, E., Boyden, E. S., & Emiliani, V. (2017). Temporally precise single-cell-resolution optogenetics. Nature Neuroscience, 20(12), 1796–1806.

Shepard, B. D., Natarajan, N., Protzko, R. J., Acres, O. W., & Pluznick, J. L. (2013). A Cleavable N-Terminal Signal Peptide Promotes Widespread Olfactory Receptor Surface Expression in HEK293T Cells. PLoS ONE, 8(7), e68758.

Shichida, Y., & Yamashita, T. (2003). Diversity of visual pigments from the viewpoint of G protein activation--comparison with other G protein-coupled receptors. Photochemical & Photobiological Sciences : Official Journal of the European Photochemistry Association and the European Society for Photobiology, 2(12), 1237–1246.

Shu, X., Lev-Ram, V., Deerinck, T. J., Qi, Y., Ramko, E. B., Davidson, M. W., Jin, Y., Ellisman, M. H., & Tsien, R. Y. (2011). A Genetically Encoded Tag for Correlated Light and Electron Microscopy of Intact Cells, Tissues, and Organisms. PLoS Biology, 9(4), e1001041.

Simpson, J. A., Fitch, W., Simpson, J. A., & Fitch, W. (1988). The excitable cell. Applied Neurophysiology, 1–15.

Sineshchekov, O. A., Govorunova, E. G., Li, H., & Spudich, J. L. (2015). Gating mechanisms of a natural anion channelrhodopsin. Proceedings of the National Academy of Sciences of the United States of America, 112(46), 14236–14241.

Sineshchekov, O. A., Govorunova, E. G., Li, H., Wang, Y., Melkonian, M., Wong, G. K.-S., Brown, L. S., & Spudich, J. L. (2020). Conductance Mechanisms of Rapidly Desensitizing Cation Channelrhodopsins from Cryptophyte Algae. MBio, 11(2).

Sineshchekov, O. A., Li, H., Govorunova, E. G., & Spudich, J. L. (2016). Photochemical reaction cycle transitions during anion channelrhodopsin gating. Proceedings of the National Academy of Sciences of the United States of America, 113(14), E1993–E2000.

Stachniak, T. J., Ghosh, A., & Sternson, S. M. (2014). Chemogenetic Synaptic Silencing of Neural Circuits Localizes a Hypothalamus→Midbrain Pathway for Feeding Behavior. Neuron, 82(4), 797–808.

Stierl, M., Stumpf, P., Udwari, D., Gueta, R., Hagedorn, R., Losi, A., Gärtner, W., Petereit, L., Efetova, M., Schwarzel, M., Oertner, T. G., Nagel, G., & Hegemann, P. (2011). Light modulation of cellular cAMP by a small bacterial photoactivated adenylyl cyclase, bPAC, of the soil bacterium Beggiatoa. The Journal of Biological Chemistry, 286(2), 1181–1188.

Stujenske, J. M., Spellman, T., & Gordon, J. A. (2015). Modeling the Spatiotemporal Dynamics of Light and Heat Propagation for In Vivo Optogenetics. Cell Reports, 12(3), 525–534.

Sun, Y., Nguyen, A. Q., Nguyen, J. P., Le, L., Saur, D., Choi, J., Callaway, E. M., & Xu, X. (2014). Cell-type-specific circuit connectivity of hippocampal CA1 revealed through Cre-dependent rabies tracing. Cell Reports, 7(1), 269–280.

Szabadics, J., Varga, C., Molnár, G., Oláh, S., Barzó, P., & Tamás, G. (2006). Excitatory effect of GABAergic axo-axonic cells in cortical microcircuits. Science (New York, N.Y.), 311(5758), 233–235.

Tang, W., Ehrlich, I., Wolff, S. B. E., Michalski, A.-M., Wölfl, S., Hasan, M. T., Lüthi, A., & Sprengel, R. (2009). Faithful expression of multiple proteins via 2A-peptide self-processing: a versatile and reliable method for manipulating brain circuits. The Journal of Neuroscience, 29(27), 8621–8629

Tracey, W. D., Wilson, R. I., Laurent, G., & Benzer, S. (2003). painless, a Drosophila Gene Essential for Nociception. Cell, 113(2), 261–273.

Turi, G. F., Li, W.-K., Chavlis, S., Pandi, I., O'Hare, J., Priestley, J. B., Grosmark, A. D., Liao, Z., Ladow, M., Zhang, J. F., Zemelman, B. V., Poirazi, P., & Losonczy, A. (2019). Vasoactive Intestinal Polypeptide-Expressing Interneurons in the Hippocampus Support Goal-Oriented Spatial Learning. Neuron, 101(6), 1150-1165.e8.

Tyan, L., Chamberland, S., Magnin, E., Camiré, O., Francavilla, R., David, L. S., Deisseroth, K., & Topolnik, L. (2014). Dendritic inhibition provided by interneuron-specific cells controls the firing rate and timing of the hippocampal feedback inhibitory circuitry. The Journal of Neuroscience, 34(13), 4534–4547.

Vesuna, S., Kauvar, I. v., Richman, E., Gore, F., Oskotsky, T., Sava-Segal, C., Luo, L., Malenka, R. C., Henderson, J. M., Nuyujukian, P., Parvizi, J., & Deisseroth, K. (2020). Deep posteromedial cortical rhythm in dissociation. Nature, 586(7827), 87–94.

Vierock, J., Rodriguez-Rozada, S., Pieper, F., Dieter, A., Bergs, A., Zeitzschel, N., Ahlbeck, J., Sauter, K., Gottschalk, A., Engel, A. K., Hegemann, P., & Wiegert, J. S. (2020). BiPOLES: a tool for bidirectional dual-color optogenetic control of neurons. BioRxiv, 2020.07.15.204347.

Vogelstein, J. T., Park, Y., Ohyama, T., Kerr, R. A., Truman, J. W., Priebe, C. E., & Zlatic, M. (2014). Discovery of brainwide neural-behavioral maps via multiscale unsupervised structure learning. Science, 344(6182), 386–392.

Volkov, O., Kovalev, K., Polovinkin, V., Borshchevskiy, V., Bamann, C., Astashkin, R., Marin, E., Popov, A., Balandin, T., Willbold, D., Büldt, G., Bamberg, E., & Gordeliy, V. (2017). Structural insights into ion conduction by channelrhodopsin 2. Science, 358(6366).

Wang, Y.-Y., Qin, J., Han, Y., Cai, J., & Xing, G.-G. (2011). Hyperthermia induces epileptiform discharges in cultured rat cortical neurons. Brain Research, 1417, 87–102.

Ward, A., Liu, J., Feng, Z., & Xu, X. Z. S. (2008). Light-sensitive neurons and channels mediate phototaxis in C. elegans. Nature Neuroscience, 11(8), 916–922.

Watanabe, H. C., Welke, K., Sindhikara, D. J., Hegemann, P., & Elstner, M. (2013). Towards an Understanding of Channelrhodopsin Function: Simulations Lead to Novel Insights of the Channel Mechanism. Journal of Molecular Biology, 425(10), 1795–1814.

Wenzel, H. J., Buckmaster, P. S., Anderson, N. L., Wenzel, M. E., & Schwartzkroin, P. A. (1997). Ultrastructural localization of neurotransmitter immunoreactivity in mossy cell axons and their synaptic targets in the rat dentate gyrus. Hippocampus, 7(5), 559–570.

Wettschureck, N., & Offermanns, S. (2005). Mammalian G Proteins and Their Cell Type Specific Functions. Physiological Reviews, 85(4), 1159–1204.

Wiegert, J. S., Gee, C. E., & Oertner, T. G. (2017a). Single-Cell Electroporation of Neurons. Cold Spring Harbor Protocols, 2017(2), pdb.prot094904.

Wiegert, J. S., Gee, C. E., & Oertner, T. G. (2017b). Viral Vector-Based Transduction of Slice Cultures. Cold Spring Harbor Protocols, 2017(2), pdb.prot094896.

Wiegert, J. S., Mahn, M., Prigge, M., Printz, Y., & Yizhar, O. (2017). Silencing Neurons: Tools, Applications, and Experimental Constraints. Neuron, 95(3), 504–529.

Wietek, J., Beltramo, R., Scanziani, M., Hegemann, P., Oertner, T. G., & Wiegert, J. S. (2015a). An improved chloride-conducting channelrhodopsin for light-induced inhibition of neuronal activity in vivo. Scientific Reports, 5(1), 14807.

Wietek, J., Broser, M., Krause, B. S., & Hegemann, P. (2016). Identification of a Natural Green Light Absorbing Chloride Conducting Channelrhodopsin from Proteomonas sulcata. The Journal of Biological Chemistry, 291(8), 4121–4127.

Wietek, J., Rodriguez-Rozada, S., Tutas, J., Tenedini, F., Grimm, C., Oertner, T. G., Soba, P., Hegemann, P., & Wiegert, J. S. (2017). Anion-conducting channelrhodopsins with tuned spectra and modified kinetics engineered for optogenetic manipulation of behavior. Scientific Reports, 7(1), 14957.

Wietek, J., Wiegert, J. S., Adeishvili, N., Schneider, F., Watanabe, H., Tsunoda, S. P., Vogt, A., Elstner, M., Oertner, T. G., & Hegemann, P. (2014). Conversion of channelrhodopsin into a light-gated chloride channel. Science, 344(6182), 409–412.

Wright, R., Raimondo, J. v., & Akerman, C. J. (2011). Spatial and Temporal Dynamics in the Ionic Driving Force for GABA A Receptors. Neural Plasticity, 2011, 1–10.

Xiang, Y., Yuan, Q., Vogt, N., Looger, L. L., Jan, L. Y., & Jan, Y. N. (2010). Light-avoidance-mediating photoreceptors tile the Drosophila larval body wall. Nature, 468(7326), 921–926.

Yamanashi, T., Maki, M., Kojima, K., Shibukawa, A., Tsukamoto, T., Chowdhury, S., Yamanaka, A., Takagi, S., & Sudo, Y. (2019). Quantitation of the neural silencing activity of anion channelrhodopsins in Caenorhabditis elegans and their applicability for long-term illumination. Scientific Reports, 9(1), 7863.

Yang, W., Carrillo-Reid, L., Bando, Y., Peterka, D. S., & Yuste, R. (2018). Simultaneous two-photon imaging and two-photon optogenetics of cortical circuits in three dimensions. ELife, 7.

Yaroslavsky, A. N., Schulze, P. C., Yaroslavsky, I. v, Schober, R., Ulrich, F., & Schwarzmaier, H.-J. (2002). Optical properties of selected native and coagulated human brain tissues in vitro in the visible and near infrared spectral range. Physics in Medicine and Biology, 47(12), 305.

Yizhar, O., Fenno, L. E., Davidson, T. J., Mogri, M., & Deisseroth, K. (2011). Optogenetics in neural systems. Neuron, 71(1), 9–34.

Yizhar, O., Fenno, L. E., Prigge, M., Schneider, F., Davidson, T. J., O'Shea, D. J., Sohal, V. S., Goshen, I., Finkelstein, J., Paz, J. T., Stehfest, K., Fudim, R., Ramakrishnan, C., Huguenard, J. R., Hegemann, P., & Deisseroth, K. (2011). Neocortical excitation/inhibition balance in information processing and social dysfunction. Nature, 477(7363), 171–178.

Zemelman, B. v, Lee, G. A., Ng, M., & Miesenböck, G. (2002). Selective photostimulation of genetically chARGed neurons. Neuron, 33(1), 15–22.

Zhang, F., Prigge, M., Beyrière, F., Tsunoda, S. P., Mattis, J., Yizhar, O., Hegemann, P., & Deisseroth, K. (2008). Red-shifted optogenetic excitation: a tool for fast neural control derived from Volvox carteri. Nature Neuroscience, 11(6), 631–633.

Zhang, F., Vierock, J., Yizhar, O., Fenno, L. E., Tsunoda, S., Kianianmomeni, A., Prigge, M., Berndt, A., Cushman, J., Polle, J., Magnuson, J., Hegemann, P., & Deisseroth, K. (2011). The microbial opsin family of optogenetic tools. Cell, 147(7), 1446–1457.

Zhang, F., Wang, L. P., Brauner, M., Liewald, J. F., Kay, K., Watzke, N., Wood, P. G., Bamberg, E., Nagel, G., Gottschalk, A., & Deisseroth, K. (2007). Multimodal fast optical interrogation of neural circuitry. Nature, 446(7136), 633–639.

Zhong, L., Hwang, R. Y., & Tracey, W. D. (2010). Pickpocket is a DEG/ENaC protein required for mechanical nociception in Drosophila larvae. Current Biology : CB, 20(5), 429–434.

Zhou, Y., Ding, M., Gao, S., Yu-Strzelczyk, J., Krischke, M., Duan, X., Leide, J., Riederer, M., Mueller, M. J., Hedrich, R., Konrad, K. R., & Nagel, G. (2021). Optogenetic control of plant growth by a microbial rhodopsin. Nature Plants, 7(2), 144–151.

8. Appendix

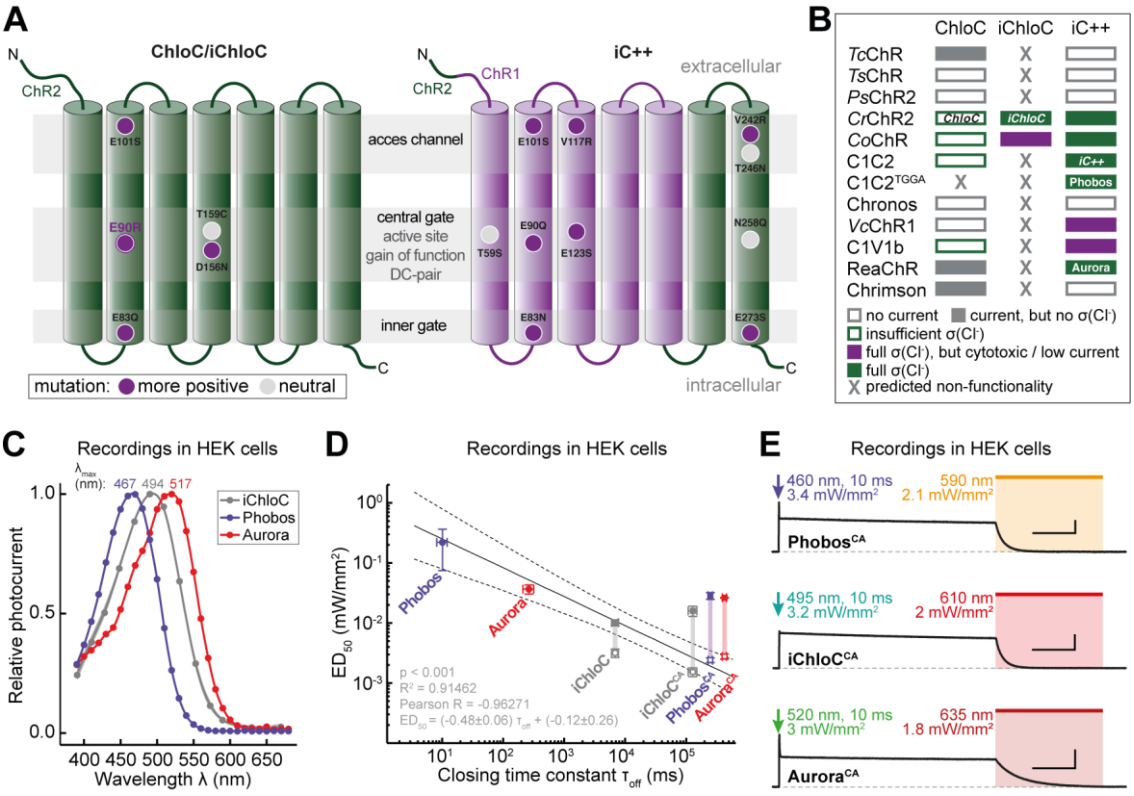

Figure A.1. Development of eACRs and characterization in HEK cells. Figure adapted from *Wietek et al. 2017*. **(C-E) Recordings in HEK cells done by Dr. Jonas Wietek. (A)** Conversion strategies yielding the eACRs ChloC/iChloC (left) and iC++ (right). The transmembrane helices of ChR2 and ChR1 are shown in green and purple, respectively. Mutations are displayed as circles at the relative position within the respective helix. ChloC has the mutations E90R and T159C, whereas in iChloC E83Q, E101S and D156N were additionally introduced. iC++ exhibits 10 mutations and a modified N-terminal sequence. **(B)** Summary of the mutation transfer approach yielding Phobos and Aurora. However, most CCR variants harboring ChloC- or iC++-mutations showed no photocurrents, or had no or only partial Cl^- conductivity ($\sigma(Cl^-)$). **(C)** Action spectra of the eACRs iChloC, Phobos and Aurora obtained by activation with a 10 ms light pulse. Peak wavelengths (indicated above) were obtained from fitting with a 3-parameter Weibull distribution. Data points show mean ± SEM (n = 6 Phobos, 7 Aurora, 6 iChloC). **(D)** ED_{50} values vs. closing time constant of eACR variants linearly correlates during extended illumination of C128A variants (12 s) except for iChloC that shows a higher sensitivity compared to other eACRs with respect to its closing time constant. Fitting statistics are shown in the figure panel. Symbols correspond to mean values ± SEM. **(E)** Typical photocurrent traces of the newly developed step-function eACRs $Phobos^{CA}$, $iChloC^{CA}$ and $Aurora^{CA}$, activated by short 10 ms light pulses at indicated wavelengths. Channel closing was facilitated with red-shifted light.

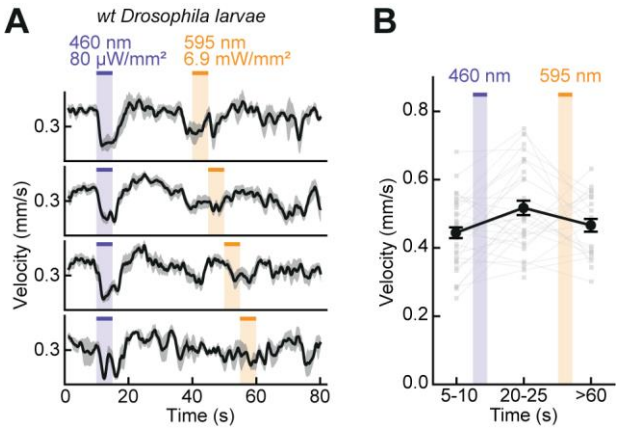

Figure A.2. Innate responses to light during *Drosophila* locomotion behavior. (A) Velocity of control *wt* larvae over time exposed to 5 s of 460 nm light and 5 s of 595 nm light (same conditions as Phobos^{CA}-expressing larvae in main figure 3.1.3, n= 38 animals, mean ± SEM). **(B)** Averaged velocity from experiments in (A) analyzed in 5 s time bins before (5-10 s), during (20-25 s) and after (>60 s) exposure to the indicated light wavelength (n= 37 animals, mean ± SEM).

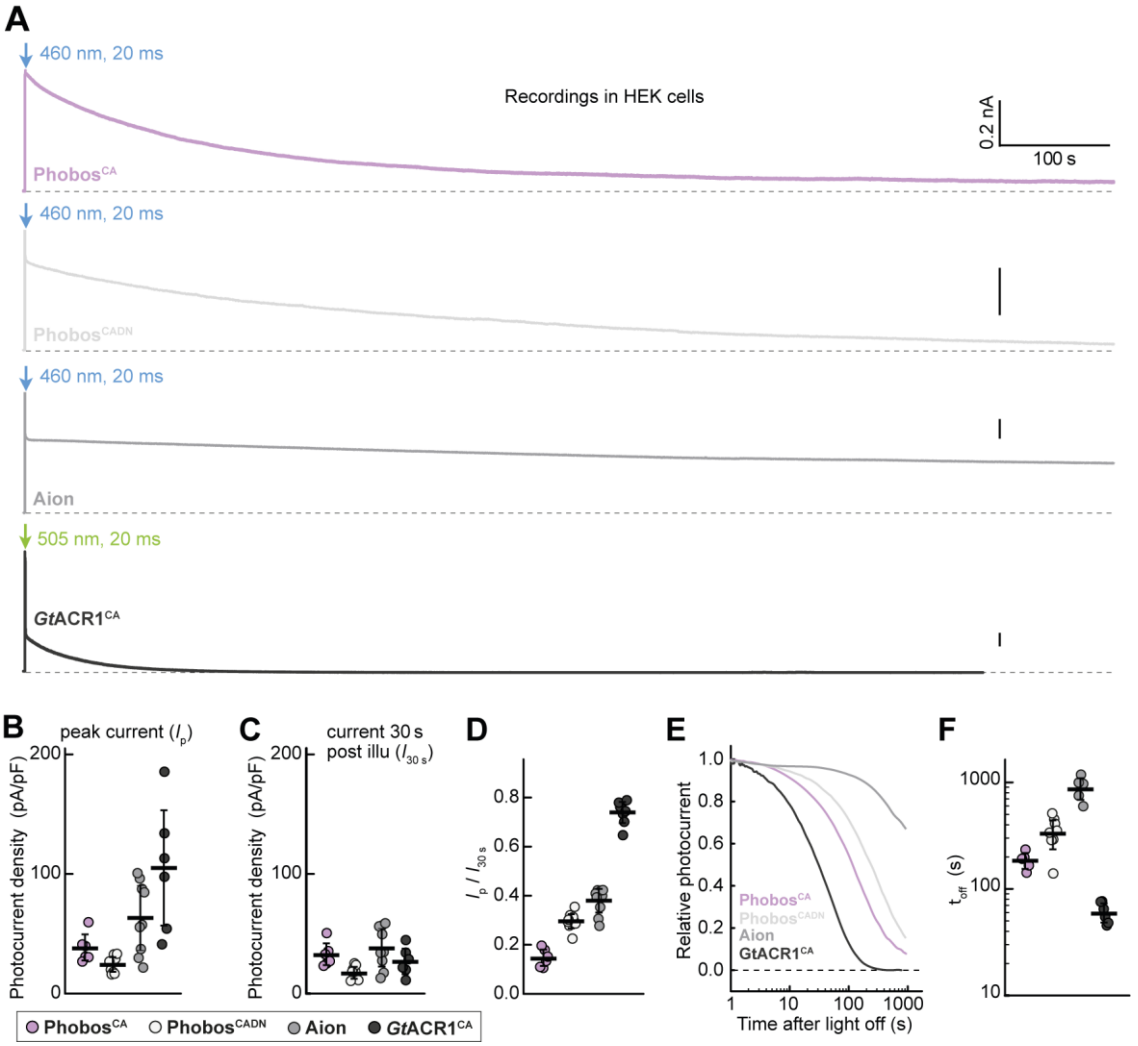

Figure A.3. Photocurrent and closing kinetics of Phobos^{CA}, Phobos^{CADN}, Aion and *Gt*ACR1^{CA} in HEK cells. Recordings done by Dr. Jonas Wietek. (A) Representative photocurrent traces of the step-function ACRs Phobos^{CA}, Phobos^{CADN}, Aion and *Gt*ACR1^{CA} activated by a short 20 ms light pulse at indicated wavelengths. **(B)** Quantification of peak photocurrent (I_p) density for each ACR. **(C)** Quantification of photocurrent density 30 s post illumination ($I_{30\,s}$). **(D)** Photocurrent ratio at 30s compared to the peak (I_p / $I_{30\,s}$). **(E)** Normalized photocurrent after light shutoff. **(F)** Closing kinetic time constants (t_{off}) for each ACR. Mean values ± SEM are shown (black lines) together with single measurement data points (circles, n = 6-8).

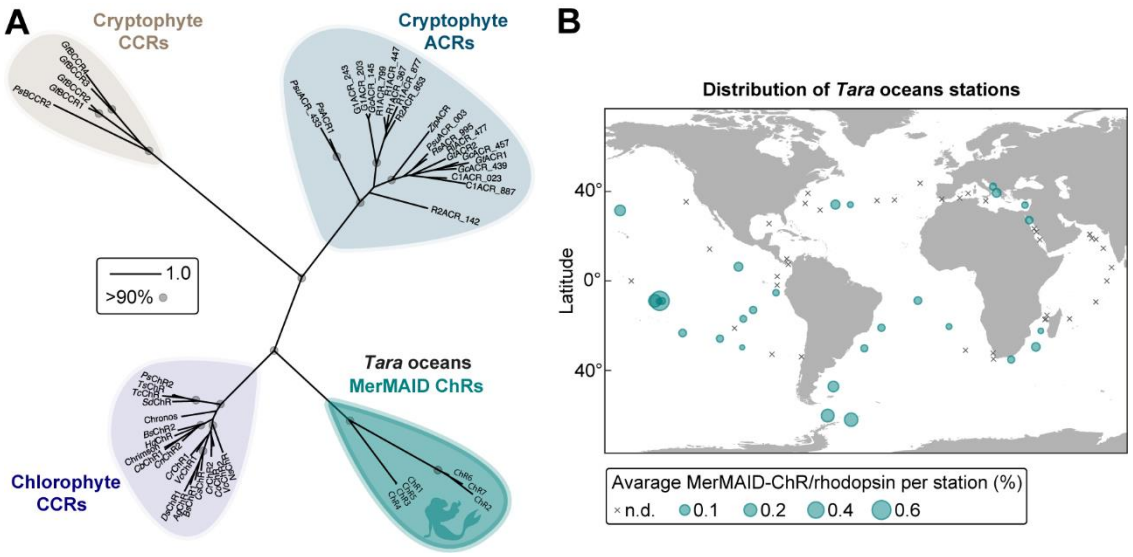

Figure A.4. Discovery of MerMAIDs from the *Tara* Oceans metagenomic datasets of marine microorganisms. Figure adapted from *Oppermann et al. 2019*. **(A)** Unrooted phylogenetic tree of the ChR superfamily, with gray circles representing bootstrap values >90%. Scale bar indicates the average number of amino acid substitutions per site. **(B)** Distribution and relative abundance of MerMAIDs in samples from the *Tara* Oceans project. Area of each circle indicates the estimated average abundance of MerMAID-like rhodopsins at different *Tara* Oceans stations. Stations were MerMAIDs were not detected (n.d.) are indicated by crosses.

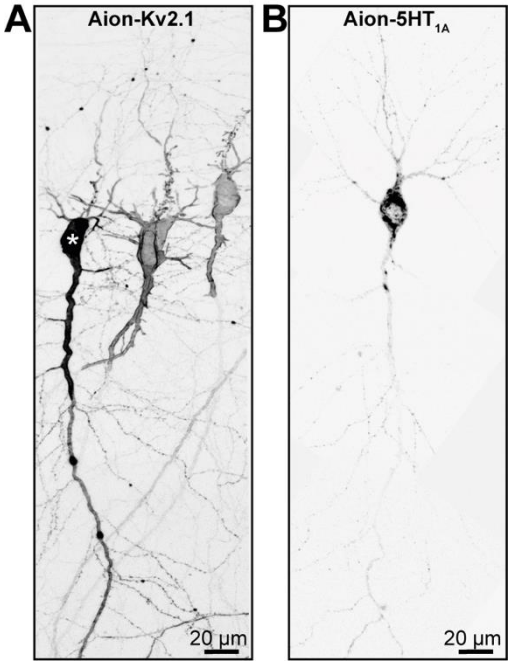

Figure A.5. Two strategies for soma-targeting of the eACR Aion. CA1 pyramidal neurons expressing soma-targeted Aion 4 to 6 days after single-cell electroporation. Images are stitched maximum intensity projections of two-photon Z-stacks. Fluorescence intensity is shown as inverted gray values. **(A)** Soma-targeting of Aion-citrine by attaching a C-terminal Kv2.1-trafficking sequence. Note efficient membrane localization of citrine fluorescence, largely restricted to the soma and main apical dendrite. In one neuron (indicated with *) strong overexpression of Aion-Kv2.1 was observed, with still apparent citrine fluorescence in the main apical dendrite further away from the soma. **(B)** Restriction of Aion-citrine to the somatodendritic compartment by adding the C-terminus domain of the 5-HT1A receptor. This strategy led to intracellular aggregates and little expression at the membrane.

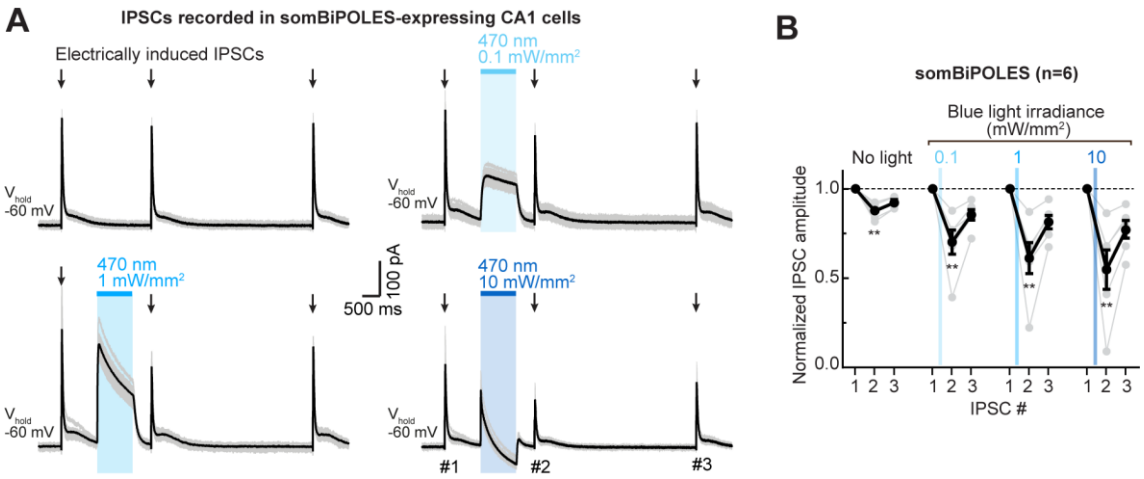

Figure A.6. Effects of prolonged blue light illumination on GABAergic currents in somBiPOLES-expressing CA1 cells. (A) Current traces of somBiPOLES-expressing CA1 pyramidal cells measured at a membrane voltage of -60 mV showing IPSCs in response to electrical stimulation (100 µA, 100 µs) of Schaffer collaterals before, 0.5 and 5 s after blue light illumination for 1 s at the indicated irradiances. To isolate GABAergic currents, glutamatergic transmission was blocked by adding NBQX and CPPene to the extracellular solution. Single trials are shown in grey and black traces represent the averaged responses. **(B)** Quantification of IPSC amplitude. For each condition, values were normalized to IPSC #1 (before blue light illumination). Grey circles and lines: averaged responses in each cell, black circles and lines: medians, n = 6, Friedman test, **p < 0.01. Note that the *Gt*ACR2-mediated outward current reverted to an inward current during illumination at 10 mW/mm^2, indicative of Chrimson conductance. Although GABAergic currents were smaller in amplitude for several seconds after blue light illumination, they were not inverted. Thus, the intracellular chloride concentration was only mildly affected.

9. Acknowledgements

This thesis would not have been possible without the support and guidance of many people.

First, I would like to thank my supervisor and mentor Prof. Dr. Simon Wiegert for his support throughout my years as a PhD student in his lab. Not only did I learn all my electrophysiology skills from you, but I have also developed as a scientist through your broad knowledge and passion for science. Your insightful feedback pushed me to sharpen my thinking and brought my work to a higher level. By supporting my attendance to conferences and summer schools I gained invaluable experience for my future career. Thank you for always having an "open door" and finding time when I needed help or advice.

I would like to thank Prof. Dr. Thomas Oertner for welcoming me to the ISP team and for his valuable guidance and helpful discussions all the way through my PhD. My thanks also to Prof. Dr. med. Andreas Engel for raising my attention to join the SFB 936 graduate program and being part of my thesis advisory committee. Special thanks to Dr. Peter Soba for a nice collaboration and for introducing me to the world of flies. I would like to thank Prof. Dr. Peter Hegemann, Dr. Johannes Vierock and Dr. Jonas Wietek for a fruitful collaboration over the years. Your contributions were crucial for this work and related publications. Prof. Dr. med. Andreas Vlachos, I truly appreciate the mentorship you have given me over the years and your belief in my future success.

I wish to express my gratitude to all the Wiegert and Oertner lab members with whom I shared my scientific journey. It has been a pleasure working with you. Special thanks to my favorite technicians Kathrin and Stefan for your work and always keeping up the good mood in the lab. Also, I would like to thank Iris Ohmert for her remarkable technical support. Wei, thank you for being my conference buddy

and for sharing your “mouse whisperer” knowledge with me. Mauro, I could not have imagined a better *colleague* to grow together with in the Wiegert lab. Brenna, you always gave me the right piece of advice – even when it comes to music, I must admit that electronic is not that bad after all – and you comforted me through all ups and downs. Maru, we both know that being away from home can sometimes be hard. Thank you for being so caring and supportive. Paul, your good vibes are contagious. You really lifted me up, whenever I needed it, in and outside the lab. Laura, you are a truly good friend. You have been my go-to person from the beginning and my main support ever since.

Outside of the lab, thanks to Carmen for her unconditional friendship, and to my dearest friend Malinka, whose unwavering support means the world to me. Also, my gratitude to Dulce María Gray for being such an inspiring woman to me. Gracias a mis abuelos maternos por ser mis mayores fans y creer siempre en mí. Yaya, todas esas velas a La Santina han surtido efecto. *Apá*, de ti heredé la vena científica. Last but not least, I would like to thank my mom, whom I cannot thank enough. Your endless support is part of my success. You raised me to be a strong, confident woman capable of achieving all my goals.

10. Curriculum Vitae

Lebenslauf wurde aus detenschutzrechtlichen Gründen entfernt

11. Eidesstattliche Versicherung

Ich versichere ausdrücklich, dass ich die Arbeit selbständig und ohne fremde Hilfe verfasst, andere als die von mir angegebenen Quellen und Hilfsmittel nicht benutzt und die aus den benutzten Werken wörtlich oder inhaltlich entnommenen Stellen einzeln nach Ausgabe (Auflage und Jahr des Erscheinens), Band und Seite des benutzten Werkes kenntlich gemacht habe.

Ferner versichere ich, dass ich die Dissertation bisher nicht einem Fachvertreter an einer anderen Hochschule zur Überprüfung vorgelegt oder mich anderweitig um Zulassung zur Promotion beworben habe.

Ich erkläre mich einverstanden, dass meine Dissertation vom Dekanat der Medizinischen Fakultät mit einer gängigen Software zur Erkennung von Plagiaten überprüft werden kann.

Unterschrift: